**Title**
Simulating Intervertebral Disc Mechanics Using Finite Element Method



**Author**
Yang, Bo

**Publication Date**
2020

Peer reviewed|Thesis/dissertation

# Simulating Intervertebral Disc Mechanics Using Finite Element Method

by

Bo Yang

A dissertation submitted in partial satisfaction of the

requirements for the degree of

Doctor of Philosophy

in

Mechancial Engineering

in the

Graduate Division

of the

University of California, Berkeley

Committee in charge:

Professor Grace D. O'Connell, Chair
Professor Tony Keaveny
Professor Per-Olof Persson

Spring 2019

**Simulating Intervertebral Disc Mechanics Using Finite Element Method**

## Abstract

Simulating Intervertebral Disc Mechanics Using Finite Element Method

by

Bo Yang

Doctor of Philosophy in Mechancial Engineering

University of California, Berkeley

Professor Grace D. O'Connell, Chair

The intervertebral disc has a complex fibrocartilaginous structure, comprised of a jel-like nucleus pulposus (NP) surrounded by the annulus fibrosus (AF) and is sandwiched between cartilaginous (CEPs) and bony endplates. Collagen fibers in AF orient in a cross-ply pattern and fiber angle to the horizontal plane decreases from $\pm 43^{\circ}$ in the inner AF to $\pm 28^{\circ}$ in the outer AF. NP, AF, and CEP are comprised primarily of water, proteoglycans (GAGs), and collagen fibers. A high GAG content gives these tissues an excellent capacity to absorb water resulting in an increase in tissue volume and swelling. *In vivo*, disc undergoes axial compression, torsion, flexion, extension, and lateral bending. Fluid flows out of the disc during the day and flows back at night exhibiting viscous effects.

Disc malfunctions including herniation and degeneration are the main contributors to low back pain. Disc herniation occurs as NP extrudes through a damaged region of the AF, compressing the spinal nerves and causing neurologic dysfunction. Painful herniations are treated with nucleotomy to remove the herniated material. Disc degeneration is noted by alterations in tissue structure and composition. These changes alter stress distributions between NP and AF, resulting in altered disc joint mechanics during loading and unloaded recovery.

Although the disc structural mechanics has been extensively studied, there are still a lot of unknowns from the literature. During my Ph.D., I studied the effects of fiber orientation, NP size and position, and nucleotomy on disc mechanics. A finite element model of the human lumbar disc based on averaged disc geometry was developed and validated. Then

the validated model was modified to do parameter studies. Simulation results showed: (1) Discs with collagen fibers oriented closer to the horizontal plane experienced a decrease in AF stresses, NP pressure, and torsional stiffness. (2) NP size had a significant impact on compressive stiffness, intradiscal pressure, and principal strain. The location of NP centroid within the disc space had a significant impact on the magnitude and distribution of intradiscal pressure in flexion and extension. (3) The effects of nucleotomy on disc mechanics differed between single and more complex loading modalities. Under single loading conditions, disc joint stiffness decreased with nucleotomy. However, more complex loading conditions resulted in an increase in bending stiffness (25 - 40%), suggesting that the disc is more resistant to bending after nucleotomy. Simulation results indicate that fiber orientation, NP size, and NP location are important factors for developing accurate computational models to study the mechanical behavior of native, injured, or degenerated discs and for creating a tissue-engineered disc. The discrepancy between single- and dual-loading conditions highlights the importance of evaluating disc joint mechanics under conditions that more closely represent *in situ* loading, which will be important for elucidating mechanisms for disc joint failure.

While multiple studies have reported disc tissues swelling, however, the effects of fiber network, fiber stiffness, GAG distribution, and boundary condition on disc swelling are not clear. Besides the relationships between disc tissue swelling and residual stress/strain/pressure formation are missing from the literature. To answer these questions, I developed finite element models for the intact disc joint and tissue subcomponents, including NP with AF and *ex situ* tissue explants (NP and CEP tissue cubes, AF rings, and rectangular AF samples based on uniaxial test specimens). Fiber orientation, fiber stiffness, and GAG content were varied to study the effects on tissue swelling and residual strain formation. Variations in GAG content and distribution replicated the healthy and degenerated discs. Simulation results showed: (1) Fiber angle, fiber architecture, and the number of lamellae in single fiber-family structures altered tissue swelling capacity, fiber deformation, and tissue rotation. (2) The kidney-bean shape played an important role in forming residual stress and strain in native AF (compressive stress and strain in the circumferential direction in the inner AF and tensile in the outer). These stretch and stress were comparable to experimental observations. GAG loss in the inner AF, as observed with degeneration, decreased circumferential direction stress by over 65%. (3) Boundary conditions created by surrounding tissues resulted in a relative decrease in swelling capacity by 40% in the NP and 25% in the AF and cartilaginous

endplate forming a uniform stretch distribution in the AF. Our model predicted a decrease in equilibrium NP pressure from 0.21 MPa in a healthy disc to 0.03 MPa in the severely degenerated disc, agreeing with data in the literature. Early degeneration decreased the circumferential-direction residual deformation by over 60% and flipped the radial-direction stretch from compressive $\sim$0.95 to tensile $\sim$1.05, which may lead to apoptosis accelerating further degeneration. Degeneration also greatly altered AF residual stress/stretch and fiber stretch in the posterior region, which may cause disc failure. Findings from these studies demonstrate the need to include the native fiber network in computational models to accurately simulate tissue-swelling behavior and the need to replicate NP swelling capacity in engineered discs to prevent degradation of the inner AF.

Water content in nucleus pulposus (NP) and annulus fibrosus (AF) decrease greatly with aging and degeneration (over 10%) resulting in altered disc joint mechanics. Water content is also a key parameter in disc computational models to simulate swelling behavior as well as nutrition transportation. Therefore, accurately measuring disc water content is important to develop accurate patient-specific disc model and to detect disc early degeneration. Using quantitative magnetic resonance imaging (MRI) to measure disc water content is a promising approach, as signal intensity depends on the single proton density within the tissue and the approach is non-invasive. However, MRI signal intensity is also dependent on scan-parameters, the concentration of free water molecules, and collagen fiber content and architecture. Therefore, how accurately MRI can quantify NP and AF water content is unclear. In this research, experiments were conducted to compare MR based water content measurement with traditional biochemical measurement (lyophilization). Experimental results showed that normalizing NP spin density by mass density provided an excellent agreement between MR measured water content and water content measured through lyophilization. However, normalizing spin density by mass density underestimated AF water content. This discrepancy is likely due to a higher concentration of bound water molecules in the AF, compared to the NP, where tightly bounded water molecules have too short T2 values to be detected in MR imaging.

To My Father, Mother, and Sisters

献给我的父亲，母亲，姐姐，和妹妹

# Contents

**Contents** **ii**

**1 Introduction** **1**
1.1 Intervertebral disc . . . 1
1.2 Low back pain & disc malfunction . . . 4
1.3 Disc modeling . . . 7
1.4 Quantitative MRI . . . 8
1.5 Dissertation outline . . . 8

**2 Effect of Collagen Fiber Orientation on Intervertebral Disc Torsion Mechanics [1]** **11**
2.1 Introduction . . . 12
2.2 Method . . . 14
2.3 Results . . . 20
2.4 Discussion . . . 26

**3 Relative Nucleus Pulposus Area and Position Alter Disc Joint Mechanics [2]** **30**
3.1 Introduction . . . 31
3.2 Method . . . 33
3.3 Results . . . 38
3.4 Discussion . . . 46

**4 Intervertebral Disc Mechanics with Nucleotomy: Differences between Simple and Complex Loading [3]** **52**
4.1 Introduction . . . 53
4.2 Method . . . 54
4.3 Result . . . 57
4.4 Discussion . . . 66

**5 Swelling of Fiber-Reinforced Soft Tissues is Affected by Fiber Orientation, Fiber Stiffness, and Lamella Structure [4]** **71**

5.1 Introduction . . . 72
5.2 Methods . . . 74
5.3 Results . . . 79
5.4 Discussion . . . 87

**6 GAG Content, Fiber Stiffness, and Fiber Angle Affect Swelling-based Residual Stress in the Intact Annulus Fibrosus [5] 94**
6.1 Introduction . . . 95
6.2 Methods . . . 97
6.3 Results . . . 103
6.4 Discussion . . . 113

**7 Intervertebral Disc Swelling Maintains Strain Homeostasis throughout the Annulus Fibrosus: Finite Element Models for Healthy and Degenerated Discs [6] 118**
7.1 Introduction . . . 119
7.2 Methods . . . 121
7.3 Results . . . 127
7.4 Discussion . . . 138

**8 Direct Quantification of Intervertebral Disc Water Content Using Magnetic Resonance Imaging [7] 144**
8.1 Introduction . . . 145
8.2 Method . . . 146
8.3 Result . . . 150
8.4 Discussion . . . 155

**9 Discussion 157**
9.1 Effects of disc structural changes . . . 157
9.2 Swelling and residual stress/strain/pressure . . . 159
9.3 Measurement of disc water content with MRI . . . 160
9.4 Future work . . . 160

**Bibliography 162**

# Acknowledgments

I would like to thank my parents and elder sister for providing almost unconditional love in my growth. Your emphasis on education has been one of the most important motivations that encourage me to pursue my Ph.D. abroad. Studying abroad is not easy for me, but I know it is also difficult for you.

I would like to thank my Ph.D. advisor Prof. Grace D. O'Connell. All my achievements during my Ph.D. are impossible without your support and guidance. Thank you for spending nights and holidays reviewing my papers, posters, and slides. I hope you can have a wonderful career and great impacts on biomechanics society.

I would like to thank Prof. Tony M. Keaveny and Prof. Per-Olof Persson. Thank you for being members of both my qualifying-exam committee and my dissertation committee. I took Orthopedic Biomechanics and Technique Writing with Prof. Keaveny. I was impressed by your thorough understanding of bone biomechanics. I had two courses on Numerical Analysis with Prof. Persson. I will always remember how concise your sample codes are. Thank you for showing me the beauty and power of Numerical Analysis.

I would like to thank Dr. Michael Wendland. I learnt all my MRI knowledge from you. Thank you for being like a grandpa and always patient.

I would like to thank my undergraduate students Colin Um and Yintong Lu. Thank you for your hard working. I am very proud of you and I know you will have great impacts some day.

I would like thank all the residents of Etcheverry 2162, especially Megan, Tongge, Saghi, Shannon, Noah, and Jonathan. I very enjoyed the time working, talking, and laughing with you.

Lastly, I want to thank Yu, you are my sunshine.

# Chapter 1

# Introduction

## 1.1 Intervertebral disc

### Structure

Human vertebral column has 33 vertebrae, which are divided into five regions: cervical region (C1 - C7), thoracic region (Th1 - Th12), lumbar region (L1 - L5), sacrum (5), and coccyx (4) (Figure 1.1). The vertebrae in the cervical, thoracic, lumbar regions, and superior sacrum are separated by intervertebral discs, which are the largest avascular tissues in the human body.

The intervertebral disc has a complex fibrocartilaginous structure, comprised of a jel-like nucleus pulposus (NP) surrounded by the annulus fibrosus (AF) and is sandwiched between cartilaginous (CEPs) and bony endplates (Figure 1.2A). The lumbar disc has a kidney-bean geometry. The NP:Disc area ratio measured from the mid-transverse plane of human cadaveric lumbar discs had an actual range between 0.25 and 0.36, with the NP centroid located posteriorly of the disc centroid by as much as 10% of the anterior-posterior width [9, 10, 11]. The AF consists of ∼20 concentric lamellae [12, 13] with collagen fibers embedded in an extrafibrillar matrix (Figure 1.2B). Fibers orient in a cross-ply pattern and fiber angle to the horizontal plane decreases from ±43° in the inner AF to ±28° in the outer AF [12].


Figure 1.1: Vertebral column structure. Figure modified from [8]

## Biochemistry

NP, AF, and CEP are comprised primarily of water, proteoglycans (GAGs), and collagen fibers, in different ratios. Specifically, healthy NP has a higher water (80-85%) and GAG content ($11.5 \pm 0.5\%$ per wet weight (ww)), and appears more gelatinous [15, 16, 17, 18]. The water content decreases to $\sim$65% in the outer AF and GAG content decreases linearly from $8.0 \pm 0.5\%$ /ww in the inner AF to $3.0 \pm 0.3\%$/ww in the outer AF [15, 19]. CEP has relative lower water (60%) and GAG contents ($3.1 \pm 0.5\%$) than NP and AF [20, 21]. In general, disc tissue has an excellent capacity to absorb water from the surrounding environment resulting in an increase in tissue volume and swelling due to a high GAG content [22, 23, 24, 25]. There are two genetic types of collagen (type I and type II) in the intervertebral disc. Central healthy NP contains exclusively type II collagen, while AF contains mainly type I collagen and I:II ratio is greater ($\sim$5) towards the periphery of the annulus [26]. The inhomogeneous distribution of collagen fibers makes the outer AF stiffer than the inner AF and anterior AF stiffer than the posterior AF [27, 28].

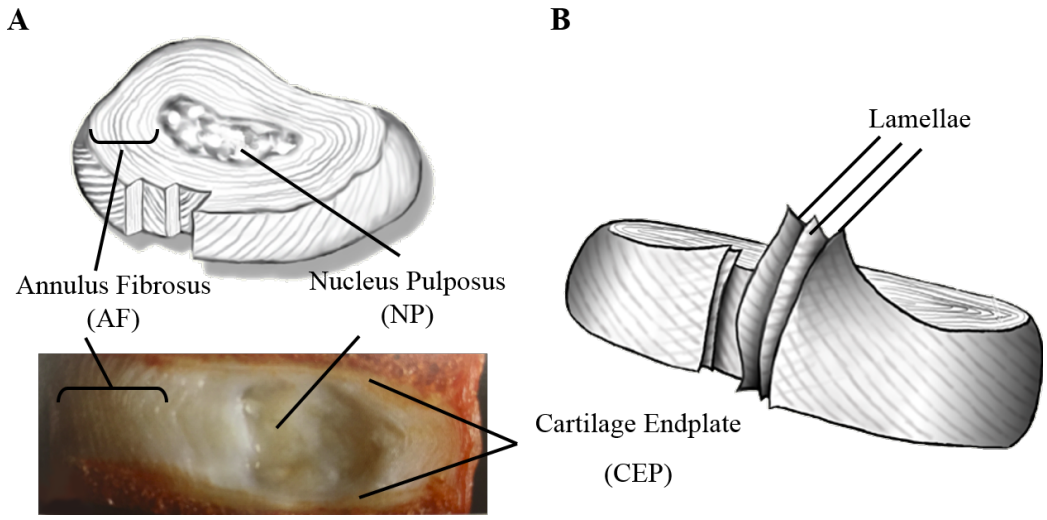


Figure 1.2: **A**. Intervertebral disc consists of nucleus pulposus (NP), annulus fibrosus (AF), and cartilage endplates (CEPs). **B**. AF has a lamellae structure. Figures modified from [9, 14]

## Mechanical function

Vertebrae column consists largely of vertebral bones providing the rigidity to the trunk, while the intervertebral discs enable the movements between the skull and pelvis including flexion, extension, lateral bending, and axial torsion [9]. *In vivo*, these movements occur in combination with axial compression due to forces placed on the vertebrae column from surrounding musculature and gravity. In healthy discs, axial compression pressurizes the NP, transferring stresses to the AF, resulting in disc bulges and tensile strains in the circumferential direction [29, 30, 31]. In flexion and extension, the NP acts as a moving pivot, migrating anteriorly and posteriorly, respectively, to redistribute the stress and strain reducing the peak values [32]. Collagen fibers have been observed in crimp status when free from load. The crimp is progressively straightened under tension, resulting in two regions of AF tissue stress-stretch curve: toe and linear regions [33, 34] (Figure 1.3).

Due to a high water content, the disc also exhibits viscous effects [35]. During the day, the disc undergoes a high dynamic load pushing water out, resulting in a decrease in disc height and volume. The disc height and volume recover back after the night's rest with water flowing back to the disc, which is driven by the chemical potential difference between

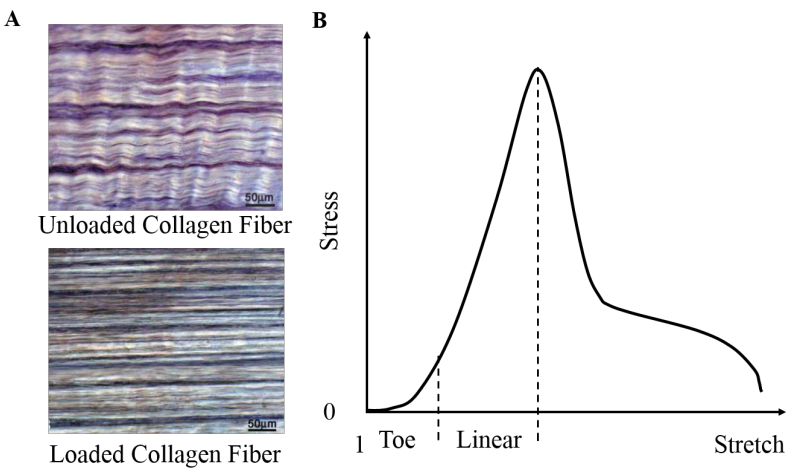


Figure 1.3: **A**. Stretching of AF sample along the collagen fiber direction. Figure modified from [33]. **B**. AF stress stretch curve has toe and linear regions.

the inner and outer disc due to a high GAG content [36, 37, 38].

Recent work showed that the inner AF experiences large region-dependent compressive residual strains, while the outer AF experiences region-dependent tensile residual strains [39, 40, 41]. The residual-strain distribution is similar to that has been observed in cardiovascular tissue, *i.e.* compressive in the inner region and tensile in the outer region [24]. Both tissue experience internal pressure under physiological loading conditions (*i.e.* NP versus blood pressure) [24, 42]. The residual stresses in the AF wall may act together with NP pressure to maintain a uniform stress distribution throughout the wall [43].

## 1.2 Low back pain & disc malfunction

Pathological changes in the intervertebral disc are thought to be a primary contributor to lower back pain, affecting over 80% of adults in the United States at some point in their lifetime [44]. Herniation and degeneration are two main causes of disc malfunctions leading to low back pain.

## Disc herniation

Each year, approximately 200,000 patients in the United States are diagnosed with a herniated or prolapsed intervertebral disc [44]. A herniated disc is one in which the gel-like NP extrudes through a damaged region of the AF, compressing the spinal nerves and causing neurologic dysfunction (Figure 1.4). Painful herniations are treated through a sub-total discectomy, a procedure that removes the herniated material as well as additional NP material, in order to reduce the risk of re-herniation. Long-term impacts of discectomy include loss of segmental stability and advanced disc degeneration, which can result in re-occurrence of lower back pain [45, 46].

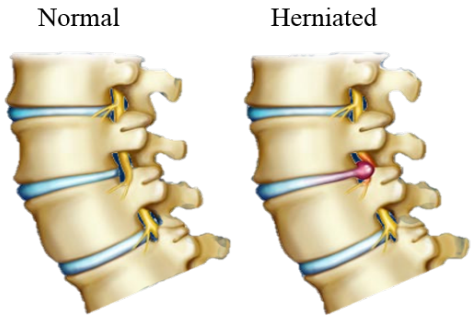


Figure 1.4: Normal and herniated discs. Figures modified from [47]

## Disc degeneration

Disc degeneration is noted by alterations in tissue structure and composition (Figure 1.5) [9, 48]. Degenerated discs are classified as Grade I-V by assessing the gross morphology of midsagittal sections or the magnetic resonance (MR) images [49, 50].

### Changes in structure

Structural changes include an increase in overall disc area, a decrease in disc height, and a decrease in the relative NP area, which is due to an increase in fibrosus at the transition zone between the NP and AF [9, 48, 51]. In addition, the development and growth of annular tears increase with aging and degeneration [52, 53]. Uniaxial tensile tests of AF specimens

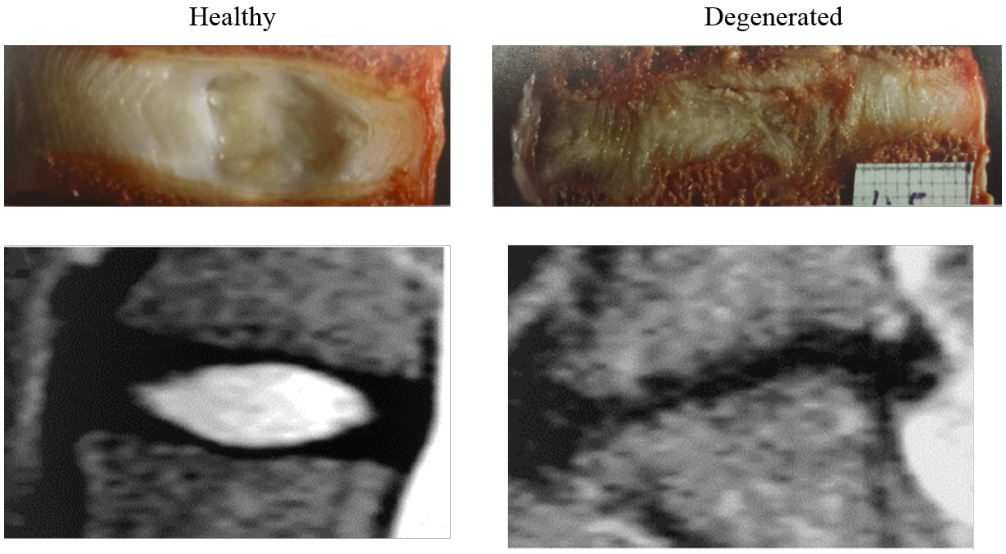


Figure 1.5: Healthy and degenerated discs. The first row presents gross morphology of the disc midsagittal section, while the second row shows the MR images of healthy and degenerated discs. Figures modified from [9, 49].

have shown that collagen fibers reoriented along the direction of applied load, and that the rate of fiber reorientation decreased with degeneration [54].

### Changes in biochemistry

NP water content decreases by up to 15% in severely degenerated discs (70-75%) [15, 17, 35, 55, 56]. GAG content also decreases greatly in the NP and inner AF. Early degeneration is marked by an initial decrease in NP GAG content, such that the NP GAG content is comparable to the inner AF GAG content (from 11%/ww to 8%/ww) [19]. Further degenerative changes result in decreases in both NP and inner AF GAG contents (> 50% decrease for Grade III degeneration) [49, 50]. In severely degenerated discs (Grades IV and V), the NP GAG content continues to decrease to concentrations below the inner AF [19]. Moreover, the CEP GAG content decreases with degeneration, particularly for discs with Schmorl's nodes [57]. In contrast, the GAG content in the outer AF remains relatively constant with degeneration [15].

### Changes in mechanics

Changes in the disc structure and material composition alter stress distributions between the NP and AF, resulting in altered disc joint mechanics during loading and unloaded recovery [29, 31, 48, 58, 59]. For example, intradiscal pressure in the NP drops greatly with degeneration, which can decrease the disc joint compressive stiffness by up to 30% [9, 35, 60]. Torsional stiffness has been shown to decrease with degeneration as well [61, 62].

## 1.3 Disc modeling

*In vivo* and *in vitro* studies have been of great value to understand lumbar disc functional biomechanics and pathological changes (herniation and degeneration). However, measuring intradiscal deformations has been a significant challenge for the field, requiring time-consuming and expensive experimental setups (*e.g.*, high resolution MR scanners or stereoradiography) [31, 58]. In addition, these experimental methods are also limited to accurately quantify fluid movement and nutrition transportation [63]. Besides, when studying disc degeneration, it is difficult to determine the contribution of each individual component, due to complex changes in tissue structure and composition that occur concurrently with degeneration.

Finite element modeling (FEM) provides an alternative tool for investigating changes in structure, composition, and mechanics in a piecewise fashion [64, 65, 66, 67, 68]. These models have been widely used to assess the role of degeneration in disc joint mechanics by altering structural or compositional properties, which can be easily altered through material property selection [65, 68]. Developing these models to mimic changes observed with injury or degeneration allows researchers to evaluate the effect of individual subcomponents on tissue- or joint-level mechanical behavior. For example, recent work using a probabilistic finite element analysis evaluated the effect of 40 different geometric parameters and found that joint level mechanics was sensitive to disc height and endplate dimensions [69].

Many models describe disc tissues as fiber reinforced hyperelastic materials (*i.e.* transversely isotropic hyperelastic) [1, 41, 65]. These materials just incorporate the solid phase and have fewer parameters to pre-determine compared to other more complicated material descriptions, such as biphasic and triphasic [38, 70], therefore are less likely to be overfitted.

However, these materials are biased as they cannot incorporate viscous effects or swelling under various aqueous solutions. To mimic soft tissue swelling, Lai and coworkers proposed a triphasic mixture material [38], which is a material that consists of a solid phase and two fluid phases (water and monovalent ions) and an imbalance in the ion concentration results in fluid movement. The triphasic material description has been used to successfully describe cartilage mechanics and nutrient diffusion in the disc [71, 72, 73, 74].

## 1.4 Quantitative MRI

MRI, as a non-invasive method, has provided great insights to diagnose disc herniation and degeneration (Figure 1.5 $2^{nd}$ row). However, these diagnoses heavily rely on the contrast of signal intensity (*i.e.* bright white versus grey or dark) [49], which is limited to detect early changes in tissue composition and develop preventative medicine strategies for injury or degeneration. To fully release the power of MRI, researchers have been trying to correlate quantitative MRI measurements with disc material compositions and properties. For example, previous studies showed that MRI quantitative measurements, such as $T_2$- or $T_{1\rho}$-weighted images, were strongly correlated with NP water and GAG contents, respectively, and could be used to detect disc early degeneration [75, 76]). Unfortunately, these quantitative approaches are limited due to the signal intensity being dependent on scan-parameters and the concentration of free water molecules in the tissue. Further difficulties in quantitative MRI may occur for tissues with a higher concentration of bound water molecules (*e.g.* $\sim$10% of water in the AF) [77], because bound water molecules have a short T2 time and do not appear in MR images [78].

## 1.5 Dissertation outline

Although disc structural mechanics has been extensively studied, there are still a lot of unknowns from the literature and my Ph.D. work has been investigating some of them.

- AF collagen fiber orientation varies widely across studies, with properties being dependent on location in the axial and transverse planes ($30°\pm 10°$) [12, 13, 27, 79, 80, 81, 82, 83]. Literature shows fiber orientation greatly affects tissue-level mechanics [84],

however, the effect of fiber orientation on disc joint mechanics, specifically disc torsion mechanics, is not well understood.

- Changes in NP size, combined with progressive structural failure, are thought to lead to mechanical dysfunction, such as an increase in disc compliance under axial compression and rotation [9, 61]. The role of NP size on disc joint mechanics, separate from changes in material properties, is not well understood and has been largely overlooked. Only a few computational studies explicitly report NP location with respect to the disc centroid [64, 85, 86, 87]. It is not clear whether the wide range of NP size and relative position of the NP within the disc space (*i.e.*, NP centroid position) affect joint-level mechanics.

- Experimental studies and finite element models have shown that NP removal affects disc joint mechanics and intradiscal deformations. Nucleotomy decreases disc joint stiffness in torsion and bending at low loads (*i.e.*, toe-region behavior), resulting in an increase in range of motion [88, 89]. Internally, nucleotomy decreases intradiscal pressure during compression, resulting in an inward bulging of the inner AF and larger maximum AF strains [30, 90, 91, 92, 93, 94]. However, all of these studies evaluated disc joint mechanics under single loading modalities, such as compression-only or bending-only loading, which are not representative of complex *in vivo* loading conditions. The effects of nucleotomy on disc mechanics under dual loading conditions (compression with torsion or bending) are not clear.

To answer these three questions, a finite element model using the hyperelastic material description was developed and validated by published experimental results. Then, parameter studies were conducted on fiber orientation, NP size and position, and nucleotomy. The results were published or submitted as three journal papers and included in this dissertation as three chapters (*i.e.* Chapters 2 - 4).

While multiple studies have reported the swelling behavior of various fiber-reinforced tissues, however, the effects of fiber orientation, fiber network complexity, fiber stiffness, and tissue geometry and boundary condition on disc swelling are not clear. Besides the relationships between disc tissue swelling and residual stress/strain/pressure formations are missing from the literature. Therefore, Chapters 5 - 7 of this dissertation focus on the study

of disc swelling. Finite element models with triphasic material description were developed and validated for parameter studies. These three chapters were also published or submitted as journal papers.

- Chapter 5 investigated the effect of collagen fiber orientation, fiber network complexity, and fiber stiffness on tissue swelling behavior.
- Chapter 6 evaluated the effect of the kidney-bean geometry on the swelling behavior of the AF, residual strain formation as a result of swelling, and the effects of GAG content, fiber angle, and fiber stiffness on swelling and residual strain formation.
- Chapter 7 studied the interactions between disc subcomponents (*i.e.* NP, AF, and CEP) under free-swelling conditions and the effect of step-wise GAG loss on disc swelling. The GAG loss replicated healthy and degenerated discs, to quantify and compare internal deformations, residual stresses and strains, and intradiscal pressure.

Accurately measuring disc water content is important to develop accurate patient-specific disc models and to detect a disc early degeneration. Using quantitative magnetic resonance imaging (MRI) to measure disc water content is a promising approach, as signal intensity depends on the proton density within the tissue and the approach is non-invasive. However, MRI signal intensity is also dependent on scan-parameters, the concentration of free water molecules, and collagen fiber content and architecture. Therefore, how accurately MRI can quantify NP and AF water content is unclear. Chapter 8, different from Chapters 2-7, focuses on experiments.

- We developed the MRI technique to measure disc water content and compared the measurement with results from the traditional lab method (lyophilization).

Following these chapters, there is a discussion chapter (*i.e.* Chater 9) that discusses the overall work, summarizes the main conclusions, and recommends future work.

# Chapter 2

# Effect of Collagen Fiber Orientation on Intervertebral Disc Torsion Mechanics [1]

## Abstract

The intervertebral disc is a complex fibro-cartilagenous material, consisting of a pressurized nucleus pulposus surrounded by the annulus fibrosus, which has an angle-ply structure. Disc injury and degeneration are noted by significant changes in tissue structure and function, which significantly alters stress distribution and disc joint stiffness. Differences in fiber orientation is thought to contribute to changes in disc torsion mechanics. Therefore, the objective of this study was to evaluate the effect of collagen fiber orientation on internal disc mechanics under compression combined with axial rotation. We developed and validated a finite element model (FEM) to delineate changes in disc mechanics due to fiber orientation from differences in material properties. FEM simulations were performed with fibers oriented at $\pm 30^\circ$ throughout the disc (uniform by region and fiber layer). The initial model was validated by published experimental results for two load conditions, including 0.48MPa axial compression and 10Nm axial rotation. Once validated, fiber orientation was rotated by $4^\circ$ or $8^\circ$ towards the horizontal plane, resulting in a decrease in disc joint torsional stiffness. Furthermore, we observed that axial rotation caused a sinusoidal change in disc height

and radial bulge, which may be beneficial for nutrient transport. In conclusion, including anatomically relevant fiber angles in disc joint FEMs is important for understanding stress distribution throughout the disc and will be important for understanding potential causes for disc injury. Future models will include regional differences in fiber orientation to better represent the fiber architecture of the native disc.

**Keywords:** Intervertebral disc; Finite element model; Torsion mechanics; Fiber orientation; Degeneration; Hyperelastic

## 2.1 Introduction

The intervertebral disc is thought to be a primary contributor to lower back pain and sciatica, with up to 80% of Americans experiencing a significant episode of debilitating back pain [44]. Occupations that consist of repetitive twisting and lifting motions result in higher rates of spine dysfunction and back pain [95, 96, 97, 98]. It is well known that the mechanical properties of the nucleus pulposus and annulus fibrosus alters disc joint mechanics. The micro-structural organization, such as collagen fiber orientation, also plays an important role in tissue- and joint-level mechanics [54]. It is difficult to determine the contribution of each individual component, due to complex changes in tissue structure and composition that occur concurrently with degeneration. Finite element models (FEMs) provide powerful tools for investigating changes in structure, composition, and mechanics in a piecewise fashion. Models that accurately describe the structural and material properties of the disc and its subcomponents are important for understanding stress distributions in healthy, injured, and degenerated discs.

The intervertebral disc is comprised of a nucleus pulposus (NP) surrounded by the annulus fibrosus (AF) and is sandwiched between two cartilaginous endplates (CEP). The AF consists of ∼20 concentric lamellae [12, 13] with fibers embedded in an extrafibrillar matrix that is comprised mostly of water and proteoglycans. Collagen fiber stiffness has been shown to be region dependent, with stiffer fibers in the outer AF than the inner AF and in the anterior AF than the posterior AF [27, 28] Cassidy et al. observed that collagen fibers are oriented at ±28° to the horizontal plane in the outer AF and increases to ±45° in the inner AF [12], while Holzapfel and coworkers reported an increase in fiber orientation from the

anterior AF to the posterior AF [27]. Few FEMs of the disc incorporate differences in fiber orientation with respect to disc location, lamellae layer, and subject variability, and these spatial differences in structural properties may play a significant role in joint-level mechanics.

*In vivo* axial rotation occurs in combination with compression, due to forces placed on the spine from surrounding musculature and gravity. In healthy discs, axial compression pressurizes the NP, transferring stresses to the AF, resulting in tensile strains in the circumferential direction [29, 30, 31]. Axial compression increases torsional stiffness of the disc joint, and early work by Shirazi-Adl suggests that the axis of rotation shifts with rotation [99, 100, 101]. While the axis of rotation is difficult to measure *in vivo*, applying pure rotation about the disc's centroid results in the AF absorbing a larger portion of the applied torque. That is, under axial rotation, AF pressure increases while NP pressure decreases, and peak tensile strains occur in the outer AF [31, 102]. Furthermore, cyclic torsional loading increases NP cell apoptosis, resulting in degeneration-like tissue remodeling and decreased torsional stiffness [95, 97, 98, 103]. However, models that simulate disc degeneration as a change in NP and AF material properties have not been successful in describing the decrease in torsional stiffness with degeneration [104]. Thus, the cause for decreased torsional stiffness may be due to structural changes rather than changes in material properties.

Disc geometry plays an important role in disc joint mechanics under axial compression, rotation, and bending [10, 105, 106, 107, 108]. For example, thicker discs experience higher axial strains, higher AF tensile stresses, and lower NP pressures during compression [107]. However, work by Nataranjan *et al.* showed that disc torsional stiffness was not sensitive to changes in disc height (fixed cross-sectional area), but was negatively correlated with changes in cross sectional area [108]. Microstructural properties, such as collagen fiber orientation, vary throughout the disc (*e.g.*, inner versus outer AF and posterior versus anterior AF). Uniaxial tensile tests of AF specimens have shown that collagen fibers reorient along the direction of applied load, and that the rate of fiber reorientation decreases with degeneration [54]. Fiber orientation affects tissue-level mechanics; however, the effect of fiber orientation on disc joint mechanics is not well understood. FEMs provide a powerful tool for investigating the effect of fiber orientation on disc joint mechanics, separate from other structural changes that occur with injury and degeneration, that are difficult to control in experiments.

AF collagen fiber orientation varies widely across studies, with properties being depen-

dent on location in the axial and transverse planes (30°±10°) [12, 13, 27, 79, 80, 81, 82, 83]. Shirazi-Adl demonstrated that fiber orientation was the controlling factor in determining whether fibers experience tensile or compressive stresses when the disc joint was exposed to axial compressive loads [100]. Therefore, the objective of this study was to determine whether structural changes account for differences in disc joint mechanics under axial rotation, since previous work demonstrated that changes in material properties does not alter torsional mechanics [109]. We hypothesize that structural properties, such as fiber orientation, is important for explaining increased range of motion in torsion for patients with lower back pain. In this study, we developed a structurally relevant FEM of the human lumbar intervertebral disc to investigate the effect of AF fiber angle orientation on torsion mechanics. Specifically, the model mimicked the native AF architecture, where fiber stiffness was dependent on spatial location and was validated using data available in the literature. Finally, fiber orientation was altered to represent the wide range of fiber orientations reported in the literature [12, 54].

## 2.2 Method

### Model geometry and mesh

Intervertebral disc geometry varies with respect to gender, location in the spine, and degeneration grade [9, 51, 61, 110, 111, 112]. In this study, we focused on the effect of fiber orientation on disc mechanics; therefore, we modeled a single bone-disc-bone motion segment without facet joints. The average disc geometry of thirteen L3L4 human male discs was used, as published by Peloquin and coworkers (age range = 50-93, mean = 67.5 years old; disc degeneration grade = 2.3-5.0 with mean of 3.3) [112, 113].

The mean disc geometry was processed with a custom written algorithm to create a three-dimensional mesh (Matlab 2013, Mathworks, Inc. Natick, MA). First, a two-dimensional quad mesh was generated for the superior and inferior planes. The superior and inferior planes had corresponding nodes with equivalent x- and y-coordinates and different z-coordinates, which was the direction that corresponded to disc height. The space between the superior and inferior plans was sectioned into thirteen separate planes (total disc height = 11 mm), and three-dimensional 8-node hexahedral elements were created by

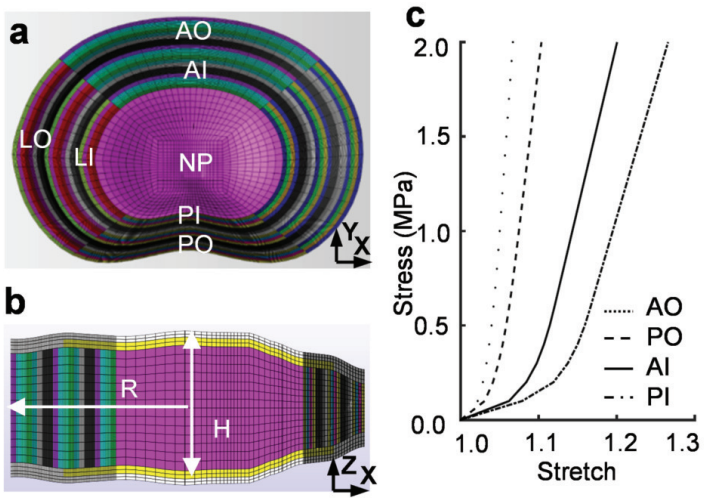


Figure 2.1: **a.** Top view of model (cartilaginous and bony endplates not shown). The NP was described as a single hyperelastic material. Material properties for AF fibers weref location-dependent: AO: anterior-outer, AI: anterior-inner, LO: lateral-outer, LI: lateral-inner, PO: posterior-outer, PI: posterior-inner. **b.** Mid-sagittal view of disc model including cartilaginous (yellow) and bony endplates (white). R: anterior-posterior radius and H: disc height. **c.** Stress-stretch of AF fibers from four regions. Material properties were selected based on experimental data reported by Holzapfel et al. [27].

connecting nodes on adjacent planes.

The total disc area was 1949 mm$^2$ with an NP area equal to 28% of the total disc area ( Fig.2.1a) [11]. The NP was assumed to have the same shape as the whole disc with its centroid offset posteriorly by 10% from the disc centroid [9, 11, 64]. The AF was divided into 20 concentric layers, resulting in layers with a thickness between 0.34 and 0.70 mm, which is comparable to reported values for human lumbar discs [12, 13, 27]. Each layer was divided into four regions, including left-lateral, right-lateral, anterior, and posterior regions (Fig.2.1a), to conveniently define material properties with spatial variation. The inner and outer AF was defined as having 10 layers each.

The CEP was defined based on dimensions reported for non-degenerated discs [114]. The CEP was described as having a uniform thickness (0.8 mm) covering the entire NP and inner AF (Fig.2.1b - material defined in yellow). A bony endplate was added to surround the CEP (thickness of 0.60 mm; Fig.2.1b - material defined in white) [115]. A mesh was created for both endplates by extruding the quad mesh on the superior and inferior planes. The

Table 2.1: Mooney-Rivlin material coefficients ($c_1$, $c_2$, and $k$) for the NP, extrafibrillar matrix of the AF, and cartilaginous endplate (CEP). All values are based on previous models (see [10]).

| Material property | NP | AF matrix | CEP |
|---|---|---|---|
| $c_1$ (MPa) | 0.05 | 0.20 | 0.50 |
| $c_2$ (MPa) | 0.01 | 0.01 | 0.01 |
| k (MPa) | 50 | 6 | 20 |

complete bone-disc-bone model had 193,556 elements. The mesh was then imported into Preview to further define material properties, boundary conditions, and loading conditions (febio.org) [116].

## Material properties

NP, CEP, and AF matrix were described as a hyperelastic material (compressible Mooney-Rivlin) due to the large deformations experienced by these tissues under physiological stresses [29, 58]. The strain energy density function of the Mooney-Rivlin material description was described by Equation 1:

$$W = c_1(I_1 - 3) + c_2(I_2 - 3) - 2(c_1 + 2c_2)lnJ + \frac{k}{2}(lnJ)^2, \tag{2.1}$$

where $I_1$ and $I_2$ are the first and second invariants of the right Cauchy-Green deformation tensor ($\boldsymbol{C}$, where $\boldsymbol{C} = \boldsymbol{F}^T\boldsymbol{F}$) and $J$ is the determinant of the deformation gradient tensor ($J = det(\boldsymbol{F})$). The three material coefficients, $c_1$, $c_2$, and $k$, were selected based on values reported in the literature for FEMs of the intervertebral disc (Table 2.1) [85]. AF extrafibrillar matrix material properties were assumed to be independent of region and layer.

AF fibers were described using a nonlinear strain energy function, which limited fibers to tension-only loading. A power stress-stretch relationship was used to define fiber mechanics at lower stretches (*i.e.*, toe region), followed by a linear response after the transition stretch ($\lambda_0$) between the toe and linear region (Equation 2.2) [116]. In Equation 2.2, the invariant $I_n = \boldsymbol{a} \cdot \boldsymbol{C}\boldsymbol{a}$, where $\boldsymbol{a}$ represents the fiber orientation in the reference configuration, $I_0$ represents the transition from the toe to the linear region ($I_0 = \lambda_0^2$), E is the elastic modulus in the linear-region (MPa, constant), and $\beta$ describes the power in the toe region (unitless). In this expression, $\lambda_0$, $E$, and $\beta$ are independent coefficients, and the constants, $\xi$, $B$, and

Table 2.2: Material coefficients for AF fibers were calibrated using data from single lamellae tension tests [27] (Fig.2.1a; AO: anterior-outer, AI: anterior-inner, LO: lateral-outer, LI: lateral-inner, PO: posterior-outer, PI: posterior-inner).

| Region | AO | AI | PO | PI | LO | LI |
|---|---|---|---|---|---|---|
| E(MPa) | 57 | 15 | 35 | 10 | 46 | 12.5 |
| $\beta$ | 4 | 5 | 4 | 6 | 4 | 5.5 |
| $\lambda_0$ | 1.06 | 1.12 | 1.07 | 1.15 | 1.065 | 1.135 |

$W_0$, were derived from Equations 2.3, 2.4, and 2.5. Finally, the complete strain energy function for the AF material was described as a summation of the extrafibrillar matrix and fibers (Equation 2.6).

$$W_{fiber} = \begin{cases} 0 & I_n < 1 \\ \frac{\xi}{2\beta} \cdot (I_n - 1)^{\beta} & 1 \leq I_n \leq I_0 \\ E(I_0^{1/2} - I_n^{1/2}) + B(I_n - I_0) + W_0 & I_0 \leq I_n \end{cases} \tag{2.2}$$

$$\xi = \frac{E}{2(\beta - 1)} I_0^{-3/2} (I_0 - 1)^{2-\beta} \tag{2.3}$$

$$B = \frac{E I_0^{-3/2}}{2} [\frac{I_0 - 1}{2(\beta - 1)} + I_0] \tag{2.4}$$

$$W_0 = \frac{\xi}{2\beta} (I_0 - 1)^{\beta} \tag{2.5}$$

$$W_{AF} = W_{matrix} + W_{fiber} \tag{2.6}$$

Differences in the fiber stiffness of the outer and inner AF were taken into consideration. The linear region modulus (E in Equation 2.2) was selected to match experimental stress-stretch response of single-lamella tissues for all four regions (Table 2.2; Fig.2.1c) [27]. Lateral region fiber properties were obtained through linear interpolation of material properties determined for the anterior and posterior regions. Finally, the cortical bone was described as a neo-Hookean material (Young's modulus = 12,000 MPa, Poisson's ratio = 0.3) [85].

## Simulation condition

Three separate simulations were conducted in FEbio (febio.org): pure compression to 0.48 MPa, pure rotation to 10 Nm torque, and ±5° rotation after 0.48 MPa compression. The compressive stress and torque used was selected to compare our model simulation results with previously reported experimental data [105, 117]. The ±5° rotation angle was selected based on the maximum rotation angle for an individual human lumbar disc under physiological levels of rotation (range = $4° - 5.7°$) [10, 109, 118, 119, 120]. Rigid bodies were defined to contact the superior and inferior bony endplates. The inferior rigid body was fixed in all degrees of freedom, while load and displacement were applied to the superior rigid body. The superior rigid body was restricted to axial displacement during compression and the axis of rotation was not specified during rotation.

## Model validation and changing fiber orientation

For model validation, a consistent fiber orientation of ±30° was used for all AF layers and regions, in order to compare model simulations to previous models of the disc joint [13]. We simulated the disc motion under axial compression and pure rotation to compare with experimental data from previous disc joint studies. The change in disc height was normalized by the original disc height and compared to experimental data reported in the literature (L4L5 discs: height = 10.91± 0.83, area = 1925±184 $mm^2$)[105]. For pure rotation, 10 Nm axial torque was applied to the superior bone, and the torque-rotation angle response was compared to experimental data from the literature (L4L5 discs)[117]. The model was considered valid for axial compression and rotation if the change in normalized disc height in compression was within one standard variation of the reported mean value and the coefficient of determinant ($R^2$) in rotation was greater than 0.9.

After validation, the fiber orientation was altered by rotating the orientation towards the transverse plane by 4° and 8°, resulting in a fiber orientation of ±26° and ±22°, respectively. These models were created to represent the fiber orientation in discs with moderate to severe degeneration [54]. All three models (uniform fiber angle orientation of ±30°, ±26° and ±22°) were used to perform compression-rotation simulations Torque-rotation curves were plotted and the effective torsional stiffness was calculated for the toe and linear regions (Fig. 2.2b - red dashed line).

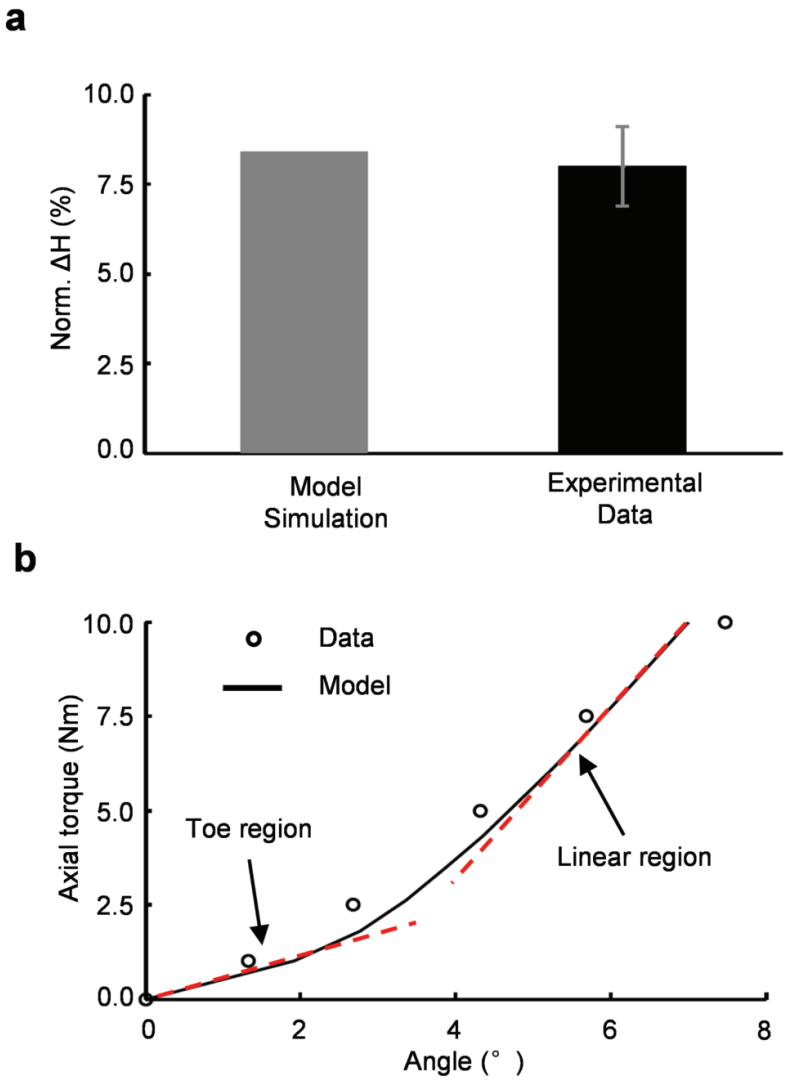


Figure 2.2: **a.** 1D axial strain under compression (0.48 MPa or 936 N) defined as the change in disc height normalized by the initial disc height. Model results were compared to experimental data (750N for disc area of 1560 $mm^2$) [105]. **b.** Axial torque versus rotation angle under pure rotation ($R^2 = 0.95$). Slopes in toe- and linear-region (red dashed lines) were used to calculate torsional stiffness.[117]

## 2.3 Results

### Model validation

The change in disc height was 0.93 mm (8.4% when normalized to the initial disc height) under 0.48 MPa of axial compression, which was less than 5% from the mean value reported in the literature ($0.08 \pm 0.01$; Fig. 2.2a) [105]. The torque-rotation response from the simulation was nonlinear and agreed well with experimental data ($R^2 = 0.95$; Fig. 2.2b) [117]. Thus, we considered our model to be valid for axial compression and axial rotation. Applying axial compressive preload, prior to rotation, reduced the toe region response and increased torsional stiffness (Fig.2.3a - blue and black solid lines).

### Effect of fiber orientation

The torque-rotation response was nonlinear for all three models, but nonlinearity was more pronounced in the $\pm 30^\circ$ model, where fibers orientation was less aligned with the horizontal plane. The torsional response under clockwise rotation (CW) was not symmetrical with counter-clockwise (CCW) rotation, such that the maximum torque at $+5^\circ$ (*i.e.*, CW) was 15% greater than the maximum torque at $-5^\circ$ (*i.e.*, CCW). The torsional stiffness in the toe region (rotation angle $\leq 2^\circ$) was similar for all three models ($\sim 0.9 \text{Nm}/\circ$, Fig. 2.3a). The torsional stiffness in the linear region decreased with fiber angle orientation, resulting in a 30% and 60% decrease in linear region torsional stiffness for the $\pm 26^\circ$ and $\pm 22^\circ$ models, respectively (Fig. 2.3b). The circumferential stresses were greater in the outer AF than the inner AF due to difference in distance from the disc centroid (*e.g.*, moment arm; Fig. 2.4). The cause for differences in CW and CCW behavior can be observed visually through the circumferential stress in adjacent layers (Fig. 2.4 -$'*'$).

The change in disc height under axial compression was not altered by fiber orientation. Similarly, the internal pressure in the NP was not altered by fiber orientation under axial compression (Fig. 2.3c). However, there was a decrease in the maximum NP pressure under rotation with fibers orientated closer to the horizontal plane, such that the NP pressure in the $\pm 22^\circ$ model was 7% lower than the NP pressure in the $\pm 30^\circ$ model (Fig. 2.3c –right group). Under axial compression, the NP pressure was higher in the posterior region than

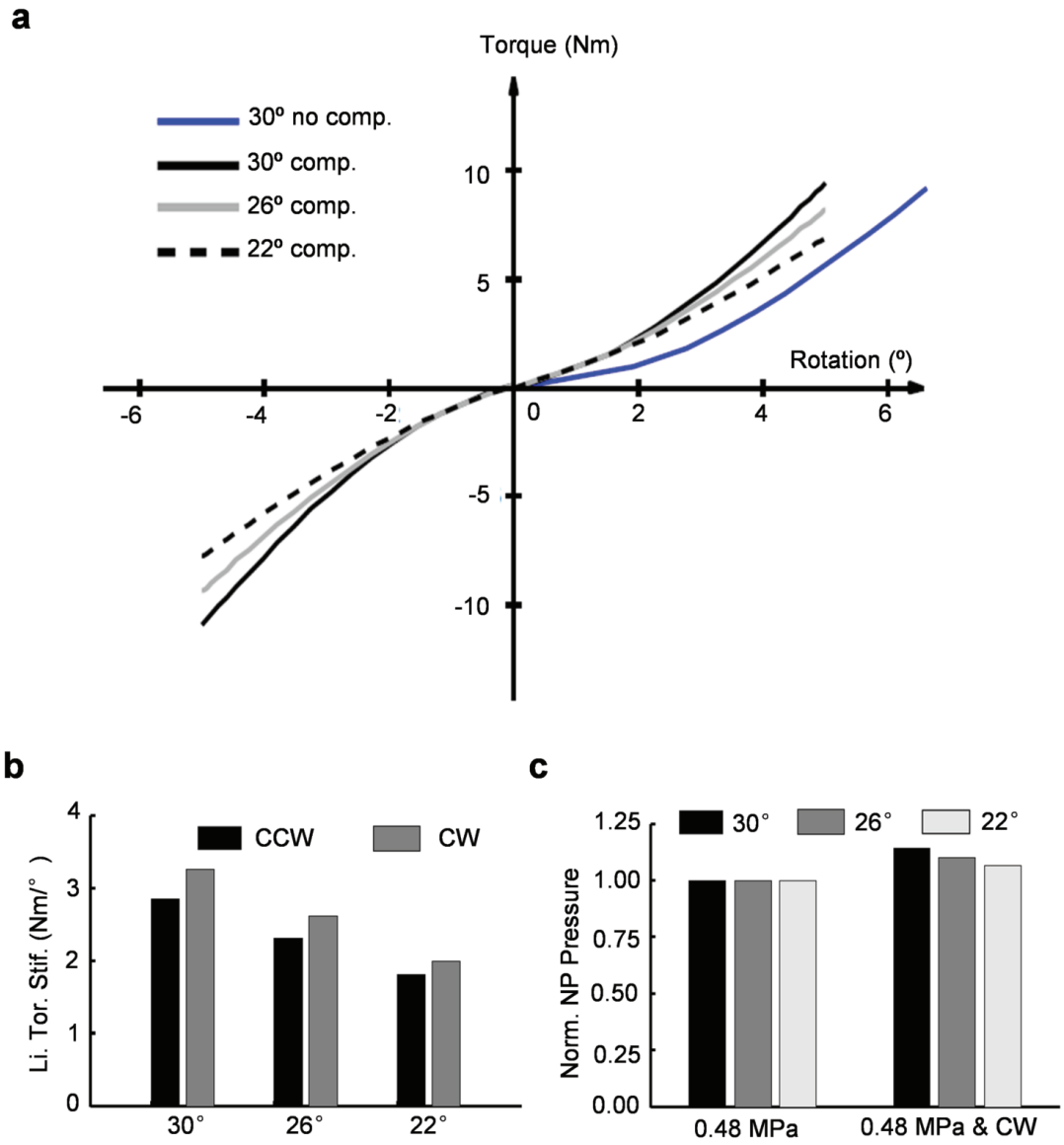


Figure 2.3: **a.** Torque-rotation response between ±5° with 0.48 MPa axial compression. The pure-rotation case (10 Nm torque, no-compression; blue line) was simulated for the ±30° model and used for validation with experimental data. **b.** Disc torsional stiffness in the linear region, which was dependent on rotation direction (counter-clockwise (CCW) and clockwise (CW)). **c.** NP average pressure at 5° rotation with 0.48 MPa compression normalized by the NP average pressure under 0.48 MPa compression. The increase in NP pressure with rotation was more pronounced for the ±30° model (black bar).

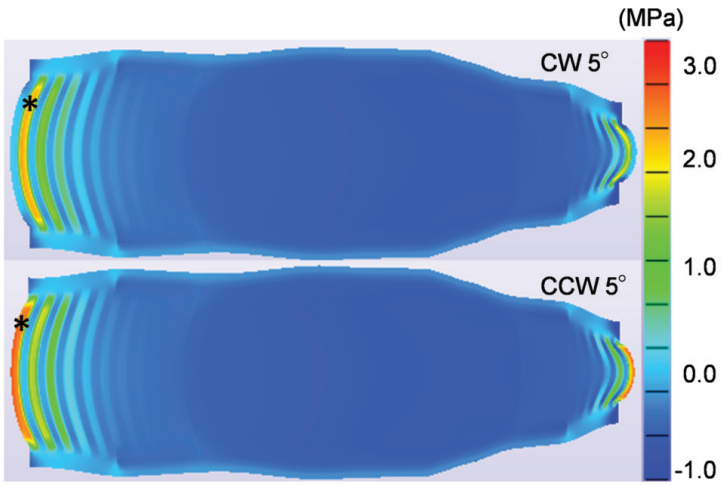


Figure 2.4: Circumferential stress at for rotation in the clockwise (CW) and counter-clockwise (CCW) direction (±30° model).

the anterior region (Fig. 2.5a). Applying axial rotation further increased NP pressure in the posterior region, with the highest NP pressure observed in the ±30° model (Fig. 2.5b-d).

A sigmoidal change in disc height was observed with axial rotation (Fig. 2.6a). The maximum increase in disc height during rotation was 0.15 mm, resulting in a 0.46 mm decrease in disc radius (±30° model; Fig. 2.6b). The change in disc height was linearly related to the change in disc bulge. An effective disc Poisson's ratio, defined as the negative slope of the height-radius curve, was 3.2 for the ±30° model and decreased with fiber reorientation towards the horizontal plane (2.8 for the ±22° model; Fig. 2.6b).

Peak shear stresses and strains were observed at the disc-bone interface in the outer anterior and posterior regions. Shear was highest in the outer AF of the anterior and posterior regions, due to disc geometry. Therefore, Fig. 2.7 only shows the outer AF from each model under 0.48 MPa compression and 5° clockwise rotation (XZ orientation). The magnitude of shear strains was comparable for all three models (Fig. 2.7a –shown for the ±30° model). However, the peak XZ shear stress was highest in the ±30° model and decreased by 30% with fiber orientation (Fig. 2.7b-d; Table 2.3).

The fibers in the outer AF experienced higher stretch than fibers located in the inner AF during compression and rotation (Fig. 2.8a,b - shown for the middle disc height and bone-disc interface). The peak fiber stretch occurred at the posterior-lateral region of the

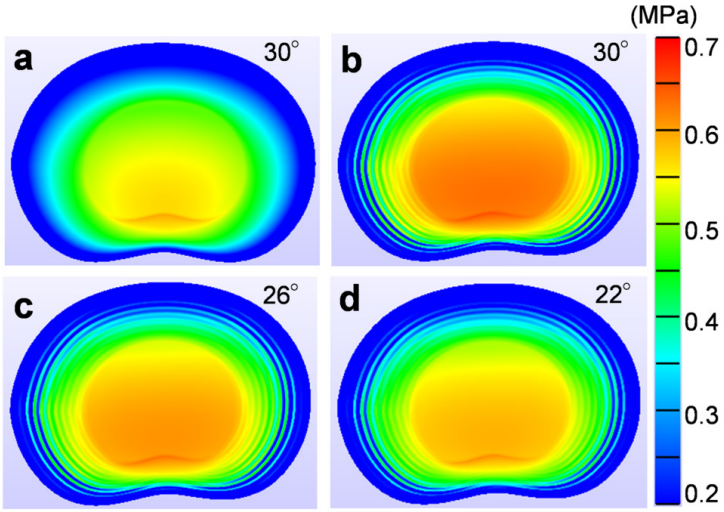


Figure 2.5: **a.** Pressure distribution at the mid-transverse plane (0.48 MPa compression). Axial compression combined with 5° rotation for the **b.** ±30°, **c.** ±26°, and **d.** ±22° models.

Table 2.3: Peak XZ stress in the outer region of the anteior and posterior AF (simulation loading: 0.48 MPa axial compression with 5° clockwise axial rotation)

| Model-XZ Stress | ±30° | ±26° | ±22° |
|---|---|---|---|
| Anterior (MPa) | 1.57 | 1.33 | 1.08 |
| Posterior (MPa) | 2.26 | 1.98 | 1.67 |

bone-disc interface (˜1.15 stretch, Fig. 2.8b). Fibers experienced affine re-orientation under deformation, and the amount of fiber re-orientation was dependent on disc location (*e.g.*, inner versus outer AF and bone-disc bone interface versus mid-disc height). Under compression, fiber re-orientation at the bone-disc interface was greater in the outer AF than the inner AF (Fig. 2.8c - top half of boxes), and the amount of fiber re-orientation was higher at the bone-disc interface than the mid-disc height. At the mid-disc height, the inner AF experienced greater fiber re-orientation than the outer AF, which was the opposite trend from the bone-disc interface (Fig. 2.8c). Under axial rotation, the change in fiber angle orientation was greater in the outer AF at both locations (mid-disc height and bone-disc interface) (Fig. 2.8d).

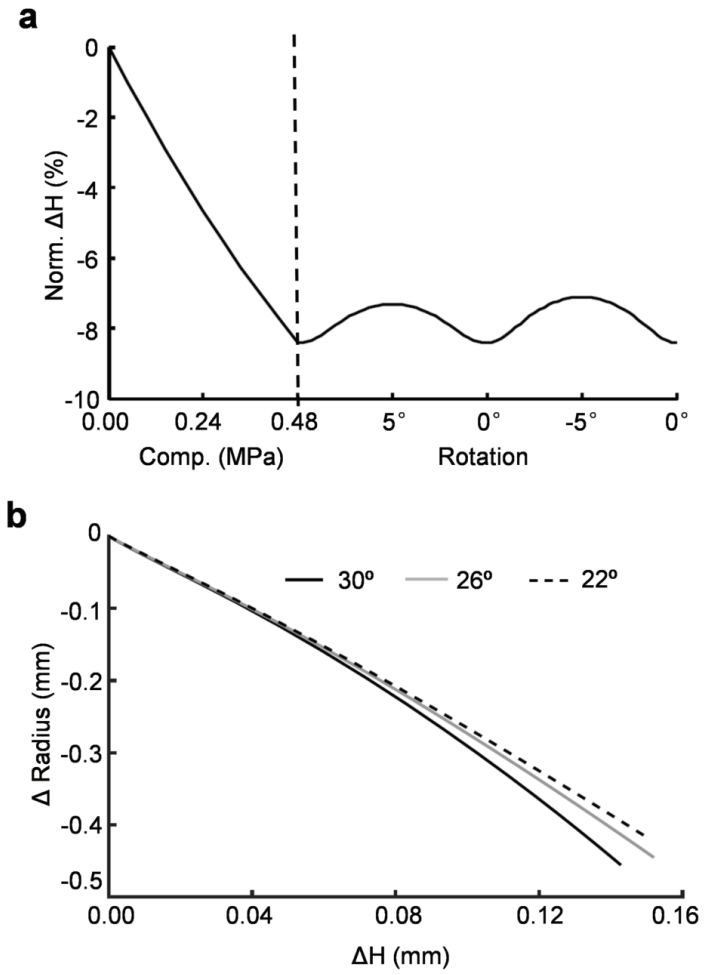


Figure 2.6: **a.** Change in disc height normalized by initial disc height shown for compression (left of vertical dashed line) and rotation (right of dashed line). **b.** A near linear relationship between the change in disc height ($\Delta H$) and radius ($\Delta R$).

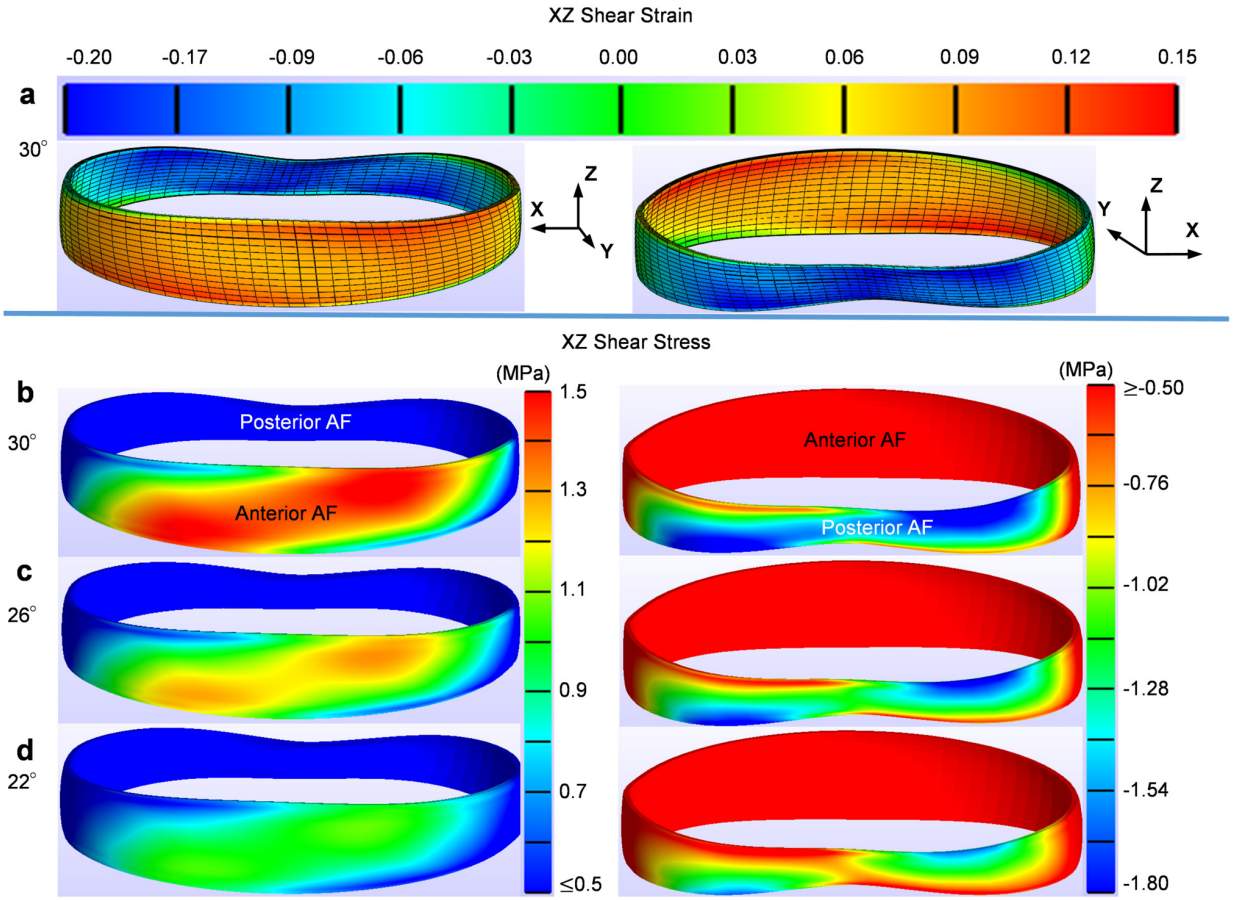


Figure 2.7: **a.** XZ shear strain in the outtermost layer of the AF was similar for all models under 0.48 MPa compression in combination with 5° clockwise rotation (only ±30° model shown). **b-d.** XZ shear stress in the outtermost layer of the AF greatly decreased in combination with 5° rotation. **Note:** The ranges used for the color bars differ between the anterior (left column) and posterior AF (right column) to better represent the stress distribution in the respective region.

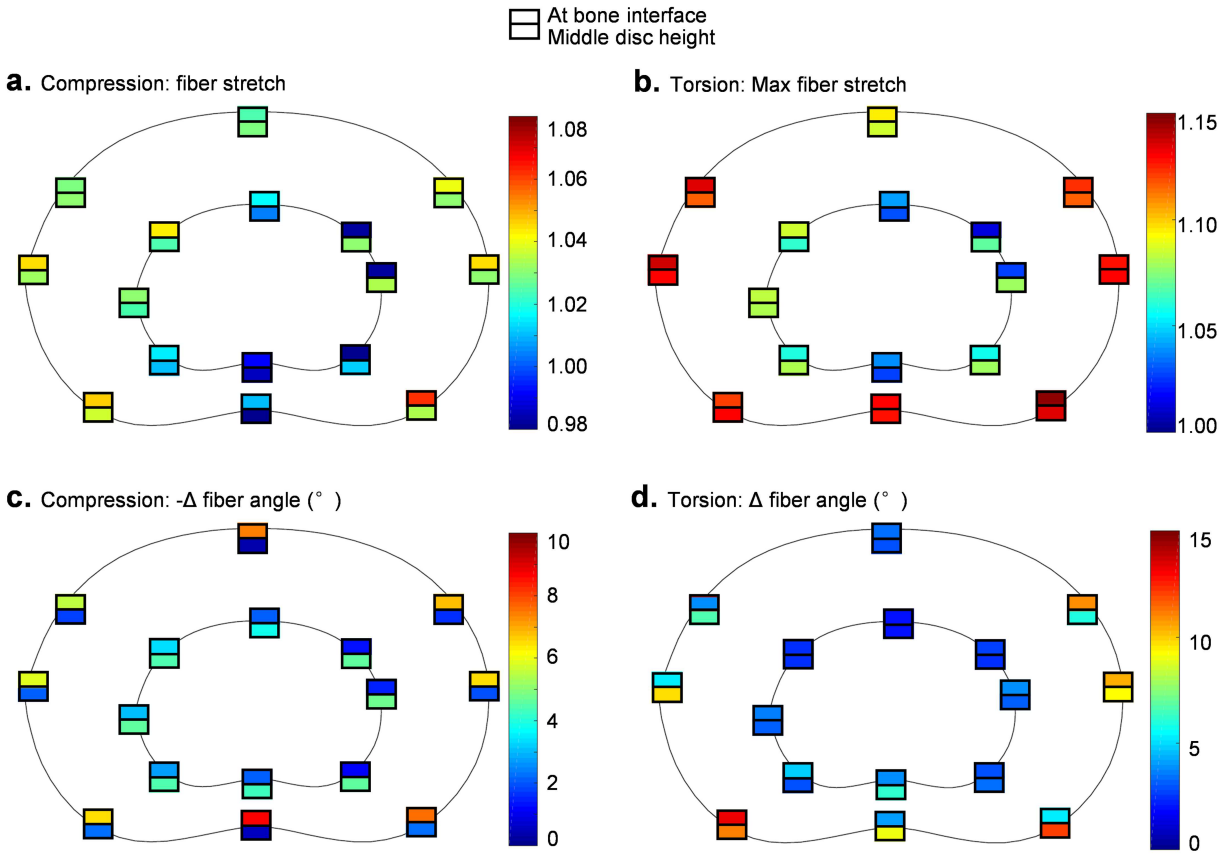


Figure 2.8: Fiber stretch for different regions along the axial and transverse planes under **a.** 0.48 MPa compression and with **b.** 5° rotation. **c.** Fiber orientation angle decrease during compression. **d.** Fiber orientation angle variation during rotation. All values shown for the ± 30° model.

## 2.4 Discussion

We evaluated the relationship between fiber angle orientation and disc joint mechanics under axial compression combined with rotation, because data in the literature noted a decrease in torsional stiffness that was not explained by degenerative changes in material properties. Disc mechanics is dependent on geometry, collagen fiber organization, and biochemical properties. Therefore, we developed a FEM of the human lumbar disc based on averaged disc geometry reported in the literature [112]. Then, we altered the AF collagen fiber orientation within the range of values reported for human lumbar discs [12]. Typically,

FEMs of the disc modify material properties to understand the effect of injury or degeneration, without altering collagen fiber orientation. By altering the fiber orientation, separate from changes in material properties, we were able to elucidate the relationship between disc structure and mechanics. The data reported here demonstrates that fiber orientation plays an important role on torsional stiffness and stress distribution throughout the intervertebral disc under complex loading conditions.

High shear strains occur at the interface between the AF and adjacent vertebral body under axial compression (radial-axial shear strains: 3-13%) and at the outer AF in rotation (circumferential-axial shear strains: 3-3.5% at the mid-disc height) [29, 31, 58]. Our model simulations agreed with previously reported experimental data, with shear strains highest at the disc-bone interface and outer AF regions (Figs. 2.4, 2.7, and 2.8). Interestingly, peak shear strains occurred at the outermost region of the posterior-lateral AF (Fig 2.8b). Disc herniations originate either as failures in the AF (mid-disc height) or due to failure at the disc-bone interface [121, 122, 123, 124]. Both failure modes for herniation agree with peak strain locations observed in this study.

AF structural properties altered NP pressure during axial rotation. That is, a disc with AF fibers oriented towards the vertical plane (*i.e.*, closer to the 30° model) had greater intradiscal stresses and torsional stiffness compared to a disc with fibers aligned closer to the horizontal plane (Fig.2.7). It should be noted that AF shear strains under rotation were similar for all models (Fig.2.7a), resulting in a increase in fiber stretch and shear stress with fiber orientated towards the vertical plane (*i.e.*, ±30° model; Fig.2.8b and Fig.2.7b, respectively). Discs that experience low mechanical loading for extended periods of time (*e.g.*, extended bed-rest or spaceflight) will likely experience affine re-orientation of AF fibers towards the axis of the spine, due to tissue swelling causing an increase in disc height [125]. Therefore, fiber alignment, as a patient-specific structural property or from affine re-orientation, is an important contributor to shear stresses at the disc-bone interface, which is a common location for disc joint failure [122]. Affine fiber re-orientation with tissue swelling may make the disc more susceptible to disc herniation, as observed in astronauts returning from spaceflight [126]. Furthermore, these findings suggest that fiber alignment may be significant contributor to the decrease in torsional stiffness with degeneration, where fibers likely align closer to the horizontal plane *in situ* due to a loss in NP pressure and disc height.

During axial rotation, a sinusoidal change in disc height and bulge was observed, agree-

ing with *in vivo* data from healthy volunteers [127]. That is, rotation increases disc height and decreases disc bulge radius, due to the Poisson effect. Cyclic compressive loading has been shown to increase nutrient transportation and tissue growth in engineered tissues [128], and the cyclic axial compressive response observed during rotation may act to improve nutrient diffusion and waste transportation in the disc [129, 130].

Mechanical loads applied to the disc are distributed between the NP and AF. For example, applying axial compressive loads to a healthy disc pressurizes the NP, causing tensile strains in the AF [29, 31]. It is likely that the sinusoidal response in disc height and radial bulge is due to the 'hooping' effect from AF fibers. Under axial rotation, AF fibers create a hooping effect that constrains the NP and shifts stresses towards the NP, resulting in an increase in the internal pressure (Fig. 2.5). The NP pressure was approximately 50% greater in the posterior NP than the anterior NP, which was likely due to the NP centroid being offset posteriorly from the disc centroid (10% offset) [11]. Taken together, NP geometry and collagen fiber orientation are important structural properties for stress distribution between disc subcomponents under complex loading conditions.

As with all computational models, the robustness of the model depends on the ability to replicate experimental data. The nonlinear torque-rotation response, increase in torsional stiffness with compression, and asymmetrical torsional stiffness agreed well with observations reported in the literature [117, 131]. However, orienting collagen fibers towards the horizontal plane did not impact compressive stiffness, which differs from the increase in compressive stiffness reported by Shirazi-Adl (computational simulation) [100]. Discrepancies between simulated data are likely due to differences in the material description for the extrafibrillar matrix (*i.e.*, linear verses nonlinear) and the use of multiple discrete fibers layers, rather than describing the AF as a composite of distinct matrix and fibers. We excluded facet joints to evaluate the biomechanical function of the disc joint itself; however, load sharing between the disc and facets would decrease stresses reported in the disc [132, 133]. Finally, the amount of axial rotation varies through the length of the spine, with the L1L2 disc rotating more than the L4L5 disc [134]. While our analysis was limited to the geometry of the L3L4 disc, it is likely that stress distributions with respect to fiber angle orientation is similar for the L1L2 disc. Future work will investigate the effect of structural (*i.e.*, NP and disc geometry) and material properties on the mechanical behavior of healthy, injured, and degenerated discs from multiple levels within the lumbar spine.

Occurrence of disc injury and chronic lower back pain is greater for patients with occupations that require lifting heavy objects with repetitive twisting [95, 96, 97, 98]. Many studies focus on the effect of NP and AF material properties on disc joint mechanics. In this study we focused on the effect of AF fiber structure on joint-level mechanics and internal stress distribution. Discs with collagen fibers oriented closer to horizontal plane experienced a decrease in AF stresses, NP pressure, and torsional stiffness. Therefore, we were able to describe changes in disc mechanics observed with degeneration solely through changes in fiber orientation. In conclusion, fiber orientation plays a crucial role in disc mechanics, and the fiber structure used in a FEM must be selected appropriately to understand the structure-function relationship in the disc. Future iterations of this model will replicate spatial and regional differences in AF fiber orientation (*e.g.*, inner versus outer AF)[12].

# Chapter 3

# Relative Nucleus Pulposus Area and Position Alter Disc Joint Mechanics [2]

## Abstract

Aging and degeneration of the intervertebral disc are noted by changes in tissue composition and geometry, including a decrease in nucleus pulposus (NP) area. The NP centroid is positioned slightly posterior of the disc's centroid, but the effect of NP size and location on disc joint mechanics is not well understood. We evaluated the effect of NP size and centroid location on disc joint mechanics under dual-loading modalities (*i.e.*, compression in combination with axial rotation or bending). A finite element model was developed to vary the relative NP area (NP:Disc area ratio range = 0.21 –0.60). We also evaluated the effect of NP position by shifting the NP centroid anteriorly and posteriorly. Our results showed that compressive stiffness and average first principal strains increased with NP size. Under axial compression, stresses are distributed from the NP to the annulus, and stresses were redistributed towards the NP with axial rotation. Moreover, peak stresses were greater for discs with a smaller NP area. NP centroid location had a greater impact on intradiscal pressure during flexion and extension, where peak pressures in the posterior annulus under extension was greater for discs with a more posteriorly situated NP. In conclusion, the findings from

this study highlight the importance of closely mimicking NP size and location in computational models that aim to understand stress/strain distribution during complex loading and for developing repair strategies that aim to recapitulate the mechanical behavior of healthy discs.

**Keyword:** Nucleus pulposus, Intervertebral disc, Finite element method, Disc degeneration, Dual-loading modalities, Disc geometry

## 3.1 Introduction

Pathological changes in the intervertebral disc are thought to be a primary contributor to lower back pain, affecting over 80% of adults in the United States at some point in their lifetime [44]. The disc is a complex structure with multiple subcomponents, including the nucleus pulposus (NP) and the annulus fibrosus (AF). These tissues act together to distribute large complex mechanical loads placed on the spine during daily activities, such as compression, flexion, extension, axial rotation, and lateral bending. During axial compression, the pressurized healthy NP bulges outward radially, which is partially restricted by the stiffer AF [135, 136, 137]. In flexion and extension, the NP acts as a moving pivot, migrating anteriorly and posteriorly, respectively [32]. Evaluating disc-joint mechanics and stress or strain distributions between subcomponents is important for understanding changes in disc mechanics with aging and failure, as well as for evaluating biological repair strategies [138, 139].

Pathological changes in the disc are noted by alterations in tissue composition and geometry, such as an increase in overall disc area, a decrease in disc height, and a decrease in the relative NP area, which is due to an increase in fibrosus at the transition zone between the NP and AF [9, 48, 51]. These changes alter stress distributions between the NP and AF [29, 31, 48, 58, 59]. However, previous observations of internal strain distributions have largely been limited to two-dimensional analyses, single loading modalities, and require expensive experimental setups. Therefore, there has been growing interest in using computational models to investigate intradiscal strains for understanding mechanisms of degeneration [63].

Finite element models that simulate pathological changes with disc degeneration have either modified geometric properties or material properties (*e.g.*, increase in NP compress-

ibility) [1, 65, 67, 68]. Recently work using a probabilistic finite element analysis evaluated the effect of 40 different geometric parameters and found that joint level mechanics was sensitive to disc height and endplate dimensions [69]. However, the role of NP size on disc joint mechanics, separate from changes in material properties, is not well understood and has been largely overlooked. In fact, only a few computational studies explicitly report NP location with respect to the disc centroid, where the NP:Disc area ratio (NP area over disc area in the transverse plane) ranges widely, from 0.31 to 0.60 [64, 85, 86, 87]. Furthermore, recent work by Mengoni et al. showed that the compressive stiffness of the disc joint decreased by 20% with a 10% increase in the relative NP size, suggesting that NP size may have a significant impact on disc-joint mechanics [41].

There are only a few experimental studies that have reported NP size and location, due to difficulties in demarcating the inner AF from the NP, especially in moderately or severely degenerated discs. The NP:Disc area ratio measured from the mid-transverse plane of human cadaveric lumbar discs had an actual range between 0.25 and 0.36, with the NP centroid located posteriorly of the disc centroid by as much as 10% of the anterior-posterior width [9, 10, 11]. A recent study reported higher NP:Disc area ratios, between 0.4 and 0.5, in healthy volunteers, where the NP position was dependent on disc level (volunteer population: n = 41, 20-35-year-old healthy Chinese individuals). That is, the NP of the L4-L5 disc was positioned posteriorly, but the NP of the L5-S1 disc was located closer to the disc center [140]. This new study highlights the difference between the structure of the healthy native disc and engineered disc, where the NP:Disc area ratio ranges between 0.1 and 0.2 [141, 142]. Changes in NP size, combined with progressive structural failure, are thought to lead to mechanical dysfunction, such as an increase in disc compliance under axial compression and rotation [9, 61]. However, it is not clear whether the wide range of NP size and relative position of the NP within the disc space (*i.e.*, NP centroid position) affects joint-level mechanics.

Thus, the aim of this study was to evaluate the effect of NP size and centroid position on disc joint mechanics under compression, flexion, extension, lateral bending, and axial rotation. To do this, we first modified our previously reported finite element model of the human lumbar disc joint and validated it [1]. Then, the relative NP size was varied in a range of values reported in experimental and computational studies (0.21 –0.60) to evaluate its effect on joint-level mechanics, intradiscal deformations, and internal pressure. Finally,

Table 3.1: Summary of model descriptions used in Series I and II. In Series I, the NP area relative to disc area was varied between 0.21 and 0.60. In Series II, the location of the NP centroid was shifted anteriorly or posteriorly, with respect to the Control model, which had a 5% posterior shift in the NP centroid (NP:Disc area ratio = 0.28). Values are reported as a percent offset from the disc centroid.

| Series | NP Geometry | NP:Disc are ratio | NP offset ratio(%) |
|---|---|---|---|
| I | 21%NP | 0.21 | 5 |
| I & II | 28%NP (Control for Series II) | 0.28 | 5 |
| I | 35%NP | 0.35 | 5 |
| I | 45%NP | 0.45 | 5 |
| I | 60%NP | 0.60 | 5 |
| II | Anteriorly Shifted NP (ASNP) | 0.28 | 0 |
| II | Posteriorly Shifted NP (PSNP) | 0.28 | 10 |

we evaluated the effect of NP centroid location, relative to the disc's centroid.

## 3.2 Method

### Model geometry & mesh

We modeled a single bone-disc-bone motion segment without facet joints to present the sample preparation used to collect much of the joint-level mechanics data in the literature. Furthermore, modeling a single motion segment allowed us to focus on disc joint-level mechanics and stress distributions within the disc, without including compounding factors of neighboring tissues. Two series of models were developed (Table 3.1, Figure 3.1A). In Series I, the NP:Disc area ratio ranged from 0.21 to 0.60, based on the NP area reported in the literature [9, 10, 11, 86, 87, 141, 142], where a reasonable value of 0.21 was picked as the lower bound of NP:Disc ratio.

In Series II, the effect of NP position was investigated by shifting the NP centroid with respect to the anterior-posterior width of the whole disc. The Control model was defined based on the NP centroid position used for all models in Series I, where the NP centroid was offset posteriorly from the disc centroid by 5% of the disc's anterior-posterior width [11]. Two additional models were created, where the NP centroid had no offset from the disc

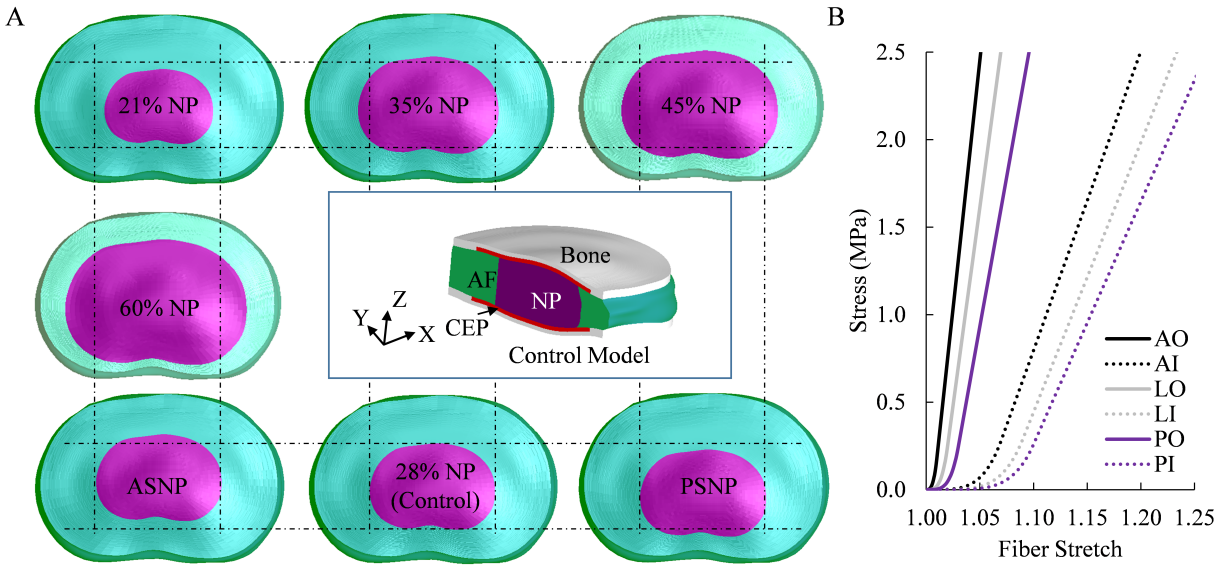


Figure 3.1: **A**) Seven models with different geometric descriptions for the nucleus pulposus (NP: purple), and, therefore, the annulus fibrosus (AF), which contained 20 lamellae in all models. In Series I (shown in the $1^{st}$ and $2^{nd}$ rows), the effect of NP size was evaluated. In Series II ($3^{rd}$ row), the effect of NP position was evaluated by creating either an anterior or posterior shift in the location of the NP centroid with respect to the Control model (see Table 3.1). Inset: Mid-sagittal cross section of the Control model. The whole disc joint model included the AF (teal), cartilaginous endplates (CEP, red), and boney endplates (grey). **B**) Stress-stretch of AF fibers from 6 regions. A: anterior, L: lateral, P: posterior, O: outer, I: inner. Material parameters were calibrated using data from single lamellae tensile tests [27].

centroid or had a 10% posterior shift with respect to disc centroid (Figure 3.2A –ASNP and PSNP, respectively). The NP:Disc area ratio was 0.28 for all models in Series II.

All seven models (*i.e.*, Series I and II) had the same disc geometry and total disc volume, which was obtained from published data of thirteen L3L4 human male discs averaged together (disc area = 1949 mm$^2$, average disc height = ∼11 mm) [112]. The NP was assumed to have the same shape as the whole disc and AF volume decreased with an increase in NP area (Figure 3.1A) [9];. Meshes were generated using a custom-written algorithm (∼260K elements for each model, MATLAB 2017, Mathworks, Inc. Natick, MA). First, two-dimensional quad meshes were generated for the superior plane, inferior plane, and 14 planes throughout the disc height. Superior and inferior plane meshes preserved the original topography and planes throughout the disc height varied in boundary shape, preserving the

Table 3.2: Material parameters for the nucleus pulposus (NP), extrafibrillar matrix of the annulus fibrosus (AF), and cartilaginous endplate (CEP). Each material was described as a Mooney-Rivlin material ($c_1$, $c_2$, k) [85, 1]

| Property | NP | AF matrix | CEP |
|---|---|---|---|
| $c_1$ (MPa) | 0.05 | 0.09 | 0.50 |
| $c_2$ (MPa) | 0.01 | 0.01 | 0.01 |
| k (MPa) | 50 | 3 | 20 |

original disc bulge. NP had a similar bulge that was promotional to the disc bulge with a factor of NP:Disc area ratio. Then, quad meshes were connected in the axial direction to create a hexahedral mesh. The AF was divided into 20 concentric layers in the radial direction [12, 13]. Each layer was divided into four regions to represent the anterior, posterior, left-lateral, and right-lateral regions [27]. AF layer thickness was dependent on NP area and in Control model the value ranged from 0.31 to 0.70 mm, which was comparable to values reported for human discs [27]. Cartilage endplates were created by extruding the superior and inferior planes of the NP and the inner half of the AF by 0.80 mm (Figure 3.1A - inset) [114]. Therefore, the size of cartilage endplates increased with NP size. Bony endplates were generated to surround the cartilage endplate (thickness = 0.6 mm; Figure 3.1A - inset) [115]. Disc subcomponents and bone were welded together through sharing nodes on the interfaces.

## Material properties

The NP, extrafibrillar matrix of the AF, and cartilaginous endplates were described as a hyperelastic material (compressible Mooney-Rivlin, Equation 3.1), where W represents strain energy density function, J represents the determinant of the deformation gradient tensor, $\boldsymbol{F}$ (J=det($\boldsymbol{F}$)), and $I_1$ and $I_2$ represent the first and second invariants of the right Cauchy-Green deformation tensor, $\boldsymbol{C}$ ($\boldsymbol{C} = \boldsymbol{F}^T\boldsymbol{F}$). Material coefficients $c_1$, $c_2$, and k were chosen based on our previous work (Table 3.2) [1, 85]. Material properties for the extrafibrillar matrix of the AF were not dependent on the radial or circumferential location.

$$W = c_1(I_1 - 3) + c_2(I_2 - 3) - 2(c_1 + 2c_2)\ln J + \frac{k}{2}(\ln J)^2 \tag{3.1}$$

The strain energy density function of the AF included contributions from collagen fibers (Equation 3.2). Fibers were described with a nonlinear stress-stretch relationship (Equation 3), which was limited to tension-only loading and separated into toe and linear regions with a threshold stretch ($\lambda_0, I_0 = \lambda_0^2$). Fiber orientation decreased from ± 43° in the inner AF to ±28° in the outer AF (with respect to XY the plane in Figure 3.1A) [12]. In Equations 3.3-3.6, I_n represents the square of the fiber stretch ($I_n = \boldsymbol{a} \cdot \boldsymbol{C} \cdot \boldsymbol{a}$, where $\boldsymbol{a}$ is a unit vector representing fiber orientation in the reference configuration), E represents the linear-region elastic modulus (MPa), and $\beta$ describes toe-region nonlinearity. Fiber parameters ($I_0$, E, and β ) were region-dependent with the outer AF being stiffer than the inner AF and the anterior region being stiffer than the posterior region (Table 3.3, Figure 3.1B) [27, 28]. Fiber parameters were calibrated using data from single lamellae tensile tests [27], as reported previously [1]. Finally, the cortical bone was described as a neo-Hookean material (Young's modulus = 12,000 MPa, Poisson's ratio = 0.3)[85].

$$W_{AF} = W + W_{fiber} \tag{3.2}$$

$$W_{fiber} = \begin{cases} 0 & I_n < 1 \\ \frac{\xi}{2\beta}(I_n - 1)^{\beta} & 1 \leq I_n \leq I_0 \\ E(I_0^{1/2} - I_n^{1/2}) + B(I_n - I_0) + W_0 & I_0 \leq I_n \end{cases} \tag{3.3}$$

$$\xi = \frac{E}{2(\beta - 1)} I_0^{-3/2} (I_0 - 1)^{2-\beta} \tag{3.4}$$

$$B = \frac{E I_0^{-3/2}}{2} [\frac{I_0 - 1}{2(\beta - 1)} + I_0] \tag{3.5}$$

$$W_0 = \frac{\xi}{2\beta}(I_0 - 1)^{\beta} \tag{3.6}$$

## Model validation

Two rigid bodies were defined superior and inferior to the disc joint to apply boundary and load conditions. The outer surfaces of the bony endplates were attached to the rigid bodies, and the inferior rigid body was fixed throughout all simulations (FEBio; febio.org) [116]. We first validated the Control model (0.28 NP:Disc ratio, 5% posterior NP centroid

Table 3.3: Material coefficients for fibers in different regions of the annulus fibrosus. AO: anterior-outer, AI: anterior-inner, LO: lateral-outer, LI: lateral-inner, PO: posterior-outer, and PI: posterior-inner. Fibers were described using a nonlinear strain energy density function, where E represents the linear region Young's modulus, $\beta$ represents toe-region nonlinearity, and $\lambda_0$ represents the transition stretch between the toe and linear region [27, 1]

| Region | AO | AI | PO | PI | LO | LI |
|---|---|---|---|---|---|---|
| E (MPa) | 57 | 18 | 35 | 15 | 46 | 16.5 |
| $\beta$ | 4 | 5 | 5 | 6 | 4.5 | 5.5 |
| $\lambda_0$ | 1.01 | 1.07 | 1.03 | 1.10 | 1.02 | 1.09 |

offset) under single loading conditions, including axial compression, axial rotation, and bending (*i.e.*, flexion, extension, and lateral bending). For axial compression, a 936 N load was applied to the superior rigid body to represent the stress experienced while standing (0.48 MPa) [135]. The superior rigid body was restricted to axial displacement (*i.e.*, displacement along the Z-axis) during compression. Extension/flexion, lateral bending, and axial rotation were simulated by applying 6 Nm torque on the superior rigid body with free axes that were parallel to the X, Y, Z-axes, respectively. The normalized change in disc height during loading was calculated as the change in disc height after loading, which was uniform throughout the disc, divided by the original average disc height (11 mm). The normalized change in disc height under axial compression, angular displacement, and torsion/bending stiffness were compared to experimental data in the literature [88, 105, 117, 143, 144]. The Control model was considered valid if all load-displacement responses and torsion/bending stiffness fell within the range of reported data.

## Altering NP and data analysis

Once the Control model was validated, mechanical responses of the seven models defined in Series I and II were simulated. To better mimic *in vivo* loading and to compare mechanical behaviors between simulations, we applied a two-step loading protocol. First, axial compression was applied (load controlled) and then an angular-displacement was applied for bending and axial rotation. For each model, a 936 N (0.48 MPa) compressive preload was first applied, and the superior rigid body was restricted to axial displacements. Loads and torques about the X-, Y-, and Z- axes due to axial compression were recorded. Then,

angular displacements were applied on the superior rigid body with free axes separately: 6.5° flexion, 4° extension, 5° lateral bending, and 4° axial rotation (7 models X 4 simulations = 28 total simulations) and torques were recorded. Angular displacement values were based on the range of motion reported for human lumbar discs [145, 146, 147]. During bending or rotation, angular displacements around other axes were restricted.

Compressive stiffness (N/mm), bending stiffness (Nm/°), and torsional stiffness (Nm/°) of the disc joint was calculated as the slope of the force-displacement curve at the linear region. The normalized compressive stiffness ($k_{norm.comp.}$, MPa) was calculated by multiplying the compressive stiffness ($k_{comp.}$, N/mm) by disc height ($H_{disc}$, mm) and dividing by disc area ($S_{disc}$, mm$^2$).

$$k_{norm.comp.} = \frac{k_{comp.} \times H_{disc}}{S_{disc}} \tag{3.7}$$

NP load support under compression was calculated by integrating axial-direction stress (*i.e.*, Z-direction stress) with respect to NP area at the superior surface. The NP support ratio was calculated as the NP support load divided by the applied compressive load (936 N). Pressure and first principal strain of each element were averaged for the NP and AF. For Series I, mechanical properties that demonstrated a linear relationship with the NP:Disc area ratio was curve-fit to a linear regression equation (*e.g.*, $y = m^*x + b$).

## 3.3 Results

### Model validation

The normalized change in disc height was 11.2% for the Control model under 0.48 MPa axial compression ($\Delta$h = 1.23 mm), which was within the range of values reported in the literature (8 - 16.2%; Figure 3.2A) [35, 105, 144]. Similarly, angular displacement versus torque behavior agreed well with previously reported data for flexion, extension, lateral bending, and axial rotation (Figure 3.2B) [117, 143]. Toe-region and linear-region stiffness for bending and axial rotation also matched reported values well (Figure 3.2C) [88, 117, 143]. Taken together, we considered the Control model to be valid for axial compression, bending, and rotation.

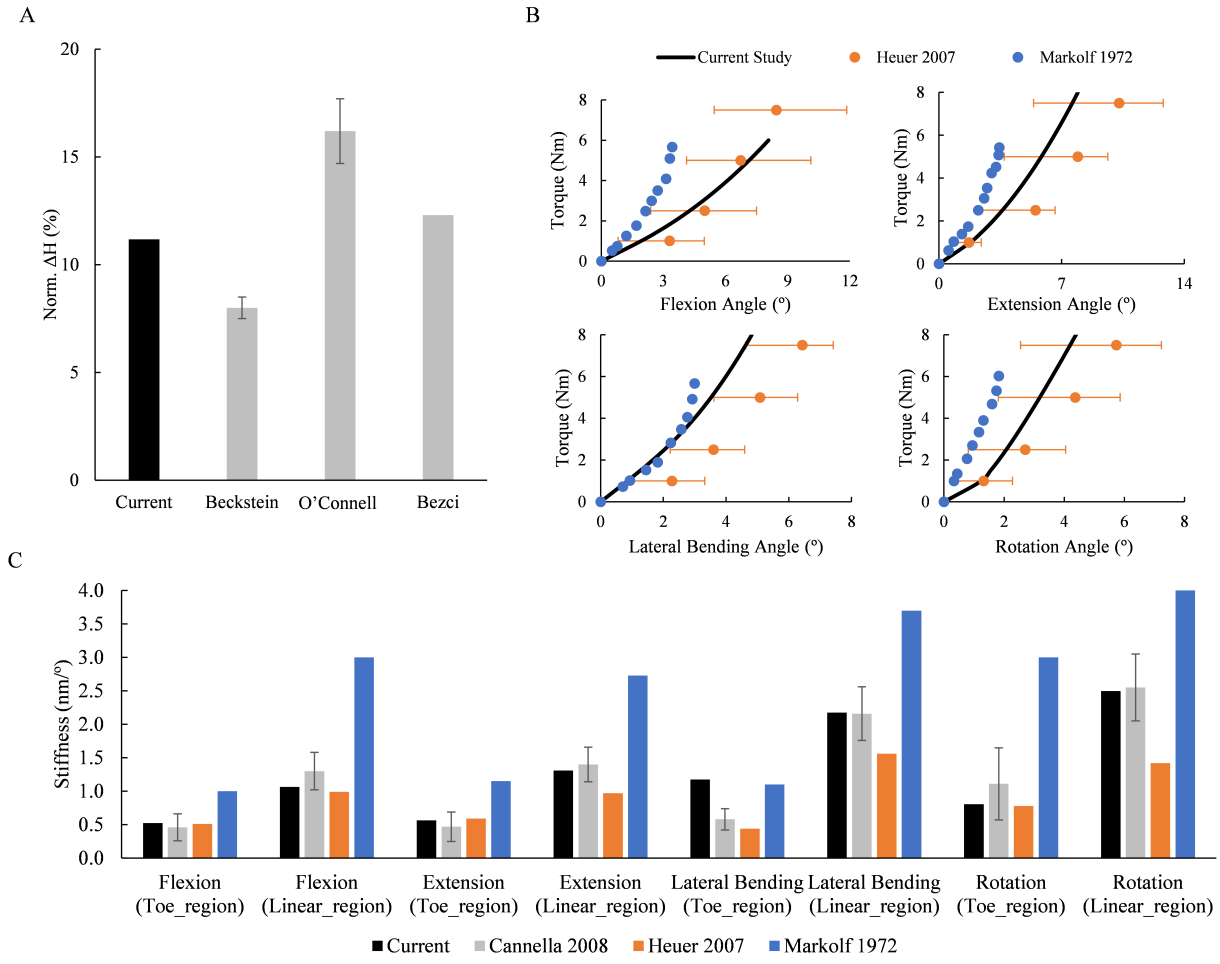


Figure 3.2: Model validation results. **A**) Results for the Control model were compared to experimental data for normalized disc height change under axial compression [35, 105, 144]. **B**) Load-displacement curves for bending and axial rotation without a compressive preload were shown for the Control model (black lines, NP:Disc area ratio = 0.28, 5% posterior NP centroid offset). Model simulation results were compared to experimental results from the literature [117, 143]. **C**) Toe-region and linear-region stiffness for bending and axial rotation without a compressive preload were shown for the Control model and compared to experimental results [88, 117, 143]. Error bar in A and C represents one standard variation while error bar in B represents range of the test result.

## Series I: Effect of NP size

The load-displacement curves under axial compression were nonlinear with a clearly defined toe region and linear region (Figure 3.3A). The normalized compressive stiffness in the toe and linear region increased linearly with an increase in NP:Disc area ratio (Figures 3.3B). The normalized disc height change under compression decreased nonlinearly with an increase in NP:Disc area ratio, from 12.0% for the 0.21 NP:Disc model to 9.3% for the 0.60 NP:Disc model (Figure 3.3C). There was almost a one-to-one correlation between the NP support ratio and NP:Disc area ratio (slope ∼1.0; Figure 3.3D). Axial compression generated follower torques of 2.20 Nm around the X-axis, 0.20 Nm around the Y-axis, and 0.09 Nm around the Z-axis, and the magnitude of torque was not dependent on NP size.

Torque versus angular displacement behavior was nonlinear when the bending moment was applied without a compressive load. However, this response became more linear with the inclusion of a compressive preload prior to bending or rotation (Figure 3.4A). In addition, joint stiffness increased with the inclusion of a compressive preload. There was no effect of NP size on bending stiffness in flexion, extension, or lateral bending. Joint stiffness for the 0.28 NP:Disc ratio model under flexion, extension, and lateral bending with a compressive preload was 0.98 Nm/°, 0.98Nm/° and 2.3 Nm/°, respectively (Figure 3.4B). There was a slight decrease in torsional stiffness for models at the upper range of NP area, where torsional stiffness decreased by ∼20% from 1.89 Nm/° to 1.46 Nm/° as the relative NP area increased from 0.21 to 0.60 (Figure 3.4B –black line).

Models with a larger NP:Disc area ratio demonstrated a more uniform pressure distribution, with lower peak pressures under compression and compression with rotation (Figure 3.5 - first and last columns). There was a shift in the high-pressure region with bending, as expected for a moving pivot joint (Figure 3.5 –$2^{nd}$ –$4^{th}$ columns). In addition, larger NP:Disc models exhibit a larger transition region from high to low pressures, with a lower overall pressure gradient for all loading conditions (*e.g.*, Figure 3.5).

Pressure distributions along the middle disc height of the mid-sagittal plane were similar for all models in Series I (Figure 3.6A –data shown for axial compression). The average NP pressure was higher than the average AF pressure for all loading conditions (Figures 3.6B & C). The average pressure in the NP and AF decreased as the relative NP size increased and this behavior was observed for all loading conditions (Figure 3.6B & C). The average

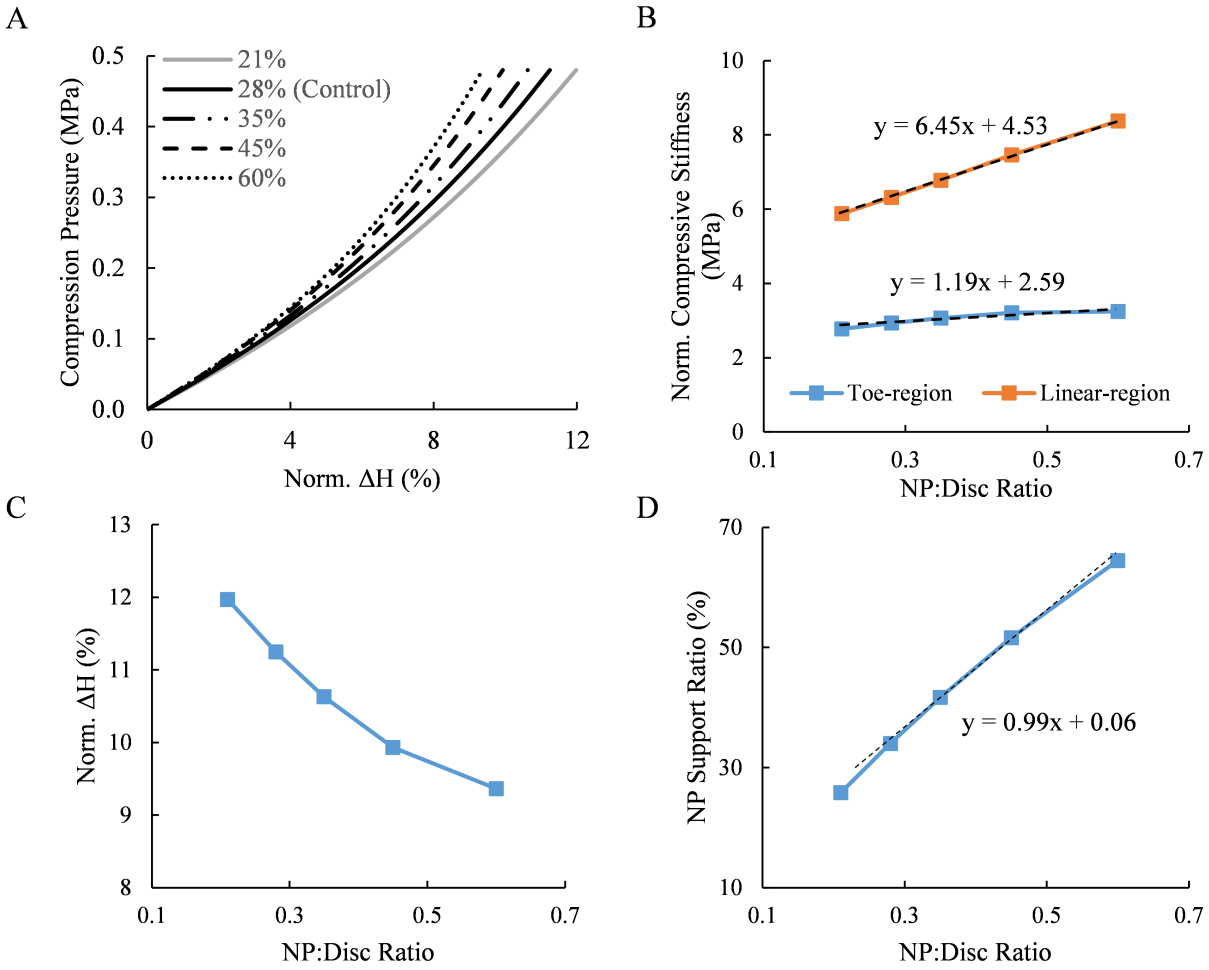


Figure 3.3: **A**) Compressive load (pressure) versus the change in disc height under load normalized to the original disc height. **B**) Normalized compressive stiffness (Stiffness x disc height/ disc area) of the toe- and linear-region versus NP:Disc area ratio. **C**) The change in disc height under compression decreased nonlinearly with an increase in NP:Disc area ratio. **D**) Percentage of NP support under 0.48 MPa compression, which was calculated as the ratio of NP support divided by applied axial compressive load. Relative NP support increased with NP:Disc area ratio. Dash lines in B and D represent a fit line with equation aside.

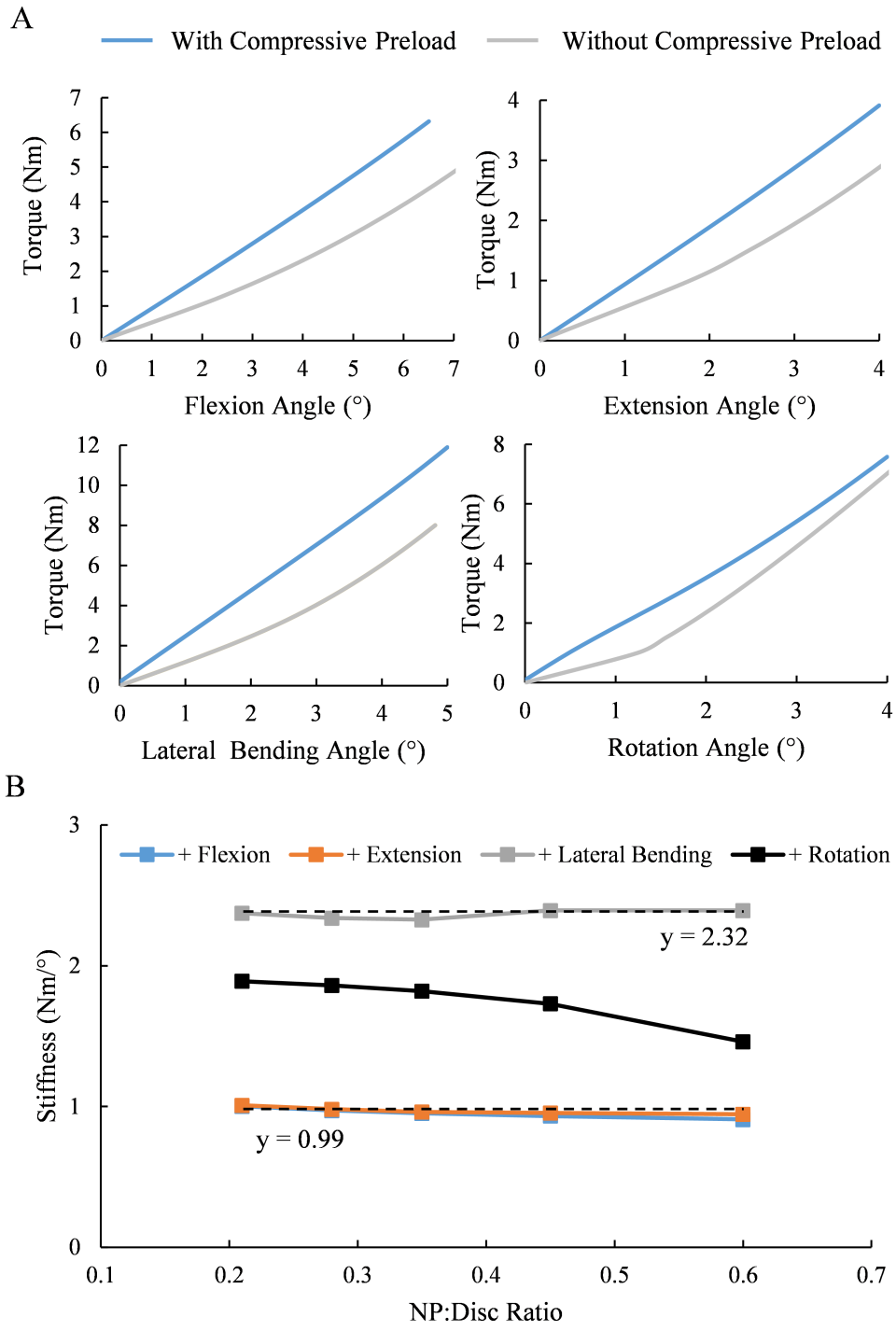


Figure 3.4: **A**) Torque versus angular displacement for the Control model under bending and rotation, with the reference configuration defined as the moment after axial compression was applied. Simulations were performed with (blue lines) or without (grey lines) a compressive preload. **B**) Disc joint stiffness under bending with a compressive preload. Disc joint stiffness under flexion, extension, and lateral bending varied little with an increase in NP:Disc area ratio. Rotational stiffness decreased slightly with a larger NP area. "+" in the legend represents inclusion of a compressive preload. Dash lines in B represent a fit line with equation aside.

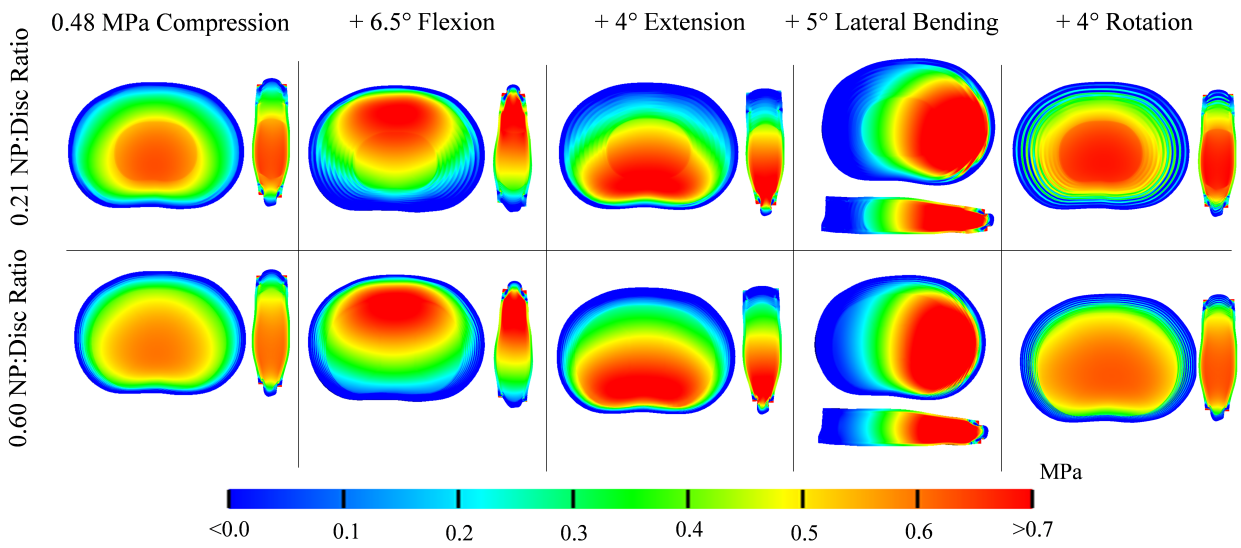


Figure 3.5: Pressure distribution at the mid-disc height (*i.e.*, mid-transverse plane) and mid-sagittal plane for the 0.21 (smallest) and 0.60 (largest) NP:Disc models under compression, bending, and rotation. For lateral bending, mid-coronal plane pressure distributions are presented instead of the mid-sagittal plane. "+" represents inclusion of a compressive preload before bending was applied.

NP pressure was greatest for axial rotation with compression (Figure 3.6B –blue line). In contrast, the average AF pressure followed the opposite trend, where the average AF pressure was lowest under axial rotation with compression (Figure 3.6C –blue line).

Compression and compression combined with extension resulted in strain concentrations located in the posterior AF of the disc, and the area of peak strains was greater for discs with a relatively larger NP area (Figure 3.7 –red area in $1^{st}$ and $3^{rd}$ columns). Compression combined with flexion resulted in strain concentrations at the anterior AF, while compression with lateral bending caused peak strains in the AF and on the side of applied lateral bending, as expected (Figure 3.7 –$2^{nd}$ and $4^{th}$ column). The area of peak strains in the AF for compression combined with flexion or lateral bending was greater for discs with a smaller NP size. Finally, compression with axial rotation resulted in strain concentrations in the posterior-lateral AF, and the area of peak strain was similar regardless of NP:Disc area (Figure 3.7 –last column).

The average first principal strain increased in both the NP and AF with NP:Disc area

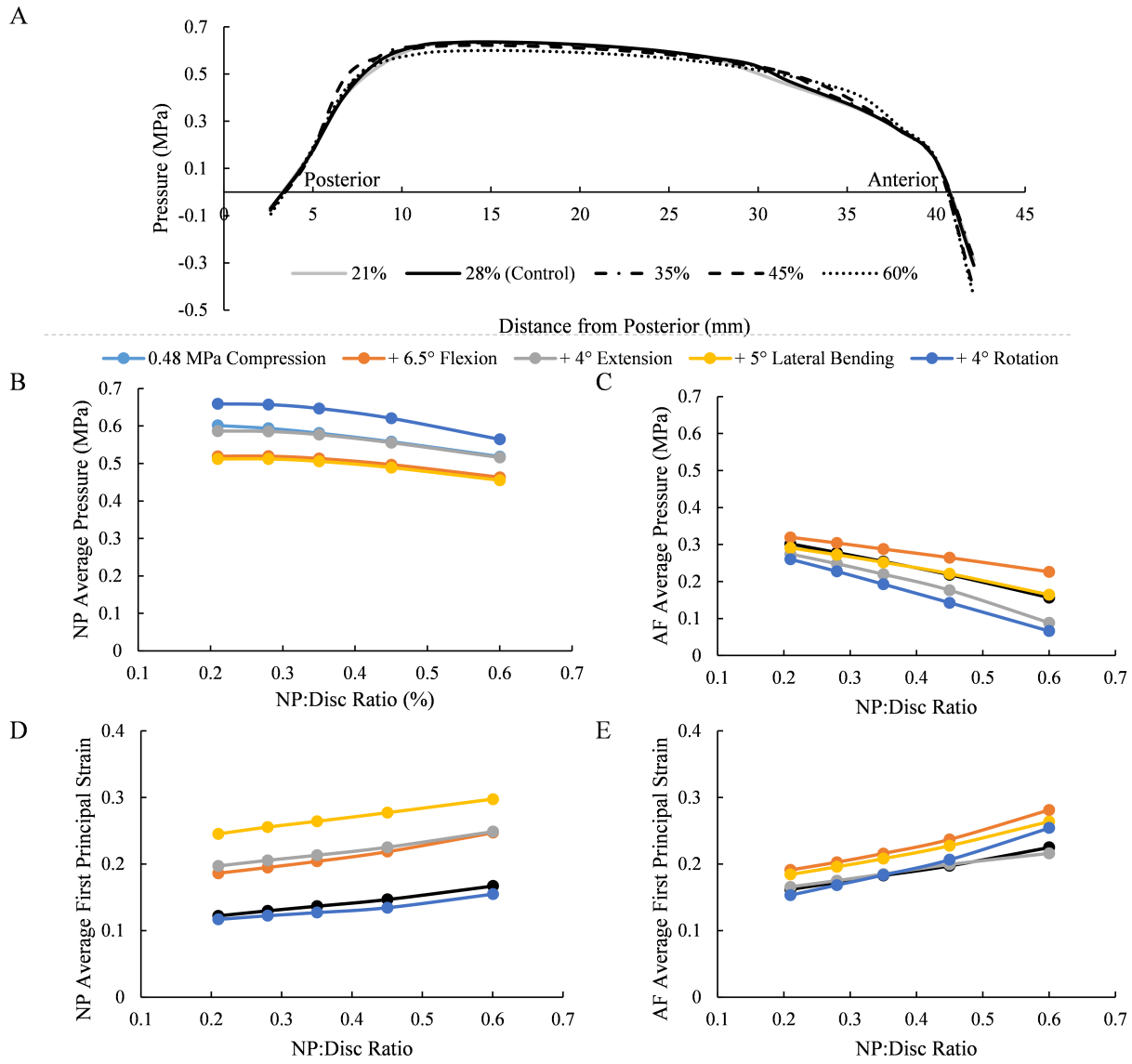


Figure 3.6: **A**) Pressure distribution along the mid-disc height from the posterior to the anterior of the mid sagittal plane under 0.48MPa axial compression. Average pressure in the **B**) NP and **C**) AF under compression, bending or rotation with respect to NP:Disc area ratio. Average first principal strain for the **D**) NP and **E**) AF under compression, bending or rotation with respect to NP:Disc area ratio. Figure 3.5**B-E** share the same legend, where "+" represents inclusion of a compressive preload.

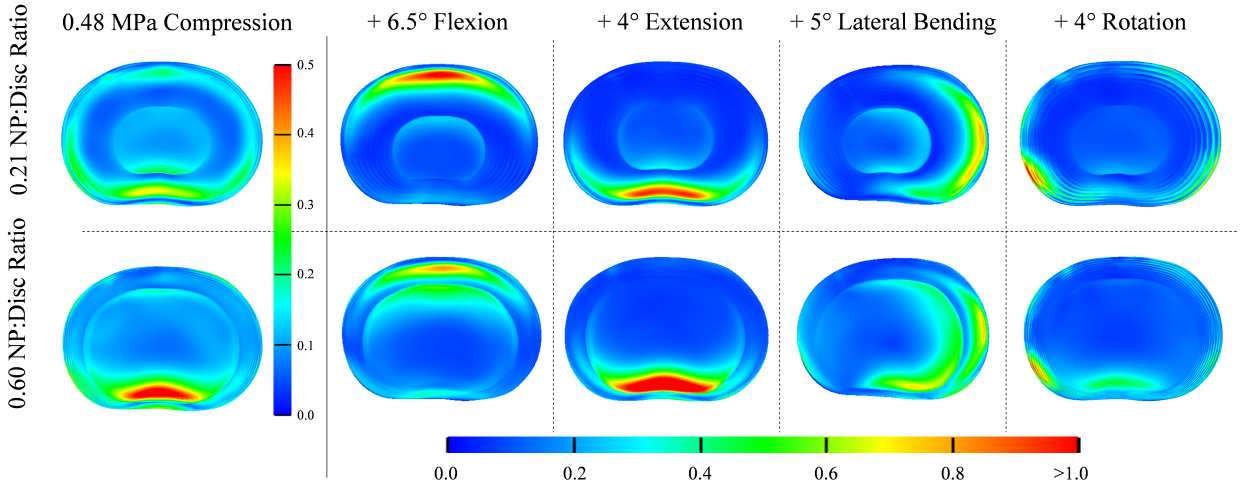


Figure 3.7: Strain distribution of the first principal strain at the mid-disc height (*i.e.*, mid-transverse plane) for the 0.21 and 0.60 NP:Disc models under compression-only loading and compression with bending or rotation. "+" represents inclusion of a compressive preload before bending was applied.

ratio (Figures 3.6D & E). In the NP, the greatest average principal strains were observed for compression with lateral bending (Figure 3.5C –left column, yellow line). The average first principal strain in the NP was similar for compression-only loading and compression with axial rotation (Figure 3.6D blue versus black lines). Similarly, the average first principal strains in the NP were comparable for compression with flexion and compression with extension (Figure 3.6D, gray and orange lines). The range of average first principal strain with loading modality was smaller for the AF (0.15 to 0.25 in the AF versus 0.1 to 0.3 in the NP), but the overall response was similar (Figure 3.6E).

## Series II: Effect of NP centroid position

ASNP and PSNP models showed the same response to axial compression as the Control model (Figure 3.3A –solid black line). Follower torque around the X-axis was lower in the ASNP model (1.92 Nm) and was greater for the PSNP model (2.48 Nm, versus 2.20 Nm for the control). However, there was no change in disc joint stiffness with NP centroid location for flexion, extension, lateral bending, or axial rotation.

Similar to the direction of movement of the NP centroid location, the pressure distri-

bution under axial compression shifted anteriorly when the NP centroid was located more anteriorly (ASNP model; Figure 3.8A –orange versus blue lines). In the same fashion, the pressure distribution shifted posteriorly when the NP centroid was shifted posteriorly (PSNP model; Figure 3.8A –grey versus blue lines). Flexion caused a high-pressure region to develop at the interface between the NP and anterior AF, and peak pressures were greater when the NP centroid was located more posteriorly (Figure 3.8B - PSNP model). The high-pressure area, which was calculated by integrate volume of elements with pressures greater than 0.7 MPa, in the ASNP model was 40% greater than the Control, while the high-pressure area of the PSNP model was 30% smaller than the Control. In extension, the high-pressure region occurred at the interface between the NP and posterior AF, as expected. The high-pressure region in the ASNP model was 30% smaller than the Control model, while the high-pressure region in the PSNP model was 60% greater than the Control (Figure 3.8C).

The average NP pressure under flexion and extension was slightly affected by the location of the NP centroid, where the average NP pressure in the ASNP model was greater than the Control in flexion but lower than the Control in extension. Conversely, the average NP pressure in the PSNP model was slightly lower than the Control in flexion and greater than the Control in extension. The average AF pressure followed the opposite trend of the average NP pressure. Overall shifts in the average pressure corresponded to relative increases in maximum pressure.

## 3.4 Discussion

Model simulations demonstrated that NP size has a significant impact on compressive stiffness, intradiscal pressure, and principal strain. The location of the NP centroid within the disc space had a significant impact on the magnitude and distribution of intradiscal pressure in flexion and extension. Dual-loading modalities, such as axial compression in combination with axial rotation or bending, were simulated to better represent complex *in vivo* loading conditions. Simulations indicated that NP geometry and location are important factors for developing accurate computational models to study the mechanical behavior of native, injured, or degenerated discs and for creating a tissue-engineered disc.

A nonlinear response was observed from the Control disc under simple rotation or

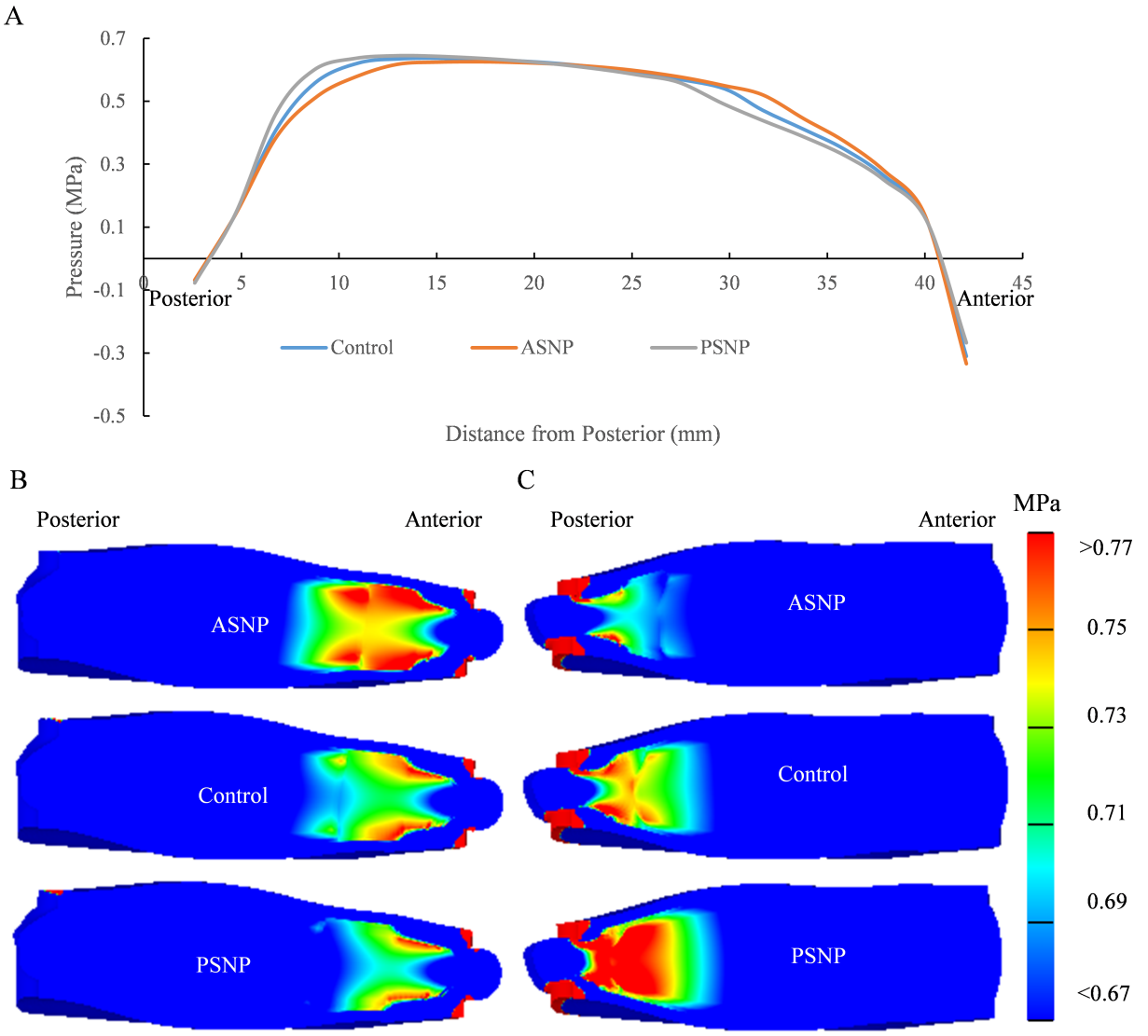


Figure 3.8: **A**) Pressure distribution along the mid-disc height under 0.48 MPa axial compression. Pressure distribution in the mid-sagittal plane for models in compression with **B**) 6.5° flexion and **C**) 4° extension. All data is displayed with the posterior AF on the left side and the anterior AF on the right side.

bending modalities (Figure 3.4A), which agreed with previous experimental and numerical results [87, 101, 117, 143, 148, 149]. Including a compressive preload, which better mimics *in vivo* loading conditions, increased disc joint stiffness and eliminated the nonlinear response in rotation and bending, which agreed with other experimental observations (Figure 3.4A) [144, 150, 151]. The loss of nonlinearity is likely due to collagen fibers being pre-stretched during compression [63]. While these results demonstrate the importance of testing the disc joint under multiple loading modalities simultaneously, multi-axial loading machines are costly, with only a few existing worldwide [121, 152].

Previous studies have shown that vertical and horizontal compressive stresses are equivalent (hydrostatic state) at the mid-disc height of healthy lumbar discs under compression [153, 154]. Moreover, the pressure distribution in healthy NPs was uniform, dropping to 0 as the pressure transducer approached the outer AF. Our simulation showed a similar profile of pressure distribution except that a negative pressure was calculated at the AF periphery, which cannot be measured by a pressure transducer (Figures 3.5 in $1^{st}$ column & 3.6A). Adding flexion and extension to compression shifted the pressure distribution anteriorly and posteriorly, respectively, which also agreed with experimental measurements (Figures 3.5 in $2^{nd}$ & $3^{rd}$ columns) [9, 154].

A marker of disc degeneration is the expansion of fibrous tissue from the inner AF and a reduction in NP area [9, 48, 58, 155]. Fibers are stiff, which would suggest that the discs with a smaller NP size (and great fiber volume) might be stiffer. However, our results showed that a decrease in relative NP area, separate from other biochemical changes, greatly decreased disc joint compressive stiffness. The effect of relative NP area had a greater impact on the linear region modulus than the toe-region modulus. That is, there was a 15% decrease in toe-region modulus and a 30% decrease in linear-region modulus between the disc with the largest NP and the disc with the smallest NP (from 0.60 model to 0.21 model; Figure 3.3B). Previous data suggest that disc joint compressive stiffness decreases by over 30% with geometric and biochemical changes with age [35, 60]. Taken together, these findings indicate NP plays an important role in supporting disc compressive load and demonstrate that geometric changes, in addition to changes in material properties, greatly contribute to alterations in joint level mechanics.

This is further supported by the change in percent NP contribution with relative NP area. The decrease in NP contribution with NP:Disc area ratio was largely due to the

decrease in area since the average NP pressure was relatively consistent (from 0.52 in the 0.60 model under compression to 0.60 in the 0.21 model). Therefore, NP material properties would need to be more incompressible and inner AF needs to be more capable to restrict NP bulge in order to maintain a consistent NP contribution with a decrease in relative NP area. However, degenerate NP is more solid like while healthy NP is more fluid like [156], likely resulting in a compound effect on disc-joint stiffness.

There has been a growing interest in developing tissue-engineered disc composites to treat degenerated or dysfunctional discs. These biological repair strategies often rely on hydrogels as an NP replacement material with fiber-embedded polymers to mimic the native AF architecture. The NP area of engineered discs is often much lower than native discs (10 - 20% for engineered discs versus ∼30% for healthy human discs) [141, 142]. The difference in NP geometry may contribute to the relatively lower disc-joint compressive stiffness. Findings from this study suggest that optimizing the relative NP area may act to maintain a homeostatic balance between pressure and principal strain (*e.g.*, NP:Disc area ratio between 0.25 and 0.40; Figures 3.6B-E). Limiting peak strains is important for reducing annular tear development or growth, which increases with age [52, 53], and to reduce catabolic remodeling [157]. On the contrary, high internal pressures are thought to be a potential cause for endplate damage [139, 158, 159].

Replicating disc herniation failure *in vitro* has been a significant challenge [122, 160]. Flexion is thought to play a critical role in developing AF wall rupture and herniation [158, 161]. However, a recent study by Berger-Roscher showed that the disc was most susceptible to failure when loaded under a combination of flexion, lateral bending, axial rotation, and axial compression, and least susceptible to failure under flexion-only loading [121]. Moreover, disc failure was observed to initiate at the NP-AF interface in ∼50% of failed discs, similar to clinical observations [138]. These findings agree with peak strain distributions (Figure 3.7), where flexion with compression resulted in peak strains in the anterior AF, rather than the posterior AF. Furthermore, loading combinations with lateral bending or rotation would increase the likelihood of failure occurring at the posterior-lateral AF.

The NP of healthy discs is located slightly posterior of the disc's centroid, and the healthy disc acts like a moving pivot that migrates anteriorly and posteriorly during flexion and extension, respectively [29, 32]. There were no differences in disc joint stiffness under

flexion and extension with respect to relative NP position. However, average pressure and pressure concentration at the NP-AF interface were altered under flexion and extension (Figure 3.8B & C). Shifting the NP centroid anteriorly or posteriorly increased pressure concentrations under extension or flexion, respectively. Although there were no differences observed with joint level mechanical behavior, there were large differences in pressure and strain, highlighting the importance of measuring internal mechanics, such as intradiscal pressure, stress, and strain distribution, in addition to load-displacement behavior.

This study was not without limitations. The current model did not include a structural description of the trabecular bone; therefore, deformations into the vertebral body, due to compression, were not considered [162]. Soft tissues of the disc joint were described using hyperelastic material descriptions; therefore, time-dependent behavior and energy dissipation were not evaluated. Biphasic and triphasic material that can simulate fluid movement will be used in the future to understand the time-dependent effects of NP size and position [38]. Since the stiffness of the fiber component in the strain energy function remained constant, the total fiber volume increased or decreased proportionally with AF volume [9, 48]. Other modeling approaches, such as using rebar elements to describe fibers, can adjust for fiber density by adjusting rebar density and cross-sectional area [101, 163]. We chose this structure to replicate lamella thickening, as observed with degeneration [13, 164]; however, AF fiber density coupled with NP size will likely alter disc joint mechanics. The Control model was validated using experimental data collected from different studies, and much of the available data was for aged or degenerated discs. Therefore, the mechanical behavior of our Control model may be a better representation of a moderately degenerated disc, rather than a nondegenerate disc. Recent work by Mengoni and coworkers developed a FEM of a bovine disc joint and showed that compressive stiffness decreased with a larger NP area [41]. The difference between their findings and ours may be due to differences in disc geometry (cylinder verses kidney-bean shape), differences in lamellae structure (1 versus 20 layers), or differences in collagen fiber orientation ($\pm 20^\circ$ versus $\pm 43^\circ$ in inner AF). Our model predicted a decrease in disc torsional stiffness with NP area, but torsional stiffness has been shown to decrease with degeneration [61, 62]. This discrepancy may indicate that changes in disc torsional stiffness with degeneration are mainly due to changes in material properties, such as NP glycosaminoglycan composition or AF fiber orientation [1, 68]. Besides, we only included materials in a single motion segment; inclusion of posterior elements will be

important for investigating stress distributions between the disc and facet joints. Lastly, the current work only focused on NP size and position; however, altering other structural and material properties will be important for understanding the effect of degeneration on disc behavior.

Computational and tissue engineering studies have adopted a wide range of NP:Disc area ratios, ranging from 0.10 to 0.60 [64, 86, 87, 141, 142]. These design decisions have a significant impact on joint-level mechanics. We showed that NP area and centroid position greatly affects disc joint stiffness, first principal strains, and pressure distributions. In conclusion, the relative NP area is important for understanding joint stiffness and strain distribution in axial compression and rotation, while the NP centroid location is important for understanding pressure distributions during flexion and extension.

# Chapter 4

# Intervertebral Disc Mechanics with Nucleotomy: Differences between Simple and Complex Loading [3]

## Abstracts

Painful herniated discs are treated surgically by removing extruded nucleus pulposus (NP) material (nucleotomy). However, nucleotomy can cause joint instability and increase the rate of degeneration. Experimental and computational studies have shown a decrease in disc stiffness with nucleotomy. However, these studies were limited to single loading modalities, such as compression-only or bending-only loading, which are not representative of *in vivo* loading conditions. The effect of nucleotomy on disc mechanics under complex loading (*e.g.*, compression in combination with bending or torsion) is not well understood. We used a previously validated bone-disc-bone finite element model (Control) to create a Nucleotomy model to evaluate the effect of dual loading conditions (compression with torsion or bending) on intradiscal deformations. While disc joint stiffness decreased with nucleotomy under single loading conditions, as commonly reported in the literature, dual loading resulted in an increase in bending stiffness, agreeing with clinical observations. More specifically, dual loading resulted in a 40% increase in bending stiffness under flexion and extension and a 25% increase in stiffness under lateral bending. The increase in bending stiffness was due to an

increase and shift in compressive stress, where peak stresses migrated from the NP-annulus interface to the outer annulus. In contrast, the decrease in torsional stiffness was due to greater fiber reorientation during compression. In general, large radial strains were observed with nucleotomy, suggesting an increased risk for delamination or degenerative remodeling. In conclusion, the effect of nucleotomy on disc mechanics depends on the type and complexity of applied loads.

**Keywords:** Nucleus pulposus, Intervertebral disc, Nucleotomy, Finite element method, Degeneration

## 4.1 Introduction

Each year, approximately 200,000 patients in the United States are diagnosed with a herniated or prolapsed intervertebral disc [44]. A herniated disc is one in which the gel-like nucleus pulposus (NP) extrudes through a damaged region of the annulus fibrosus (AF), compressing the spinal nerves and causing neurologic dysfunction. Painful herniations are treated through a sub-total discectomy, a procedure that removes the herniated material as well as additional NP material, in order to reduce the risk of re-herniation. Long-term impacts of discectomy include loss of segmental stability and advanced disc degeneration, which can result in re-occurrence of lower back pain [45, 46]. In the laboratory, discectomies are mimicked through nucleotomy, where NP material is removed by creating a large annular defect or by drilling through an adjacent vertebral body [88, 165].

Experimental studies and finite element models have shown that NP removal affects disc joint mechanics and intradiscal deformations. Nucleotomy decreases disc joint stiffness in torsion and bending at low loads (*i.e.*, toe-region behavior), resulting in an increase in range of motion and an increase in contact forces at the facet joints [88, 89]. Internally, nucleotomy decreases intradiscal pressure during compression, resulting in an inward bulging of the inner AF and larger maximum AF strains [30, 90, 91, 92, 93, 94]. However, all of these studies evaluated disc joint mechanics under single loading modalities, such as compression-only or bending-only loading, which are not representative of complex *in vivo* loading conditions.

Unfortunately, few studies have evaluated disc mechanics under complex loading conditions. Recent studies that have applied complex six degrees of freedom loading have been

successfully in initiating disc failure in intact healthy discs (*e.g.*, compression with torsion or bending) [121, 152]. These findings have been valuable for directing computational models aimed at predicting disc joint failure [158]. However, separating the role of each loading modality to potential failure or overloading has been difficult due to the wide range of loading configurations applied simultaneously. Our previous work evaluated the effect of compression in combination with bending or torsion [58, 92, 144] and showed that torsional disc joint stiffness is dependent on the compressive preload. Moreover, partial nucleotomy alters stain distributions throughout the disc, applying more stress directly to the annulus fibrosus. However, experimental measurements of intradiscal strains have been largely limited to two-dimensional strain analysis(*e.g.*, mid-sagittal or mid-coronal) [29, 31, 58].

Therefore, the aim of this study was to evaluate the effect of nucleotomy on disc joint mechanics using a finite element model. Specifically, we evaluated the effect of single versus dual loading on disc mechanics. For dual loading conditions, axial compression was applied as the primary loading configuration. Then, torsion, flexion, extension, or lateral bending was applied after compression. We hypothesized that disc stiffness increases with nucleotomy when tested under dual loading conditions, but will decrease under single loading conditions. To test this hypothesis, we used our previously reported and validated finite element model of the human lumbar disc (Control model) to create a Nucleotomy model by completely removing the NP [2]. Joint-level mechanics and internal stress and strain distributions were compared between Control and Nucleotomy models under various loading conditions.

## 4.2 Method

### Model development

The Control model was a single bone-disc-bone motion segment with geometry based on thirteen L3L4 human male discs averaged together (disc height = 11mm, disc area = 1949 $mm^2$, NP area = 546 $mm^2$, Figure 4.1; ) [1, 112]. The Control model included separate material descriptions for the NP and AF, which were sandwiched between cartilage and bony endplates (Figure 4.1). Disc subcomponents and bones were welded together by sharing nodes on the interface. The AF was divided into 20 concentric layers [13] and each layer was sub-divided into four anatomical regions to assign region-dependent material properties

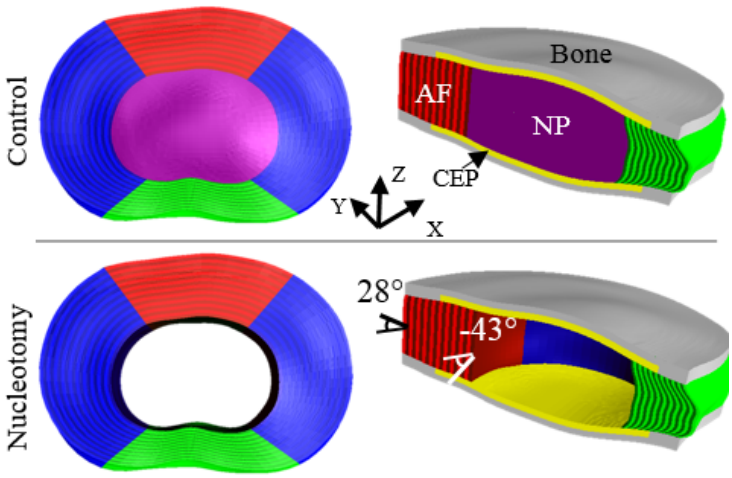


Figure 4.1: Schematic of Control and Nucleotomy models. The annulus fibrosus (AF) was separated into four anatomical regions (red = anterior, blue = lateral, and green = posterior). Fiber orientation alternated between layers, decreasing from ±43° with respect to the horizontal plane in the inner AF to ±28° in the outer AF. The model also included material descriptions for the nucleus pulposus (NP, purple, only in Control model), cartilaginous endplates (CEP, yellow), and boney endplates (grey).

[27, 28].

The NP, cartilage endplates, and bony endplates were described as isotropic hyperelastic Mooney-Rivlin materials. The AF was described as a material with nonlinear elastic fibers, limited to tension-only loading, embedded within an extrafibrillar matrix. Material coefficients for the NP, endplates, and AF matrix were selected from literature (Table 4.1) [85], while fiber coefficients were calibrated using data from single lamellae tensile tests (Table 4.2) [1, 27]. Therefore, the outer AF was stiffer than the inner AF and the anterior AF was stiffer than the posterior AF [27, 28]. A cross-ply fiber architecture was defined, such that each adjacent lamellae had opposing fiber orientations, and the fiber orientation decreased from ±43° in the innermost layer to ±28° in the outermost layer [12]. NP material was removed from the Control model to create the Nucleotomy model, representing an extreme case of the nucleotomy procedure.

Table 4.1: Material parameters for the nucleus pulposus (NP), extrafibrillar matrix of the annulus fibrosus (AF), and cartilaginous endplate (CEP). Each material was described as a Mooney-Rivlin material ($c_1$, $c_2$, k) [1, 85]

| Property | NP | AF matrix | CEP |
|---|---|---|---|
| $c_1$ (MPa) | 0.05 | 0.09 | 0.50 |
| $c_2$ (MPa) | 0.01 | 0.01 | 0.01 |
| k (MPa) | 50 | 3 | 20 |

Table 4.2: Material coefficients for fibers in different regions of the annulus fibrosus. AO: anterior-outer, AI: anterior-inner, LO: lateral-outer, LI: lateral-inner, PO: posterior-outer, and PI: posterior-inner. Fibers were described using a nonlinear strain energy density function, where E represents the linear region Young's modulus, $\beta$ represents toe-region nonlinearity, and $\lambda_0$ represents the transition stretch between the toe and linear region [1, 27]

| Region | AO | AI | PO | PI | LO | LI |
|---|---|---|---|---|---|---|
| E (MPa) | 57 | 18 | 35 | 15 | 46 | 16.5 |
| $\beta$ | 4 | 5 | 5 | 6 | 4.5 | 5.5 |
| $\lambda_0$ | 1.01 | 1.07 | 1.03 | 1.10 | 1.02 | 1.09 |

## Model simulation and data analyses

Our previous study validated the mechanical behavior of the Control model by comparing model results from single loading conditions, such as axial compression, torsion, flexion, extension, and lateral bending, to experimental data [2]. In short, the normalized change in disc height under axial compression and joint stiffness agreed well with values in the literature [35, 105, 144]. Moreover, the angular displacement-torque response in flexion, extension, lateral bending, and axial rotation agreed well with the behavior reported in the literature [88, 117, 143]. For this study, a 936 N (0.48 MPa) compressive load was first applied. Then, angular displacements of 4° in axial rotation or torsion, 6.5° in flexion, 4° in extension, and 5° in lateral bending were applied and evaluated separately (2 models X 4 simulations = 8 total simulations). Angular displacements were selected based on the range of motion of human lumbar discs [120, 145, 147]. All simulations were conducted in FEBio [116].

The normalized change in disc height was calculated as displacement in the axial direction divided by the initial disc height. Compressive stress was averaged across all elements in the disc and plotted against the normalized change in disc height. Peak stress and strains

were calculated by sorting stress and strain data for all elements and averaging the top 10% of elements with a weight of the element volume. Normalized compressive stiffness (MPa) was calculated as the slope of the stress-normalized displacement curve in the toe and linear regions (nonlinear response). Torsional and bending stiffness (Nm/°) was calculated as the slope of the torque versus angular displacement curves, which had a linear behavior. Stress and strain distributions were evaluated with respect to the disc's natural axes (*i.e.*, axial, radial, and circumferential directions). Fiber stretch and fiber reorientation were calculated for each element and a weighted average was calculated for each layer, using the volume of each element as a weighting factor. Only fibers in tension were included in the data analysis. The volume ratio of stretched fibers in each layer was calculated as the volume of fibers in tension divided by the total layer volume.

## 4.3 Result

### Disc joint mechanics: compression-only loading

The normalized change in disc height for the Nucleotomy model in axial compression was 2-fold greater than the Control model (2.63 mm or 23.9% versus 1.23 mm or 11.2%, Figure 4.2A). There was a ∼60% decrease in toe-region compressive stiffness and a ∼40% decrease in linear-region stiffness with nucleotomy (Figure 4.2B). While a wide range of values for disc joint compressive modulus has been published for intact (4-25 MPa) and partial or complete nucleotomy discs (2-29 MPa) [138], based on average data in the literature, the relative trends observed were comparable to behavior reported in the literature. The decrease in compressive stiffness was also within one standard deviation of reported values for total nucleotomy [88]. Thus, we considered the Nucleotomy model valid for assessing changes in intradiscal stress and strain distributions.

### Disc joint mechanics: dual loading conditions

While torque versus rotation behavior for bending only loading (*i.e.*, no compressive preload) was nonlinear, applying a compressive preload prior to bending resulted in a linear torque-rotation response (Figure 4.3A). Torsional stiffness decreased by more than 30% with

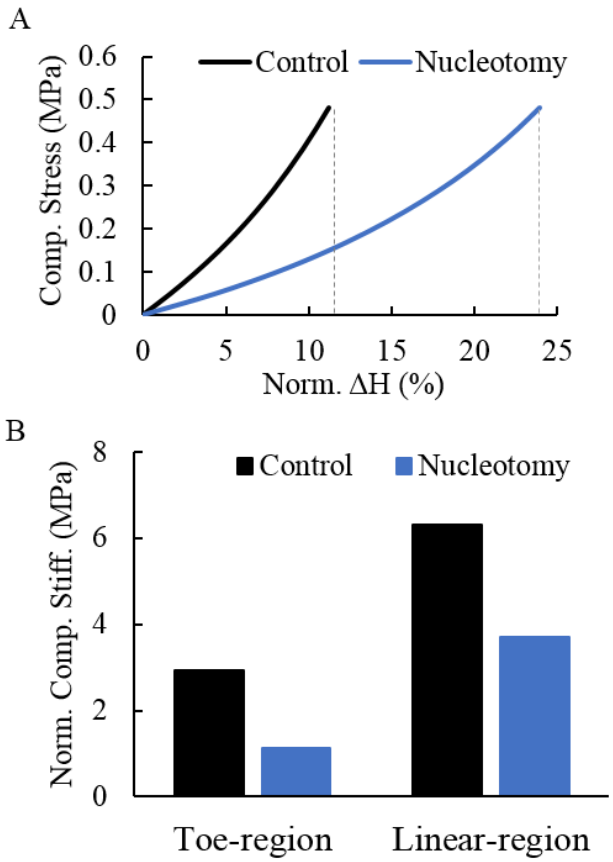


Figure 4.2: **A**) Compressive stress versus the normalized change in disc height. **B**) Normalized compressive stiffness in the toe and linear regions was calculated as the slope of the compressive stress versus normalized change in disc height.

nucleotomy. However, bending stiffness in flexion and extension increased by more than 40% and lateral bending stiffness increased by 25% with nucleotomy (Figure 4.3B). Since dual-loading conditions provide a better representation of *in vivo* loading, further data analyses (*e.g.*, stress and strain distributions, and fiber reorientation under bending) were performed only on dual loading simulations, with compression-only loading used as a control.

## Stress distributions

In the Control model, average axial compressive stress at the mid-transverse plane was highest in the NP (magnitude: $\sim$0.63 MPa in the NP versus the AF $<$ 0.5 MPa; Figure 4.4).

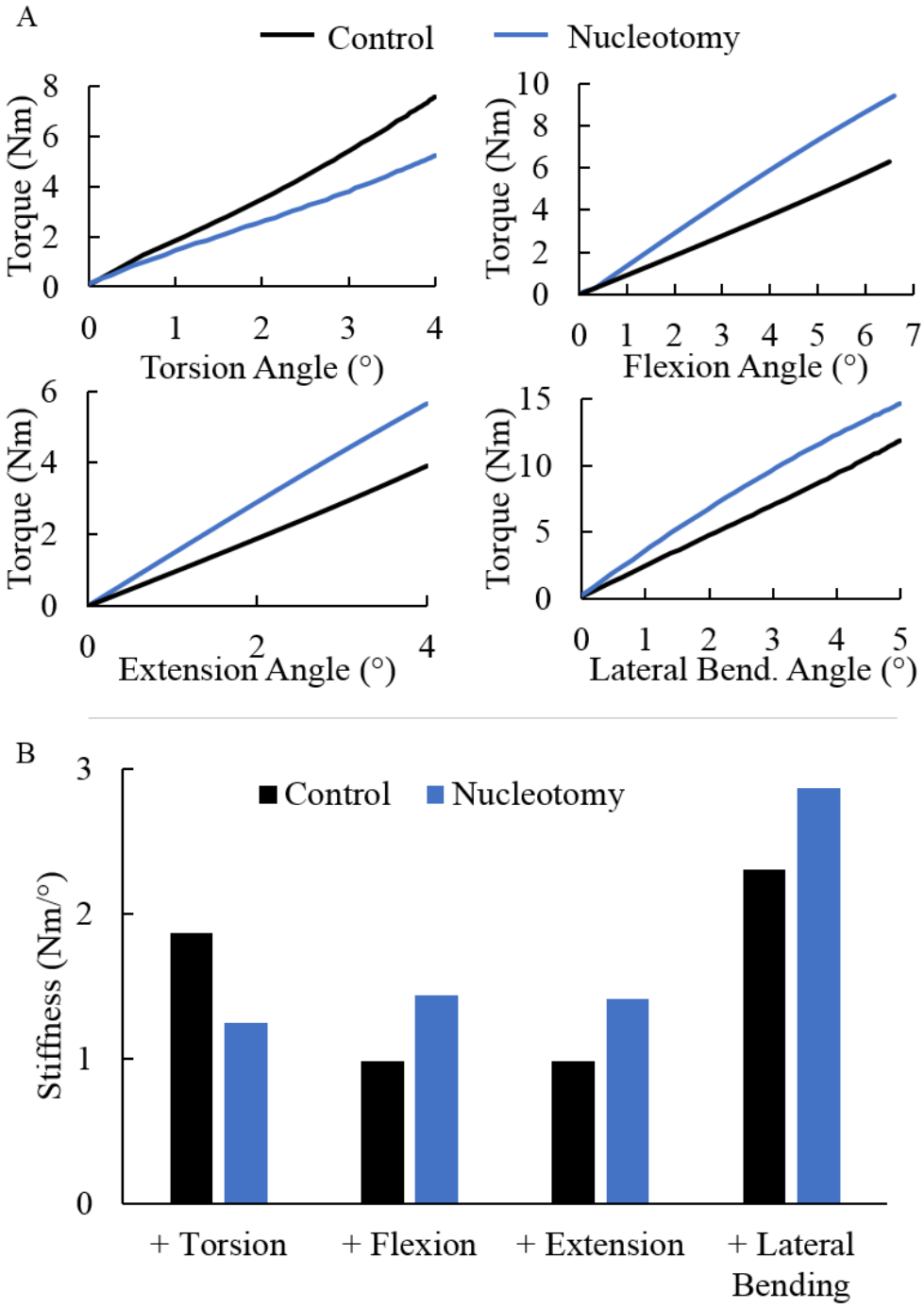


Figure 4.3: **A**) Torque versus rotation angle for Control (black) and Nucleotomy (blue) models under axial torsion, flexion, extension, and lateral bending. A 948 N compressive load was applied prior to bending. **B**) Disc joint stiffness was calculated as the slope of each torque-rotation curve. '+' indicates each loading condition was applied in combination with axial compression.

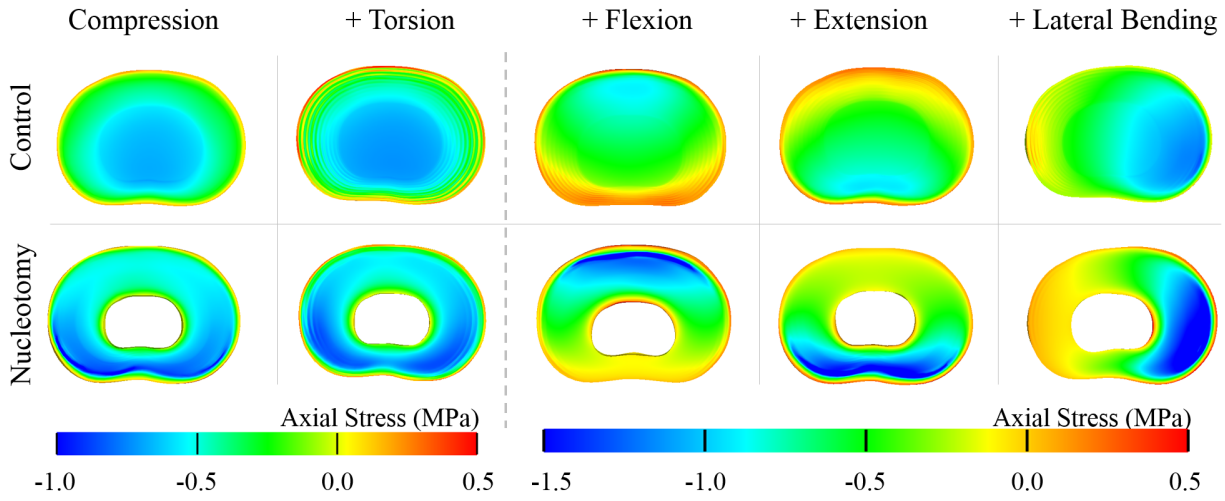


Figure 4.4: Axial stress distribution at the mid-transverse plane for the Control ($1^{st}$ row) and Nucleotomy ($2^{nd}$ row). Axial torsion, flexion, extension, or lateral bending was applied after axial compression. Peak compressive stress was ∼50% higher in bending; therefore, a separate legend was used for clarity.

Peak axial compressive stresses in the AF shifted towards the outer posterolateral region in the Nucleotomy model, with a 57% increase in stress magnitude (Control ≈ 0.51 MPa and Nucleotomy ≈ 0.80 MPa; Figure 4.4 - $1^{st}$ column). Applying torsion after compression did not alter axial stress distributions in either the Control or Nucleotomy model (Figure 4.4 –$1^{st}$ column versus $2^{nd}$ column). Flexion, extension, or lateral bending combined with compression shifted the location of peak axial compressive stress towards the side of loading (Figure 4.4 - $3^{rd}$ -$4^{th}$ columns). In the Control model, peak axial compressive stresses were located in the inner or inner-middle AF. Removal of the NP slightly shifted the location of peak axial compressive stresses to the outer AF, resulting in a ∼53% increase in peak stress from 0.89 MPa to 1.36 MPa.

In the Control model, the NP also experienced high compressive stress in the radial and circumferential directions (magnitude > 0.5 MPa, Figure 4.5 –$1^{st}$ and $3^{rd}$ rows). The median radial-direction stress in the NP was -0.59 MPa and the magnitude of maximum stress, calculated as the average of the top 10% volume of peak stress in the NP, was -0.64 MPa. Similar to axial direction compressive stress, bending resulted in a shift in the location of peak radial stress and circumferential stress as well as a slight increase in the

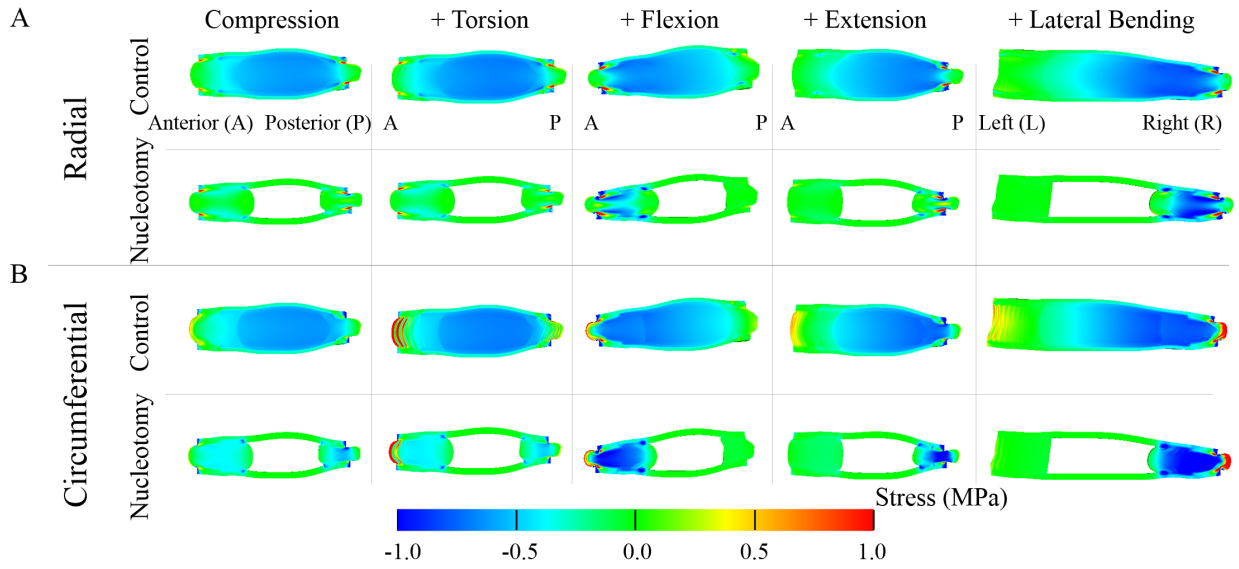


Figure 4.5: **A**) Radial and **B**) circumferential direction stress distributions at the mid-sagittal plane for Control (top row) and Nucleotomy (bottom row) models. '+' indicates axial torsion, flexion, extension, or lateral bending was applied after compression.

magnitude of peak stress ( 5% increase). In the Nucleotomy model, peak compressive radial and circumferential stress occurred in the middle AF layers and was located on the side of loading when bending was applied (Figure 4.5 –$3^{rd}$ –$4^{th}$ columns). In both Control and Nucleotomy models, tensile circumferential direction stresses increased in the outer AF with bending and torsion (Figure 4.5B –red regions), with greater tensile stresses occurring in the Control disc.

## Strain distributions

In the Control model, axial direction strains in the Control model under compression were similar in the NP and AF, where peak compressive axial strains occurred at the mid-disc height (Figure 4.6A –$1^{st}$ column). Removal of the NP resulted in greater compressive axial strains in the AF, with inward bulging of the inner annulus, and these peak strains still occurred at the mid-disc height (Figure 4.6A - $1^{st}$ column). Applying torsion after compression did not alter axial strain maps (Figure 4.6A - $1^{st}$ column versus $2^{nd}$ column). Flexion, extension, and lateral bending in the Control model shifted the location of peak

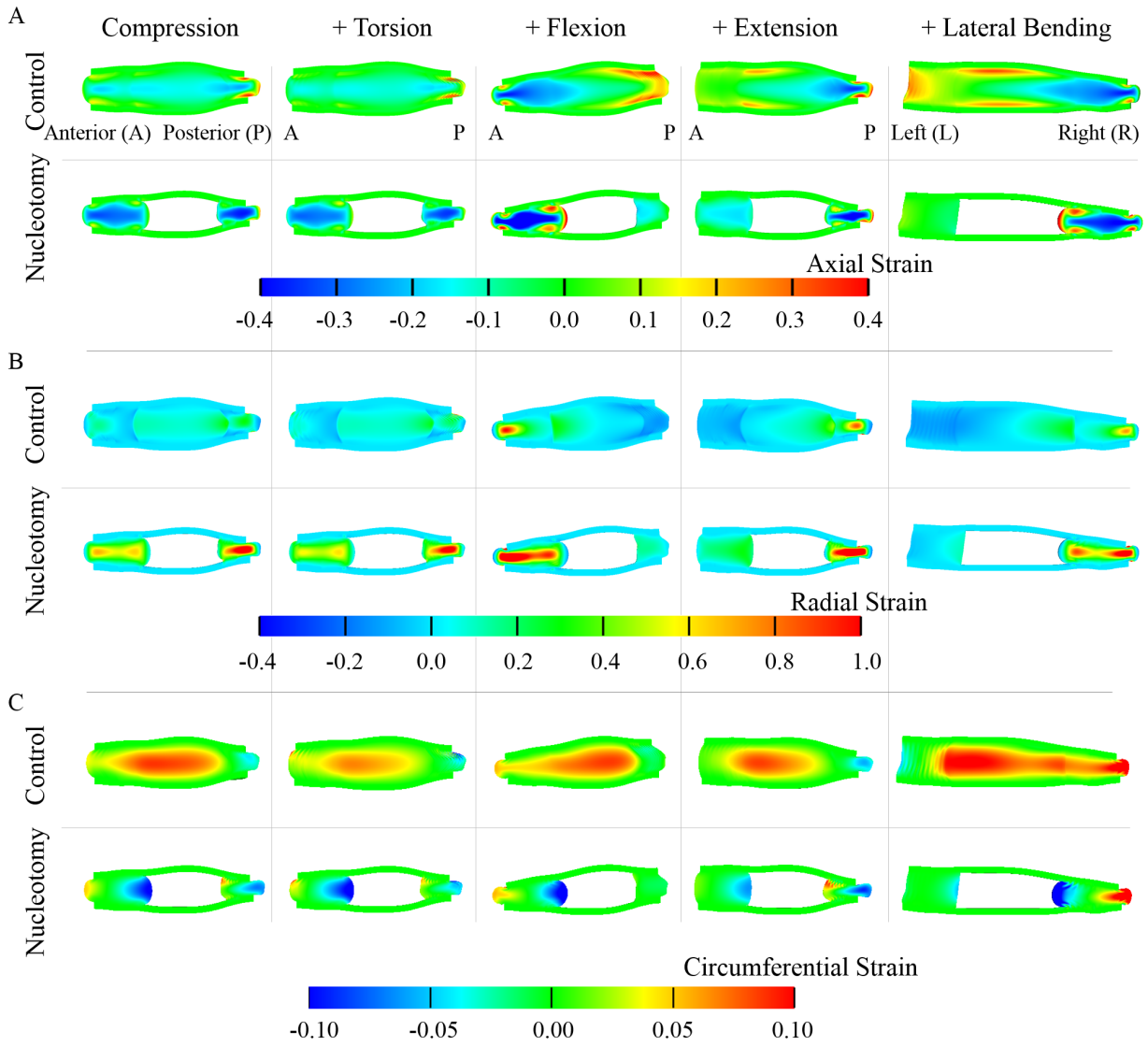


Figure 4.6: **A**) Axial, **B**) radial, and **C**) circumferential strain distributions at the mid-sagittal plane for Control (top row) and Nucleotomy (bottom row). '+' indicates axial torsion, flexion, extension, or lateral bending was applied after compression.

compressive axial strains to the side of loading, while the opposite side (*e.g.*, posterior AF under flexion) experienced tensile axial strains (Figure 4.6A - columns 3-5, top row). In contrast, peak tensile and compressive axial strains occurred on the same side as applied loading in the Nucleotomy model (Figures 4.6A - columns 3-5, bottom row).

Due to the Poisson effect, large tensile radial strains developed at the location of peak compressive axial strains (Figure 4.6B). Similarly, large compressive radial strains developed at locations of tensile axial strains. Lastly, the magnitude of circumferential strains was much lower (< 25%) than the magnitude of axial or radial strains (<0.1 versus <0.4 MPa; Figure 4.6C). In the Control model, tensile circumferential direction strains were higher in the NP. However, tensile circumferential direction strains in the Nucleotomy model only developed as localized strain concentrations at innermost (*i.e.*, extension) or outermost regions of the AF (*e.g.*, flexion and lateral bending).

## Fiber stretch

In the Control model, approximately 35% of inner AF fibers (*i.e.* stretch volume ratio $\approx$ 0.35) and $\sim$85% of outer AF fibers were loaded in tension during disc joint compression (Figure 4.7A –black, Figure 4.8 - $1^{st}$ column). Nucleotomy decreased fiber engagement in the inner AF during compression, with only $\sim$20% of inner AF fibers loaded in tension. However, fiber engagement in the outermost AF layers were not affected by Nucleotomy (last $\sim$2-3 layers; Figure 4.7A –blue). In the Control, fibers that were engaged during compression experienced relatively uniform stretch throughout the AF (average stretch $\sim$1.02; Figure 4.7B). Layer-averaged fiber stretch in the inner AF increased 2-3-fold with nucleotomy (Figure 4.7B –black versus blue 'x's).

Applying torsion after compression resulted in total fiber engagement in every other layer and complete unloading of fibers in adjacent layers (Figure 4.7C –black triangles alternating between 0.0 and 1.0 for the Control model). Engagement of only half of the available fiber during torsion resulted in a 100% increase in fiber stretch (fiber stretch increased from 1.02 to >1.04; Figure 4.7B versus 7D), where peak fiber stretch occurred in the posterior and posterior-lateral AF (Figure 4.8 - $2^{nd}$ column). In the Nucleotomy model, fiber engagement under torsion followed similar trend, but maximum fiber engagement in the inner AF was 40% lower than the Control (Figure 4.7C), resulting in slight differences in fiber stretch (Figure 4.7B versus 4.7D –blue lines). Fiber engagement and fiber stretch in the outer AF during compression combined with torsion did not change with nucleotomy.

Fiber engagement during bending with compression was relatively uniform throughout the AF, increasing in the outer 25% of the annulus (Figure 4.7E). Bending increased inner

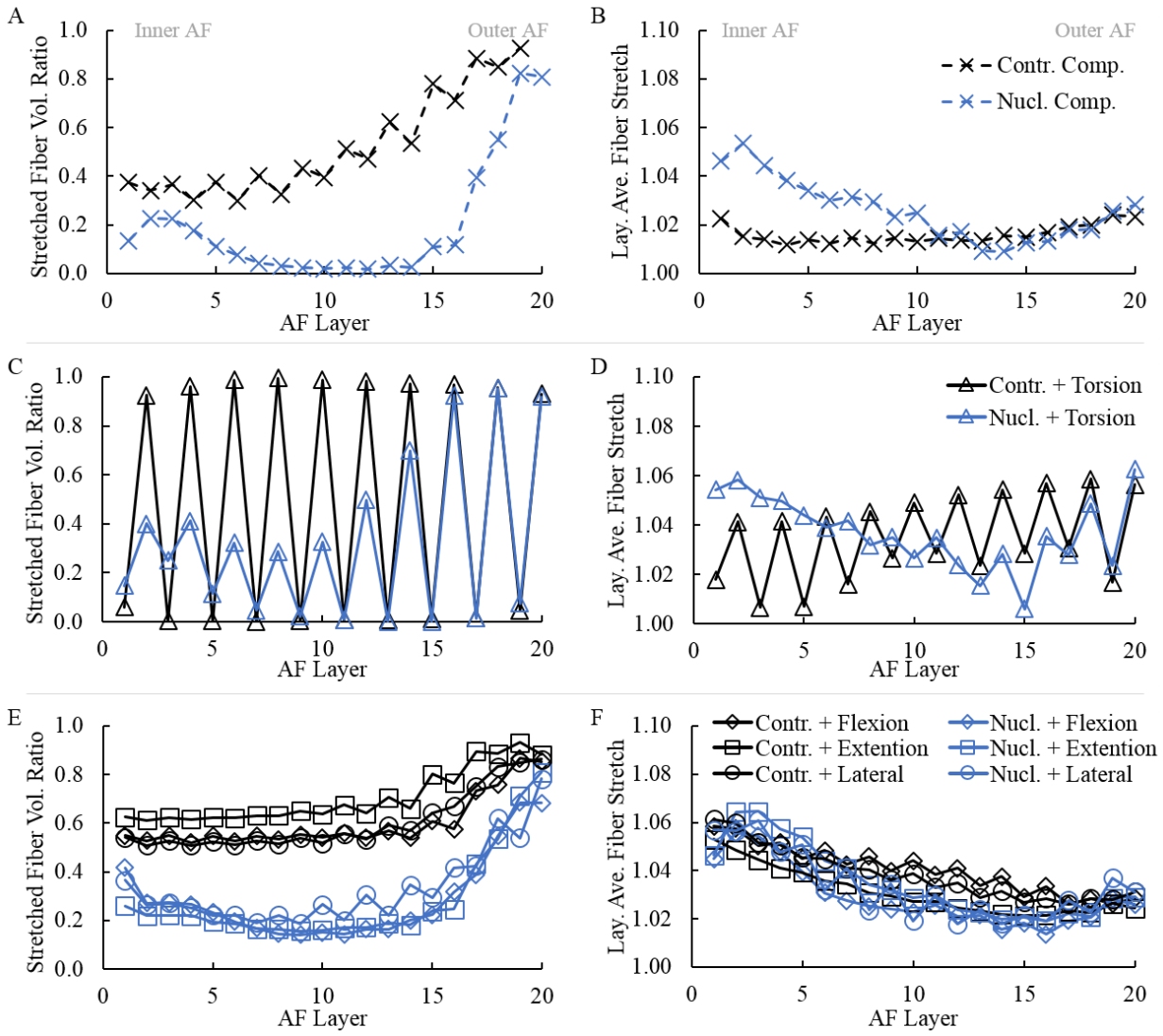


Figure 4.7: Data shown in the left column represents volume ratio of fiber elements under tension for each lamellae. Data shown in the right column represents layer-averaged fiber stretch with respect to lamellae layer. For all plots, Layer 1 represents the innermost layer and Layer 20 represents the outermost layer. Fiber stretch is shown for (**A** & **B**) compression-only loading, (**C** & **D**) compression with torsion, and (**E** & **F**) compression with bending. Black lines represent data the Control model and blue lines represent data from the Nucleotomy model. Figures in the same row shared the same legend.

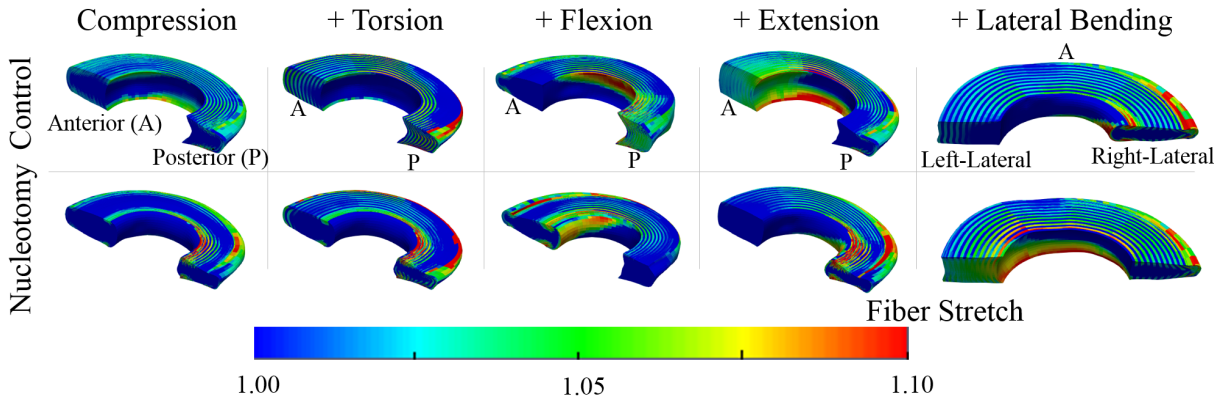


Figure 4.8: Fiber stretch for the Control (top row) and Nucleotomy (bottom row) model under torsion, flexion, extension, and lateral bending, which was applied after axial compression (represented by '+').

AF fiber engagement by 50% in the Control. Similarly, in the Nucleotomy model, inner and mid-AF fiber engagement increased from relatively no fiber engagement to 20% of fibers being loaded under tension (Figure 4.7A versus 4.7E –blue lines) Although the Control model had a greater percentage of loaded fibers throughout the AF (Figure 7E), the average fiber stretch of loaded fibers was comparable between models (Figure 4.7F). In the Control, fiber stretch was greatest in the anterior-lateral to lateral AF under all loading configurations (Figure 4.8 - $3^{rd}$ –$5^{th}$ columns). However, the location of peak fiber stretch shifted to the side of bending with Nucleotomy (Figure 4.8 –bottom row, columns 3-5). Thus, peak fiber stretch occurred in the posterior AF under extension and the anterior AF under flexion.

## Fiber reorientation

Under axial compression, fibers reoriented towards the transverse plane in both Control and Nucleotomy models; however, the magnitude of fiber reorientation was 2X greater in the Nucleotomy model (∼10° versus ∼5°; Figure 4.9A). Furthermore, greater fiber reorientation occurred in the posterior AF with Nucleotomy (Figure 4.10 –$1^{st}$ column). Torsion resulted in a zigzagged pattern in layer-averaged fiber reorientation, where AF layers with greater fiber stretch corresponded with layers that had more fiber reorientation (Figures 4.7D & 4.9B). Bending resulted in relatively few changes in fiber reorientation (Figure 4.9A), but

region-dependent changes were observed in both models (Figure 4.10 - $3^{rd}$ –$5^{th}$ columns). For example, flexion increased fiber reorientation in the anterior AF and decreased fiber reorientation in the posterior AF (Figure 4.10 –$1^{st}$ versus $3^{rd}$ column). Lastly, fibers in the inner AF of the Nucleotomy model reoriented away from the transverse plane, likely due to inward bulging of the AF (Figure 4.10).

## 4.4 Discussion

Simulation results verified our hypothesis that the effect of nucleotomy on disc mechanics differs between single and more complex loading modalities. Under single loading conditions, such as compression-only or bending-only loading, disc joint stiffness decreased with nucleotomy, agreeing with previous experimental and computational studies [30, 88, 89, 91, 117, 166]. However, more complex loading conditions, such as compression combined with bending, resulted in an increase in bending stiffness, suggesting that the disc is more resistant to bending after nucleotomy. An increase in bending stiffness corresponds to a decrease in disc joint range of motion, agreeing with a recent *in vivo* study that reported decreased joint flexibility after nucleotomy [166]. The discrepancy between single- and dual-loading conditions highlights the importance of evaluating disc joint mechanics under conditions that more closely represent *in situ* loading, which will be important for elucidating mechanisms for disc joint failure [152, 158].

The disc is often compared to a pressurized tire or jelly donut; however, the loss of NP pressure, either through severe degeneration or nucleotomy, causes the disc to behave more like a compressed O-ring with much of the applied stress being absorbed directly by the AF [6]. Nucleotomy resulted in high tensile radial strains and inward bulging of the inner AF, which agreed well with experimental observations [30, 91, 92, 94, 160]. Large tensile radial strains occurred more frequently in the mid-AF (Figure 4.6B). Large tensile radial strains may lead to annular delamination, which is known to increase in frequency with age and degeneration [52, 53, 160]. Moreover, herniated discs have also been shown to have 70 - 160% thicker lamellae, which may be a result of a tissue remodeling or permanent deformation due to the increase in radial tensile strains [46, 160, 167].

The increase in joint stiffness under bending was largely due to the applied loading

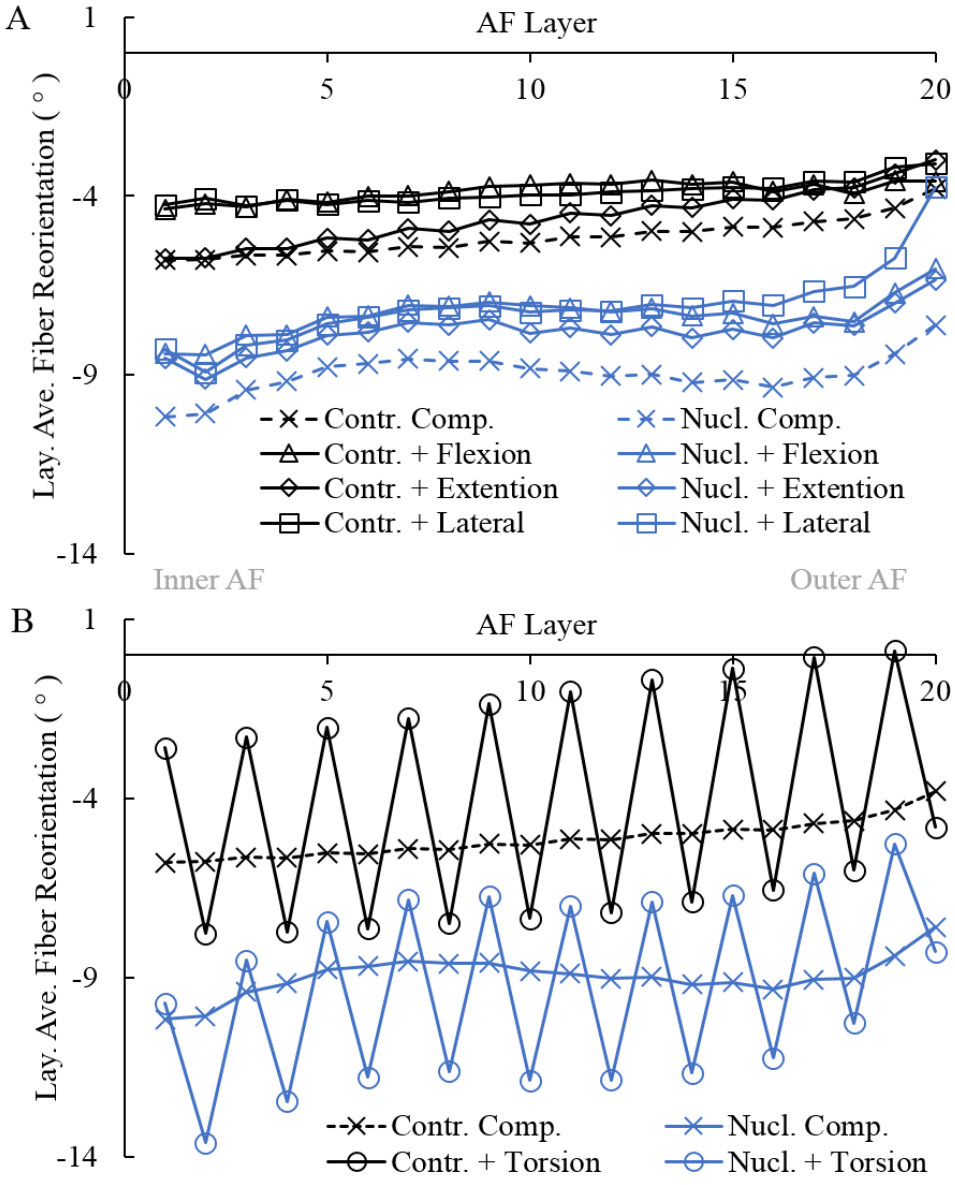


Figure 4.9: Layer-averaged fiber reorientation for each AF layer shown for Control (black) and Nucleotomy (blue) models. **A**) Flexion (triangles), extension (diamonds), lateral bending (squares), and **B**) torsion (circles) was applied after axial compression. Positive values represent fiber reorientation towards the axial plane, while negative values represent reorientation towards the transverse plane.

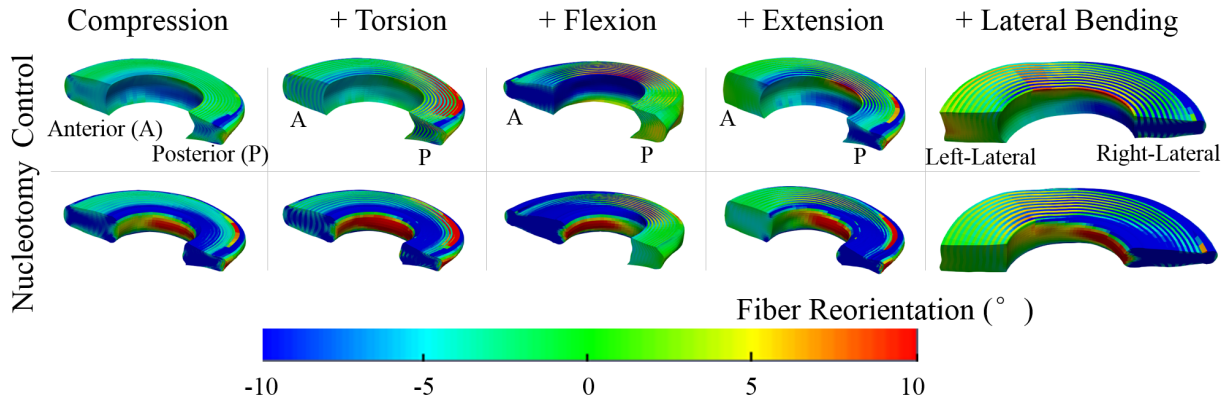


Figure 4.10: Fiber reorientation in the Control ($1^{st}$ row) and Nucleotomy ($2^{nd}$ row) models under torsion, flexion, extension, and lateral bending following compression. Positive values represent fiber reorientation towards the axial plane, while negative values represent reorientation towards the transverse plane.

being placed entirely on the AF, rather than being distributed between the AF and softer NP [92]. The healthy intact disc acts as a moving pivot joint, with the pivot point located near the NP-AF interface. The pivot point of nucleotomy discs in bending shifted towards the outer AF, which may contribute to disc joint instability. The shift in pivot point during bending also reflects a shift in the concentration of applied stress; therefore, the increase in disc joint stiffness is largely due to greater compressive stresses (∼50% increase) and nonlinear material properties [27, 136]. Thus, biological repair strategies that aim to restore NP function following nucleotomy should act to re-shift the pivot point towards the disc centroid or NP-AF interface [138, 168].

Dual loading resulted in an increase in joint stiffness for flexion, extension, and lateral bending after nucleotomy, but joint stiffness decreased under axial rotation. Previous studies have shown that AF damage, as observed in herniated discs, also results in a decrease in axial rotation stiffness (commonly performed through torsion-only loading experiments) [169, 170, 171]. The loss in torsional stiffness with annular injury was due to a reduction in fiber engagement during torsion, where fibers in alternating layers experience tensile deformations [1]. Taken together, this suggests that the Nucleotomy model likely underestimates the decrease in disc joint stiffness under rotation. Regardless, the decrease in joint stiffness under torsion observed here was largely due to differences in behavior that occurred during

the axial compressive preload. That is, AF fibers reorientation towards the horizontal plane during compression and the amount of fiber reorientation increased with nucleotomy. Our previous work showed that discs with fibers orientated close to the horizontal plane have lower torsional stiffness and maximum shear strains, which may make the disc more susceptible to annular damage and remodeling [1]. More importantly, a decrease in disc joint torsional stiffness has been shown to occur in patients with lower back pain [109], but restoring disc joint torsional stiffness with annular or disc repair strategies has been a significant challenge [172].

Nucleotomy and Control models differed greatly with respect to fiber stretch and fiber engagement (Figure 4.7). In the Nucleotomy model, fewer fibers were engaged under compression or torsion loading. Therefore, fibers that were engaged during loading experienced greater strains (fiber stretch), which may cause the inner AF to be more susceptible to further damage accumulation. This observation agrees well with work by Guterl et al., which showed that herniated discs with more damage in the inner annulus had a higher risk of re-herniation [173]. Thus, NP repair strategies that re-pressurize the disc may act to decrease fiber stretch in the inner AF, reducing the risk of additional inner AF damage and re-herniation [174, 175].

Surgical treatment for painful disc herniation requires a balance between relieving pain, reducing the risk of re-herniation, and minimizing the amount of material removed. In this study, we evaluated an extreme case of nucleotomy; however, the actual amount of NP material removed during surgery can vary widely based on injury severity, disc health, and surgeons' approach. In healthy or moderately degenerated discs, remaining NP material would re-swelling to fill the nuclear space, partially or fully restoring disc function; however, a drop in intradiscal pressure may still cause an increase in tensile radial strains, material failure, and tissue remodeling [92, 160]. In this study, load-controlled compression was applied to better represent *in vivo* loading. That is, we assumed little to no change in muscle forces or body weight would occur immediately after nucleotomy. Moreover, the Nucleotomy model did not describe AF damage that typically occurs in the posterolateral region, which would affect the magnitude of predicted stresses and strains near the injury site [138, 165]. Lastly, soft tissues in the model were described as hyperelastic materials, which does not account for time dependent behaviors. Thus, understanding the effect of nucleotomy on short-time scales (viscoelasticity) or long-time scales (tissue remodeling) could

not be assessed.

In conclusion, the effect of nucleotomy on disc mechanics was dependent on the type and complexity of the applied loading condition. While disc joint stiffness decreased with nucleotomy under single loading conditions, as commonly reported in the literature, dual-loading conditions resulted in an increase in bending stiffness, agreeing with clinical observations. Dual loading with nucleotomy resulted in an increase in strain magnitude and altered the distribution of AF stresses and strains, which may lead to further damage accumulation and degenerative remodeling.

# Chapter 5

# Swelling of Fiber-Reinforced Soft Tissues is Affected by Fiber Orientation, Fiber Stiffness, and Lamella Structure [4]

## Abstract

Native and engineered fiber-reinforced tissues are composites comprised of stiff collagen fibers embedded within an extrafibrillar matrix that is capable of swelling by absorbing water molecules. Tissue swelling is important for understanding stress distributions between collagen fibers and extrafibrillar matrix, as well as for understanding mechanisms of tissue failure. The swelling behavior of fiber-reinforced tissues in the musculoskeletal system has been largely attributed to the glycosaminoglycan content. Recent work demonstrated anisotropy in the swelling response of the annulus fibrosus in the intervertebral disc. It is well known that collagen fiber orientation affects elastic behavior, but the effect of collagen fiber network on tissue swelling behavior is not well understood. In this study, we developed three series of models to evaluate the effect of collagen fiber orientation, fiber network architecture (*i.e.*, single or multi-fiber families within a layer), and fiber stiffness on bulk tissue swelling, which was simulated by describing the extrafibrillar matrix as a triphasic material,

as proposed by Lai et al. Model results were within one standard deviation of reported mean values for changes in tissue volume, width, and thickness under free swelling conditions. The predicted swelling response of single-fiber family structures was highly dependent on fiber orientation and the number of lamellae in the bulk tissue. Moreover, matrix swelling resulted in tissue to twist, which reduced fiber deformations, demonstrating a balance between fiber deformation and matrix swelling. Large changes in fiber stiffness (20X increase) had a relatively small effect on tissue swelling (∼2% decrease in swelling). In conclusion, fiber angle, fiber architecture (defined as single- versus multiple fiber families in a layer), and the number of layers in a single fiber family structure directly affected tissue swelling behavior, including fiber stretch, fiber reorientation, and tissue deformation. These findings support the need to develop computational models that closely mimic the native architecture in order to understand mechanisms of stress distributions and tissue failure.

**Keywords:** Fiber-reinforced Soft Tissue, Swelling, Fiber Orientation, Intervertebral disc

## 5.1 Introduction

Native and engineered fiber-reinforced tissues, such as the annulus fibrosus (AF), arterial walls, tendons, ligaments, and cartilage, are composite structures that include stiff collagen fibers embedded within an extrafibrillar matrix [136, 176, 177, 178]. Many of these tissues have an excellent capacity to absorb water from the surrounding environment because of the glycosaminoglycans (GAGs) in the extrafibrillar matrix, which is essential for fibril sliding during loading [22, 23, 24, 25]. Fiber-reinforced tissues display a wide range of fiber orientations depending on the stresses experienced *in situ* [12, 177], resulting in anisotropy of bulk tissue mechanical properties and swelling behavior [22, 110]. However, the effect of the collagen fiber network on bulk tissue swelling response is not well understood. As biological repair strategies aim to recapitulate the mechanical behavior of healthy native tissues, elucidating the effect of fiber architecture on swelling behavior is important for understanding stress distributions between subcomponents.

There has been extensive research evaluating the role of collagen fiber orientation on elastic mechanical properties [110, 179, 180, 181, 182]. Differences in tissue mechanics arise

from differences in fiber orientation, fiber architecture complexity, and other secondary constituents (*e.g.*, elastin and types of collagen fibers) [12, 26]. That is, tissues with highly aligned collagen fibers have significant anisotropy and are stiffer than tissues with fibers aligned off-axis from the primary loading direction [110, 180]. Moreover, constitutive models of the AF showed that fiber-matrix interactions act to maintain bulk tissue tensile mechanical behavior with degeneration [136, 183]. However, there has been limited research investigating the role of the extrafibrillar matrix, which accounts for 75-95% of the tissue's wet-weight (*i.e.*, GAGs plus water) [184, 185, 186].

The role of GAGs and tissue swelling is of particular interest for understanding stress distributions between collagen fibers and the extrafibrillar matrix, as well as for understanding mechanisms of tissue failure [187]. For example, the intervertebral disc is complex organ comprised of distinct fibro-cartilaginous materials, including the nucleus pulposus, which is surrounded by the AF. Differences in biochemical composition and architecture contribute to differences in swelling response of explants from the two regions, which, in turn, altered joint-level mechanical behavior [22, 125, 188]. The swelling capacity of AF explants was shown to be approximately 70% of nucleus pulposus explants [125]. Moreover, AF swelling, similar to mechanical properties, is highly anisotropic, with more swelling occurring in the radial direction (21 $\pm$ 4%) than the axial (14 $\pm$ 6%) or circumferential directions (-2 $\pm$ 4%) [22]. Large direction-dependent swelling deformations have also been observed in cervical tissue during pregnancy and cardiovascular vessels with disease [189, 190].

While multiple studies have reported the swelling behavior of various fiber-reinforced tissues, it is difficult to compare findings and discern the role of fiber orientation on tissue swelling, due to other differences in tissue composition. Computational models provide a powerful tool for understanding the role of matrix swelling on bulk tissue behavior. However, many finite element models of fiber-reinforced tissues rely on hyperelastic material descriptions, which do not include fluid-dependent behaviors and cannot elucidate the role of fiber-matrix interactions [191, 192]. The triphasic mixture theory, originally proposed by Lai et al., can be used to describe material deformations as a combination of fiber stretch, elastic deformations from the extrafibrillar matrix, and osmotic pressure [38]. This approach has been successful in describing cartilage mechanics and swelling of engineered cartilage constructs [71, 72].

Thus, the objective of this study was to determine the effect of collagen fiber orientation

and fiber network complexity on tissue swelling behavior and resulting deformations from osmotic loading. We developed a series of tissue-level finite element models that represents specimen orientations commonly used for uniaxial tensile testing [136, 137, 193, 194]. Material parameters for the models were determined by curve-fitting experimental data from the AF; however, the overall observations, with respect to fiber orientation and tissue swelling, are applicable to other fiber-reinforced tissues. The findings from these models highlight difficulties in comparing mechanical properties between studies, where the stated reference configuration may vary significantly depending on hydration conditions [22, 195].

## 5.2 Methods

### Model geometry and mesh

Three series of models were developed (Table 5.1). Models in Series I evaluated the effect of multi-lamella structures on tissue swelling, where each layer included a single fiber-family population with a defined orientation. Fiber orientation in adjacent layers alternated about the z-axis (Figure 5.1A). Single and multi-lamella structures were evaluated, including models with 1-, 2-, 3-, 4-, or 6-layers (Figure 5.1C-G). Models in Series II evaluated the effect of multiple fiber families in single lamellae on bulk tissue swelling behavior (Figure 5.1B). For this study, we limited the analysis to a two-fiber family description. Models in Series III evaluated the effect of fiber stiffness on tissue swelling by simulating a 20-fold increase in fiber stiffness. Therefore, nine separate fiber network configurations were evaluated (Table 5.1).

All models were developed and meshed in Preview 1.19.0 (FEBio Preprocessor, febio.org) [116]. Lamellae dimensions in the reference configuration were 2 mm, 0.2 mm, and 10 mm for the width, thickness, and length, respectively ($\sim$24,000 hexahedral elements per lamella). Lamellae thickness was chosen based on the average AF lamellae thickness [12], and the length and width were selected based on ASTM standards for uniaxial test specimens (aspect ratio = 5) [196].

Fibers were orientated between 0° and 90° with respect to the vertical axis (Figure 5.1C - G). The effect of fiber orientation was assessed in increments of 15° for each model. Thus, models with fibers oriented at 0° represented the fiber orientation observed in tendons

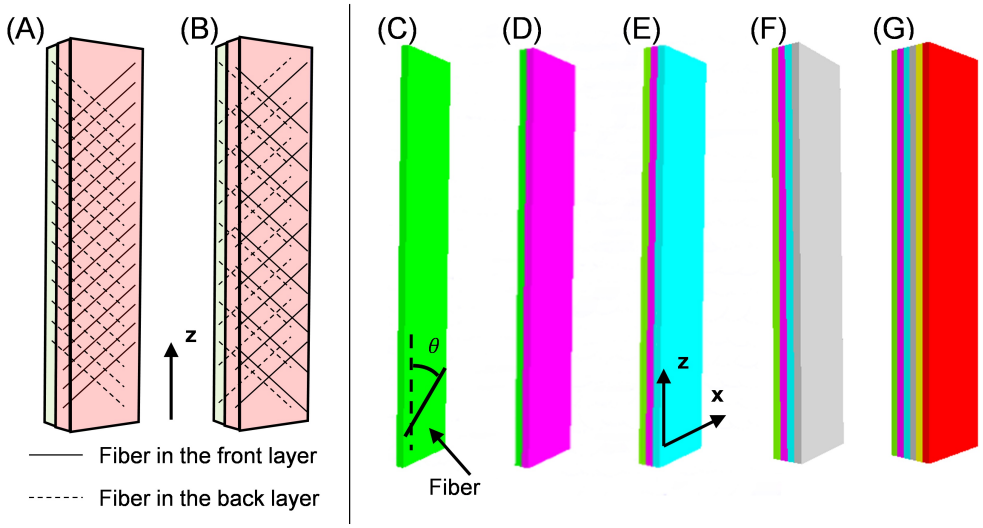


Figure 5.1: In Series I, each layer consisted of a single fiber-family population, where fiber orientation alternated about the z-axis between layers (**A**). In Series II, each layer consisted of two-fiber family populations with each population alternating about the z-axis (**B**). Multi-lamella structures were developed for Series I (**C**-**G**). Note: A multi-layer description does not alter the response for a two-layer fiber family description.

Table 5.1: Nine fiber network configurations were developed. In Series I the effect of multi-lamellae structures on bulk tissue swelling was evaluated (single fiber family description). Series II investigated the effect of a two-fiber family description on tissue swelling. Series III evaluated the effect of fiber stiffness on tissue swelling.

| | Fiber Property | Model |
|---|---|---|
| Series I | Alternating fiber orientation | 1-layer<br>2-layer<br>3-layer<br>4-layer<br>6-layer |
| Series II | 2 family | 2-layer, 2 fiber family<br>3-layer, 2 fiber family |
| Series III | 20X stiffer | 3-layer, stiffer fibers<br>3-layer, 2 fiber family, stiffer fibers<br>3-layer, 2 fiber family |

and ligaments tested along the longitudinal direction, while the 90° models mimicked the fiber orientation of tendons or ligaments tested in the transverse direction. Models with fibers oriented between 30° and 60° were developed to replicate fiber orientation of the AF [12, 197]. A 'No-Fiber' case was developed as a control case. Therefore, a total of 72 models were developed (8 fiber orientations × 9 fiber network configurations).

## Material properties

Triphasic mixture theory was used to describe the tissue as a combination of three phases: a solid phase and two fluid phases (water and monovalent ions) [38, 72, 116]. The solid phase (Equation 5.1) consisted of the extrafibrillar matrix (Equations 5.2-5.4) and nonlinear fibers (Equations 5.5-5.8), where $W_i$ represented strain energy functions [116]. The extrafibrillar matrix was defined as a compressible hyperelastic material using the Holmes-Mow description (Equation 5.2). Matrix material properties were assumed to be spatially uniform throughout the tissue and consistent across all models. Material coefficients ($E_m$, $\nu$, and $\beta$) were selected based on values reported in the literature (Table 5.2) [20].

$$W = W_{matrix} + W_{fiber} \tag{5.1}$$

$$W_{matrix}(I_1, I_2, J) = \frac{1}{2}c(e^Q - 1) \tag{5.2}$$

where Q and c were expressed as:

$$Q = \frac{\beta}{\lambda + 2\mu}[(2\mu - \lambda)(I_1 - 3) + \lambda(I_2 - 3) - (\lambda + 2\mu)\ln J^2] \tag{5.3}$$

$$c = \frac{\lambda + 2\mu}{2\beta} \tag{5.4}$$

$I_1$ and $I_2$ are the first and second invariants of the right Cauchy-Green deformation tensor, $\boldsymbol{C}$ ($\boldsymbol{C} = \boldsymbol{F}^T\boldsymbol{F}$), $J$ is the Jacobian of the deformation gradient tensor, $\boldsymbol{F}$ ($J = \det(\boldsymbol{F})$), and $\lambda$ and $\mu$ are the Lamé coefficients, which are related to the Young's modulus and Poisson's ratio. Fibers were defined using a nonlinear stress-stretch relationship with a defined toe- and linear-region separated by a squared transition stretch, $I_0$ (Equations 5.5-5.8) [136]. In Equation 5.5, $\gamma$ described the toe-region nonlinearity (unitless), the invariant $I_n$ represented squared fiber stretch ($I_n = \boldsymbol{a}\cdot\boldsymbol{C}\cdot\boldsymbol{a}$, where $\boldsymbol{a}$ is the unit vector that described the fiber orientation in the reference configuration), and $E_f$ represented the linear-region elastic

Table 5.2: Material parameters used in all models. $E_m$: Extrafibrillar matrix modulus, $\nu$: Poisson ratio, $\beta$: non-linear parameter for the Holmes-Mow description, Ef: collagen fiber modulus ($*E_f = 23$ for each fiber family in Series II, $E_f = 920$ for single-fiber family description in Series III, and $E_f = 460$ for the 2-fiber family description in Series III (Table 5.1).), $\gamma$: exponential term for the toe-region response of the fibers, $I_0$: the stretch ratio between the toe- and linear-region, $\phi_0$: tissue solid fraction, $k_0$: hydraulic permeability in the reference configuration, $M$: nonlinear parameter for permeability, $\phi$: osmotic coefficient, FCD: fixed charge density, $D_{free}$: ion diffusivity in water, $D$: ion diffusivity within tissue, and $S$: ion solubility.

| Solid Phase | | Fluid Phase | |
|---|---|---|---|
| $E_m(MPa)$ | 0.025 | $k_0(\text{mm}^4/(\text{Ns}))$ | 0.0064 |
| $\nu$(unitless) | 0.16 | $M$(unitless) | 4.8 |
| $\beta$(unitless) | 3.3 | $\varphi_0$(unitless) | 0.938 |
| $E_f^*$(MPa) | 46 | FCD(mmol/L) | 100 |
| $\gamma$(unitless) | 4.5 | $D_{free}(\text{mm}^2/\text{s})$ | 0.00147 |
| $I_0$(unitless) | $1.06^2$ | $D(\text{mm}^2/\text{s})$ | 0.0008 |
| $\Phi_0$(unitless) | 0.3 | $S$(unitless) | 1 |

modulus (MPa, constant). In this expression, $\gamma$, $I_0$, and $E_f$ were independent coefficients selected from our previous model, which was calibrated to experimental data from the outer AF (Table 5.2) [1]. $E_f$ was divided in half for models with two-fiber families, such that the total fiber stiffness within a layer remained constant. In Series III, a 20-fold increase in $E_f$ was simulated based on differences in tensile stiffness between tendons or ligaments and the outer AF (tendons/ligament modulus ~1 GPa, outer AF modulus ~50 MPa) [27, 198]. All fibers were limited to acting only in tension.

$$W_{fiber} = \begin{cases} 0 & I_n < 1 \\ \frac{\xi}{2\gamma}(I_n - 1)^\gamma & 1 \le I_n \le I_0 \\ E_f(I_0^{1/2} - I_n^{1/2}) + B(I_n - I_0) + W_0 & I_0 \le I_n \end{cases} \tag{5.5}$$

$$\xi = \frac{E_f}{2(\gamma - 1)} I_0^{2-\gamma} \tag{5.6}$$

$$B = \frac{E_f}{2}\left[\frac{I_0 - 1}{2(\gamma - 1)} + I_0\right] \tag{5.7}$$

$$W_0 = \frac{\xi}{2\gamma}(I_0 - 1)^\gamma \tag{5.8}$$

In triphasic theory, negative fixed charge density (FCD) in the solid description was used to represent GAGs in the extrafibrillar matrix by assuming 2 moles of charge per mole of GAG in the tissue and a molecular weight of 502.5 g/mole GAG (Equation 5.9) [199]. An initial FCD of -100 mmol/L was chosen to represent the outer AF GAG content [19]. Total fix charges was conservative therefore local FCD depended on local volume change (Equation 5.10, where $\Phi_0$ was tissue solid fraction in the reference configuration, Table 5.2).

$$FCD = \frac{2\ mmol\ charges}{0.5025\ g\ GAG}\frac{W_{GAG}}{1\ L} \tag{5.9}$$

$$FCD = \frac{1-\Phi_0}{J-\Phi_0}FCD \tag{5.10}$$

Fluid (*i.e.*, water) and ion phases were included to simulate tissue swelling (Table 5.2) [200, 201]. FCD affected fluid's and ions' movements by affecting their electrochemical potentials. Free diffusivity ($D_{free}$) and diffusivity ($D$) were used to describe how fast ion diffuse in water and tissue. Permeability ($k$) was used to describe the capability of tissue to allow fluid to pass through it. Tissue permeability was strain-dependent, and the parameters $k_0$ and $M$ were selected based on experimental data of the AF (Holmes-Mow permeability model; Equation 5.11; Table 5.2) [20]. Influx of fluid will caused an increase of interstitial fluid pressure, which acted on solid matrix resulting in swelling.

$$k(J) = k_0(\frac{J-\Phi_0}{1-\Phi_0})^2 e^{\frac{1}{2}\ M(J^2-1)} \tag{5.11}$$

## Simulation, model validation, and data analyses

All simulations were conducted in FEBio [116]. Boundary conditions for all models were set such that one end was fixed, while the opposite end was allowed to freely elongate and rotate. The reference configuration represented a state of osmotic dehydration, where FCD was 0. The steady-state swelling was simulated by increasing the magnitude of the FCD from zero to the specified value (-100 mmol/mL), while the surrounding environment was fixed at a value representing 0.15 M phosphate buffered saline (150 mmol/L).

Deformations caused by the free-swelling conditions were measured and recorded. The swelling ratio was calculated as the volume in the deformed condition divided by the volume in the reference configuration. Fiber stretch and fiber reorientation were calculated for each element: deformation gradient tensor $\boldsymbol{F}$ was evaluated for each element first by tracking all

the node positions and then $\boldsymbol{F}$ acted on unit fiber vector ($\boldsymbol{a}$) of the element resulting in deformed fiber vector $\boldsymbol{a'}$ ($\boldsymbol{a'} = \boldsymbol{F}\boldsymbol{a}$). Fiber stretch and fiber reorientation were calculated to be $|\boldsymbol{a'}|$ over $|\boldsymbol{a}|$ and angle between $\boldsymbol{a'}$ and $\boldsymbol{a}$, respectively. In addition, first principal strains ($\varepsilon_1$) were calculated for each element. Fiber stretch, fiber reorientation and fist principal strains were averaged for all elements within the simulated tissue to calculate average fiber stretch, average fiber reorientation, and average first principal strain, respectively. Only fibers under tensile stretch were included in the calculation for average fiber stretch. Finally, swelling ratio was correlated with average fiber stretch and first principal strain.

To validate model simulations, changes in dimensions and volume for the 6-layer model with fibers oriented at $\pm 60^\circ$ in Series I (control model) were compared to free swelling experiments of AF explants from bovine discs [22, 125]. Model results were considered valid if changes in length, width, thickness, and volume fell within the range of data reported in the literature.

## 5.3 Results

### Model validation

The volume of the 6-layer model with fibers oriented at $\pm 60^\circ$ (control model) increased by 46% under free-swelling conditions, which was within the wide range of values reported in the literature (20 - 70%) [22, 125]. Swelling of the control model resulted in a 27% increase in thickness and a 15% increase in length, which was comparable to respective increases in length along the radial ($21 \pm 4\%$) and axial directions ($14 \pm 6\%$) of the AF [22]. Furthermore, the control model had a -3% change in width, which agreed with a change in circumferential direction length of AF explants during swelling ($-2 \pm 4\%$). Since model results were within one standard deviation of reported mean values for three of the four parameters (changes in volume, width, and thickness) and within two standard deviations of the mean for the change in length, we considered the model to be valid for studying swelling behavior of fiber-reinforced tissues.

## Swelling ratio

The 'No Fiber' model, which represents the extrafibrillar matrix without fibers, had a 62% increase in tissue volume under free-swelling conditions (swelling ratio = 1.62; Figures 5.2-5.4 & Figure 5.5 - black solid line). For models in Series I, adding fibers to single-layer models decreased tissue swelling by ∼10%, and the decrease in swelling ratio was consistent, regardless of fiber orientation (swelling ratio = 1.52; Figure 5.2A, Figure 5.5 –solid light blue line). For 2-layer models in Series I, the swelling ratio was dependent on fiber orientation, as the cross-ply fiber architecture further reduced tissue swelling (swelling ratio = 1.44 for the ±45° model; Figure 5.2B & Figure 5.5 –solid purple line). There was a nonlinear relationship between the decrease in swelling ratio and the number of lamellae included. That is, the swelling ratio for multi-lamella structures was comparable for tissues with three or more lamellae (Figure 5.2C-E; Figure 5.5 - inset).

As expected, the two-fiber family structure used in Series II models eliminated any effect of multi-lamella architecture on swelling behavior. As such, 2- and 3-layer models exhibited the same response (Figure 5.4). Multi-lamellae models in Series II did not exhibit signs of rotation or twisting and the swelling ratio was uniform throughout the material (Figure 5.3). Two-fiber family structure Tissue swelling decreased tissue swelling capacity, with the largest difference observed in models with fibers orientated at ±45° (from 1.45 to 1.40; Figure 5.5-purple dashed line verses respective models from Series I: solid purple line for 2-layers and solid red line for 3-layers). Fiber stiffness had a minor influence on swelling ratio (Figure 5.4), where a 20-fold increase in fiber stiffness resulted in less than a 2% reduction in swelling ratio (Figure 5.5 - solid gray line versus solid red line and gray dashed line versus purple dashed line).

## Swelling deformation and first principal strain

Dimensions of the 'No Fiber' models increased uniformly in all directions (17.3% increase in length, width, and thickness). Elongation along the z-direction was observed for all 1-layer models in Series I (Figure 5.2A), but z-direction elongation depended on fiber orientation in multi-lamellae models (Series I-III; Figures 5.2B-E, 3 & 5.4). That is, minimal tissue elongation was observed for models with fibers oriented between 0° and ±45° (<3.5% of

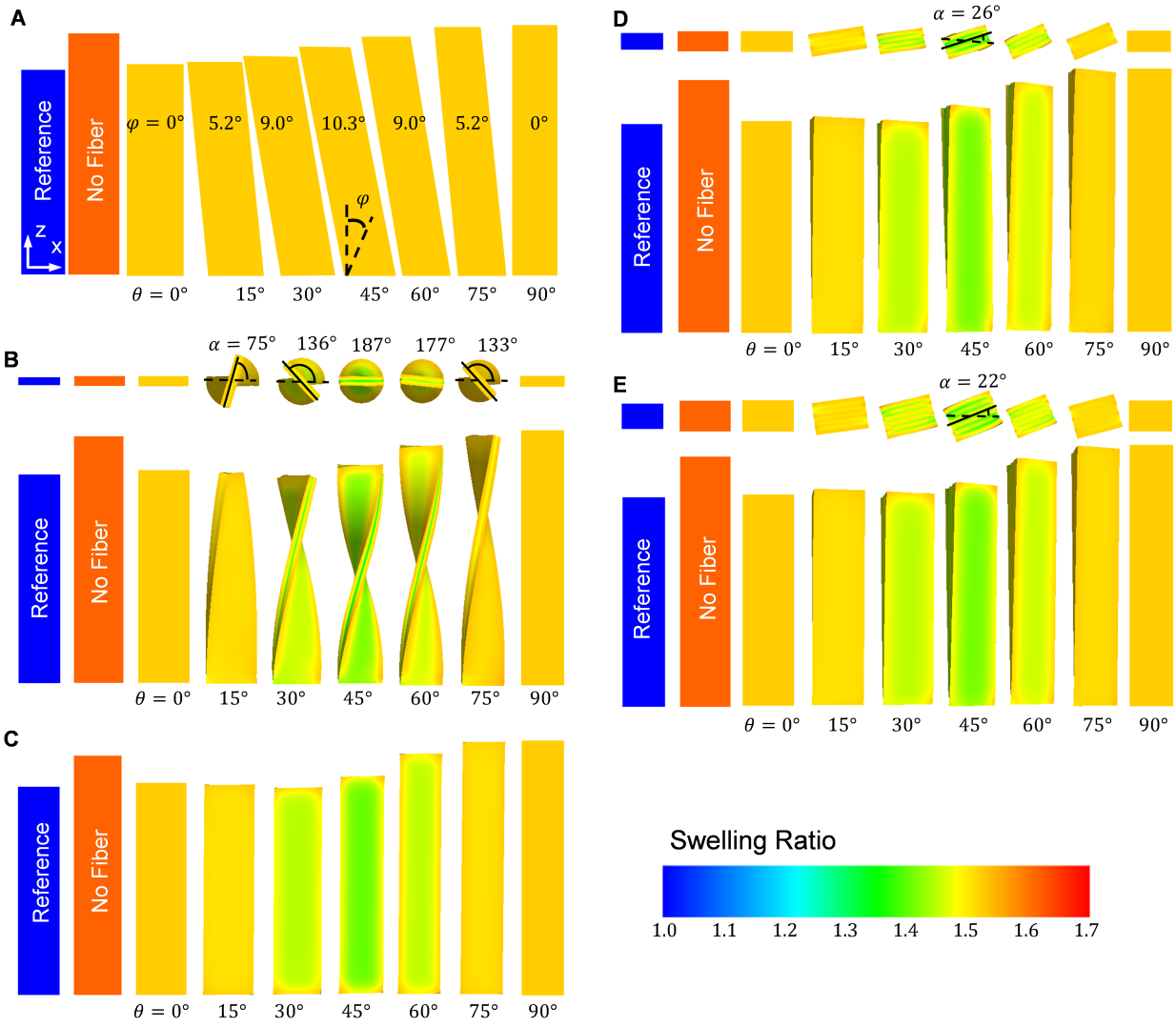


Figure 5.2: Configurations for models in Series I before ('Reference' configuration) and after swelling: 1-layer (**A**), 2-layer (**B**), 3-layer (**C**), 4-layer (**D**), and 6-layer (**E**) models. The color bar represents swelling ratio, which was defined as the volume after swelling divided by the volume before swelling. $\varphi$ represents fiber reorientation angle about the y-axis and $\alpha$ represents tissue rotation angle about the z-axis.

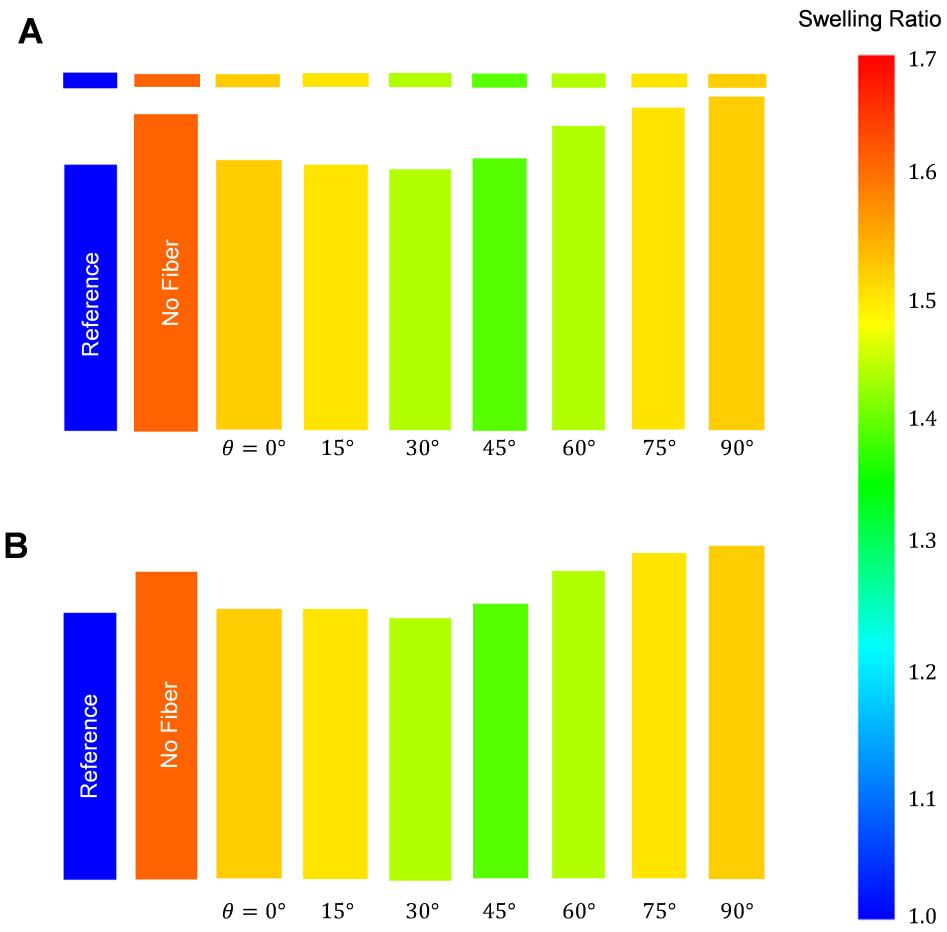


Figure 5.3: Configurations for models in Series II before ('Reference' configuration) and after swelling: 2-layer, 2 fiber family (**A**) and 3-layer 2-fiber family (**B**) descriptions. Swelling behavior was not dependent on the number of lamella within a tissue when a multiple fiber family description was used. Color map represents the swelling ratio.

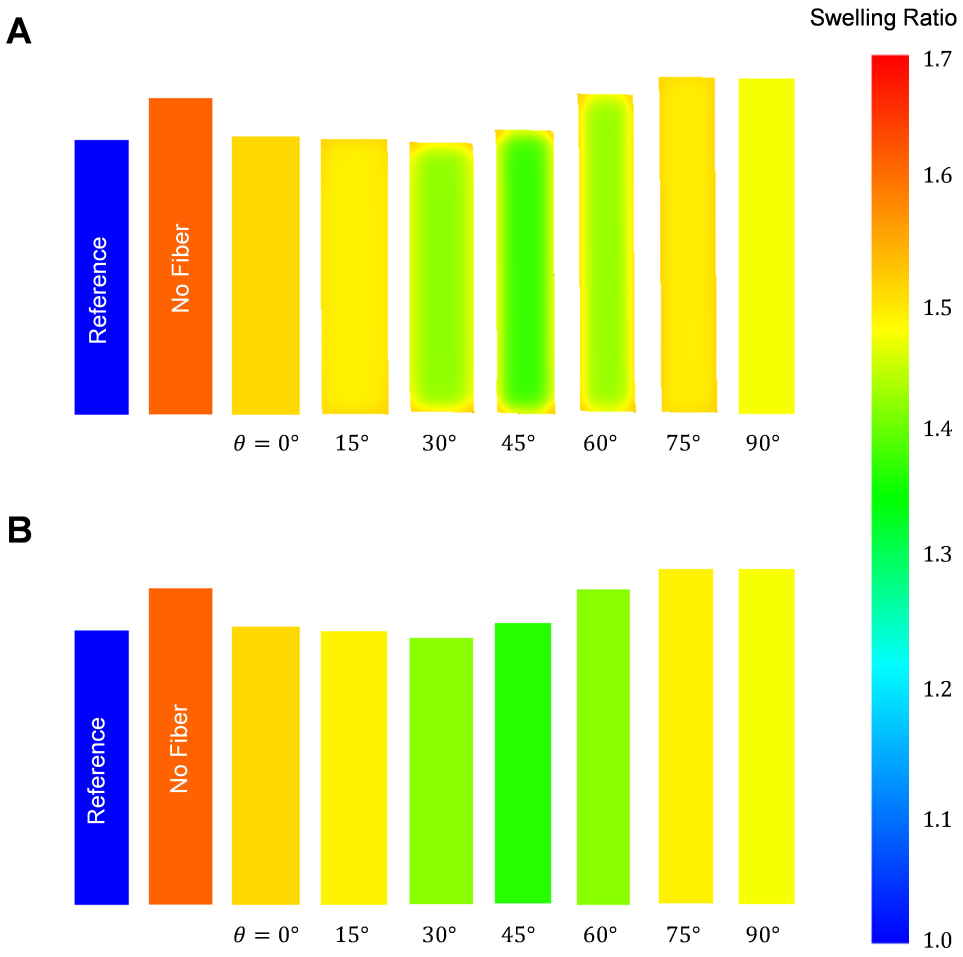


Figure 5.4: Configurations for models in Series III before ('Reference' configuration) and after swelling: 3-layer model with stiffer fibers (**A**) and 3-layer 2 fiber family description with stiffer fibers (**B**). There was a slight decrease in swelling ratio with fiber stiffness (compared to Figure 2C and 3B, respectively). Color map represents the swelling ratio.

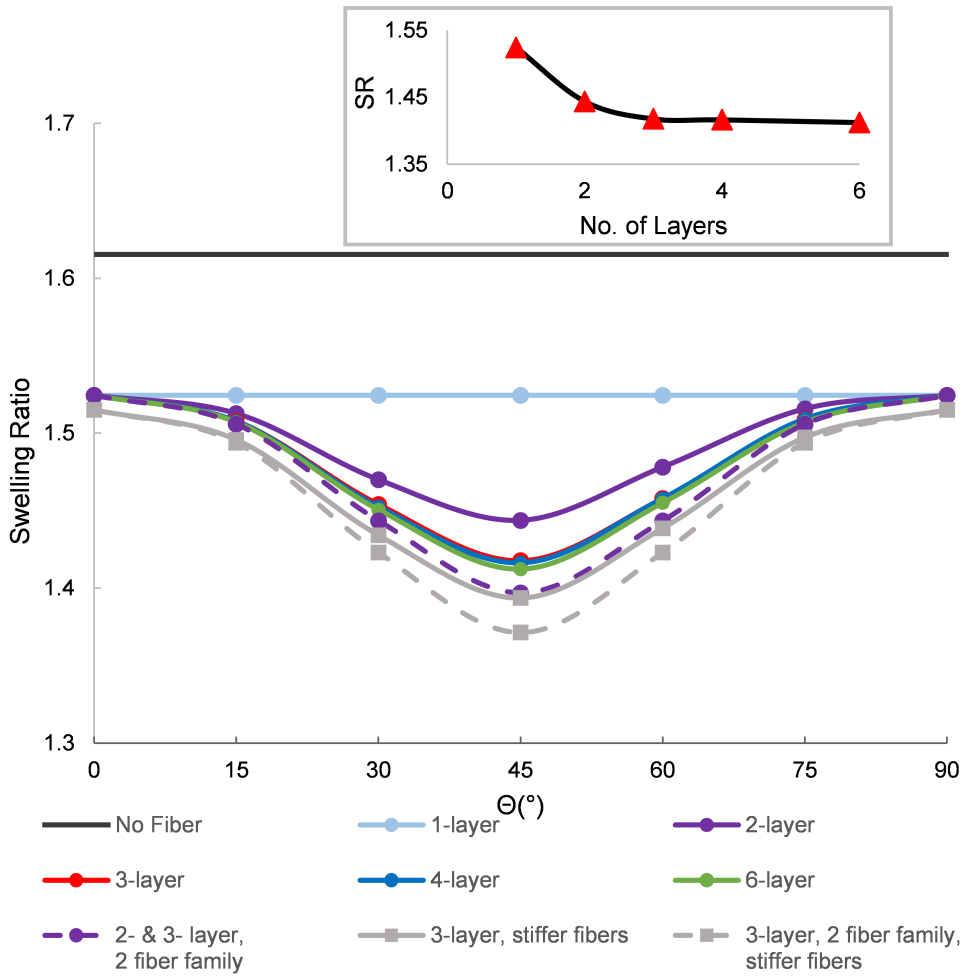


Figure 5.5: Swelling ratio (SR) with respect to initial fiber orientation for all models in Series I, II, and III. Inset: Swelling ratio with respect to the number of layers in Series I. ***Note*** –Values on the y-axis do not start at 1.0 (*i.e.*, case with no swelling in the tissue).

original length), while tissue elongation was up to 22% of the original length for models with fibers oriented between ±45° and ±90° (Figures 5.2-5.4).

The increase in tissue thickness (*i.e.*, orientation perpendicular to fibers) was greater than 25% for all fiber-reinforced models. Similarly, strains were greatest in the orientation perpendicular to the fibers, and, therefore, was the direction of the first principal strain (Figure 5.6A). In Series I, the first principal strain for 1-layer models was consistent, regardless of fiber orientation ($\varepsilon_1 = 0.25$; Figure 5.6A –light blue). For all other models in Series I (*i.e.*, multi-lamellae models), the average first principal strain depended on fiber orientation, where the ±45° models exhibited the largest average first principal strains (Figure 5.6A). There were little differences in average first principle strain for multi-lamellae models in Series I and for models from Series II or III (*i.e.*, with respect to multi-fiber families or fiber stiffness, Figure 5.6A –*e.g.*, solid red line verses purple or gray lines).

Tissue rotation or twisting was observed in single and multi-lamella models from Series I. Single layer models (1-layer models) rotated about the y-axis, which was the axis perpendicular to the fibers (Figure 5.2A), resulting in shear strains in the xz plane ($\varepsilon_{xz}(\theta)$, Figure 5.6B). Multi-lamella models with an even number of layers in Series I resulted in rotation about the z-axis (Figure 5.2B). The amount of rotation depended on fiber orientation, where maximum rotation occurred for models with fibers oriented at $\sim$ ±45° (Figure 5.2B). Twisting about the z-axis decreased as the number of lamellae increased from two to six layers. That is, the rotation angle for the ±45° model decreased from 187° in the 2-layer model to 26° and 22° in the 4- and 6-layer models, respectively (Figure 5.2B, D, and E).

## Fiber stretch and reorientation

Swelling caused fiber deformations, which were reported as fiber stretch. The magnitude of fiber stretch was consistent for all 1-layer models in Series I (fiber stretch = 1.02; Figure 5.7A). The average fiber stretch was comparable between 1- and 2-layer models in Series I (Figure 5.7A –purple line versus light blue line). However, for models with three or more layers, the fiber stretch depended on fiber orientation, where models with fibers orientated at ±45° had the greatest fiber deformations (Figure 5.7A - solid red, dark blue, green, and gray lines). Models in Series II experienced higher fiber deformations than Series I models, and this difference was more pronounced for the 2-layer cases (Figure 5.7A - solid versus

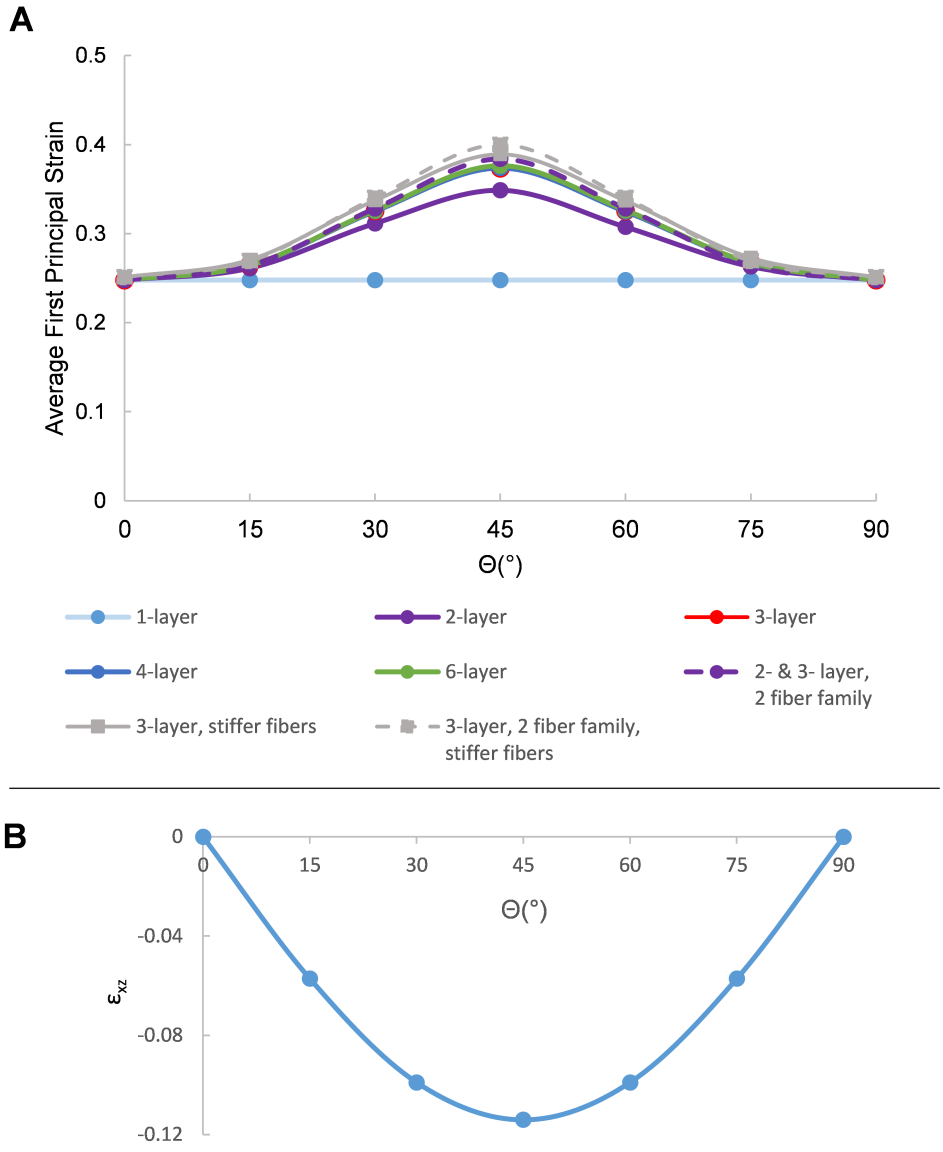


Figure 5.6: Average first principal strain with respect to the initial fiber orientation for all models (**A**). In-plane shear strain ($\varepsilon_{xz}$) for 1-layer models in Series I with respect to fiber orientation (**B**).

dashed purple line). For models in Series III, an increase in fiber stiffness decreased fiber deformations by ∼50% for all fiber orientations (Figure 5.7A - gray lines).

Free swelling conditions caused fibers to reorient either towards (negative change in fiber angle) or away from the z-axis. For Series I models, rotations about the y-axis were observed in 1-layer models, resulting in fibers reorienting away from the z-axis (Figure 5.2A; Figure 5.7B - light blue solid line). Fiber reorientation response was relatively consistent for all other models (Series I-III), and the direction of fiber reorientation depended on the initial fiber orientation. That is, models with fibers initially orientated between 0 and ±45° reoriented away from the z-axis, while fibers that were initially oriented at > ±45° reoriented towards the longitudinal or z-axis (Figure 5.7B).

### Relationship between swelling ratio and fiber deformations

Lastly, we looked at the relationship between swelling ratio and fiber deformations for each fiber network configuration. There was a negative linear relationship between swelling ratio and average fiber stretch (Figure 5.8A). The decrease in tissue swelling with respect to fiber stretch was more pronounced for models with stiffer fibers (Figure 5.8A –gray lines for Series III versus multi-colored lines for Series I and II). Similarly, there was a negative linear relationship between swelling ratio and average principal strain (Figure 5.8B). The decrease in swelling ratio with respect to the average principal strain was consistent for all fiber network configurations (Series I-III, slope = ∼ -0.94; Figure 5.8B).

## 5.4 Discussion

Our previous work and work by others showed that tissue hydration affects tissue- and joint-level mechanics [22, 125, 188]. Our previous experimental studies showed that the AF swelling capacity was ∼70% of the nucleus pulposus. However, it was difficult to discern whether differences in swelling capacity was entirely due to differences in glycosaminoglycan composition or differences in fiber network, as recent work showed anisotropic swelling behavior in the AF [22]. Therefore, in this study, we developed three series of finite element models to evaluate the effect of collagen fiber orientation (Series I), fiber network architecture (Series I & II), and fiber stiffness (Series III) on tissue swelling. The model was validated by

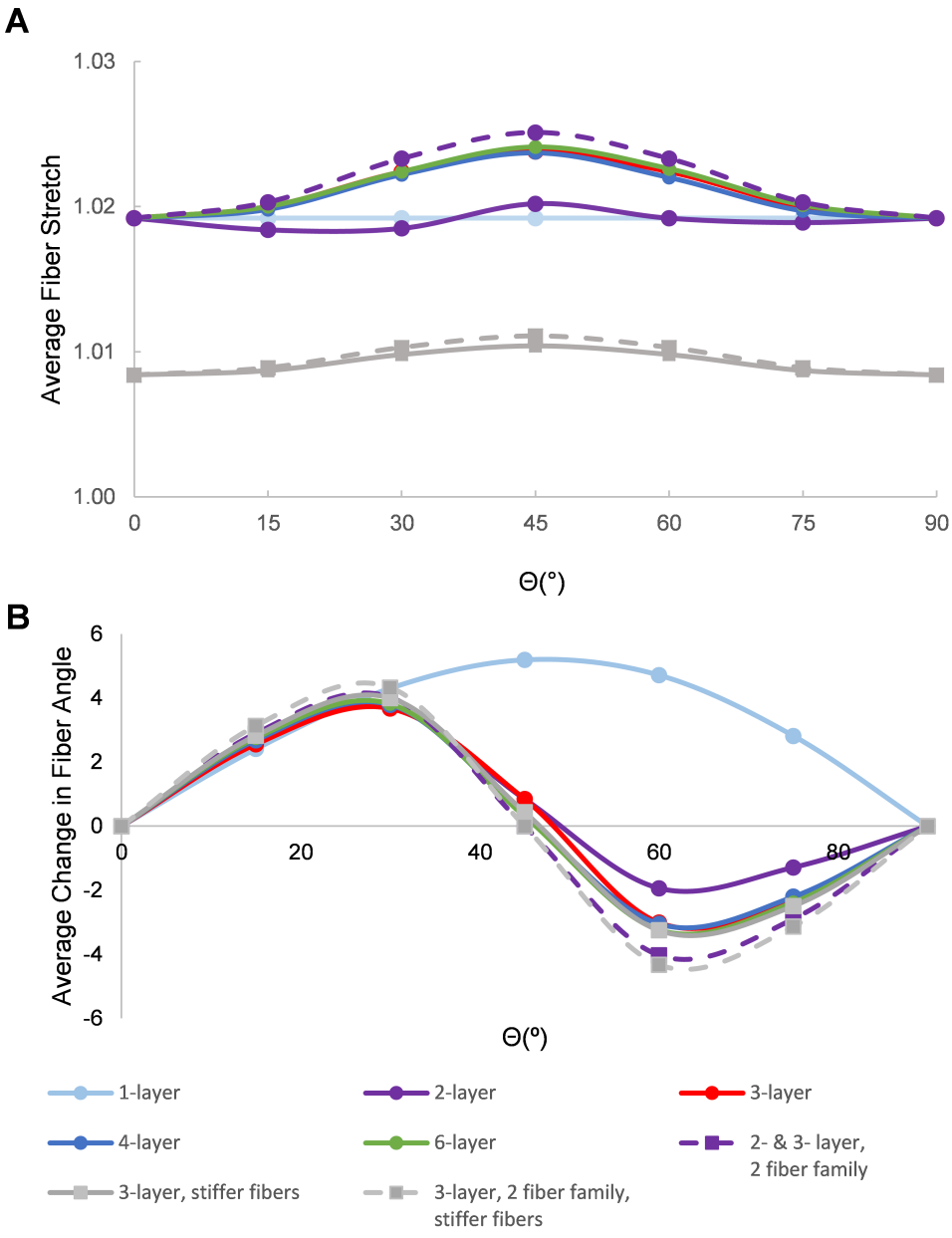


Figure 5.7: Average fiber stretch due to swelling with respect to the initial fiber orientation for all models (**A**) and average change in fiber orientation with swelling (**B**).

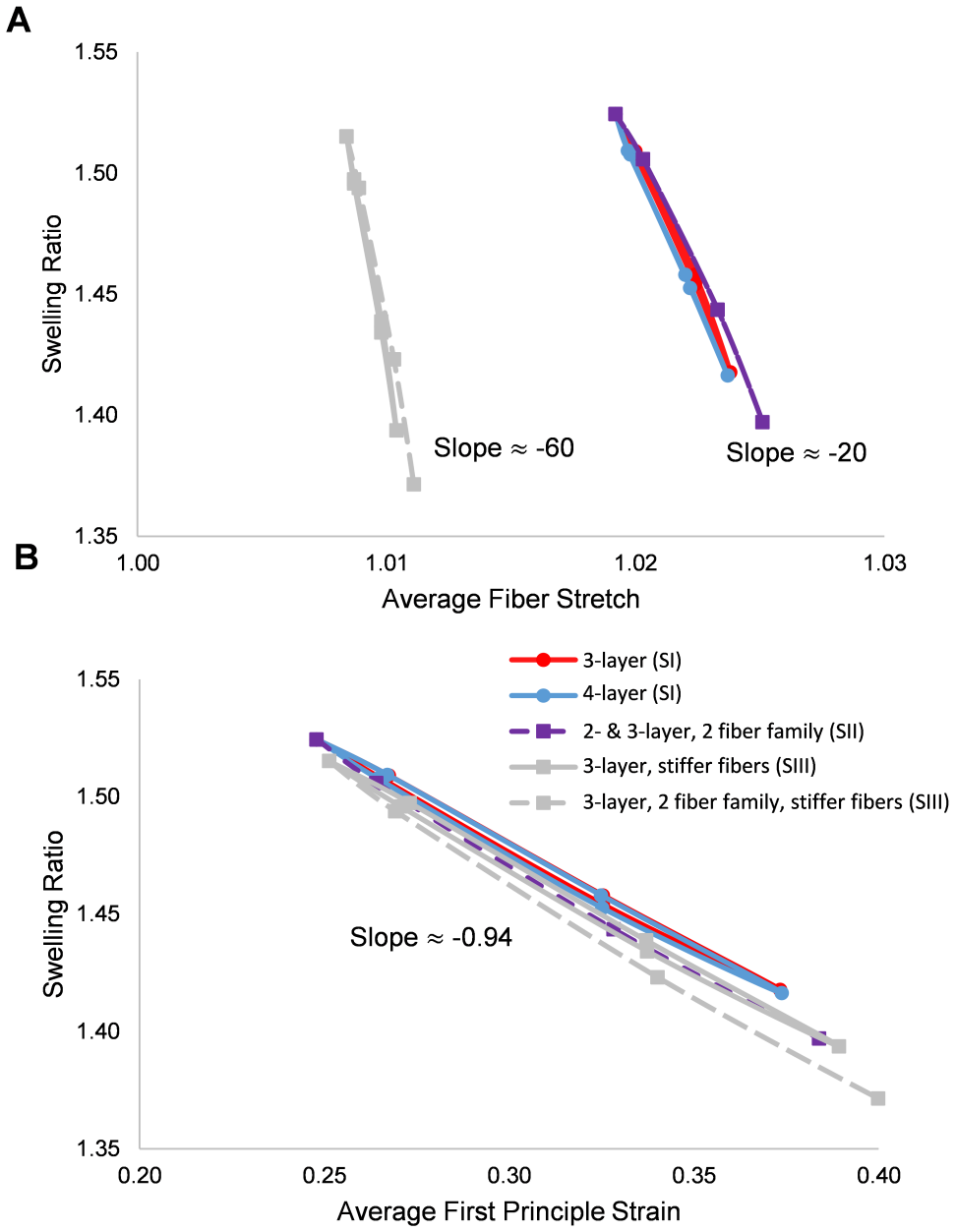


Figure 5.8: Swelling ratio with respect to the average fiber stretch (**A**) and swelling ratio with respect to the average first principal strain (**B**) for models from all three network configurations (SI = Series I, SII = Series II, and SIII = Series III).

comparing simulated swelling response with experimental results from AF explants [22, 125]. Simulations from these models showed that fiber angle, fiber architecture, and the number of lamellae in single fiber-family structures alters tissue swelling capacity, fiber deformation, and tissue rotation.

Accurate characterization of healthy and diseased biological tissues is important for developing materials for repairing or replacing damaged and diseased tissues. Ideally, replacement materials will mimic the mechanical function of the healthy native tissue, but the mechanical properties (*e.g.*, Young's modulus) of biological tissues are highly dependent on hydration condition [22, 28, 163, 202]. The largest dimensional increase observed in this study occurred in the thickness direction, which would greatly affect the cross-sectional area and, therefore, stress and modulus calculations. Some of the differences in mechanical properties reported in the literature have been attributed to changes in cross-sectional area [195]. However, other studies suggest that changes in tissue mechanics are also due to non-geometric tissue changes [22, 203]. The findings from this study agree with that notion and suggest that fiber rotation may be responsible in part for non-geometric changes that lead to differences in material properties (Figure 5.7A).

Fiber reorientation and uncrimping act to reduce stresses on collagen fibrils during tensile loading [204]. In this study, we observed greater fiber reorientation and fiber stretch in models that represented AF anatomy, compared to models that more closely represent tendon anatomy (*i.e.*, AF anatomy: $\sim \pm 5^{\circ}$ fiber rotation and average fiber stretch $\sim$1.023; tendon anatomy: no fiber rotation and average fiber stretch $\sim$1.019; Figure 5.7). Previous experimental studies on AF and tendon mechanics demonstrated fiber reorientation towards the direction of tensile loading [54, 205]. Guerin et al. reported that fibers realigned by 5o towards the loading direction under tissue strains between 4-6% (*i.e.*, stretch = 1.02-1.03) [54]. Taken together, fiber reorientation during swelling may contribute to the pronounced toe-region observed in AF tissues, which is not as pronounced in stress-strain curves of more aligned tissues, such as tendons or ligaments, or AF specimens tested in air [28, 136, 163, 206].

Tissue swelling was due to a balance between matrix swelling and fiber stretch. Tendons and ligaments have a higher collagen content and a lower GAG content than the outer AF (collagen: 80% versus 70% per dry weight, GAG: <3% verses 10% per dry weight, respectively). Moreover, collagen fibrils in tendons and ligaments are more aligned and stiffer than fibrils from the AF [12, 180]. These differences in tissue composition are related

to a limited overall swelling capacity (∼10% increase in tendon volume in saline verses ∼40% increase in AF volume) [16, 184, 207, 208, 209, 210]. Our findings showed that tissues with fibers aligned in a single direction (*i.e.*, no cross-ply pattern) have less ability to resist matrix swelling. In contrast, fibers in a cross-ply configuration are effective in resisting matrix swelling, resulting in greater fiber stretch. Therefore, tissues with fibers aligned along a single direction (*i.e.*, 0° or 90°) would need stiffer fibers or fewer GAGs to reduce matrix swelling and achieve the same swelling capacity as tissues with a cross-ply architecture, which agrees with biochemical differences between tendons and AF.

Tissue twisting about the z-axis was observed in a subset of models in Series I, specifically, in models with an even number of lamellae. Twisting or curling has been observed in maturing electrospun constructs (thickness = 0.56 –0.9 mm) [211]; however, it is difficult to separate curling due to cell contraction from matrix swelling [212]. Recent analytical work also observed specimen twisting when simulating swelling in a hollow cylinder comprised of curved fibers along the radial direction [213]. Twisting has not been widely reported for native fiber-reinforced materials, which may be due to test specimens containing more than four lamellae (twisting angle <25°) or the application of a nominal preload to ensure specimen alignment prior to mechanical testing [136, 191]. The decrease in tissue rotation with additional lamella was likely due to opposing rotation angles in adjacent layers (Figure 5.9). These findings agree with work by Nerukar et al. that observed high shear stresses between cross-ply lamellae, which led to an increase in bulk tissue stiffness in engineered fiber-reinforced tissues [214].

The two fiber family description is a more commonly used fiber description for computational models of fiber-reinforced materials [1, 86, 189, 192, 215], but the alternating single fiber family description more closely aligns with the native fiber network of the AF and media of vascular walls [12, 13, 216, 217]. Our findings showed that bulk tissue swelling behavior was dependent on the fiber architecture description, especially in tissues with less than three layers. That is, the two-fiber family description had lower predicted increases in volume (Figure 5.3 & 5.4B), more uniform swelling distribution, and did not exhibit signs of twisting or rotation (Figure 5.2 versus 5.3). Therefore, as computational models shift from describing the extrafibrillar matrix as a hyperelastic material to a material with fluid-dependent behaviors (*e.g.*, biphasic or triphasic descriptions) [63, 72], an accurate description of the fiber architecture will become essential for predicting internal stresses and strains that

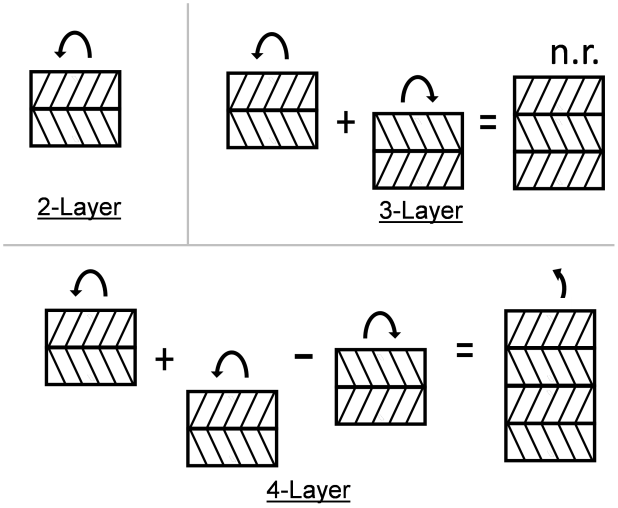


Figure 5.9: Schematic of twisting for 2-, 3-, and 4-layer rectangular models with cross-ply fiber description. Models with an odd number of lamellae did not experience twisting due to opposing rotations between layers (n.r. = no rotation).

may lead to damage.

There are some limitations to the current study. GAGs are the primary contributor to tissue swelling behavior; however, the effect negative charge density (*i.e.*, GAG composition) on swelling of fiber-reinforced soft tissue was not investigated in this study to focus model simulations on understanding the role of the fiber network on tissue swelling. Although lamellae fibers and fiber dispersion have been observed [218, 219], these properties were not included in the models for computational simplicity. Secondly, all models were described using a homogenized material description, where each element is occupied by both a fiber and matrix description, which is not representative of the native tissue. Moreover, we used a rectangular geometry, based on uniaxial test specimens to compare differences due to fiber orientation; however, *in situ* boundary conditions, such as a circular ring for arteries or the kidney shape for the AF, may lead to more complex stress and strain distributions that may affect overall tissue swelling [23, 40]. Finally, material properties were tuned to experimental data from the AF, which may affect swelling ratio and fiber stretch values calculated for non-AF tissues.

Developing constitutive models with an accurate description of the fiber network and swelling behavior of the extrafibrillar matrix is important for designing replacement materials

that recapitulate the mechanical function of the native tissue. For example, tensile stiffness increases with more aligned fibers (*e.g.*, from $\pm 45^\circ$ to $0^\circ$) and shear modulus increases as the fiber orientation approaches $\pm 45^\circ$ [54, 84, 220, 221]. The findings of this study demonstrate the need to include the native fiber network in computational models to accurately simulate tissue-swelling behavior, and, therefore, subfailure and failure mechanics. In conclusion, fiber architecture including fiber orientation and lamellae structure had the greatest impact on the swelling capacity of fiber-reinforced tissues. Future work will expand upon this work by evaluating interactions between fiber network and GAG composition on tissue swelling.

# Chapter 6

# GAG Content, Fiber Stiffness, and Fiber Angle Affect Swelling-based Residual Stress in the Intact Annulus Fibrosus [5]

## Abstract

Biological tissues with a high glycosaminoglycan (GAG) content have an excellent ability to swell by absorbing water molecules from the surrounding environment. Our recent work showed that anisotropy in tissue swelling depends on the fiber-network architecture, including fiber angle, fiber stiffness, and lamellae structure. However, that work did not evaluate the effect of *in situ* boundary conditions, such as the kidney-bean shape of the annulus fibrosus (AF), on swelling behavior. The biochemical composition of intact AF is inhomogeneous with respect to GAG composition, collagen fiber angle, and fiber stiffness. Moreover, the GAG content in the inner AF decreases significantly with degeneration. In this study, we investigated the role of GAG content, fiber angle, and fiber stiffness on AF swelling and residual strain development using a finite element model based on a human lumbar disc. Our results showed that the annular ring structure had a great impact on swelling by developing region-dependent compressive stress/stretch in the inner layers and

tensile stress/stretch in the outer AF. Swelling-based residual stretch was comparable to experimentally measured values, suggesting an important role of tissue swelling for maintaining residual stresses. Moreover, GAG loss in the inner AF, as observed with degeneration, decreased circumferential direction stress by over 65%. Homogeneous distributions of fiber angle and stiffness overestimated or underestimated AF swelling behavior, such as swelling ratio, circumferential/axial stretch, and fiber stretch/reorientation. These findings demonstrate the need to include native fiber architecture in finite element models, to accurately predict tissue failure, as well as to cultivate engineered discs.

**Keyword:** Swelling, Residual Stress, Residual Strain, Annulus Fibrosus, Intervertebral Disc, Fiber Angle, Degeneration

## 6.1 Introduction

Many native and engineered fiber-reinforced tissues, such as the annulus fibrosus (AF) and arterial walls, have an excellent capacity to absorb water molecules from the surrounding environment ($>$ 50% increase in volume) [24, 188]. Water uptake is directly related to the glycosaminoglycans (GAG) composition, and tissue deformations due to swelling lead to development of residual stresses and strains, altering tissue- and joint-level mechanics [22, 23, 24, 25, 28, 125, 188, 222, 223, 224]. Previous experimental and computational studies have shown that tissue-swelling behavior of fiber-reinforced materials is anisotropic and dependent on the fiber-network architecture (*i.e.*, fiber angle, lamellae, and fiber stiffness) [4, 22]. Tissue swelling occurs as a balance between fiber deformation, fiber rotation, and matrix swelling [4, 213]. However, the effect of complex tissue geometry, such as the kidney-bean shape of the intervertebral disc, on swelling behavior and residual stress formation is not clear.

Recent work showed that the inner AF experiences large region-dependent compressive residual strains, while the outer AF experiences region-dependent tensile residual strains [39, 40, 41]. Similar residual-strain distribution, *i.e.* compressive in the inner region and tensile in the outer region, has also been observed in cardiovascular tissues [24]. In addition, residual strains in arterial wall depend on tissue composition and spatial location (*i.e.*, through the wall thickness and distance from the heart) [24, 42]. Comparisons can be drawn between the intervertebral disc and the arterial wall and, in that the healthy nucleus pulposus

(NP) acts to pressurize the inner AF during loading. It is thought that residual stresses in the arterial wall act together with blood pressure to maintain a uniform stress distribution throughout the arterial wall [43]. More recent work has shown that stress homeostasis through the arterial wall greatly depended on local GAG composition [189]. Interestingly, work by Roccabianca et al. showed that an increase in GAGs confined to a small region of the arterial wall increased radial stresses and strains that may cause arterial wall delamination [189].

The biochemical composition of the AF is inhomogeneous from outer to inner with respect to GAG content, collagen fiber angle, and fiber stiffness. In non-degenerate discs, the GAG content increases from 3.0 ± 0.3 % per wet weight in the outer AF to 8.0 ± 0.5 % per wet weight in the inner AF [15, 19]. Age and degeneration are noted by a ∼60% decrease in GAG composition in the inner AF, while the GAG content in the outer AF remains relatively constant [15]. Fiber angle, with respect to the transverse plane, increases from ±28° in the outer AF to ±43° in the inner AF [12]. Lastly, collagen fibers in the outer AF are 2-3X stiffer than fibers in the inner AF, due to differences in collagen type and content (*i.e.*, higher ratio of collagen type I:II in the outer AF) [26, 27, 28, 225]. Fiber stiffness is thought not to change greatly with degeneration [193]. Although there are large spatial variations in GAG content, fiber angle, and fiber stiffness, the role of these properties in AF swelling and residual strain development are not well understood.

Computational models are widely used to better understand stress distributions between tissues in the spine, and to assess the role of degeneration in disc joint mechanics [64, 65, 68]. Many of these previous models described the AF using hyperelastic material descriptions, which are not capable of describing swelling behavior under various aqueous solutions observed *in vivo*. Moreover, these models described the AF as having a homogeneous fiber angle (±30°) and stiffness [1, 13, 87]. Similarly, tissue-engineered strategies commonly use homogenized fiber stiffness and/or angle (either 0° or ±30°) to create de novo intervertebral discs [141, 142, 226, 227].

Our previous work evaluated the effect of the collagen fiber network on tissue-level swelling, where specimen geometry was based on the rectangular geometry commonly used for uniaxial testing [4]. However, *in situ* AF swelling will be affected by boundary conditions due to the kidney-bean geometry of the human disc. Therefore, the first objective of this study was to evaluate the effect of the kidney-bean geometry on the swelling behavior of the

AF. The second objective was to evaluate residual strain formation as a result of swelling. Finally, we evaluated the effect of GAG content, fiber angle, and fiber stiffness on swelling and residual strain formation.

## 6.2 Methods

We developed two series of models (Table 6.1). Models in Series I contained 1 to 4 annular layers and were used to evaluate the effect of the kidney-bean geometry on annular ring swelling (Figure 6.1A). The thin annular ring structures allowed us to compare annular ring results to our previous swelling results on rectangular specimens [4]. In addition, we included a 20-layer rectangular model to compare to the full AF annular ring model, which represented the native architecture of healthy human discs (Figure 6.1B&C) [13]. Models in Series II were all 20-layer annular-ring models to represent the native AF (Figure 6.1B). However, material properties in Series II models were modified to evaluate the role of inhomogeneous GAG composition, fiber angle, and fiber stiffness. In the Control model used for Series II, spatial distributions of GAG, fiber angle, and fiber stiffness through the annulus wall thickness were inhomogeneous and selected based on properties of healthy non-degenerate human lumbar discs reported in literature [1, 12, 15, 19, 27]. In Series II, these parameters were modified to create a homogeneous distribution (denoted by H in front of the properties, Table 6.1), by changing the material properties in the inner AF to match the values in the outer AF (n = 8 models; Table 6.1).

### Model geometry and mesh

The model geometry and mesh were extracted from our previous joint-level model (Figures 6.1 A& 6.1B) [1]. Briefly, AF geometry and meshes were generated using a custom-written algorithm to process published data containing averaged disc geometry from human male L3-L4 discs (n = 13; Matlab 2013, Mathworks, Inc. Natick, MA) [112]. In Series I models, annular rings were created by starting at the outermost layer (Figure 6.1A) and building inwards for multi-layered models. The 20-layer rectangular model had same layer length, width, and thickness as our previous study. Fibers were orientated at $\pm 30^{\circ}$ with respect to the transverse plane for annular ring models and with respect to Z axis for the

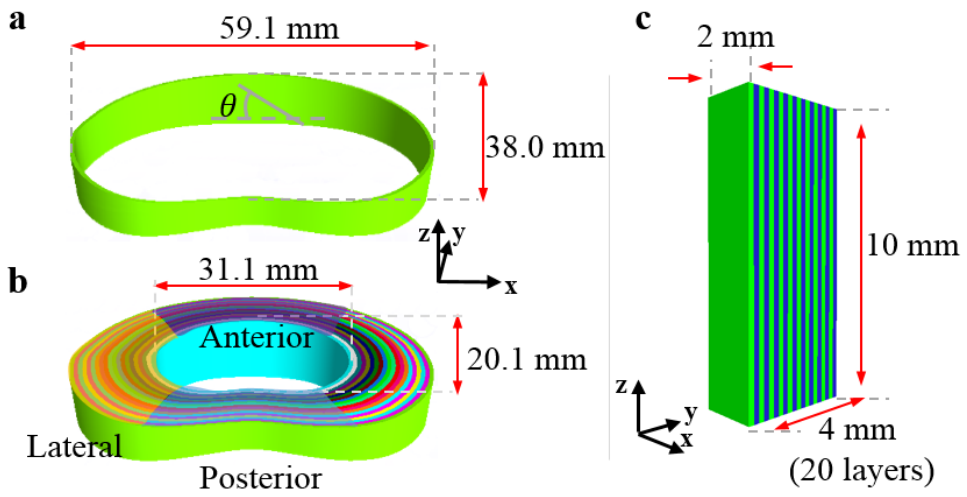


Figure 6.1: (**A**) Representative model of annular rings (1-layer shown). (**B**) Complete AF model with 20 layers shared the same anterior-posterior width and lateral width as the 1-layer model. Anterior, posterior, and lateral regions were marked by transparent purple, yellow, and blue. (**C**) Rectangular model with 20 layers.

20-layer rectangular model (Figure 6.1C). Models in Series II contained AF geometry of the complete annulus fibrosus (20 layers), representing the native AF architecture (Figure 6.1B). The fiber angle in Series II models was defined as either homogeneous ($\pm 30°$) or inhomogeneous, ranging from $\pm 43°$ in the innermost AF layer and decreasing linearly to $\pm 28°$ in the outermost AF layer [12].

## Material properties

Triphasic mixture theory was used to describe the tissue as a combination of three phases: a solid phase and two fluid phases (water and monovalent ions) [38, 72, 116]. The solid phase consisted of the extrafibrillar matrix and nonlinear fibers, where Wi represents strain energy density functions (Equation 6.1) [116]. The extrafibrillar matrix was defined as a compressible hyperelastic material using the Holmes-Mow description (Equations 6.2-6.4). Matrix material properties were assumed to be spatially uniform and held consistent across all models. Material coefficients ($E_m$, $\nu$, and $\beta$) were selected based on values reported in the literature (Table 6.2) [20]. $E_m$, $\nu$, and $\beta$ represented Young's modulus, Poisson's ratio,

Table 6.1: Series I evaluated the effect of annulus ring (AR) geometry on bulk tissue swelling of single and multi-lamellae structures. A 20-layer rectangular (REC) specimen was added to our previous simulations for comparison [4]. Series II investigated the effect of GAG distribution (G), fiber angle (A), and fiber stiffness (S) on AF swelling behavior. An H in front of G, A, or S, represents a homogeneous distribution of the material property, where the default condition was an inhomogeneous distribution that represented native tissue architecture. HG-HA-HS model in Series II was same as 20REC in Series I.

| | Model | Total # of Layers |
|---|---|---|
| Series I | 1AR | 1 |
| | 2AR | 2 |
| | 3AR | 3 |
| | 4AR | 4 |
| | 20AR | 20 |
| | 20REC | 20 |
| Series II | G-A-S (Control) | 20 |
| | HG-A-S | 20 |
| | G-HA-S | 20 |
| | HG-HA-S | 20 |
| | G-A-HS | 20 |
| | HG-A-HS | 20 |
| | G-HA-HS | 20 |
| | HG-HA-HS | 20 |

and material exponential stiffening coefficient, respectively.

$$W = W_{matrix} + W_{fiber} \tag{6.1}$$

$$W_{matrix}(I_1, I_2, J) = \frac{1}{2}c(e^Q - 1) \tag{6.2}$$

where Q and c were expressed as:

$$Q = \frac{\beta}{\lambda + 2\mu}[(2\mu - \lambda)(I_1 - 3) + \lambda(I_2 - 3) - (\lambda + 2\mu)\ln J^2] \tag{6.3}$$

$$c = \frac{\lambda + 2\mu}{2\beta} \tag{6.4}$$

I1 and I2 are the first and second invariants of the right Cauchy-Green deformation tensor, $\boldsymbol{C}$ ($\boldsymbol{C} = \boldsymbol{FTF}$) and J are the Jacobian of the deformation gradient tensor, $\boldsymbol{F}$ (J = det($\boldsymbol{F}$)).

Table 6.2: Material parameters for models in Series I. $E_m$: Extrafibrillar matrix modulus, $\nu$: Poisson ratio, $\beta$: non-linear parameter for the Holmes-Mow description, $E_f$: collagen fiber modulus, $\gamma$: exponential term for the toe-region response of the fibers, $I_0$: the stretch ratio between the toe- and linear-region, $\varphi_0$: tissue solid fraction, $k_0$: hydraulic permeability in the reference configuration, $M$: nonlinear parameter for permeability, $\phi$: osmotic coefficient, FCD: fixed charge density, $D_{free}$: ion diffusivity in water, $D$: ion diffusivity within tissue, and S: ion solubility [1, 19, 20, 27].

| Solid Phase | | Fluid Phase | |
|---|---|---|---|
| $E_m(MPa)$ | 0.025 | $k_0(\text{mm}^4/(\text{Ns}))$ | 0.0064 |
| $\nu$(unitless) | 0.16 | $M$(unitless) | 4.8 |
| $\beta$(unitless) | 3.3 | $\phi_0$(unitless) | 0.938 |
| $E_f$(MPa) | 46 | FCD(mmol/L) | -100 |
| $\gamma$(unitless) | 4.5 | $D_{free}(\text{mm}^2/\text{s})$ | 0.00147 |
| $I_0$(unitless) | $1.06^2$ | $D(\text{mm}^2/\text{s})$ | 0.0008 |
| $\varphi_0$(unitless) | 0.3 | $S$(unitless) | 1 |

$\lambda$ and $\mu$ are the Lamé coefficients, which are related to Young's modulus ($E_m$) and Poisson's ratio ($\nu$).

Fibers were defined using a nonlinear stress-stretch relationship with defined toe- and linear-region separated by a transition stretch value ($\lambda_0$, ⟦$I_0 = \lambda_0^2$ Equations 6.5-6.8) [136]. In Equation 6.5, $\gamma$ described the toe-region nonlinearity (unitless), the invariant In represented the square of the fiber stretch ($I_n = \boldsymbol{a} \cdot \boldsymbol{C} \cdot \boldsymbol{a}$, where a was the unit vector that described the fiber angle in the reference configuration), and Ef represented the fiber linear-region elastic modulus (MPa, constant). In this expression, $\gamma$, $I_0$, and $E_f$ were independent coefficients, which were calibrated using data from single-lamellae tensile tests [27], as described previously [1]. Fiber stiffness in Series I models was homogeneous and calibrated to the stiffness of single-lamellae from the outer AF (Table 6.2). The fiber stiffness in Series II models was either held constant throughout the AF or inhomogeneous, increasing linearly from the inner AF to outer AF (Table 6.3). All fibers were limited to acting only in tension.

$$W_{fiber} = \begin{cases} 0 & I_n < 1 \\ \frac{\xi}{2\gamma}(I_n - 1)^{\gamma} & 1 \leq I_n \leq I_0 \\ E_f(I_0^{1/2} - I_n^{1/2}) + B(I_n - I_0) + W_0 & I_0 \leq I_n \end{cases} \tag{6.5}$$

Table 6.3: Additional material parameters for models in Series II (other parameters are shown in Table 6.2). For inhomogeneous model descriptions values were linearly interpolated from the inner AF to the outer AF. Ef: collagen fiber modulus, $\gamma$: exponential term for the toe-region response of the fibers, $I_0$: the stretch ratio between the toe- and linear-region, FCD: fixed charge density [1, 12, 15, 19, 27].

| | | Inhomogeneous | | Homogeneous |
|---|---|---|---|---|
| | | Inner AF | Outer AF | |
| FCD (mmol/L) | | -300 | -100 | -100 |
| Fiber Angle | | 43° | 28° | 30° |
| | $E_f$ (MPa) | 16.5 | 46 | 46 |
| Fiber Stiffness | $\gamma$ (unitless) | 5.5 | 4.5 | 4.5 |
| | $I_0$ (unitless) | 1.09 | 1.06 | 1.06 |

$$\xi = \frac{E_f}{2(\gamma-1)} I_0^{-3/2} (I_0 - 1)^{2-\gamma} \tag{6.6}$$

$$B = \frac{E_f I_0^{-3/2}}{2} \left[ \frac{I_0 - 1}{2(\gamma - 1)} + I_0 \right] \tag{6.7}$$

$$W_0 = \frac{\xi}{2\gamma} (I_0 - 1)^{\gamma} \tag{6.8}$$

In the triphasic mixture theory, the negative fixed charge density (FCD) in the solid description was used to represent the GAG composition in the extrafibrillar matrix by assuming 2 moles of charge per GAG mole (molecular weight = 502.5 g/mole; Equation 6.9) [199]. An FCD of -100 mmol/L was used for annular rings in Series I, representing the GAG content in the outer AF [19]. Similar to fiber angle and stiffness, the GAG distribution of models in Series II was either held fixed at -100 mmol/L or was inhomogeneous, decreasing linearly from -300 mmol/L in the inner AF to -100 mmol/L in the outer (Table 6.3) [15, 19]. The total number of fixed charges was conserved; therefore, the local FCD depended on volumetric changes (Equation 6.10; $\varphi_0$ represents the solid volume fraction in the reference configuration, subscript '0' for FCD represents the reference configuration, while '1' represents the swollen configuration; Table 6.2).

$$FCD_0 = \frac{2\ mmol\ charges}{0.5025\ g\ GAG} \frac{W_{GAG}}{1\ L} \tag{6.9}$$

$$FCD_1 = \frac{1 - \varphi_0}{J - \varphi_0} FCD_0 \tag{6.10}$$

Fluid (*i.e.*, water) and ion phases were included to simulate tissue swelling (Table 6.2) [200, 201]. FCD influenced fluid and ions movement by affecting their electrochemical potential. Free diffusivity ($D_{free}$) and diffusivity ($D$) were used to describe how quickly ions diffused through the water and the tissue. Permeability ($k$) was used to describe fluid flow through the tissue, and was strain-dependent. Parameters $k_0$ and $M$ were selected based on AF experimental data (Holmes-Mow permeability model; Equation 6.11; Table 6.2) [20].

$$k(J) = k_0(\frac{J-\varphi_0}{1-\varphi_0})^2 e^{\frac{1}{2}\ M(J^2-1)} \tag{6.11}$$

## Simulation, model validation, and data analyses

All simulations were conducted in FEBio [116]. Boundary conditions for all models allowed specimens to freely deform, except that bulk tissue translational movement was restricted. This was achieved by fixing one degree of freedom of a few nodes, such that the X-position was fixed for three nodes on the bottom and mid-sagittal planes (YZ plane), the Y-position was fixed for three nodes on the bottom and anterior region, and the Z-position was fixed for six nodes on the mid-transverse plane (XY plane). These nodes were picked to utilize AF swelling symmetry. The reference configuration represented a state of osmotic dehydration, which is equivalent to the tissue hydrated under an infinitely high concentration of saline. Steady-state swelling (quasi-static) condition was simulated by increasing the FCD from zero to the specified value (10 steps in 1-second simulation), while the saline condition of the surrounding environment remained constant (0.15 M phosphate buffered saline; 150 mmol/L). Since the simulation was quasi-static, water and ion redistribution and tissue deformation reached equilibrium at each time-step.

Deformations caused by free-swelling conditions were analyzed. The swelling ratio was calculated as the volume in the deformed condition divided by the volume in the reference configuration. Swelling ratio, fiber stretch, and fiber reorientation were calculated for each element. Weighted averages were calculated for each parameter, using element volumes as a weighting factor. For complete AF ring models (20 layers), circumferential, axial, and radial stretch and stress were calculated for each element. Weighted averages were calculated for each layer, as well as for the whole model, to calculate layer-averaged and model-averaged values. It should be noted that circumferential and radial directions referred to local coordinates (*i.e.*, normal to and aligned with the lamellae, respectively). Lastly,

region-dependent swelling was evaluated for the anterior, lateral, and posterior regions of the innermost and outermost layers (Figure 6.1B). Only fibers in tension were included in the calculation of average fiber stretch.

In our previous study, rectangular models that represented samples used in uniaxial tensile tests were validated by comparing volumetric and dimensional changes from swelling to free-swelling experiments on bovine AF explants [4, 22, 125]. In the current study, annular rings in Series I used the same material properties and fiber angle. Further validation was performed for the Control model in Series II. The circumferential-direction stretch was compared with experimentally measured residual stretches of bovine discs [39, 40]. The Control model was considered valid if the circumferential stretch in inner and outer AF followed the same behavior of experimental observations and the magnitude was within one standard deviation of the reported mean.

## 6.3 Results

### Model validation

The volume of the Control AF model increased by 58% under free-swelling conditions, which was comparable to values reported in the literature (up to 70%) (Bezci et al. 2015; Żak and Pezowicz 2016). Swelling of the Control AF model resulted in compressive circumferential stretch in the innermost AF layer (layer-averaged stretch = 0.92) and tensile circumferential stretch in the outermost AF layer (stretch = 1.076), which was within one standard deviation of the residual stretch measured in bovine AF explants (Figure 6.2) [39, 40]. Since model results were comparable to reported values, the Control AF model was considered valid for evaluating AF swelling behavior.

### Effect of annular rings (Series I)

In general, within 1-4 layers, annular ring models had a similar response to $\pm 30^{\circ}$ rectangular models with respect to swelling ratio, fiber stretch, and fiber reorientation. For the 1-layer annular ring model, there was a 52% increase in volume with swelling (swelling ratio = 1.52; Figure 6.3A & 6.3B), resulting in an average tensile fiber stretch of 1.019, and fiber

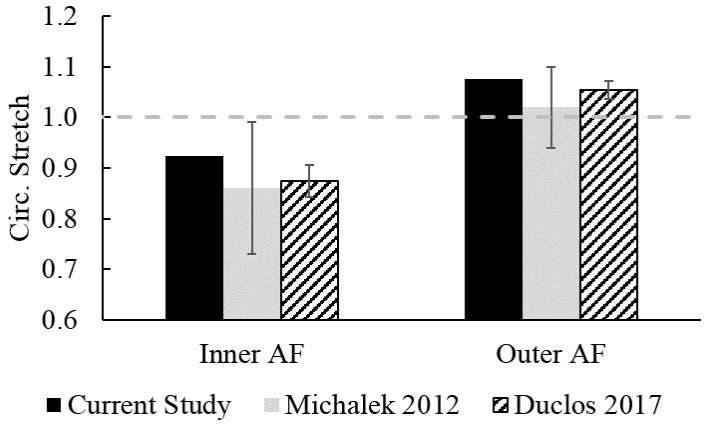


Figure 6.2: Circumferential stretch due to osmotic swelling in the inner and outer AF for the Control model was within one standard deviation of the reported mean in the literature [39, 40]. Gray dashed line represents a stretch-free condition.

reorientation of ∼5°. Annular ring models with 2-4 layers had a decrease in lateral width and an increase in anterior-posterior width with swelling, making the specimens slightly more rounded (Figure 6.3A - $2^{nd}$ row). The 2-layer annular ring model experienced twisting, which was similar to observations for even-layered rectangular specimens; however, twisting was not observed in annular ring specimens with four or more layers (Figure 6.3A). The largest difference in swelling ratio between rectangular and annular ring specimens was observed with 2- and 20-layer models, where the kidney-bean geometry resulted in less tissue swelling (swelling ratio for 20-layer models = 1.45 for rectangular versus 1.41 for the annular ring; Figure 6.3B).

There were large differences in the swelling behavior of the 20-layer annular ring model when compared to the 20-layer rectangular model. Swelling with a kidney-bean geometry resulted in the formation of inhomogeneous stretch and stress in the circumferential direction. The circumferential direction stretch and stress were compressive in the inner layers and tensile in the outer layers (Figure 6.3C & 6.3D).

## Complete AF model (Series II)

Swelling caused dimensional changes for all 8 models in Series II. The anterior-posterior width of the outer AF increased by 19% in the HG-HA-HS model (*i.e.*, homogeneous de-

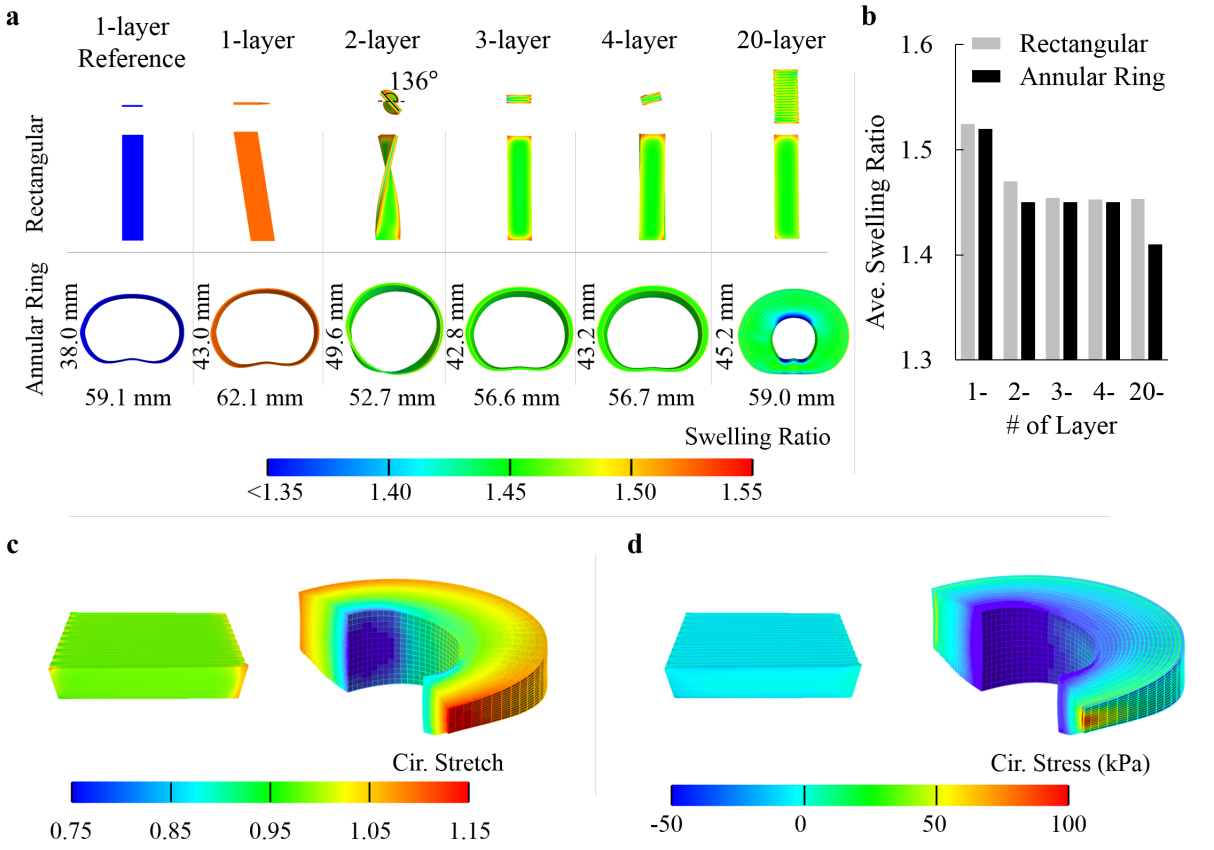


Figure 6.3: (**A**) Swelling and bulk deformations of rectangular models and annular ring models. Images for 1-4 layer rectangular specimens adapted from Yang and O'Connell (2018)[4]. (**B**) Model-averaged swelling ratio for rectangular and annular ring models. (**C**) Longitudinal stretch (Z axis) in the 20-layer rectangular model and circumferential-direction stretch in the 20-layer annular ring model (full AF model) after swelling. (**D**) Longitudinal stress (Z axis) in the 20-layer rectangular model and circumferential stress in the 20-layer annular ring model after swelling.

scription) and 31% in the G-A-S model (*i.e.*, spatial variation in properties). In contrast, the lateral width of the outer AF was relatively consistent with swelling (< 3% change from reference configuration), making the final specimen geometry slightly more circular after swelling (Figures 6.4 & 6.5 - $1^{st}$ row). The anterior-posterior width of the inner AF also increased with swelling; however, the lateral width of the inner AF experienced contraction (Figures 6.4 & 6.5 - $2^{nd}$ row).

The average swelling ratio was between 1.41 (HG-HA-HS) and 1.61 (G-HA-S; Figures 6.4 & 6.5 –$1^{st}$ row). The swelling ratio of models with an inhomogeneous GAG distribution (1.53-1.61) was greater than the swelling ratio of models with a homogeneous GAG distribution (1.41-1.44). The swelling ratio was higher in the lateral AF than in the anterior and posterior AF, regardless of the spatial distribution of GAGs, fiber angle, or fiber stiffness (Figure 6.6A & 6.6B). Homogeneous distribution of GAGs (HG) throughout the AF reduced swelling in the inner AF by ∼50% (Figure 6.7-blue lines versus black lines). Swelling of the inner AF was also decreased by a homogeneous distribution of fiber stiffness (HS; Figure 6.7 - triangles versus circles), but increased by a homogeneous fiber angle (HA; Figure 6.7 –dashed line versus solid line).

Along the circumferential direction, all models developed compressive stretch and stress in the inner AF and tensile stretch and stress in the outer AF (Figures 6.4 & 6.5 –$2^{nd}$ & $3^{rd}$ rows). Region-based differences showed that the compressive stresses in the inner AF was highest in the anterior AF and lowest in the lateral AF (Figure 6.6C –black bars). Tensile stresses in the outer AF were highest in the posterior AF, and was 2-3.5X greater than the tensile stresses in the anterior and lateral AF (Figure 6.6D –black bars). A homogenous GAG distribution decreased stresses in the inner and outer AF of all three regions by over 60%, with the largest absolute drop observed in the anterior inner AF and the posterior outer AF (Figure 6.7C & 6.7D –black bar versus grey bar). Layer-averaged circumferential direction stress also highlighted the decrease in stress with a homogenous description of GAGs (Figure 6.8B - blue versus black lines). Using a homogeneous fiber angle (HA) or fiber stiffness (HS) description had a relatively little impact on region-dependent circumferential direction stress, except for the tensile stresses in the outer posterior AF (Figure 6.6D –black bar versus patterned bars).

A homogeneous distribution of GAGs (HG) had little impact on the circumferential direction stretch in the inner AF, but caused a 50% decrease in the circumferential-direction

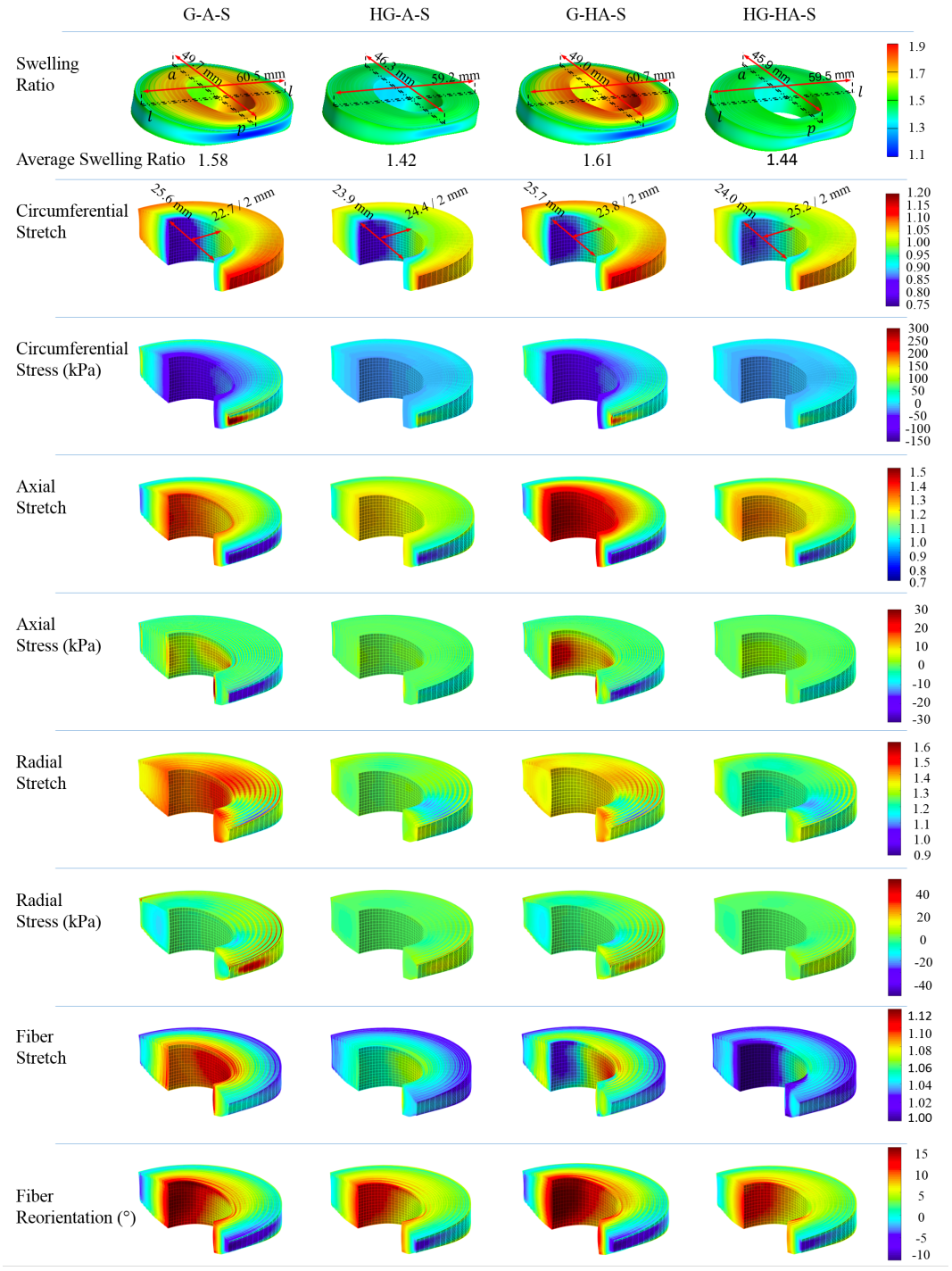


Figure 6.4: Swelling ratio, stretch and stress in the circumferential, axial, and radial directions, fiber stretch, and fiber reorientation. Data shown for G-A-S (Control model), HG-A-S, G-HA-S, and HG-HA-S models (n = 4/8; data for the other models are shown in Figure 6.5). In the last row, positive value represents fiber reorientation toward axial direction, while negative value represents fiber reorientation toward the transverse plane.

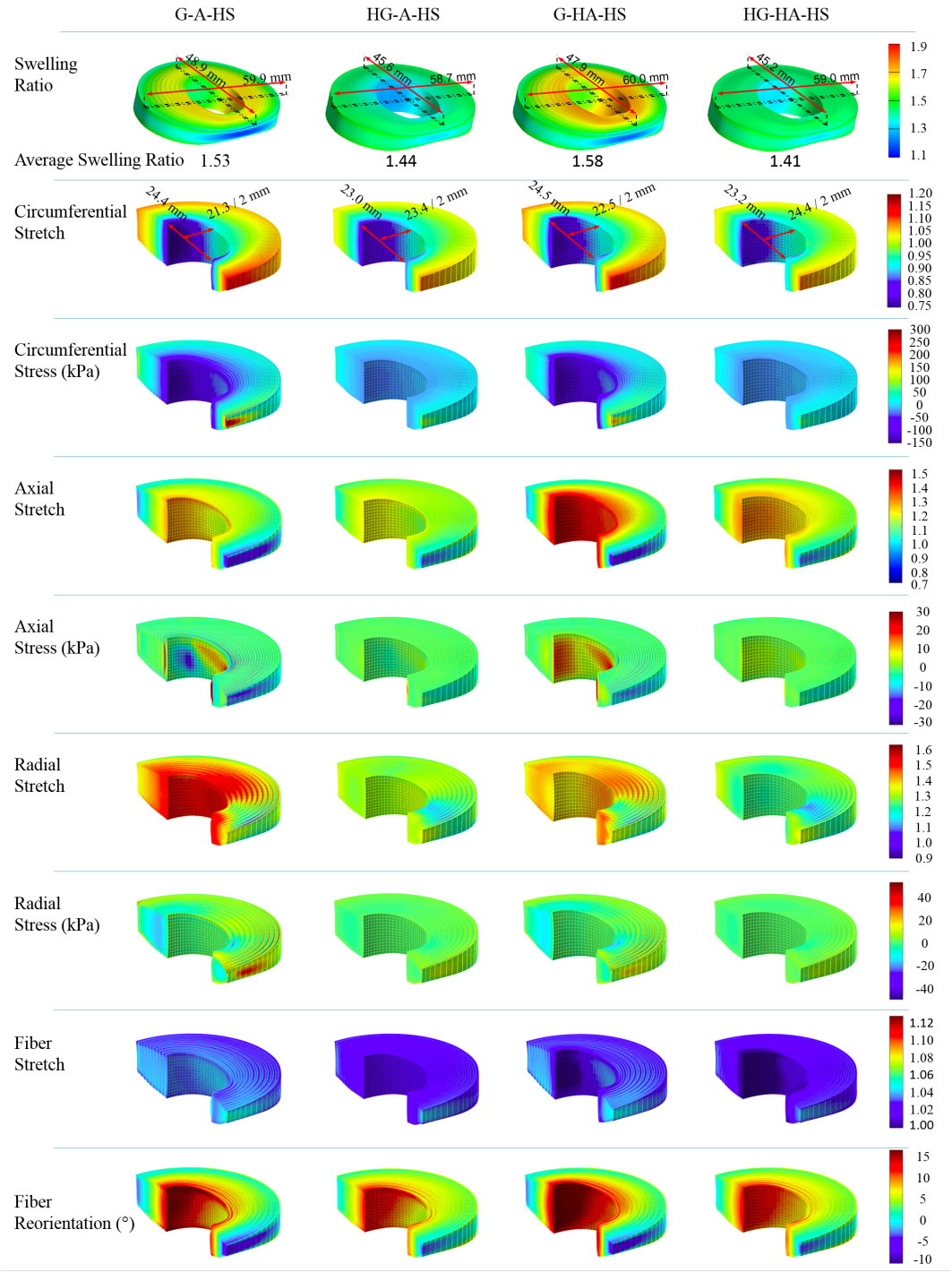


Figure 6.5: Swelling ratio, stretch and stress in the circumferential, axial, and radial directions, fiber stretch, and fiber reorientation. Data shown for G-A-HS, HG-A-HS, G-HA-HS, and HG-HA-HS models (n = 4/8; data for the other models are shown in Figure 6.4). In the last row, positive value represents fiber reorientation toward axial direction, while negative value represents fiber reorientation toward the transverse plane.

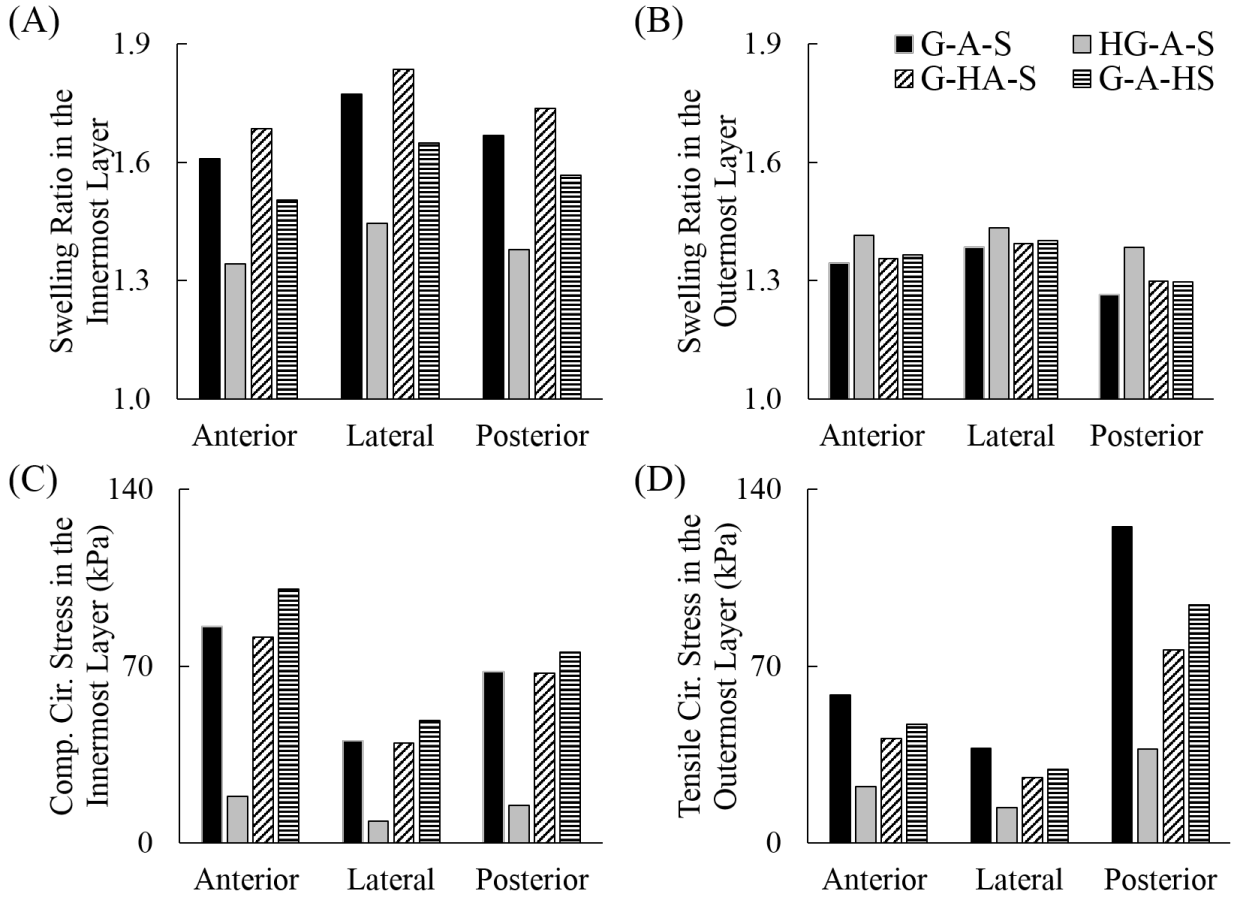


Figure 6.6: Swelling ratio averaged for the anterior, lateral, and posterior regions of innermost (**A**) and outermost (**B**) layers for G-A-S, HG-A-S, G-HA-S, and G-A-HS models. Compressive and tensile circumferential stress averaged for the anterior, lateral, and posterior regions of innermost (**C**) and outermost (**D**) layers for G-A-S, HG-A-S, G-HA-S, and G-A-HS models.

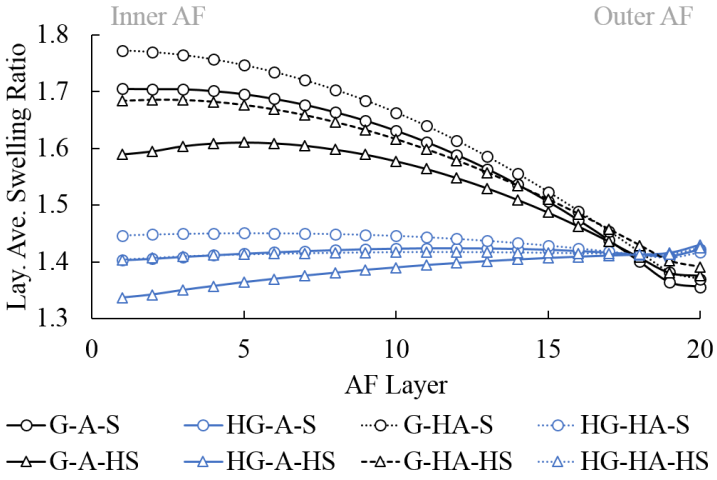


Figure 6.7: Layered-averaged swelling ratio for each layer within an AF model (shown for all eight models in Series II). Black lines represent models with inhomogeneous GAG distribution (black for G), while blue lines represent models with a homogeneous distribution in GAG (blue for HG). Solid lines represent models with an inhomogeneous distribution in fiber angles, while dashed lines represent models with a homogeneous distribution in fiber angles. Circles represent models with an inhomogeneous distribution in fiber stiffness, while triangles represent models with a homogeneous distribution in fiber stiffness.

tensile stretch in the outer AF (Figure 6.8A - blue versus black lines). Homogeneous fiber stiffness (HS) increased the circumferential direction compressive stretch at the inner AF by more than 50%, but had a relatively little impact on the circumferential direction stretch in the outer AF (Figure 6.8A - triangles versus circles). A homogeneous distribution of fiber angle (HA) had a relatively small effect on the stretch in the circumferential direction (Figure 6.8A - dashed versus solid lines).

In general, all models developed tensile stretch in the axial direction of the inner AF, (Figures 6.4 & 6.5 - $4^{th}$ row). In the Control model, the tensile stretch was 1.27 in the inner AF and the magnitude decreased linearly from the inner AF to the outer AF, such that the axial direction stretch was compressive in the outer AF (Figures 6.4 & 6.5 –$4^{th}$ row). A homogeneous distribution of GAGs and fiber stiffness (HG & HS) resulted in relatively uniform axial direction stretch throughout the AF. That is, there was a 30% decrease in axial direction stretch from the inner AF to the outer AF in the G-HA-S model, but only decreased by 8% in the HG-A-HS model (Figure 6.8C - blue versus black lines).

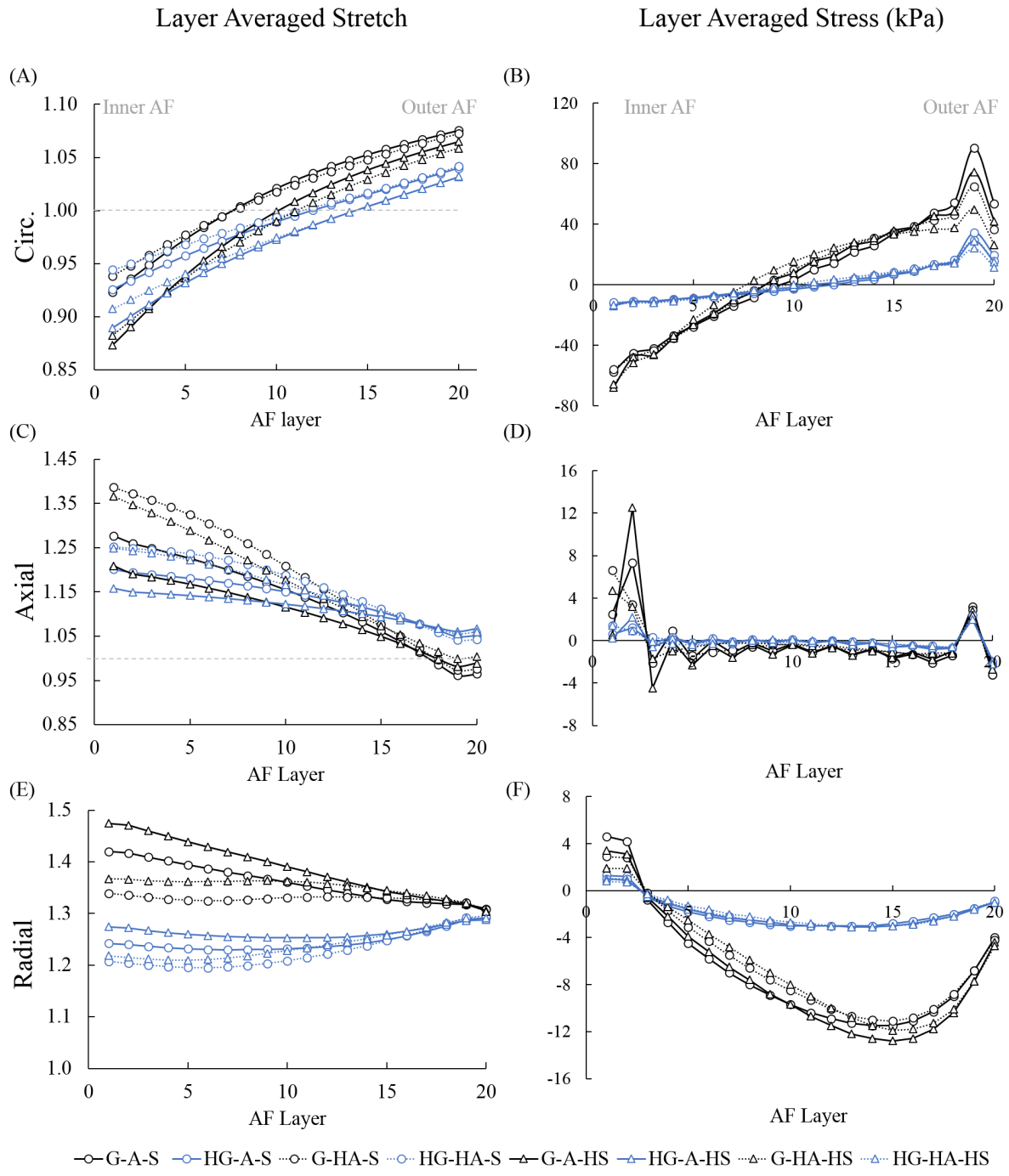


Figure 6.8: Layer-averaged stretches and stresses for models in Series II. Layer-averaged (**A**) circumferential stretch, (**B**) circumferential stress, (**C**) axial stretch, (**D**) axial stress, (**E**) radial stretch, and (**F**) radial stress. Black lines represent models with inhomogeneous GAG distribution (black for G), while blue lines represent models with a homogeneous distribution in GAG (blue for HG). Solid lines represent models with an inhomogeneous distribution in fiber angles, while dashed lines represent models with a homogeneous distribution in fiber angles. Circles represent models with an inhomogeneous distribution in fiber stiffness, while triangles represent models with a homogeneous distribution in fiber stiffness.

The axial direction tensile stress in the inner AF decreased with a homogeneous distribution of GAGs or fiber stiffness (HG & HS; Figure 6.8C - blue versus black lines or triangles versus circles) and increased with a homogeneous distribution of fiber angle (HA; Figure 6.8C –solid versus dashed lines). Axial direction stress was relatively low in all models, save for the innermost and outermost layers, which experienced tensile and compressive stresses, respectively (Figures 6.4 & 6.5 - $5^{th}$ row and Figure 6.8D).

Large tensile deformations were observed in the radial direction, with the lowest values observed in the posterior-lateral AF (Figures 6.4 & 6.5 - $6^{th}$ row). Layer-averaged radial stretches greater than 1.2, with values near 1.3 in the outer AF for all models (Figure 6.8E). Layer-averaged radial stretch was higher in the inner AF than the outer AF of models with an inhomogeneous GAG distribution, while the layer-averaged radial stretch was relatively consistent throughout the AF in models with a homogeneous GAG distribution (HG; Figure 6.8E –blue versus black lines). Radial stretch decreased with a homogeneous distribution in fiber angle (HA; Figure 6.8E - dashed versus solid lines) and increased with a homogeneous distribution in fiber stiffness (HS; Figure 6.8E - triangles versus circles). Radial direction stresses were relatively low throughout the AF ($\leq$ 13 kPa; Figures 6.4 & 6.5 - $7^{th}$ row and Figure 6.8F). Layered-averaged radial stresses were slightly higher in the middle layers of the AF for models with inhomogeneous GAG distribution (Figure 6.8F - blue versus black lines).

Fiber stretch in the inner AF was lower in the anterior and posterior regions than the lateral regions, but, in the outer AF, fiber stretch was highest in the anterior and posterior regions (Figure 6.4 & 6.5 - $8^{th}$ row). All models had similar fiber stretch in the outermost layer (average = 1.03; Figure 6.4 & 6.5 - $8^{th}$ row; Figure 6.9A). Fiber stretch was greatly reduced by a homogeneous distribution in fiber stiffness and GAG (HS & HG; Figure 6.9A - triangles versus circles and blue versus black lines). Fiber stretch in the inner AF decreased with a homogeneous distribution of fiber angle (HA), but did not alter fiber stretch in the middle or outer AF (Figure 6.9A - dashed versus solid lines). The greatest layer-averaged fiber stretch occurred in the inner AF of the Control (G-A-S) model (1.10), and the lowest layer-averaged fiber stretch occurred in the inner AF of the homogeneous (HG-HA-HS) model (1.01; Figure 6.9A - black solid line with circles versus blue dashed line with triangular markers).

The behavior of fiber reorientation with swelling was similar for all models (Figure 6.4 & 6.5 - last row). Fibers in the inner AF reoriented toward the axial direction (positive

fiber reorientation; Figures 6.4 & 6.5 - last row), while fibers in the anterior and posterior region of the outer AF reoriented towards the transverse plane (Figure 6.9B –black lines). A homogeneous distribution of GAGs (HG) decreased the magnitude of fiber reorientation throughout the AF (Figure 6.9B –blue versus black lines).

## 6.4 Discussion

Simulations showed that the annular ring geometry for specimens with 4 or fewer layers had little impact on swelling ratio, fiber stretch, and fiber reorientation. However, the kidney-bean shape played an important role as the number of lamellae increased towards the native AF architecture (20 layers), such that circumferential direction stretch and stress in the full AF model were compressive in the inner AF and tensile in the outer AF. These stretch and stress were comparable to experimental observations (Figures 6.3 and 6.4 –$2^{nd}$ row) [39, 40]. Altering the distribution of GAGs, fiber stiffness, or fiber angle affected the magnitude and distribution AF swelling, stress and stretch, fiber reorientation, and fiber stretch.

Previous studies showed that residual strains of the bovine AF and arterial walls are compressive at the inner layers and tensile at the outer layers [39, 40, 41, 24, 42]. Inhomogeneous distributions of circumferential-direction stresses (compressive at the inner wall and tensile at the outer wall) are important to maintain a uniform tensile circumferential stress distribution throughout the wall during physiological loading [43]. These findings suggest that AF residual stress is driven largely by the inner AF GAG content. This is further supported by the AF having a larger GAG content than other fiber-reinforced tissues that only experience tensile residual strains (*e.g.*, 10 –50 times higher GAG content than tendons or ligaments) [207, 228].

Material properties in the full AF models were region-independent, but residual stretch, residual stress, fiber stretch, and fiber reorientation were region-dependent due to the asymmetrical AF geometry (Figures 6.4-6.6). Larger compressive strains were predicted in the circumferential direction of the anterior inner AF, which agreed well with experimental observations. However, Duclos and Michalek reported tensile compressive strains in the posterior AF and regional-differences that showed greatest tensile strains in the outer AF of the lateral AF, which did not agree well with our model predictions [39]. In both the bovine and human

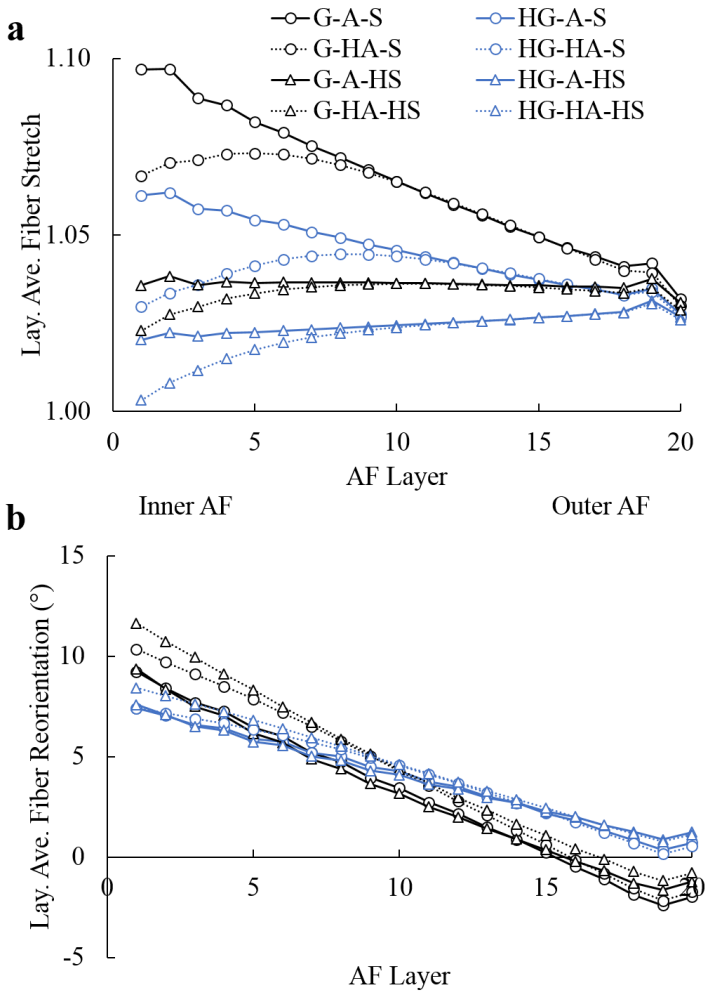


Figure 6.9: Layer-averaged (**A**) fiber stretch and (**B**) fiber reorientation for each layer. Positive value represents fiber reorientation toward axial direction, while negative value represents fiber reorientation toward the transverse plane. Black lines represent models with inhomogeneous GAG distribution (black for G), while blue lines represent models with a homogeneous distribution in GAG (blue for HG). Solid lines represent models with an inhomogeneous distribution in fiber angles, while dashed lines represent models with a homogeneous distribution in fiber angles. Circles represent models with an inhomogeneous distribution in fiber stiffness, while triangles represent models with a homogeneous distribution in fiber stiffness.

discs, peak tensile residual strains in the outer AF corresponded to areas with the smallest radius of curvature in the inner AF. Outer dimensions of the bovine disc are cylindrical, but the NP is more elliptical with the long axis along the lateral width [11]. Similarly, the kidney-bean shape of the human disc results in a lower radius of curvature in the posterior AF. The kidney-bean shape of human lumbar discs combined with layer-dependent material properties resulted in more complex distributions of residual stress and strain [27, 15, 12, 28].

In this study, GAG loss in the inner AF was described by a decrease in fixed charge density to match the fixed charge density of the outer AF. Diurnal loading causes a fluctuation in fluid volume by up to 20% [229], altering disc joint stiffness [125, 188, 223, 224]. Regardless of hydration condition, the swelling capacity of the healthy AF has been shown to be approximately 70% of the NP [125]. Therefore, AF swelling and residual strains likely fluctuate with the diurnal loading and hydration conditions.

The quantity and quality of GAGs in the inner AF decreases greatly with age and degeneration [15, 19, 155]. We showed that GAG loss in the inner AF impacts swelling capacity, tissue deformations, and development of residual strains (Figures 6.4-6.8 - HG versus G). Radial pressure from the NP, applied to a hydrated AF, would decrease the magnitude of stress and strain in the circumferential direction. Early degenerative changes are noted with a decrease in NP GAG content and intradiscal pressure [48]. These changes, however, may increase the magnitude of compressive strains in the inner AF during physiological loading. Thus, it is likely that tissue remodeling in the inner AF occurs with age and degeneration to maintain stress homeostasis throughout the AF. The findings from this study support the notation that tissue remodeling through GAG deletion, rather than collagen stiffening, is more effective in reducing residual strains.

While the motivation for studying GAG distribution on residual strain formation in the AF was based on arterial wall research, there are interesting differences that should be noted. The GAG content in arterial walls increases due to an increase in blood pressure with disease [189]. Together these findings support the notion that GAGs are crucial for maintaining stress homeostasis with disease and degeneration, especially in annular ring structures. Moreover, variations in local GAG composition may result in regional differences in circumferential strains that may increase the risk of annular tears [39].

A decrease GAGs in the inner AF resulted in a reduction in the magnitude of axial direction stretch and fiber reorientation (Figures 6.8C & 6.9B). This finding is comparable

to the decrease in fiber reorientation with degenerated AF tissue under *ex situ* tensile loading [54]. Fiber reorientation in tissue-level specimens increases fiber engagement during tensile loading [54]. Moreover, changes in fiber orientation affect joint-level mechanics, such that discs with fibers oriented closer to the axial plane have a higher torsional stiffness and larger shear strains at the AF-bone boundary [1]. Therefore, a decrease in fiber reorientation with GAG remodeling in the inner AF may help to protect the fibers from experiencing larger deformations during complex joint loading (*e.g.* compression with bending).

Our previous work showed that fiber orientation affected the swelling behavior of rectangular tissue specimens, while fiber stiffness only affected fiber stretch [4]. However, in the annular ring structure, both fiber orientation and fiber stiffness (HA & HG) altered swelling behavior. A homogeneous fiber angle (HA) description resulted in an overestimation of swelling ratio, axial stretch, and fiber reorientation, while predictions for radial stretch and fiber stretch were underestimated (G-A-S versus G-HA-S model). A homogenous description of fiber stiffness (HS; *i.e.*, an increase in inner AF fiber stiffness), decreased swelling ratio, stretch in the circumferential and axial directions, and fiber stretch (Figures 6.7-6.9). A decrease in circumferential direction residual stretch due to stiffer fibers may lead to an underestimation of deformations during mechanical loading. Taken together, these findings suggest that recapitulating spatial variations in fiber stiffness and fiber angle is important for properly describing AF mechanics and, therefore, joint-level mechanics.

While the current model included spatial variations in GAG content, fiber stiffness, and fiber orientation, regional differences in fiber stiffness, fiber angle, and matrix composition were not investigated and may result in more complex strain distributions (*i.e.*, differences between anterior and posterior AF) [27, 28, 39]. Due to a lack of experimental data, comparisons between model predictions and experimental data were limited to comparing results from bovine discs. The difference in disc geometry (kidney-bean shape vs cylindrical shape) likely contributed to differences in residual strains in the posterior AF [39]. Finally, our current model did not include the NP, cartilage endplate, and bony endplate, which will alter tissue swelling, and, therefore, the formation of residual stresses/strains and fiber reorientation of the full intact motion segment. Future work will investigate the effect of hydration on strain distributions throughout the disc joint.

In conclusion, the annular ring structure greatly impacts tissue swelling of thick-walled structures (*e.g.*, 20 layer model versus $< 4$ layers). Development of swelling-based residual

stretch in the AF was region-dependent and comparable to experimental data, suggesting an important role of water absorption and swelling in stress homeostasis. Model simulations also suggest that GAG remodeling in the inner AF, due to a decrease in intradiscal pressure from the NP, likely acts to balance stress distributions throughout the AF. Lastly, findings from this study demonstrate the need to recapitulate native fiber architecture and matrix swelling behavior, as these properties will affect sub-failure and failure mechanics predicted by computational models as well as the mechanical behavior of engineered discs.

# Chapter 7

# Intervertebral Disc Swelling Maintains Strain Homeostasis throughout the Annulus Fibrosus: Finite Element Models for Healthy and Degenerated Discs [6]

## Abstract

Soft tissues with a high glycosaminoglycan (GAG) content have an excellent capacity to absorb water. GAG content decreases linearly from the center of the disc (nucleus pulposus, NP) to the outer annulus fibrosus (AF). Our recent work demonstrated that AF fiber network and GAG distribution contributed to the development of inhomogeneous residual stresses and strains, from compressive strains in the inner layer to tensile strains in the outer. GAG loss in the inner AF, as observed with early to moderate degeneration, reduced swelling capacity and circumferential-direction stress by more than 50%. However, our previous model was not capable of evaluating interactions between disc subcomponents during swelling. In this study, the effect of GAG distribution, or tissue swelling capacity, on residual stress development throughout the disc was assessed by altering swelling capacity in the NP and

AF, as reported in the literature for human discs. Comparing *in situ* swelling capacity from healthy tissue explants resulted in a 40% reduction in NP swelling and 25% reduction in the AF and cartilaginous endplate swelling. A reduction of NP swelling capacity was sufficient for replicating the decrease in NP pressure observed with degeneration (healthy = 0.21 MPa; severe degeneration = 0.03 MPa). Early degeneration decreased the circumferential-direction residual deformation by over 60% and flipped the radial-direction stretch from compressive ∼0.95 to tensile ∼1.05. Degeneration greatly altered AF residual stress/stretch and fiber stretch in the posterior region, which is primary damage region in herniated discs. In conclusion, our finds demonstrate relatively large changes in local strains with early and moderate degeneration, which may impact cell response from matrix production to catabolic behavior or apoptosis.

**Keyword:** Swelling, Intervertebral Disc, Degeneration, Residual Stress, Residual Pressure, Annulus Fibrosus, Nucleus Pulposus.

## 7.1 Introduction

The intervertebral disc is a complex fibrocartilaginous structure, comprised of a nucleus pulposus (NP) surrounded by the annulus fibrosus (AF) and is sandwiched between cartilaginous (CEPs) and bony endplates. The NP and AF are comprised primarily of water, proteoglycans (GAGs), and collagen fibers, in different ratios between the two tissues [12, 13]. Specifically, the NP has a higher GAG-to-collagen ratio and appears more gelatinous in healthy discs, while the collagen fibers in the AF are highly aligned and organized in concentric lamellae in a cross-ply pattern ( 20 layers). Previous experimental studies showed that both healthy NP and AF tissues have an excellent swelling capacity, with increases in tissue volume greater than 50% [22, 125]. While a decrease in tissue swelling is a hallmark of disc degeneration, the role of tissue swelling on intradiscal deformations is not well understood.

Previous observations have noted significant increases in disc volume after removing the disc from surrounding vertebral bodies due to a partial release of residual stresses. However, tissue-level experiments and simulations have shown that these tissues have an ability to swell further once tissue-level residual stresses are released [4, 5, 19, 38, 125]. Moreover,

AF tissue swelling is anisotropic, dependent on the fiber network architecture (*i.e.*, fiber angle and lamellae), and geometry [4, 22]. Specifically, the annular ring geometry results in compressive residual strains in the inner layer that becomes tensile towards the outer AF [5, 39, 40]. While these studies highlighted the role of tissue swelling on residual stress and strain formation in an annular ring, interactions between the NP and AF during *in situ* swelling is not clear.

Measuring intradiscal deformations has been a significant challenge, requiring time-consuming and expensive experimental setups (*e.g.*, high resolution magnetic resonance scanners or stereo-radiography) [31, 58]. Finite element modeling provides an alternative tool for quantifying intradiscal stresses and strains. These models have been widely used to assess the effect of degeneration on disc joint mechanics by altering structural properties [65, 68]. Developing models that mimics native joint mechanics allows researchers to evaluate the effect of degeneration of individual subcomponents on intradiscal deformations [1, 2, 64, 65]. These models typically employ hyperelastic material to describe large deformations observed in biological tissues, but these models do not account for tissue swelling, which has been observed for many biological tissues [1, 41, 65]. To mimic soft tissue swelling, Lai and coworkers proposed a triphasic mixture material [38], which describes a material as a combination of a solid phase and two fluid phases (water and monovalent ions) and fluid movement results as an imbalance in the ion concentration between the tissue and surrounding environment. The triphasic material description has been successful in describing cartilage mechanics and nutrient diffusion in the disc [71, 72, 73, 74].

Disc degeneration has been noted with large decreases in GAG content and intradiscal pressure in the NP and inner AF. In healthy discs, NP and CEP GAG contents are 11.5 $\pm$ 0.5% and 3.1 $\pm$ 0.5% per wet weight (ww), respectively [15, 19, 21], while AF GAG content decreases linearly from 8.0 $\pm$ 0.5% /ww in the inner AF to 3.0 $\pm$ 0.3%/ww in the outer AF [15, 19]. Early degeneration is marked by an initial decrease in NP GAG content, such that the NP GAG content is comparable to the inner AF (from 11%/ww to 8%/ww) [19]. As degenerative changes progress, both NP and inner AF GAG contents decrease (more than 50% decrease for Grade 3 discs) [49, 50]. Finally, with severe degeneration (Grades 4 and 5), NP GAG content is less than the GAG content in the inner AF [19]. CEP GAG content also decreases with degeneration, particularly for discs with Schmorl's nodes [57], but the decreases in CEP GAG content are not as drastic as the NP and inner AF. Lastly, the outer

Table 7.1: Total 18 models were developed to represent intervertebral disc and its subcomponents at different levels of degeneration.

| | Intact Disc | NP+AF | NP explant (NP) | CEP explant (CEP) | AF ring (AF) |
|---|---|---|---|---|---|
| Models | Healthy (H) | H | H | H | H & D1 |
| | Healthy (H) | H | H | H | |
| | Healthy (H) | H | H | H | D2 & D3 |
| | Healthy (H) | H | H | H | |

AF GAG content remains relatively constant with age and degeneration [15].

Our previous work simulated swelling of an annular ring structure as a stand-alone material. We showed that GAG loss in the inner AF decreased swelling ratio and circumferential-direction stress by more than 50% [5]. However, the effect of GAG composition on *in situ* disc swelling and stress or strain distributions between disc subcomponents was not investigated. Therefore, the objectives of this study were to evaluate interactions between disc subcomponents under free swelling conditions, and to elucidate the effect of step-wise GAG loss on disc swelling. Models were developed to replicate healthy and degenerated discs.

## 7.2 Methods

To study stress and strain distributions between disc subcomponents, models were developed for the Intact Disc (ID) and disc subcomponents, such as the NP with the AF (NP+AF) and tissue explants (NP and CEP explants, and an intact AF ring; five model geometries; Table 7.1; Figure 7.1). GAG content and distribution was varied to investigate the effect of progressive degeneration (three levels of degeneration evaluated: D1-3) on swelling behavior (n = 18 model simulations; Table 7.1).

### Model geometry and mesh

The NP explant geometry was a 1 mm cube, and the CEP explant geometry had dimensions of 1 X 1 X 0.5 mm (1000 elements). Meshes for AF rings included 20 individual lamellae with 109K elements, while the NP+AF model contained 123K elements, and the Intact Disc had 193K elements. Geometry for the Intact Disc was extracted from our previ-

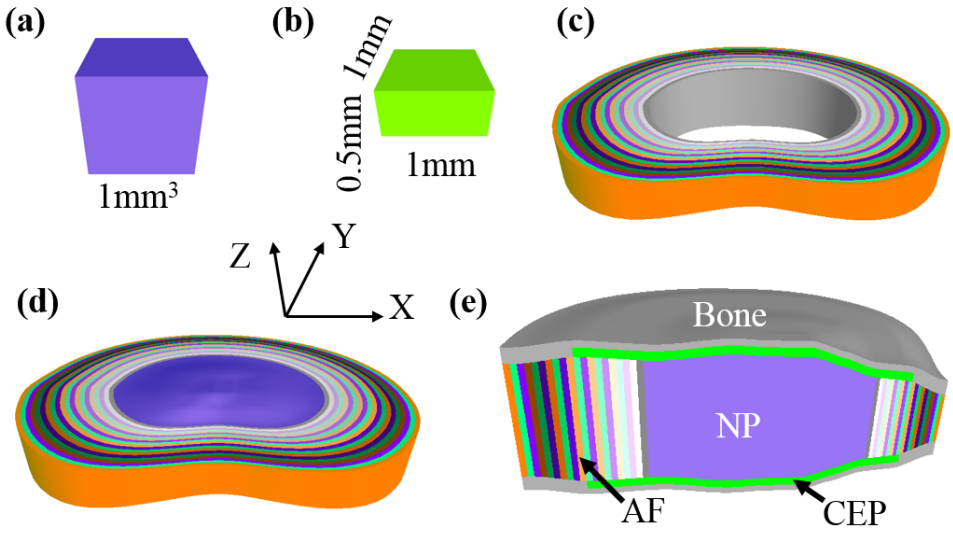


Figure 7.1: Models: **(a)** NP explant, **(b)** CEP explant, **(c)** AF, **(d)** NP + AF, **(e)** Disc (mid sagittal view).

ously published joint-level model [1]. Briefly, geometries and meshes were generated using a custom-written algorithm to process published data containing averaged disc geometry from 13 human male lumbar discs (L3-L4; Matlab 2013, Mathworks, Inc. Natick, MA) [112]. In models that had more than one component (*e.g.*, NP + AF model), subcomponents were welded together by sharing nodes at the interfaces.

## Material properties

Triphasic mixture theory was used to describe disc tissues as a combination of three phases, including a solid phase and two fluid phases (water and monovalent ions) [38, 72, 116]. The solid phase was defined by using a strain energy density function (W). The extrafibrillar matrix of the NP, CEP, and AF were described as a compressible hyperelastic material (Holmes-Mow material model, Equations 7.1-7.3). The solid phase of the bone was described as a neo-Hookean material (Young's modulus = 12000 MPa, Poisson's ratio = 0.3) [85].

$$W(I_1, I_2, J) = \frac{1}{2}c(e^Q - 1) \tag{7.1}$$

Table 7.2: Material parameters for models in Series I. $E_m$: Extrafibrillar matrix modulus, $\nu$: Poisson ratio, $\beta$: non-linear parameter for the Holmes-Mow description, $E_f$: collagen fiber modulus, $\gamma$: exponential term for the toe-region response of the fibers, $I_0$: the stretch ratio between the toe- and linear-region, $\varphi_0$: tissue solid fraction, $k_0$: hydraulic permeability in the reference configuration, $M$: nonlinear parameter for permeability, $\phi$: osmotic coefficient, FCD: fixed charge density, $D_{free}$: ion diffusivity in water, $D$: ion diffusivity within tissue, and S: ion solubility [1, 19, 20, 21, 27, 64]

| | Parameters | NP | CEP | AF |
|---|---|---|---|---|
| Solid Phase | $E_m$(MPa) | 0.0649 | 0.305 | 0.025 |
| | $\nu$(unitless) | 0.24 | 0.18 | 0.16 |
| | $\beta$(unitless) | 0.95 | 0.29 | 3.3 |
| | $E_f$(MPa) | | | 16.5 (46)* |
| | $\gamma$(unitless) | N/A | N/A | 5.5 (4.5)* |
| | $I_0$(unitless) | | | 1.14 (1.06)* |
| | $\varphi_0$(unitless) | 0.21 | 0.4 | 0.3 |
| Fluid Phase | $k_0$(mm$^4$/(Ns)) | 0.0055 | 0.0056 | 0.0064 |
| | $M$(unitless) | 1.92 | 3.79 | 4.8 |
| | $\phi$(unitless) | 0.938 | 0.938 | 0.938 |
| | FCD(mmol/L) | -400 | -124 | -300(-100)* |
| | $D_{free}$(mm$^2$/s) | 0.00147 | 0.00147 | 0.00147 |
| | $D$(mm$^2$/s) | 0.0008 | 0.0008 | 0.0008 |
| | $S$(unitless) | 1 | 1 | 1 |

* Fiber stiffness increased while FCD magnitude decreased linearly from the inner AF to the outer (values in parentheses).

where Q and c were expressed as:

$$Q = \frac{\beta}{\lambda + 2\mu}[(2\mu - \lambda)(I_1 - 3) + \lambda(I_2 - 3) - (\lambda + 2\mu)\ln J^2] \tag{7.2}$$

$$c = \frac{\lambda + 2\mu}{2\beta} \tag{7.3}$$

$I_1$ and $I_2$ in Equation 7.2 are the first and second invariants of the right Cauchy-Green deformation tensor, $\boldsymbol{C}$ ($\boldsymbol{C} = \boldsymbol{F}^T\boldsymbol{F}$), J is the Jacobian of the deformation gradient tensor, $\boldsymbol{F}$ (J = det($\boldsymbol{F}$)), and $\lambda$ and $\mu$ are the Lamé coefficients, which are related to Young's modulus and Poisson's ratio. $\beta$ represented exponential stiffening and all material coefficients were selected from the literature (Table 7.2) [20, 220]

In addition to the extrafibrillar matrix, the AF solid phase had a second component to describe the mechanical behavior of nonlinear fibers using a power-linear stress-stretch relationship with toe- and linear- regions separated by a transition stretch ($\lambda_0$, $I_0 = \lambda_0^2$; Equations 7.4-7.8) [136]. In Equation 7.5, $\gamma$ described nonlinearity in the toe-region (unitless), the invariant $I_n$ represented the square of the fiber stretch ($I_n = \boldsymbol{a} \cdot \boldsymbol{C} \cdot \boldsymbol{a}$, where a was the unit vector for fibers in the reference configuration), and $E_f$ represented the linear-region elastic modulus of the fibers (MPa, constant). Independent coefficients (*i.e.*, $\gamma$, $I_0$, and $E_f$) were calibrated using data from single-lamellae tensile tests [27], as previously described [1]. Fiber stiffness increased linearly from the inner AF to the outer AF (Table 7.2), while fiber angle decreased linearly from ±43° in the inner AF to ±28° in the outer AF [12]. All fibers were limited to acting only in tension.

$$W_{AF} = W_{matrix} + W_{fiber} \tag{7.4}$$

$$W_{fiber} = \begin{cases} 0 & I_n < 1 \\ \frac{\xi}{2\gamma}(I_n - 1)^{\gamma} & 1 \leq I_n \leq I_0 \\ E_f(I_0^{1/2} - I_n^{1/2}) + B(I_n - I_0) + W_0 & I_0 \leq I_n \end{cases} \tag{7.5}$$

$$\xi = \frac{E_f}{2(\gamma - 1)} I_0^{-3/2} (I_0 - 1)^{2-\gamma} \tag{7.6}$$

$$B = \frac{E_f I_0^{-3/2}}{2} \left[ \frac{I_0 - 1}{2(\gamma - 1)} + I_0 \right] \tag{7.7}$$

$$W_0 = \frac{\xi}{2\gamma}(I_0 - 1)^{\gamma} \tag{7.8}$$

In the triphasic mixture theory, the negative fixed charge density (FCD) was used to represent GAGs in the tissue by using the relationship shown in Equation 7.9 (molecular weight = 502.5 g/mole) [199]. In healthy models, FCD was set to -400 mmol/L for the NP and decreased linearly from -300 mmol/L in the inner AF to -100 mmol/L in the outer AF (Table 7.2) [15, 230]. CEP had an FCD of -124 mmol/L and FCD in the bone was assumed to be zero [19, 21].

To mimic GAG loss with degeneration, FCD was reduced in degeneration models (D1-3; Table **7.3**; [15, 19, 21, 57, 230]. During swelling, the total number of fixed charges was conserved; therefore, the local FCD depended on volumetric changes, where $\varphi_0$ represents the

Table 7.3: Fixed-charge density (FCD) for NP, CEP, and AF at healthy and degenerative statuses [15, 19, 21, 57, 230].

| | H | D1 | D2 | D3 |
|---|---|---|---|---|
| NP | -400 | -300 | -150 | -100 |
| CEP | -124 | -90 | -45 | -30 |
| AF* | -300(-100) | | -150(-100) | |

*FCD magnitude decreased linearly from the inner AF to the outer (values in parentheses).

solid volume fraction in the reference configuration (Equation 7.10 subscript '0' represents the reference configuration, and '1' represents the swollen or deformed configuration; Table 7.2).

$$FCD_0 = \frac{2\ mmol\ charges}{0.5025\ g\ GAG}\frac{W_{GAG}}{1\ L} \tag{7.9}$$

$$FCD_1 = \frac{1-\varphi_0}{J-\varphi_0}FCD_0 \tag{7.10}$$

Fluid (*i.e.*, water) and ion phases were included to simulate soft tissue swelling (Table 7.2) [200, 201]. FCD influenced fluid and ions movement by affecting their electrochemical potential. Free diffusivity ($D_{free}$) and diffusivity ($D$) were used to describe ion diffusion rates through water and the tissue, respectively. The Holmes-Mow permeability model (k) was used to describe fluid flow through the tissue and was strain-dependent. Parameters $k_0$ and M were selected based on AF experimental data (Equation 7.11; Table 7.2) [20].

$$k(J) = k_0(\frac{J-\varphi_0}{1-\varphi_0})^2 e^{\frac{1}{2}\ M(J^2-1)} \tag{7.11}$$

## Simulation condition, data analyses, and model validation

All simulations were conducted in FEBio [116]. Boundary conditions for all models allowed specimens to freely deform, except that bulk tissue translational movement was restricted. For Disc models, this was achieved by fixing the bottom surface of the posterior bony endplate. For NP+AF, NP explant, CEP explant, and AF models, 3 nodes were picked to fix X and Y degrees of freedom and all 6 nodes were fixed in the Z-direction. For example, in AF and NP+AF models, the X-position was fixed for three nodes on the inferior and mid-sagittal plane (YZ plane) to eliminate translational movement in the X direction.

The reference configuration represented a state of osmotic dehydration, which was equivalent to the tissue being hydrated in a saline bath with an infinitely high salt concentration. Steady-state quasi-static swelling was simulated by increasing FCD from zero to the specified value (10 - 30 steps in 1-second simulations), while the saline concentration of the surrounding environment remained constant (0.15 M phosphate-buffered saline; 150 mmol/L). Since the simulation was quasi-static, water and ion distribution and tissue deformation reached equilibrium at each step.

Deformations caused by free-swelling conditions were analyzed. The swelling ratio (SR) was calculated as the volume in the deformed condition divided by the volume in the reference configuration. Then, the relative SR was calculated by normalizing SR from each subcomponent by the SR of healthy explants. For the NP, swelling-based residual pressure was calculated for each element and weighted averages were calculated using element volumes as a weighting factor. To evaluate the impact of surrounding tissues on intradiscal pressure (*i.e.*, NP pressure) a relationship between NP pressure and the change in NP SR was evaluated, where the change in NP SR was calculated as NP SR *in situ* (*e.g.*, NP+AF and intact disc models) subtracted by the SR from NP explants. For the AF, circumferential, axial, and radial stretch and stress, and fiber stretch/reorientation were calculated for each element. For the intact disc models, changes in disc height and radial bulging at the mid-disc height of the NP and intact whole disc (anterior-posterior and lateral width) were measured. Weighted averages were calculated for each layer to obtain layer-averaged values in the AF, NP+AF, and intact disc models. It should be noted that circumferential and radial directions referred to local coordinates (*i.e.*, normal to and aligned with the lamellae, respectively).

Our previous work validated AF swelling models to dimensional changes and residual stresses and strains from free-swelling experiments on bovine explants [4, 5, 22, 39, 125]. Models in this study employed the same material properties, except when FCD was altered to represent changes with disc degeneration. Further model validation was performed by comparing relative NP and AF swelling ratios from the healthy model to data in the literature [22, 125]. Moreover, swelling-based NP pressure was compared with *in vivo* and *in vitro* data [135, 139, 230, 231]. Models were considered valid if the relative swelling ratio and residual pressure were comparable to reported values in the literature.

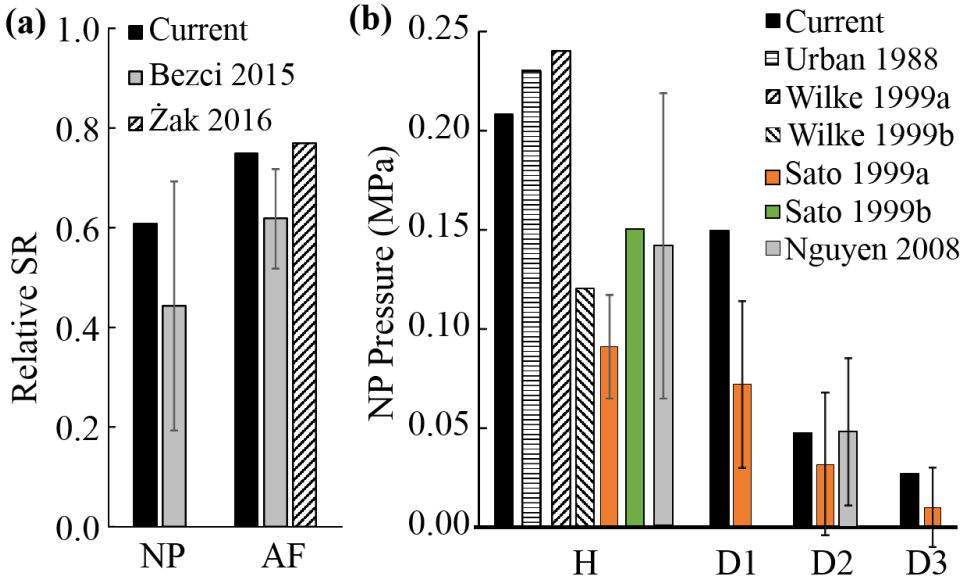


Figure 7.2: (**a**) Relative swelling ratio and (**b**) swelling-based residual pressure in NP were within one standard deviation of the reported mean in the literature [22, 125, 135, 139, 230, 231]. Orange, blue, and green bars in (**b**) represent samples that might be not fully swelled due to mechanical loading in the daytime.

## 7.3 Results

### Model validation

Healthy NP explants more than doubled in volume, while the healthy AF explant tissue had over 50% increase in volume. The relative SR for healthy NP and AF tissues *in situ*, calculated as the *in situ* SR divided by the explant SR, was 0.60 and 0.75, respectively. Thus, the model predicted that the NP and AF would experience a 34-64 % increase in volume when removed from the disc, which is comparable to observations in the literature (Figure 7.2a) [22, 125]. Similar to native discs, NP swelling in the healthy Intact Disc model increased the intradiscal pressure to 0.21 MPa and degeneration resulted in a decrease in internal pressure to 0.03 MPa (D3 Intact Disc model; Figure 7.2b). The internal pressure in the NP was comparable to *in vivo* and *in vitro* values reported for human lumbar discs (Figure 7.2b) [135, 139, 231, 230]). Therefore, the models were considered valid for evaluating the intervertebral disc swelling behavior.

## Swelling ratios and disc bulging

NP and CEP explants maintained their three-dimensional geometry (*i.e.*, cubic or rectangular cuboid) during swelling, while the AF ring experienced a slight change in lateral and anterior-posterior widths, as previously reported [5]. The NP explant SR decreased from 2.35 for the healthy condition to 1.45 with degeneration (D3; Figure 7.3a-d). Similarly, SR of the CEP and AF decreased with degeneration, from 1.23 and 1.58 for healthy tissues to 1.02 and 1.47, respectively, for degenerated tissues. SRs of tissue explants decreased with degeneration by 30% in the NP, 17% in the CEP, and 7% in the AF (Figure 7.3f-h - bars with diagonal pattern).

Semi-confining the NP with an intact AF (NP+AF model) resulted in a ∼10% reduction in NP swelling capacity and resulted in NP swelling along the Z-direction (specifically in the Healthy and D1 models, Figure 7.3a-d), which agrees with laboratory observations (Figure 7.4). In healthier NP+AF models, annular twisting was observed due to stiff collagen fibers in the inner AF resisting large deformations from NP swelling (Healthy and D1 NP+AF models; Figure 7.3a&b). As degeneration progressed, annular twisting was eliminated (*i.e.*, D2 and D3 models; Figure 7.3c&d). Regardless of the extent of degeneration, NP SR from NP+AF models was consistently 10% lower than the respective SR of NP explants (Figure 7.3a-d & 3f - diagonal patterned bars versus grey bars). Similarly, the AF SR decreased with the additional boundary constraint, but the effect was greater for AF in the healthy model, where a 10% decrease in AF swelling capacity was observed for the healthy NP+AF model and only a 3% decrease in AF swelling was observed in the degenerated NP+AF model (Figure 7.3a-d & h - diagonal patterned bars versus grey bars).

Further boundary constraints from the intact disc model resulted in larger reductions in NP and AF swelling, relative to the respective explants, but NP and AF tissues continued to exhibit an increase in tissue volume with intact disc swelling. The intact healthy disc model had an overall swelling ratio of 1.23. The *in situ* NP swelling ratio was 25-40% lower than the swelling capacity of NP explants, while *in situ* AF swelling ratio was 15-25% lower than the swelling capacity of the AF ring (Figure 7.3a-d). In contrast, the healthy CEP experienced compaction *in situ* with a swelling ratio of 0.94, which was a 24% reduction in tissue swelling compared to the CEP explant model.

As expected, NP swelling *in situ* decreased with degeneration and the effect of physical

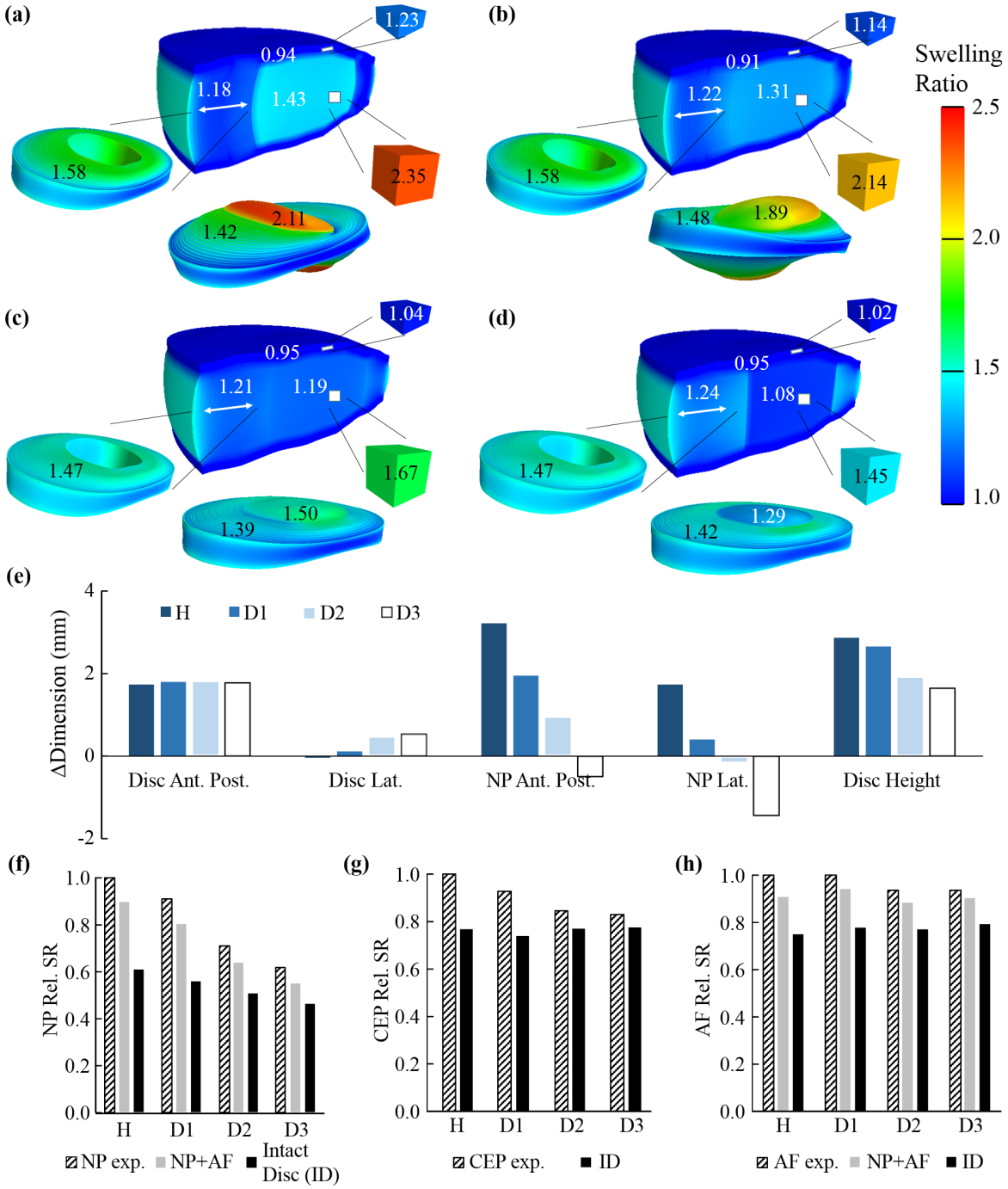


Figure 7.3: Swelling and bulk deformations of NP, CEP, AF, NP+AF, and Disc models at (**a**) healthy status (H) and (**b-d**) degenerated level 1-3 degenerated statuses (D1-D3). Values represent tissue swelling ratios for disc subcomponents. (**e**) Swelling caused changes in Disc and NP dimensions at middle disc height including the anterior-posterior dimension (Ant. Post) and the lateral dimension (Lat.). Raise in disc height at NP center decreased with degeneration. The relative swelling ratio for (**f**) NP, (**g**) CEP, and (**h**) AF at different health statuses.

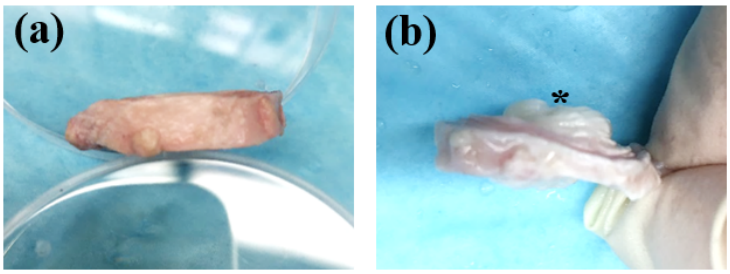


Figure 7.4: OX tail intervertebral disc (**a**) had the nucleus pulposus bulged outward (**b**) in the axial direction after swelling.

boundary constraints on NP swelling lessened with degeneration (Figure 7.3f - diagonal patterned bars versus black bars). Interestingly, AF *in situ* swelling *in situ* increased by 5% with degeneration from 1.18 in the healthy model to 1.24 in the severely degenerated model (Figure 7.3a-d & h - black bars). The decrease in NP *in situ* swelling was balanced by the slight increase in AF *in situ* swelling, resulting in relatively small changes in the overall disc swelling ratio with degeneration (5% decrease in whole disc SR: 1.18 for D2 and 1.17 for D3 model).

Swelling resulted in radial bulging of the intact disc model at the mid-disc height (Figure 7.3a-d), where the anterior-posterior width increased by 1.75 mm, regardless of changes in GAG composition with degeneration (Figure 7.3e). There was a slight increase in the lateral width with swelling ($< 0.5$ mm) and the increase was more pronounced in the severely degenerated disc (Figure 7.3e). Similarly, NP radial bulging was observed, with large increases in the anterior-posterior and lateral widths in the healthy disc (anterior-posterior = 3.2 mm increase, lateral = 1.7 mm increase; Figure 7.3e). However, the amount of outward NP radial bulging decreased with degeneration, and inward bulging of the NP-AF interface was observed in the severely degenerated model (Figure 7.3e - bars with dots). The increase in disc height was most sensitive to changes with degeneration. Disc height increased with swelling for all intact disc models, but the relative increase in disc height was dependent on degeneration (2.9 mm increase in the healthy disc and 1.6 mm in the severely degenerated disc; Figure 7.3e).

Layer-averaged swelling throughout the AF was dependent on the physical boundary conditions (Figure 7.5). In AF ring and NP+AF models, layer-averaged swelling ratios were

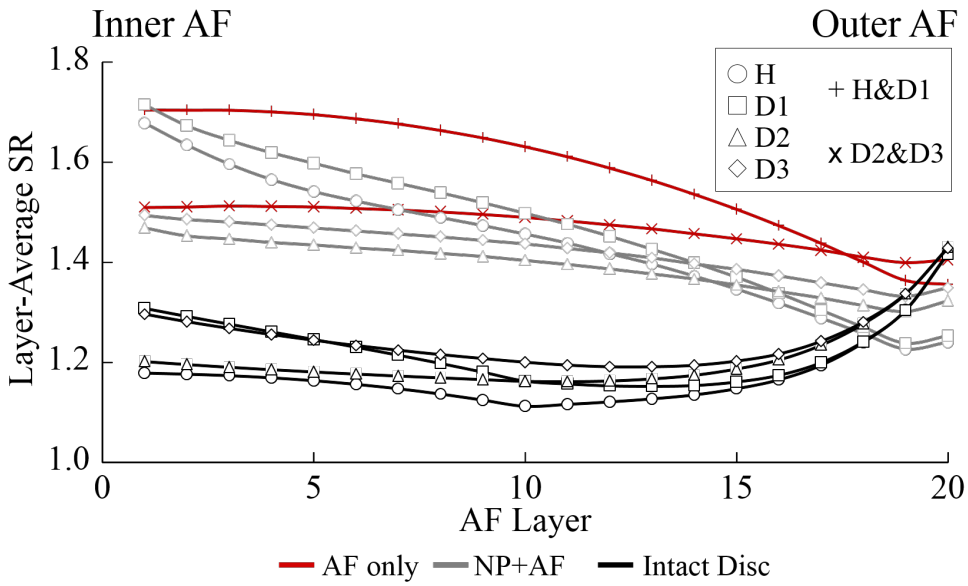


Figure 7.5: Layer swelling ratio for each AF layer (shown for Intact Disc, NP+AF, and AF models at different healthy statuses). Red, grey, and black lines represent AF layers AF models, NP + AF, and Intact Disc, respectively. Circles represent Healthy (H) models; rectangles represent Degenerated Level 1 models (D1); triangles represent Degenerated Level 2 models (D2); rhombuses represent models in Degenerated Level 3 models (D3).

greater in the inner AF(Figure 7.5 - red and grey lines). The relative difference between inner and outer AF swelling ratios decreased with degeneration (Figure 7.5 - *e.g.*, red line with '+'s versus 'x's). In contrast, layer-averaged swelling ratios in the intact disc model were consistent through much of the AF (layers 1-15), regardless of degeneration (Figure 7.5 - black lines).

## NP residual pressure

The average NP pressure decreased with degeneration in NP+AF and intact disc models. The NP pressure in the healthy intact disc was 0.21 MPa and decreased to 0.03 MPa with severe degeneration (Figure 7.6a&b). Removal of the CEP and bony endplates (NP+AF model) decreased NP pressure by 85% in the healthy disc (Figure 7.6b). Similar to the intact disc, NP pressure in the NP+AF model decreased by more than 70% with severe degeneration (from 0.03 MPa to 0.008 MPa). There was a nonlinear positive relationship

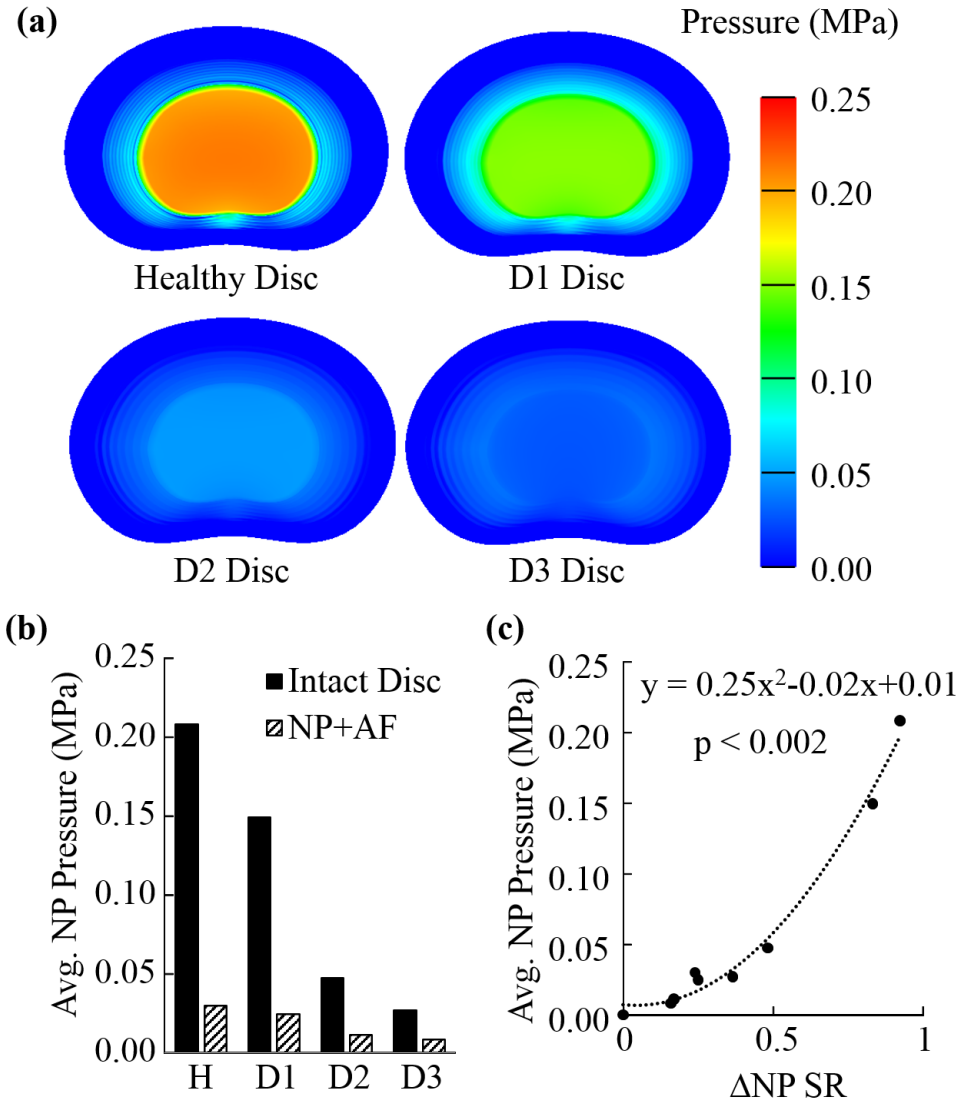


Figure 7.6: (**a**) Pressure distribution at the mid-transverse plane of the Disc models at healthy and degenerated statuses. (**b**) Average NP pressure in Intact Disc and NP+AF models at healthy and degenerated statuses. (**c**) Average NP pressure with respect to NP swelling ratio drops from explant models and NP+AF or Intact Disc models.

between NP pressure and the relative NP swelling ratio ($p < 0.002$; Figure 7.6c).

## AF Residual stretch and stress

### Circumferential direction

In AF ring models, residual circumferential stretch was compressive in the inner AF (average = 0.92) and tensile in the outer AF (average = 1.08; Figures 7.7 - $1^{st}$ column of $1^{st}$ & $2^{nd}$ rows and Figure 7.8a - red lines). Adding the NP resulted in a tensile shift in circumferential-direction stretches (NP+AF model; Figures 7.7 - Rows 3-6 & Figure 7.8a - red versus grey lines). Further constraining the AF with CEP and bony endplates, resulted in a more uniform distribution in circumferential-direction stretches (Figures 7.7 - $1^{st}$ column, rows 7-10 and Figure 7.8a - black lines). Circumferential-direction stretch in the inner AF was most affected by degeneration, where the circumferential stretch was tensile in the innermost layer of the healthy disc (stretch = 1.06) and became compressive with severe degeneration (0.97; Figure 7.8a –Layer 1).

Circumferential-direction stress was near zero in AF ring models (-0.06 - 0.09 MPa, Figures 7.7 - $2^{nd}$ column, Rows 1-2 and Figure 7.8b - red lines). The addition of physical boundary constraints increased circumferential-direction stress throughout the AF (Figure 7.8b - red lines versus grey and black lines). CEP and bony endplates decreased circumferential-direction stress in the inner AF (Layer 1-10), but increased stresses in the middle and outer AF of healthier discs (Layers 10-20; Figure 7.8b - black lines). Tensile stresses in the middle to outer AF were 3X greater in healthy discs than degenerated discs (Figure 7.8b - black lines - circles or rectangles versus triangles or rhombuses). Changes in circumferential-direction stresses with degeneration were more pronounced in the posterior AF (Figures 7.7 - $2^{nd}$ column, Rows 7-10).

## Axial direction

In AF ring and NP+AF models, layer-averaged axial-direction stretch decreased from the inner to the outer AF (Figures 7.7 - $3^{rd}$ column, $1^{st}$ - $6^{th}$ rows). Including the NP decreased axial-direction AF stretch, where stretch was less tensile in the inner AF and compressive in the outer AF (Figure 7.8c - red versus grey lines). The decrease in axial-direction stretch was more pronounced in the posterior AF of healthy models (Figures 7.7 - $3^{rd}$ column, $3^{rd}$ & $4^{th}$ rows). The endplate boundary constraint caused axial-direction stretch

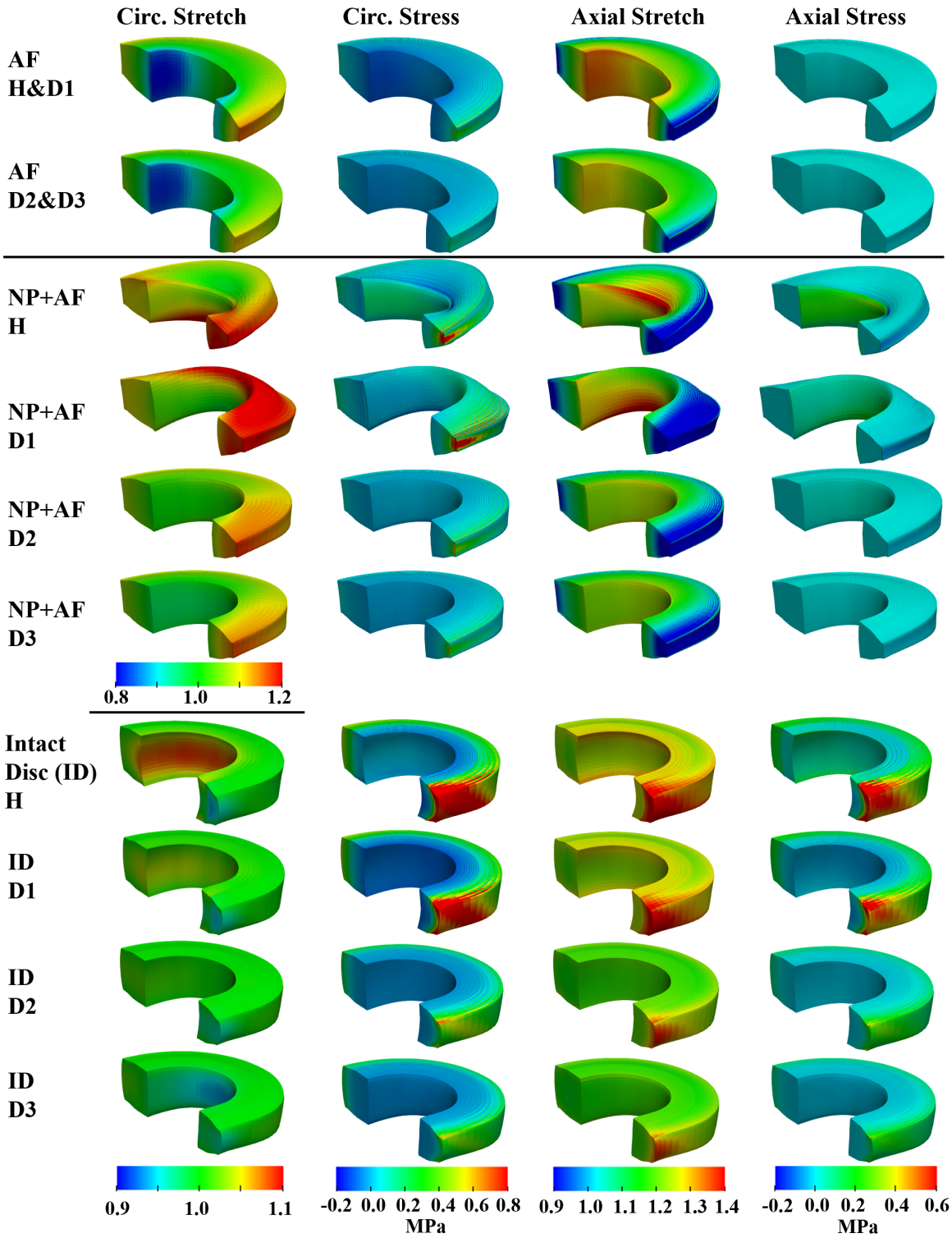


Figure 7.7: Stretch and stress in the circumferential and axial directions of the annulus fibrosus. Data shown for AF ring, NP + AF, and Disc models at healthy status (H) and degenerated level 1-3 degenerated statuses (D1-D3).

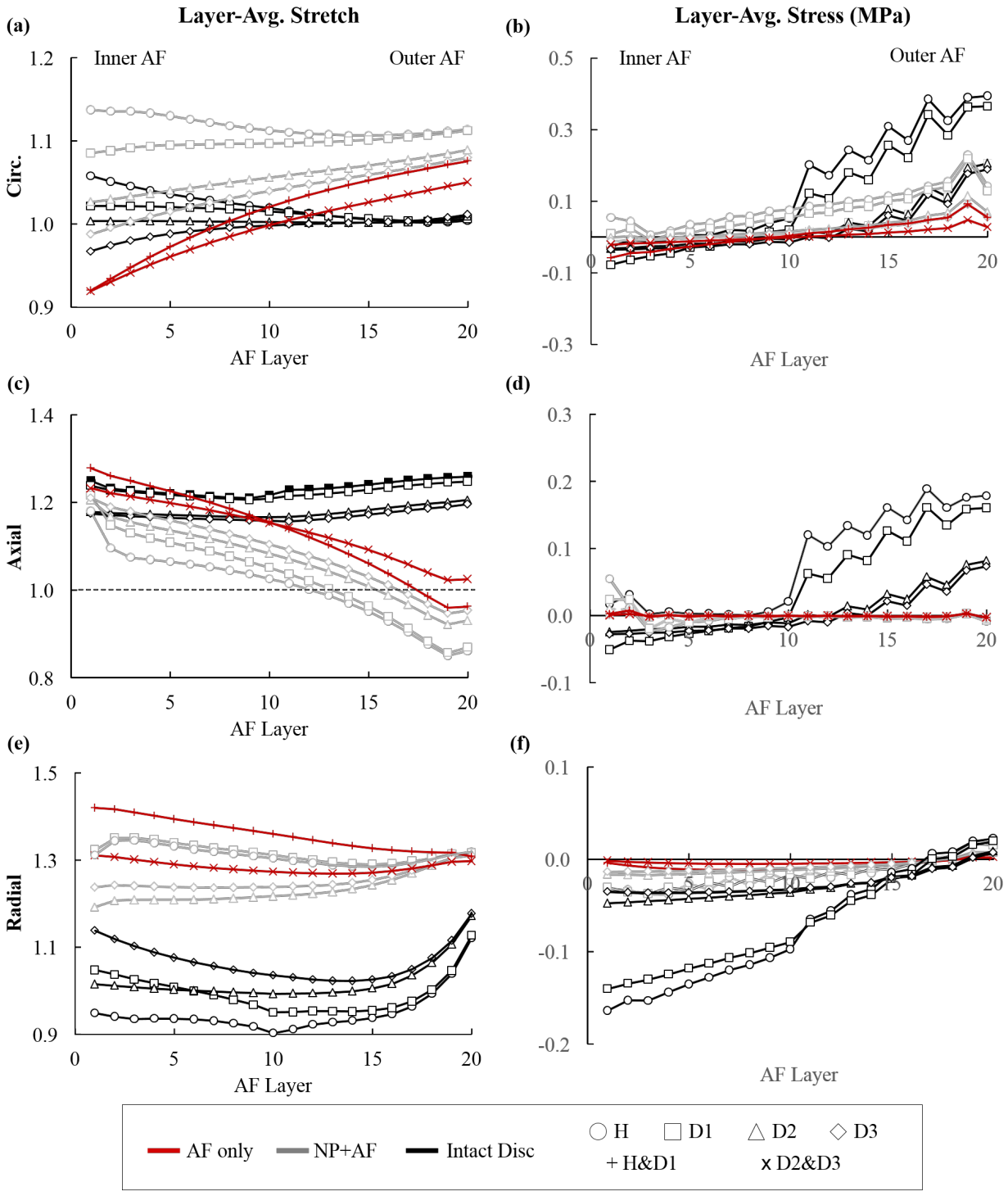


Figure 7.8: Layer-averaged stretches and stresses of annulus fibrosus in Disc, NP+AF, and AF models. (**a**) circumferential stretch, (**b**) circumferential stress, (**c**) axial stretch, (**d**) axial stress, (**e**) radial stretch, and (**f**) radial stress. Black, grey, and red lines represent AF layers in the AF ring, NP+AF, and Intact Disc (ID) models, respectively. Circles represent Healthy (H) models; rectangles represent degenerated level 1 models (D1); triangles represent degenerated level 2 models (D2); rhombuses represent degenerated level 3 models (D3).

in the outer AF to be more tensile (Figures 7.7 - $3^{rd}$ column $7^{th}$ - $10^{th}$ rows), resulting in relatively consistent axial direction stretch throughout the AF (Figure 7.8c - black lines). Degeneration decreased layer-averaged axial stretch throughout the AF (Figure 7.8c - black lines triangles and rhombuses versus circles and rectangles).

Axial-direction residual stress was very low in the AF ring and NP+AF models (Figures 7.7 - $4^{th}$ column, $1^{st}$ - $6^{th}$ rows and Figure 7.8d - red and grey lines). In the intact disc model, axial-direction stress was slightly compressive in the inner AF ($< 0.03$MPa) and tensile in the outer AF (Figure 7.8d - black lines). Tensile stresses in the outer AF was more pronounced in the posterior region, and decreased by over 50% with degeneration (Figures 7.7 - $4^{th}$ column, $7^{th}$ & $8^{th}$ rows and Figure 7.8d).

## Radial direction

AF-only models developed large radial-direction stretches (layer average between 1.26 and 1.42), which decreased by ∼10% (in the NP+AF model; Figure 7.8e - red and grey lines). Further constraining the AF with endplates continued to reduce radial-direction stretch (Figure 7.8e - black lines with circles). Degeneration resulted in a gradual increase in radial-direction stretch from compressive to tensile throughout the AF (Figure 7.8e –black circles for the healthy disc versus diamonds for severely degenerated). Early degeneration caused the innermost layer to flip its radial-direction stretch from compressive ∼0.95 to tensile ∼1.05.

Similar to the axial-direction stresses, radial-direction stresses were relatively low in the AF and NP+AF models (layer averages between -0.04 and 0.02 MPa; Figures 7.9 - $2^{nd}$ column, $1^{st}$ - $6^{th}$ rows and Figure 7.8f - red and grey lines). Healthy and D1 Intact Disc models had large compressive radial-direction stress in the inner and mid-AF and large tensile stress in the outer layers of the posterior AF (Figures 7.9 $2^{nd}$ column $7^{th}$ - $8^{th}$ rows and Figure 7.8f - black circles and rectangles). Compressive radial-direction stress decreased greatly with degeneration (Figures 7.9 - $2^{nd}$ column, $9^{th}$ & $10^{th}$ rows versus $7^{th}$ row and Figure 7.8f - black lines: circles or square versus triangles or rhombuses).

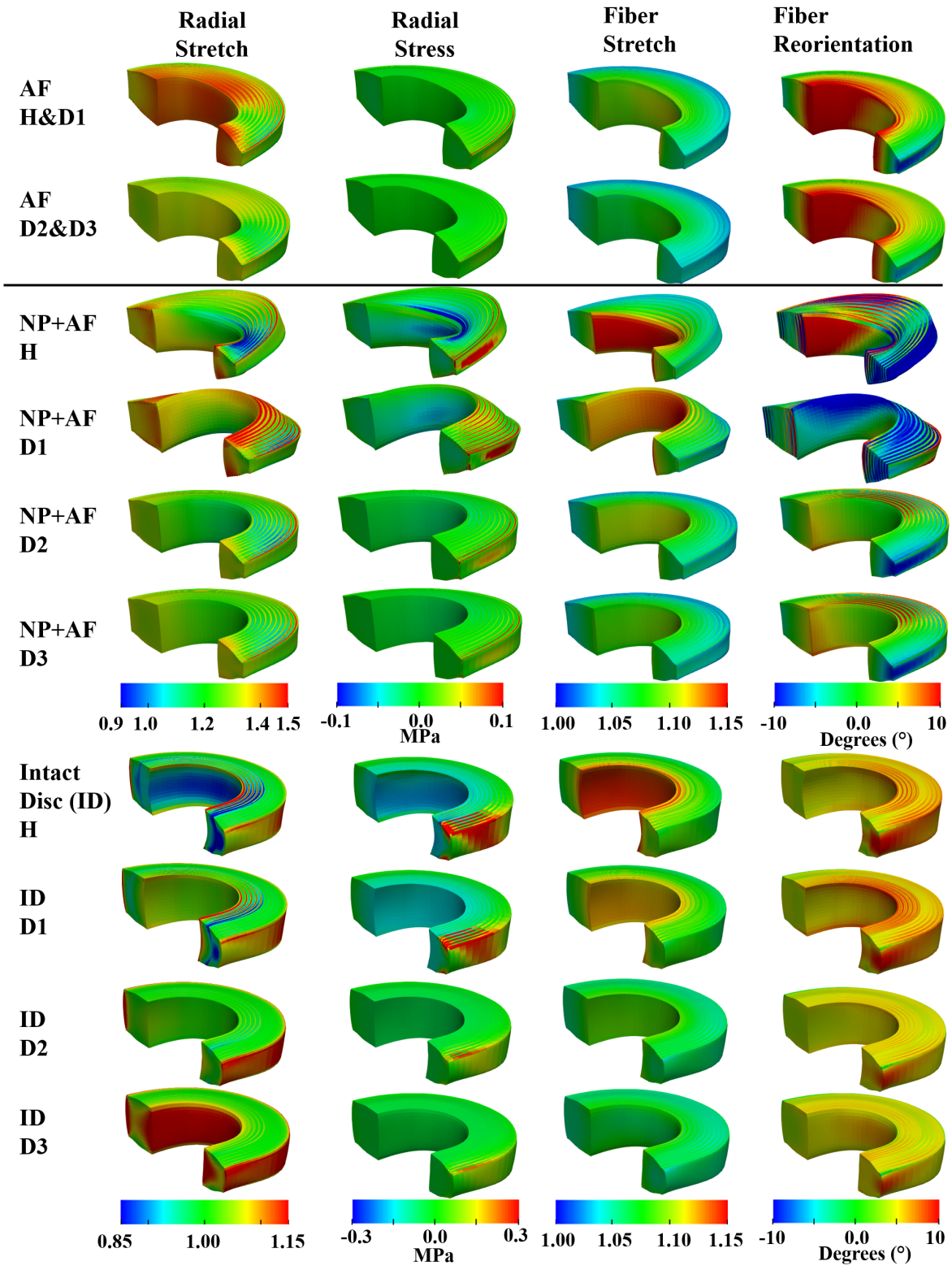


Figure 7.9: Stretch and stress in the radial directions, fiber stretch, and fiber reorientation. In the last column, a positive value represents fiber reorientation toward axial direction, while negative value represents fiber reorientation toward the transverse plane. Data shown for AF ring, NP + AF, and Intact Disc models at healthy status (H) and degenerated level 1-3 statuses (D1-D3).

### Fiber stretch and reorientation

Fibers stretch was greatest in the inner AF and decreased linearly throughout the AF, regardless of boundary constraints (max fiber stretch = 1.14; Figures 7.9 - $3^{rd}$ column and Figure 7.10a). Fiber deformation decreased by 20-50% with degeneration in the Intact Disc models (Figure 7.10a - *e.g.*, black lines: circles versus diamonds). In AF-only models, fibers in the inner AF reoriented toward the axial direction (positive fiber reorientation), while fibers in the anterior and posterior regions of the outer AF reoriented toward the transverse plane (Figures 7.9 - $4^{th}$ column, $1^{st}$ & $2^{nd}$ rows and Figure 7.10b red lines). Inclusion of the NP decreased fiber reorientation in the inner AF by 50% (Figure 7.10b - grey lines versus red lines). Tissue twisting in Healthy and D1 NP+AF models resulted in negative fiber reorientation in outer layers (Figures 7.9 - $4^{th}$ column, $3^{rd}$ & $4^{th}$ rows and Figure 7.10b - grey lines with circles or squares). Fiber reorientation in the Intact Disc models was consistent throughout the AF, with a 5o reorientation towards the axial plane (Figure 7.10b - black lines). Lastly, fiber reorientation in the posterior region was greater than fiber reorientation in the anterior region (Figure 7.9 - $4^{th}$ column, $7^{th}$ - $10^{th}$ rows).

## 7.4 Discussion

Residual stress are thought to drive tissue remodeling by altering the stresses and strains experienced by cells within the tissue [24]. While our simulations are presented in the order of increasing boundary constraints, the opposite approach is conducted in the laboratory, where intact discs are dissected into tissue explants for analysis. For intact discs, we observed a tradeoff between NP and AF swelling. That is, as the NP swelling capacity decreased with NP GAG loss as observed in early to moderate degeneration, the *in situ* AF swelling capacity increased, which acted to maintain residual strain homeostasis throughout the AF and overall disc swelling capacity. Removing the disc from surrounding endplates results in a 20-50% increase in NP swelling, depending on degeneration, with an additional ∼10% increase in NP volume when the tissue was separated from the AF (Figure 7.3). The overall 30% increase in AF volume and 60% increase in NP volume from the intact disc model to the explant model agreed well with experimental values in the literature [125, 22].

Previous experimental and computational studies showed that residual stresses and

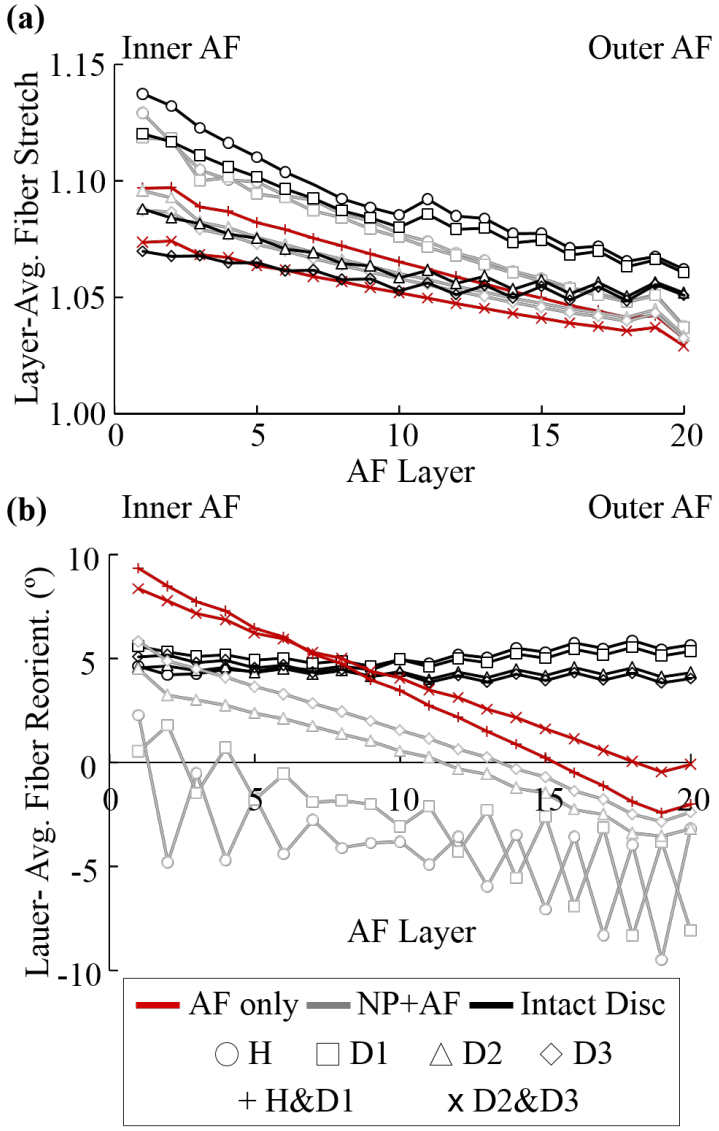


Figure 7.10: Layer-averaged (**a**) fiber stretch and (**b**) fiber reorientation for each annulus layer. A positive value represents fiber reorientation toward axial direction, while negative value represents fiber reorientation toward the transverse plane. Black, grey, and red lines represent AF layers in the AF ring, NP+AF, and Intact Disc models, respectively. Circles represent Healthy (H) models; rectangles represent degenerated level 1 models (D1); triangles represent degenerated level 2 models (D2); rhombuses represent models in degenerated level 3 models (D3).

strains in the AF transition from being compressive in the inner AF to tensile in the outer AF [5, 40, 39]. Researchers have quantified residual strains in cardiovascular tissues and their role in healthy and disease mechanics since the 1980s [42, 24, 232]. In cardiovascular tissues, the osmotic differential due to negatively charged proteoglycans causes formation of residual strains throughout the vessel wall, and these strains are important for maintaining homeostatic stress once an internal pressure (i.e., blood pressure) is applied [23, 233, 234]. Similarly, results from this study demonstrate that NP pressure acts to establish a homeostatic strain profile throughout the AF. However, there are differences in mechanical homeostasis between cardiovascular tissues and the AF, as residual stresses varied throughout the AF and depended on degeneration.

Swelling in AF-only models resulted in an inhomogeneous distribution of circumferential-direction stretch, where residual strains were compressive in the inner AF and tensile in the outer, which agreed with findings in bovine discs [39]. The radial difference in circumferential-direction residual stretch has been believed to be important for maintaining uniform stretch throughout the wall during physiological loading [5, 39, 40, 43]. This notion was partially supported by our findings, where circumferential, axial, and, to some extent, radial-direction strains were homogenous throughout the AF in the intact disc model (Figure 7.8a, c, e –black lines). However, homogenous distribution in residual stretch was not related to a homogenous distribution in stress, where residual circumferential and axial stresses were greater in the outer AF (Figure 7.8b&d). The difference between inner and outer AF residual stresses are likely due to the lack of a cartilaginous endplate over the outer AF, which ended at Layer 10 in the intact disc model, and restricted fluid flow diffusion from the surrounding environment into the disc.

Degeneration was largely simulated as changes in GAG composition in the NP and inner AF, based on quantitative magnetic resonance studies that have shown early detection in water and GAG composition in the NP prior to drastic morphologic changes with degeneration [235, 236]. Changes in tissue composition resulted in large changes in residual stretch in the inner AF (Figure 7.8a & e), due to swelling-based interactions between the NP and AF. That is, a decrease in NP swelling capacity allowed for additional swelling of the inner AF (Figure 7.5 - black rectangles versus circles).The great change in residual strains in the inner AF occurred with early degeneration, where strains decreased by over 60% (stretch = 1.06 to stretch = 1.02). Recent work with tissue engineered AF tissues showed that a

decrease in tensile strains increases apoptosis [237], which suggests that a decrease in tensile residual strains in the inner AF due to a decrease in NP GAGs may initiate or accelerate degenerative remodeling at the NP-AF interface.

Many studies have reported decreases in NP GAG content, water content, and intradiscal pressure occurring concurrently with degeneration [15, 19, 48, 139, 231]. This study, for the first time, demonstrated a quadratic relationship between NP pressure and NP swelling capacity (Figure 7.6c), suggesting that decreases in NP swelling capacity will result in much larger changes in NP pressure. These findings highlight the importance of biological NP repair strategies to replicate NP swelling capability or internal pressure [91, 141, 142, 238]. Moreover, restoring NP swelling capacity will act to ensure adequate strains are applied to the inner AF.

The majority of finite element models of the disc alter material properties, such as material stiffness, to simulate disc degeneration [1, 2, 65, 68]. However, these findings demonstrate that triphasic mixture theory can be used to simulate biochemical changes with degeneration that lead to commonly observed morphological changes in degenerated discs. In this study, our severe degeneration model only simulated changes in biochemical composition and did not simulate geometric changes, such as a loss in disc height. Regardless, our model showed that a decrease in GAG content in the NP and inner AF caused inward bulging of the inner AF, while maintaining a outward bulging of the disc boundary, and showed a relative decrease in disc height growth from swelling (∼40% decrease; Figure 7.3e –H versus D3). These findings are important for understanding changes with severe degeneration, which has been noted with inward bulging of the inner AF, increased outward bulging of the disc boundary, and a decrease in disc height [9, 239]. Moreover, the shift in radial displacements with degeneration may contribute to the increase in radial tears with age and degeneration [52, 53, 239].

As mentioned above, free swelling of the intact disc resulted in an increase in disc height (Figure 7.3e), which agrees with the change in patient height after diurnal loading [240, 241]. Swelling induced increases in disc height, whether from bed rest or extended bed rest, causes fibers to reorient towards the axial plane (Figure 7.10b). Our previous work showed that discs with fibers oriented closer to the axial-direction are stiffer under torsional loading and have greater maximum shear strains near the bone-disc interface [1]. Disc herniations have been shown to occur as failure of AF tissue or of the AF-bony interface (∼50:50 split between

two failure types) [121, 122]. Taken together, these findings suggest that over-hydrated discs (*e.g.*, discs in the morning or after extended bed rest) may be more vulnerable to failure at the bone-disc interface, which agrees with the 3-fold increase disc herniation rates for astronauts returning to Earth [242, 243, 244].

Disc herniation due to mechanical overload most often occurs in lumbar discs of patients aged 30-40 years [48, 245, 246]. Furthermore, disc injury and herniations primarily occur in the posterior-lateral AF [121, 122, 138]. In the Intact Disc models, residual stresses and strains were highest in the posterior AF (Figures 7.6 & 7.8), which was likely due to the kidney bean shape of human discs. Moreover, NP centroid is position posteriorly to the disc centroid [11], resulting in larger stresses in the posterior AF during extension [3], compared to a disc designed with the NP located more anteriorly (*e.g.*, biological disc replacements) [141, 142]. Thus, large mechanical loads, lordosis of the lumbar spine, the kidney bean shape of the intervertebral disc, and the posterior position of the NP all contribute to greater risks of annular failure or herniation occurring in the posterior AF.

This study is not without its limitations. Although layer dependent fiber stiffness and fiber orientation were considered, regional differences were not included in the current model. That is, single lamellae testing showed that the anterior AF is stiffer than the posterior AF, which would suggest that the posterior AF would experience greater strains than predicted here [27, 28]. As mentioned above, we only varied GAG content to simulated degeneration, which provided excellent agreement with laboratory observations, but changes in tissue structure (*e.g.* height and AF layer thickness) and composition (*e.g.*, collagen cross linking) may impact disc swelling behavior [6, 13, 48, 164]. Lastly, only one motion segment was included in the model, without posterior elements; therefore, the effects of spine curvature and other restrictions on disc deformation (*e.g.*, spinal ligaments) were not considered.

The NP and AF are tissues with an excellent swelling capacity. NP and AF swelling is greatly constricted *in situ* due to boundary constraints of the surrounding soft and hard tissues in the disc joint. In conclusion, we showed that restriction of NP swelling capacity resulted in large intradiscal pressures in the healthy disc (average = 0.21 MPa). Moreover, *in situ* boundary conditions resulted in near-homogeneous residual strain distributions throughout the AF, regardless of GAG loss in the NP and inner AF with degeneration. Moreover, preservation of residual strain throughout the AF was coupled with minimum residual stresses in the inner AF. In conclusion, findings from this study demonstrate the

need to replicate NP swelling capacity in NP replacement strategies to prevent degradation and remodeling of the inner AF.

# Chapter 8

# Direct Quantification of Intervertebral Disc Water Content Using Magnetic Resonance Imaging [7]

## Abstract

Water content in nucleus pulposus (NP) and annulus fibrosus (AF) decrease greatly with aging and degeneration (over 10%) resulting in altered disc joint mechanics. Water content is also a key parameter in disc computational models to simulate swelling behavior as well as nutrition transportation. Therefore, accurately measuring disc water content is important to develop accurate patient specific disc model and to detect disc early degeneration. Currently, measuring tissue water content is dependent on destructive techniques (e.g., lyophilization), therefore, is limited to *ex situ* tissues. Alternatively, magnetic resonance imaging (MRI) has been used to estimate disc water content and detect early degeneration, as signal intensity depends on the proton density within the tissue. However, MRI signal intensity is dependent on scan-parameters, the concentration of free water molecules, and collagen fiber content and architecture. Therefore, how accurately MRI can quantify NP and AF water content is unclear. The objective of this study was to directly measure disc tissue water content using MRI. NP and AF water contents were measured noninvasively using T2 relaxation imaging and compared with traditional techniques. Experimental results showed that water

content measured by using MRI correlated well with traditional method for both NP and AF. There was an excellent agreement between water contents measured through MRI and lyophilization for NP. However, normalizing spin density by mass density underestimated the AF GWC. This discrepancy is likely due to a higher concentration of bound water molecules in the AF, compared to the NP. Where tightly bounded water molecules have too short T2 values to be detected in MR imaging

## 8.1 Introduction

The intervertebral disc is consists of the nucleus pulposus (NP) surrounded by the annulus fibrosus (AF), and is comprised primarily of water (80-85% in the healthy NP, decreasing to ∼65% in the outer AF) [15, 16, 17, 18]. Aging and degeneration have been noted by a continuous decrease in NP water content (70-75% with severe degeneration), resulting in altered disc joint mechanics during loading and unloaded recovery [15, 17, 35, 55, 56]. Detecting early changes in tissue composition is important for developing preventative medicine strategies for injury or degeneration. Previous studies showed that parameters from noninvasive measurement techniques, such as $T_2$- or $T_{1\rho}$-weighted magnetic resonance (MR) imaging, are strongly correlated with NP water and GAG contents, respectively, and can be used to detect early degeneration [75, 76]). However, those studies have largely relied on correlations to biochemical composition and not direct measurements of water content, which is an important parameter for computational models that simulate tissue swelling or nutrient diffusion [4, 5, 6, 38, 66, 247].

Currently, water content measurements are dependent on destructive techniques (*e.g.*, lyophilization) and, therefore, limited to *ex situ* tissues [15, 16, 17]. Alternatively, signal intensity from MR images has been used to estimate tissue water content, as signal intensity depends on proton density within the tissue [247, 248, 249, 250]. However, the MRI measurements were not validated versus traditional method. Unfortunately, the MRI approach is limited due to MR signal intensity being dependent on scan-parameters and the concentration of free water molecules in the tissue. Further difficulties in directly measuring water content may occur for tissues with a higher concentration of bound water molecules (*e.g.*, ∼3% of water in the NP and ∼10% of water in the AF) [77], because bound water molecules

have a short T2 time and do not appear in MR images [78].

Thus, it is not clear whether MR imaging can be used to accurately quantify NP and AF water content noninvasively. The objective of this study was to directly measure water content of disc tissues (NP and AF tissues) using T2-weighted MR images. MR based water content measurements were compared with traditional biochemical assays (DMMB). Tissue water content was altered through compression loading, where mechanical loading forced fluid to flow out of the disc.

## 8.2 Method

### Sample preparation

Skeletally mature bovine caudal spine sections were obtained from a local abattoir (age 18-24 months). Bone-disc-bone motion segments were prepared by removing surrounding musculature and cutting through the superior and inferior vertebra (n = 20) to create parallel surfaces for mechanical loading based dehydration. Motion segments were stored fresh-frozen at -20°C before imaging. Specimens were thawed and hydrated in 0.15 M phosphate-buffered saline (150 mmol/L 1x PBS) for 24 hours in a refrigerator (4°C) and equilibrated to room temperature for one hour prior to imaging.

### MR imaging and analysis

To calculate tissue spin density, T2 relaxation of deionized gadolinium water, which has a known VWC, served as a reference phantom. First, preliminary work was performed to determine the appropriate gadolinium concentration to match T2 relaxation times of biological tissues (Table 8.1). Based on these findings a 2.0 ml tube of 2.5 mmol/L gadolinium water (T2 relaxation time = 62 msec) was chosen and imaged next to all disc specimens (Figure 8.1a) [251]. Before scanning, disc samples were placed into a custom-built compression device made of non-magnetic materials in order to maintain mechanical dehydration during imaging (Figure 8.1a). Images were first acquired without a compressive load.

Each sample was first imaged using a 3D Fast Low Angle Shot (FLASH) sequence for 3D geometric imaging (7T Bruker MRI machine; FOV = 3.2 X 3.2 X 2.8 cm, 64 slices, in-plane

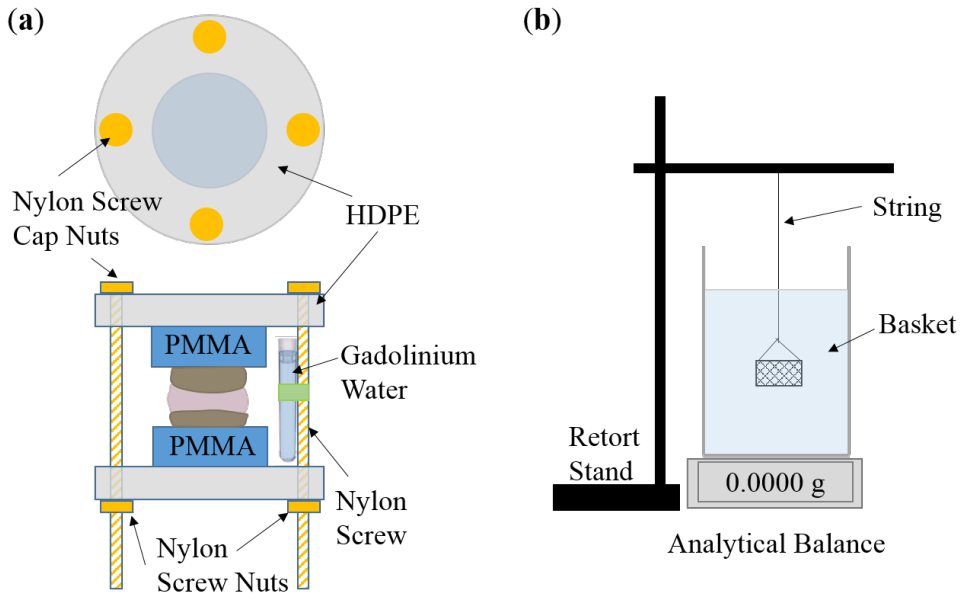


Figure 8.1: (**a**) Custom-built plastic mechanical compressor used to compress a bone-disc-bone sample with a 2.0 ml tube gadolinium water (2.5 mmol/L) aside. The mechanical compressor has two high-density polyethylene (HDPE) discs, which can be tightened by 4 nylon screws and nuts. Two poly (methyl methacrylate) (PMMA) plates were put between disc joint and HDPE discs to ensure enough space for the tube. (**b**) A device used to measure tissue an explant volume. It consists of a retort stand and a string that connects a basket submerged in a beaker with deionized water on an analytical balance [252].

Table 8.1: T2 values of gadolinium water at different concentrations measured in 7T Bruker MRI machine (185 data points for each concentration).

| Gadolinium Concentration (mmol/L) | 0 | 0.5 | 1 | 2.5 | 5 |
|---|---|---|---|---|---|
| T2 (ms) | 1333 | 341 | 201 | 62 | 38 |
| Mean ± Std | ±89 | ±7 | ±8 | ±1 | ±1 |

resolution = 0.25 mm/pixel, slice thickness = 0.4375 mm/pixel). Then, a 2D transverse image was acquired at the mid-disc height using a T2 Rapid Imaging with Refocused Echoes (RARE) sequence, which was used to calculate T2 relaxation times (Echo times, TE = 7, 21, 35, 49, and 63 msec, FOV = 5 X 5 X 0.12 cm, slice thickness = 1.2 mm, in-plane resolution = 0.3906 mm/pixel). The repetition time (TR) was set to 8 seconds to allow for full relaxation from both the gadolinium water and disc specimens (Table 8.1) [253].

Then, samples were compressed in compression device that applied a fixed displacement by fastening four screws. Samples were mechanically dehydrated in a saline bath for 24-hours at 4°C. Applied displacements were randomized to create scatter in the amount of water forced out of the disc during loading. After loading, samples were equilibrated to room temperature for one hour prior to MR imaging, using the same protocol described above. Five samples were not subjected to the mechanical compression and the second set of scans represented discs in a fully hydrated condition. Image sequences reconstructed to evaluate changes in disc volume (v), maximum transverse cross-section area ($s_m$), and height (h), defined to be volume/maximum transverse cross-section area.

Gravimetric water content (GWC), defined as water mass divided by tissue mass ((wet –dry) / wet), is related to volumetric water content (volume fraction, VWC) through tissue and water mass densities ($\rho$, $\rho_{water} = 1\text{g}/cm^3$, Equation 1). Although GWC is widely used to report water content, MR signal intensity (SI) is directly correlated with VWC or spin density (SI(echo time = 0) $\propto$ VWC). T2 relaxation times were calculated on a pixel-by-pixel basis by curve fitting the signal intensity measured at each echo time (Equation 2; ***fit*** function in Matlab 2018a, MathWorks Natick MA)). Results from the curve-fitting process resulted in the T2 time, which is commonly reported as T2-relaxation time, and SI0, which represents the y-intercept (Equation 2, TE: echo time; relaxation rate R2 = 1/T2) [37]. However, tissue mass density is required to directly compare MR-based water content measurement with traditional techniques (GWV). Lastly, spin density (SD) was calculated by normalizing tissue $SI_0$ by $SI_0$ of gadolinium water. NP and AF regions of interest were selected (6mm in diameter) to calculate the average SD, T2, and R2 value in each region.

$$GWC = \frac{V_{water}\rho_{water}}{V_{tissue}\rho_{tissue}} = VWC\frac{\rho_{water}}{\rho_{tissue}} = \frac{VWC}{\rho_{tissue}} \tag{8.1}$$

$$SI = SI_0 exp^{-\frac{TE}{T2}} \tag{8.2}$$

## Biochemistry

After imaging, samples were unloaded and removed from the compression device. A mid-transverse section of the disc was prepared using a scalpel (1-2 mm thickness). NP and AF explants were acquired using a 6 mm diameter biopsy punch (Miltex Inc). Explant wet mass ('wet-mass') was measured on an analytical balance (0.1 mg readability, Mettler-Toledo Inc.). Then, tissue volume was calculated by measuring volume displacements according to Archimedes' principle [252]. Briefly, a beaker with deionized water was placed on the balance, and specimens were placed in a porous basket that hung into the water-filled beaker (Figure 8.1b). Placing a specimen in the basket caused the water surface to elevate, and the displacement of the explant within the bath was related to its buoyancy. Thus, the change in the readout from the balance reflected tissue weight supported by the water, while the remaining tissue weight was supported by the string connected to the basket (Figure 8.1b). Tissue mass density was calculated as the wet-mass divided by tissue volume.

Explants were lyophilized for 48 hours to obtain the dry mass of the tissue (Labconco FreeZone). As mentioned above, gravimetric water content (GWC) was calculated as water mass divided by tissue mass ((wet –dry) / wet). Dried samples were digested overnight with proteinase K at 56°C (∼16 hours). Total GAG content was determined using the 1, 9 dimethyl-methylene blue (DMMB) assay. GAG contents were normalized by dry weight.

## Statistics

SD and SD normalized by mass density were correlated with GWC. Mass density, R2, and GAG content were correlated with GWC and spin density. All correlations were evaluated using Pearson's correlation to determine the strength of the correlation, $\rho$, and the statistical significance of the correlation (p). A weak correlation was defined as $\rho < 0.5$, a moderate correlation was defined as $0.5 \leq \rho < 0.7$ and $\rho \geqslant 0.7$ was considered a strong correlation. Significance was assumed for $p \leq 0.05$. Means and standard deviations of tissue GWC, mass density, spin density, and T2 relaxation time were calculated for NP and AF for fully hydrated discs and discs after mechanical dehydration. Paired-sample t-test or unpaired-sample t-test analysis (***ttest*** or ***ttest2*** function in Matlab 2018a, MathWorks Natick MA) was conducted to determine the significance of the differences in these result

values due to different locations (NP versus AF) or loading statuses (fully swelled versus mechanically dehydrated). Significance was assumed for $p \leq 0.05$.

## 8.3 Result

Three samples were excluded due to damages in the NP (e.g., blood in the disc from a fractured endplate), which was first evident as abnormal MR images and confirmed during dissection. Reconstructed 3D volumes showed a decrease in disc height (20% ± 10%, range: -1.0% to 33.5%) and volume (10% ± 6%, range: 0.6% to 18.3%) and an increase in maximum cross-section area (16.3% ± 7%, range: -1.5% to 23.7%) after dehydration (Figure 8.2a). MRI signal intensity decayed with echo time, as expected, and the decay in signal intensity was more pronounced for dehydrated samples (Figure 8.2b –left versus right column). T2 relaxation time (Figure 8.2c) and spin density (Figure 8.2d) were greatest in the center of the disc (NP region) and decreased radially to the outer AF. Both values decreased with mechanical dehydration (Figure 8.2c & 8.2d).

Mechanical compression successfully dehydrated disc samples and generated a wide range of NP GWCs in healthy discs (range = 0.69 - 0.84). There was a strong correlation between MR spin density in the NP and GWC ($\rho = 0.93$; $p < 0.001$; Figure 8.3a- open circles), but NP spin density values were consistently greater than NP GWC (Figure 8.3a- open circles versus y=x line). Moreover, the slope of the linear model was 0.68, which was much less than 1.0.

Normalizing SD by the mass density $\rho$_tissue resulted in a near perfect match with GWC (slope = 1.02, $\rho = 0.95$, $p < 0.001$; Figure 8.3a-black dots versus y=x line). NP mass density ranged between 1.07 and 1.17 g/cm$^3$, and NP mass density was negatively correlated with NP GWC and SD ($\rho > 0.8$, $p < 0.001$; Figure 8.3c). Similarly, NP relaxation rate (R2) was negatively correlated with both GWC and spin density ($\rho > 0.86$; $p < 0.001$; Figure 8.3c & 3e). NP T2 values (1/R2) (44 –105 ms) increased with GWC and SD, as expected. NP GAG content was 38.6 ± 7.9% by dry weight (range = 24.2 –48.9%/ dry weight). There was a moderate negative correlation between NP GWC and NP GAG content ($\rho = 0.54$; $p = 0.03$; Figure 8.4a). There was also a weak, but significant, positive correlation between NP mass density and NP GAG content ($\rho = 0.4954$; $p = 0.0304$; Figure 8.4b). There was

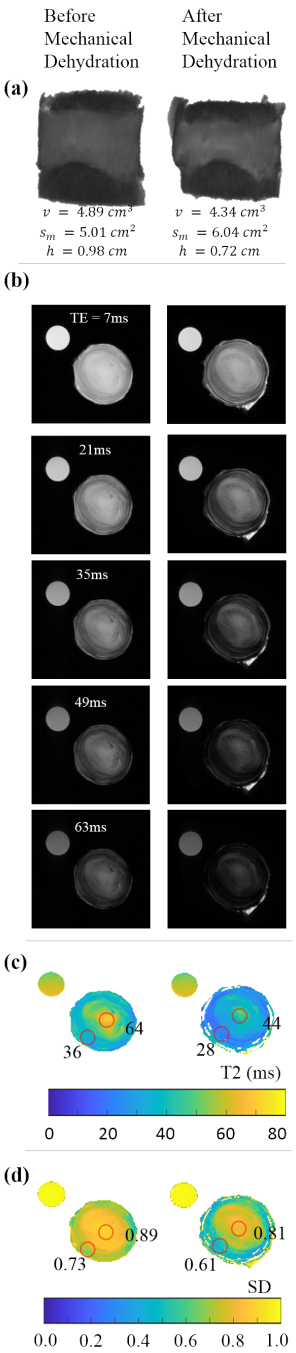


Figure 8.2: Representative sample before (left column) and after mechanical dehydration (right column): (**a**) 3D volume reconstruction showing a 26.6% decrease in disc height and a 20.6% increase in maximum transverse cross-section area (i.e. ∼9.5% radial bulge), which resulted in an 11.2% decrease in disc volume. (**b**) T2 relaxation sequences with gadolinium water used as a phantom control. (**c**) T2 relaxation time and (**d**) spin density (SD) maps of the mid-transverse plane. In (**c**) and (**d**), red circles represent regions of interest for the NP and AF, which were compared to biochemical assays (6mm in diameter).

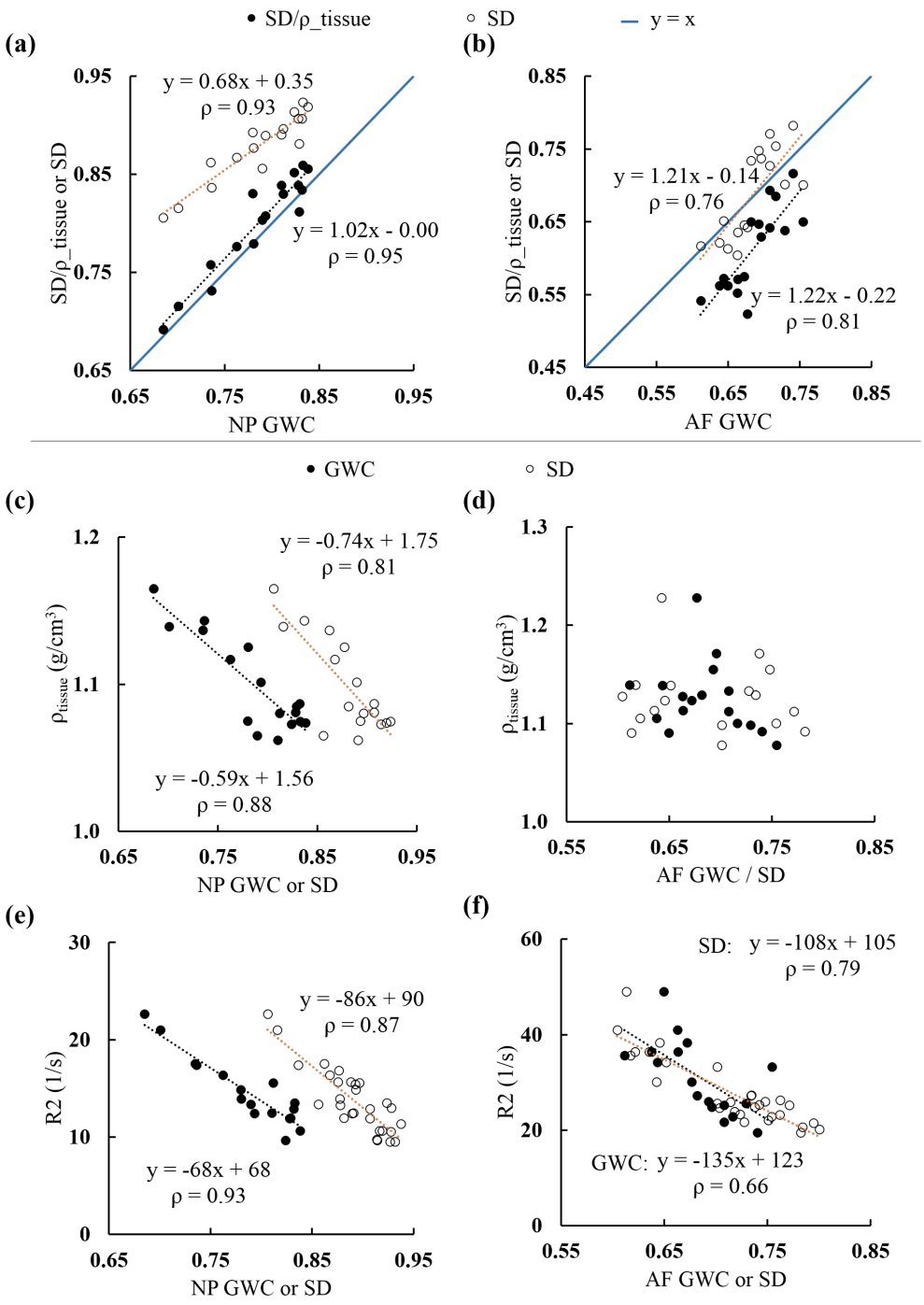


Figure 8.3: Experimental results of NP (1st column) and AF (2nd column): (**a** & **b**) Spin density (SD) and SD normalized by mass density ($\rho$_tissue) versus gravimetric water content (GWC). (**c** & **d**) Mass density versus GWC and SD. (**e** & **f**) R2 versus GWC and SD. (**a**) and (**b**) share the same legend, while (**c**)-(**f**) shared the same legend. P-values were smaller than 0.005 for all linear regression models shown in (**a**)-(**c**), (**e**), and (**f**). There was no correlation between AF mass density and AF GWC ($p > 0.2$).

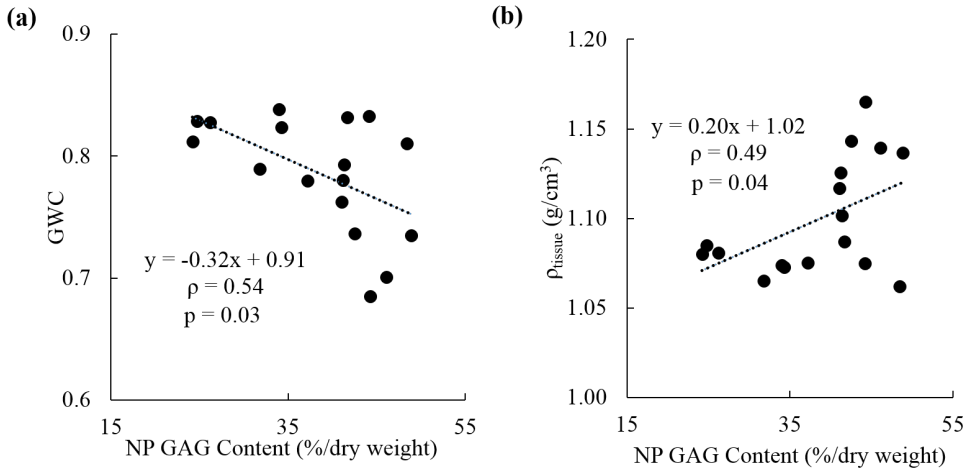


Figure 8.4: (**a**) A moderate negative correlation was observed between gravimetric water content (GWC) and NP GAG content ($\rho = 0.54$; p = 0.03). (**b**) A weak positive correlation was observed between mass density ($\rho$_tissue) and NP GAG content ($\rho = 0.49$; p = 0.04).

no correlation between NP GAG content and spin density or R2 (p > 0.1).

Similar to the NP, there was a strong positive correlation between AF SD and AF GWC, (range for both values = 0.60 –0.78; $\rho = 0.76$, p < 0.001; Figure 8.3b –open circles). AF SD measured from MR images had a near perfect agreement with AF GWC (Figure 8.3b –open circles versus y=x line); therefore, normalizing AF SD by mass density resulted in values that were lower than AF GWC ($\rho = 0.81$, p < 0.001; Figure 8.3b –black dots versus y=x line). AF mass density ranged between 1.08 and 1.23 g/cm$^3$, and, unlike the NP, there was no correlation between AF mass density and GWC or spin density (p > 0.2, Figure 8.3d). AF relaxation values (R2) were approximately 2X greater than NP R2 values (Figure 8.3e & 8.3f). There was a strong negative correlation between AF R2 and AF SD ($\rho = 0.89$, p < 0.001; Figure 8.3f –black dots). Similarly, there was a negative moderate correlation between AF R2 and AF GWC ($\rho = 0.66$, p < 0.005; Figure 8.3f –open circles). AF GAG content was 60% lower than the NP (14.7 ± 5.4%/ dry weight). There were no significant correlations between AF GAG content and GWC, mass density, spin density, or R2 (p > 0.1).

In fully swelled or over hydrated discs (*i.e.*, 5 samples with no mechanical dehydration applied), NP had 15% higher GWC than AF (83% ± 0.4% vs 72% ± 1.8% , p < 0.001 from paired t-test) (Figure 8.5a). The difference of mass density between NP and AF was not significant based on the results of 5 samples ((1.08 ± 1.006 versus 1.11 ± 0.026 g/cm$^3$, p

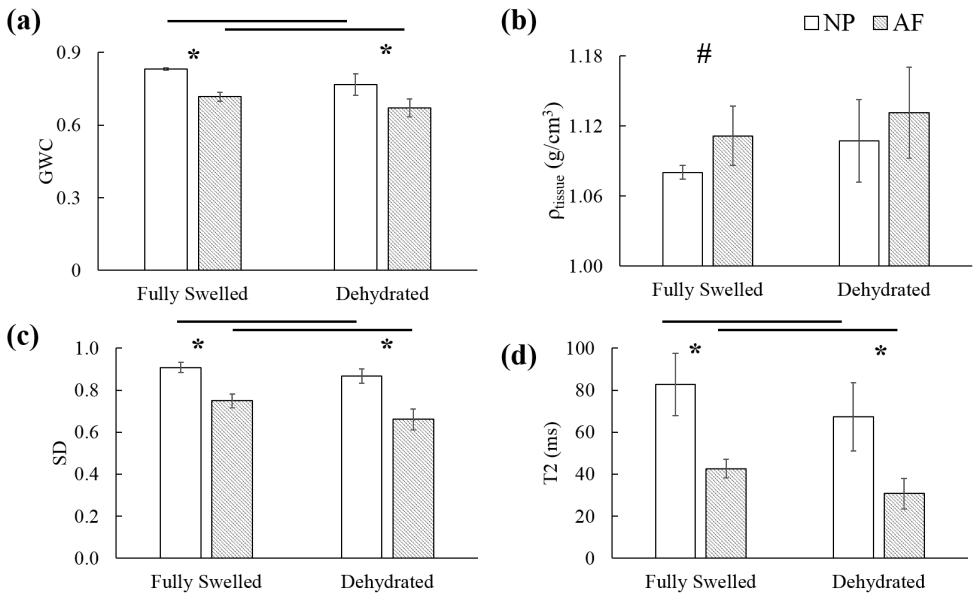


Figure 8.5: Results of NP and AF in fully swelled and mechanically dehydrated discs including mean and standard variation (error bar) of: (**a**) gravitational water content (GWC), (**b**) mass density ($\rho$_tissue), (**c**) spin density (SD), and (**d**) T2 values. Means and standard deviations of GWC and mass density for fully swelled discs were calculated from 5 samples that did not undergo mechanical compression. Means and standard deviations of GWC and mass density for mechanically dehydrated discs were calculated from 12 samples that underwent mechanical compression. Means and standard variations of SD and T2 were calculated based on all 17 samples. *($p < 0.01$) and # ($p = 0.07$) between NP and AF; "-" ($p < 0.05$) between fully swelled and mechanically dehydrated samples.

$= 0.07$ from paired t-test) (Figure 8.5b). All samples ($n = 17$) were scanned at their fully swelled status, which showed 20% higher spin density in NP than in the AF ($0.91 \pm 0.02$ vs $0.75 \pm 0.03$, $p < 0.001$ from paired t-test) (Figure 8.5c), while T2 value in NP was twice that in AF ($84 \pm 14$ vs $42 \pm 4$ ms, $p < 0.001$ from paired t-test) (Figure 8.5d).

Mechanical dehydration significantly decreased NP GWC by 7.8% ($p < 0.01$ from unpaired t-test), SD by 4.5% ($p < 0.001$ from paired t-test), and T2 by 18.5% ($p < 0.01$ from paired t-test) (Figure 8.5a, c, and d). AF GWC, SD and T2 values were also decreased significantly by 6.4%, 11.8%, and 27.6%, respectively, after compressive loading ($p \leqslant 0.05$ from paired t-test) (Figure 8.5c & 8.5d). The effects of mechanical loading on NP and AF mass densities were not significant ($p > 0.05$ from unpaired t-test) (Figure 8.5a & 8.5b).

## 8.4 Discussion

Experimental results showed that normalizing NP spin density by mass density provided an excellent agreement between MR measured water content and water content measured through lyophilization (Figure 8.3a –black dash line). However, normalizing spin density by mass density underestimated AF GWC (Figure 8.3b –black dash line). This discrepancy is likely due to a higher concentration of bound water molecules in the AF, compared to the NP (∼3% in NP and ∼10% in AF) [77], where tightly bounded water molecules have too short T2 values to be detected in MR imaging [254].

Direct measurements of tissue water content are largely limited to destructive methods that require drying out tissue explants [15, 16, 17, 18]. Fast measurements of water content with a high resolution, on the order of minutes (vs. days) and half of a millimeter (vs several millimeters), using noninvasive techniques is valuable for tracking tissue hydration with loading, disease progression, or biological repair, as tissue hydration affects joint-level mechanics. Quantitative MR parameters, such as T2 or $T_{1\rho}$ relaxation times, were strongly correlated with glycosaminoglycan or water content and used to detect disc degeneration [76, 75, 250]. However, these parameters are not direct measurement of water content, which is a important parameter to develop accurate disc computational models [4, 5, 6, 38, 66, 247].

To the best of our knowledge, this is the first study to report disc tissue mass density. In addition, NP mass density decreased with an increase in water content, but was always greater than 1.0, resulting in spin density values that were consistently larger than GWC. Direct measuring water content using MRI have been demonstrated to work well on other homogenous soft tissue, such as brain and articular cartilage [255, 256]. However these studies either did not consider the correction of mass density or assumed a large constant mass density (1.37 g/ml for cartilage). In a supplement experiment of this study, fresh bovine knee cartilage mass density was measured to be 1.10 ± 0.02 g/ml at ∼80% water content (5 samples).

Measurements of the current study showed a good agreement with previous studies. GWC and GAG contents measured for bovine caudal disc matched previous experimental measurements for human samples (Figures 8.4a & 8.5a)[15, 16, 17, 18]. Mechanical loading decreased the disc volume by up to ∼18%, which also agreed with the dehydration due to long standing in human disc [36, 37]. In addition, T2 value measured for the disc tissue also

agreed with the value reported in the literature (Figure 8.5d) [257, 258].

The current study has its limitations. Mechanical compression and imaging were conducted on healthy bovine discs, which, compared to the degenerated disc, has less NP collagen content [17]. In degenerated disc, bonded water content may increase with collagen content decreasing water visibility in NP. In addition, current imaging was taken in a strong magnetic field (7T), T2 value increases as the field strength decreases [259]. Besides, previous studied showed good correlation between GAG distribution and water content distribution [15, 16, 17, 18], while the current study showed a week correlation between NP GAG content and NP water content and no correlation between AF GAG content and AF water content (Figure 8.4a). This discrepancy may be caused by the separated analyses for NP and AF in the current study.

In conclusion, normalizing quantitative MR parameters with mass density or using the empirical formula (GWC vs SD in Figure. 8.3a & 8.3b) allow for noninvasive measurements of NP and AF water content.

# Chapter 9

# Discussion

There were three motivations in this research. The first motivation was to understand the effect of disc structural changes on disc mechanics including collagen fiber reorientation, changes in NP size and position, and nucleotomy. The second motivation was to study disc fiber-reinforced tissue swelling and swelling-based residual stress/strain/pressure formations. The third motivation was to accurately measure disc water content using non-invasive quantitative MRI method.

## 9.1 Effects of disc structural changes

For the first motivation, we conducted three studies using the finite element method with a hyperelastic material description.

First, we evaluated the relationship between fiber angle orientation and disc joint mechanics under axial compression combined with rotation, because data in the literature noted a decrease in torsional stiffness that was not explained by degenerative changes in material properties. We developed and validated a FEM of the human lumbar disc based on averaged disc geometry reported in the literature [112]. Then, we altered the AF collagen fiber orientation within the range of values reported for human lumbar discs [12]. Discs with collagen fibers oriented closer to the horizontal plane experienced a decrease in AF stresses, NP pressure, and torsional stiffness. The simulation results demonstrate that fiber orientation plays a crucial role in disc mechanics, and the fiber structure used in a FEM must be selected

appropriately to understand the structure-function relationship in the disc.

Secondly, we modified the finite element model of the human lumbar disc joint and further validated it under axial compression followed by bending [1]. Then, the relative NP size was varied in a range of values reported in experimental and computational studies (0.21 –0.60) to evaluate its effects on joint-level mechanics, intradiscal deformations, and internal pressure. We also evaluated the effects of NP centroid location, relative to the disc's centroid. Model simulations showed that NP size had a significant impact on compressive stiffness, intradiscal pressure, and principal strain. The location of the NP centroid within the disc space had a significant impact on the magnitude and distribution of intradiscal pressure in flexion and extension. Simulations indicate that NP geometry and location are important factors for developing accurate computational models to study the mechanical behavior of native, injured, or degenerated discs and for creating a tissue-engineered disc.

Thirdly, we modified our finite element model of the human lumbar disc (Control model) to create a Nucleotomy model by completely removing the NP [2]. Joint-level mechanics and internal stress/strain distributions were compared between Control and Nucleotomy models under various loading conditions to evaluate the effects of nucleotomy on disc mechanics. Specifically, we evaluated the effects under single (compression-only or bending-only) versus dual loading (torsion, flexion, extension, or lateral bending was applied after compression). Simulation results showed that the effects of nucleotomy on disc mechanics differed between single and more complex loading modalities. Under single loading conditions disc joint stiffness decreased with nucleotomy, agreeing with previous experimental and computational studies [30, 88, 89, 91, 117, 166]. However, more complex loading conditions resulted in an increase in bending stiffness, suggesting that the disc is more resistant to bending after nucleotomy. An increase in bending stiffness corresponds to a decrease in disc joint range of motion, agreeing with a recent *in vivo* study that reported decreased joint flexibility after nucleotomy [166]. The discrepancy between single- and dual-loading conditions highlights the importance of evaluating disc joint mechanics under conditions that more closely represent *in situ* loading, which will be important for elucidating mechanisms for disc joint failure [152, 158].

## 9.2 Swelling and residual stress/strain/pressure

For the second motivation, we conducted three studies using the finite element method with a triphasic material description.

First, we developed three series of finite element models to evaluate the effect of collagen fiber orientation (Series I), fiber network architecture (Series I & II), and fiber stiffness (Series III) on tissue swelling. The models had rectangular geometry based on uniaxial test specimens and were validated by comparing the simulated swelling response with experimental results from AF explants [22, 125]. Simulations from these models showed that fiber angle, fiber architecture, and the number of lamellae in single fiber-family structures altered tissue swelling capacity, fiber deformation, and tissue rotation. The findings of this study demonstrate the need to include the native fiber network in computational models to accurately simulate tissue-swelling behavior, and, therefore, subfailure and failure mechanics.

Secondly, we evaluated the effect of the kidney-bean geometry on the swelling behavior of the AF, residual strain formation as a result of swelling, and the effect of GAG content, fiber angle, and fiber stiffness on swelling and residual strain formation. Simulation results showed that the annular ring geometry for specimens with 4 or fewer layers had little impact on swelling ratio, fiber stretch, and fiber reorientation. However, the kidney-bean shape played an important role as the number of lamellae increased towards the native AF architecture (20 layers), such that circumferential direction stretch and stress in the full AF model were compressive in the inner AF and tensile in the outer AF. These stretch and stress were comparable to experimental observations [39, 40]. Altering the distribution of GAGs, fiber stiffness, or fiber angle affected the magnitude and distribution AF swelling, stress and stretch, fiber reorientation, and fiber stretch.

Thirdly, we evaluated the interactions between disc subcomponents under free-swelling conditions and effects of step-wise GAG loss on disc swelling. Models were developed for the intact disc joint and tissue subcomponents, including the NP with the AF and *ex situ* tissue explants (NP and CEP tissue cubes, and an intact AF ring). GAG content and distribution was varied for all models to replicate healthy and degenerated discs. Simulation results showed NP, AF, and endplates restricted each other during *in situ* swelling. The suppression of NP swelling in the disc resulted in the formation of a large residual intradiscal pressure in the healthy disc (0.21 MPa). Including endplates to the disc model had a great impact on

swelling-based residual stress and stretch, fiber stretch, and fiber reorientation throughout the AF. Importantly, describing disc swelling *in situ* demonstrated preservation of residual strain homeostasis throughout the AF, with minimum residual stresses in the inner AF. Disc degeneration had a great impact on disc tissue swelling capacity but had a relatively low impact on intact disc joint swelling. That is, NP residual pressure and residual stress, stretch, and fiber stretch in the AF were all greatly affected by degeneration. Lastly, findings from this study demonstrate the need to replicate NP swelling capacity in engineered discs to prevent degradation of the inner AF.

## 9.3 Measurement of disc water content with MRI

In this research, I also conducted experiments to test if MRI is capable to accurately measure disc water content by comparing MR based water content measurement with traditional biochemical measurement (lyophilization). Experimental results showed that normalizing NP spin density by mass density provided an excellent agreement between MR measured water content and water content measured through lyophilization. However, normalizing spin density by mass density underestimated AF water content. This discrepancy is likely due to a higher concentration of bound water molecules in the AF, compared to the NP, where tightly bounded water molecules have too short T2 values to be detected in MR imaging [254].

## 9.4 Future work

The findings of this research generate new questions to explore for future work. First, we would like to understand how NP size and position work together with posterior elements, such as facet joints, to optimize disc stress and strain distribution under different loading conditions. Secondly, this research only studied the static swelling of disc tissues, and the time factor was investigated. Future work can investigate disc dynamical swelling as well as nutrition transportation. In addition, the effect of mechanical loading on disc swelling and the effect of residual stress/strain/pressure on disc mechanical behavior are also worth investigating. Lastly, quantitative MRI has been shown having the ability to accurately

measure disc water content in a non-invasive way, specifically for NP. Studies that use this method to investigate disc fluid movement, detect early disc degeneration, and develop more accurate disc models will help us better understand disc mechanics and pathological changes.

# Bibliography

[1] Bo Yang and Grace D O' Connell. Effect of collagen fibre orientation on intervertebral disc torsion mechanics. *Biomechanics and modeling in mechanobiology*, 16(6):2005–2015, 2017.

[2] Bo Yang, Yintong Lu, Colin Um, and Grace D O'Connell. Relative nucleus pulposus area and position alters disc joint mechanics. *Journal of biomechanical engineering*, 2019.

[3] Bo Yang, Klineberg Eric, and Grace D O'Connell. Intervertebral disc mechanics with nucleotomy: Differences between simple and complex loading. *Journal of biomechanics*, 2019 in review.

[4] Bo Yang and Grace D O' Connell. Swelling of fiber-reinforced soft tissues is affected by fiber orientation, fiber stiffness, and lamella structure. *Journal of the mechanical behavior of biomedical materials*, 82:320–328, 2018.

[5] Bo Yang and Grace D O' Connell. Gag content, fiber stiffness, and fiber angle affect swelling-based residual stress in the intact annulus fibrosus. *Biomechanics and modeling in mechanobiology*, pages 1–14, 2018.

[6] Bo Yang and Grace D O'Connell. Intervertebral disc swelling maintains strain homeostasis throughout the annulus fibrosus: Finite element models for healthy and degenerated discs. *Submitting*, 2019 in review.

[7] Bo Yang, Michael F Wendland, and Grace D O'Connell. Direct quantification of intervertebral disc water content using magnetic resonance imaging. *Submitting*, 2019 in review.

[8] Spine - anatomy. https://www.goodmancampbell.com/spine-anatomy. [online; access 1-May-2019].

[9] Adams Michael, Bogduk Nikolai, Burton Kim, and Dolan Patricia. *The biomechanics of back pain.3rd ed.* Churchill Livingstone/Elsevier. viii, Edinburgh, New York, 2013.

[10] Brent L Showalter, Jesse C Beckstein, John T Martin, Elizabeth E Beattie, Alejandro A Espinoza Orias, Thomas P Schaer, Edward J Vresilovic, and Dawn M Elliott. Comparison of animal discs used in disc research to human lumbar disc: torsion mechanics and collagen content. *Spine*, 37(15):E900, 2012.

[11] Grace D O' connell, Edward J Vresilovic, and Dawn M Elliott. Comparison of animals used in disc research to human lumbar disc geometry. *Spine*, 32(3):328–333, 2007.

[12] JJ Cassidy, A Hiltner, and E Baer. Hierarchical structure of the intervertebral disc. *Connective tissue research*, 23(1):75–88, 1989.

[13] Francoise Marchand and Abdul M Ahmed. Investigation of the laminate structure of lumbar disc anulus fibrosus. *Spine*, 15(5):402–410, 1990.

[14] Can you really 'slip a disc'. http://www.meadowheadphysiotherapy.co.uk/news/can-you-really-slip-a-disc/. [online; access 1-May-2019].

[15] John Antoniou, Thomas Steffen, Fred Nelson, Neil Winterbottom, Anthony P Hollander, Robin A Poole, Max Aebi, and Mauro Alini. The human lumbar intervertebral disc: evidence for changes in the biosynthesis and denaturation of the extracellular matrix with growth, maturation, ageing, and degeneration. *The Journal of clinical investigation*, 98(4):996–1003, 1996.

[16] James C Iatridis, Jeffrey J MacLean, Mary O' brien, and Ian AF Stokes. Measurements of proteoglycan and water content distribution in human lumbar intervertebral discs. *Spine*, 32(14):1493, 2007.

[17] Gillian Lyons, Sweet M Eisenstein, and MBE Sweet. Biochemical changes in intervertebral disc degeneration. *Biochimica et Biophysica Acta (BBA)-General Subjects*, 673:443–453, 1981.

[18] JPG Urban, S Roberts, and JR Ralphs. The nucleus of the intervertebral disc from development to degeneration. *American Zoologist*, 40(1):53–061, 2000.

[19] JPG Urban and A Maroudas. The measurement of fixed charged density in the intervertebral disc. *Biochimica et Biophysica Acta (BBA)-General Subjects*, 586(1):166–178, 1979.

[20] Daniel H Cortes, Nathan T Jacobs, John F DeLucca, and Dawn M Elliott. Elastic, permeability and swelling properties of human intervertebral disc tissues: a benchmark for tissue engineering. *Journal of biomechanics*, 47(9):2088–2094, 2014.

[21] Yongren Wu, Sarah E Cisewski, Yi Sun, Brooke J Damon, Barton L Sachs, Jr VD Pellegrini, Elizabeth H Slate, and Hai Yao. Quantifying baseline fixed charge density in healthy human cartilage endplate: A two-point electrical conductivity method. *Spine*, 42(17):E1002–E1009, 2017.

[22] Małgorzata Żak and Celina Pezowicz. Analysis of the impact of the course of hydration on the mechanical properties of the annulus fibrosus of the intervertebral disc. *European Spine Journal*, 25(9):2681–2690, 2016.

[23] Evren U Azeloglu, Michael B Albro, Vikrum A Thimmappa, Gerard A Ateshian, and Kevin D Costa. Heterogeneous transmural proteoglycan distribution provides a mechanism for regulating residual stresses in the aorta. *American Journal of Physiology-Heart and Circulatory Physiology*, 2008.

[24] YC Fung. What are the residual stresses doing in our blood vessels? *Annals of biomedical engineering*, 19(3):237–249, 1991.

[25] Hazel RC Screen, Vivek H Chhaya, Steve E Greenwald, Dan L Bader, David A Lee, and Julia C Shelton. The influence of swelling and matrix degradation on the microstructural integrity of tendon. *Acta biomaterialia*, 2(5):505–513, 2006.

[26] David R Eyre and HELEN Muir. Types i and ii collagens in intervertebral disc. interchanging radial distributions in annulus fibrosus. *Biochemical Journal*, 157(1):267–270, 1976.

[27] Gerhard A Holzapfel, CAJ Schulze-Bauer, G Feigl, and Peter Regitnig. Single lamellar mechanics of the human lumbar anulus fibrosus. *Biomechanics and modeling in mechanobiology*, 3(3):125–140, 2005.

[28] DL Skaggs, M Weidenbaum, James C Iatridis, A Ratcliffe, and Van C Mow. Regional variation in tensile properties and biochemical composition of the human lumbar anulus fibrosus. *Spine*, 19(12):1310–1319, 1994.

[29] Grace D O'connell, Edward J Vresilovic, and Dawn M Elliott. Human intervertebral disc internal strain in compression: the effect of disc region, loading position, and degeneration. *Journal of Orthopaedic Research*, 29(4):547–555, 2011.

[30] JR Meakin and DWL Hukins. Effect of removing the nucleus pulposus on the deformation of the annulus fibrosus during compression of the intervertebral disc. *Journal of biomechanics*, 33(5):575–580, 2000.

[31] John Jack Costi, Ian A Stokes, Mack Gardner-Morse, JP Laible, Heather M Scoffone, and JC Iatridis. Direct measurement of intervertebral disc maximum shear strain in six degrees of freedom: motions that place disc tissue at risk of injury. *Journal of biomechanics*, 40(11):2457–2466, 2007.

[32] Anthony J Fennell, Andrew P Jones, and David WL Hukins. Migration of the nucleus pulposus within the intervertebral disc during flexion and extension of the spine. *Spine*, 21(23):2753–2757, 1996.

[33] Celina A Pezowicz, Peter A Robertson, and Neil D Broom. Intralamellar relationships within the collagenous architecture of the annulus fibrosus imaged in its fully hydrated state. *Journal of anatomy*, 207(4):299–312, 2005.

[34] Grace D O'connell. Degeneration affects the structural and tissue mechanics of the intervertebral disc. 2009.

[35] Grace D O' Connell, Nathan T Jacobs, Sounok Sen, Edward J Vresilovic, and Dawn M Elliott. Axial creep loading and unloaded recovery of the human intervertebral disc and the effect of degeneration. *Journal of the Mechanical Behavior of Biomedical Materials*, 4(7):933–942, 2011.

[36] DW McMillan, G Garbutt, and MA Adams. Effect of sustained loading on the water content of intervertebral discs: implications for disc metabolism. *Annals of the Rheumatic Diseases*, 55(12):880–887, 1996.

[37] Neil Roberts, David Hogg, Graham H Whitehouse, and Peter Dangerfield. Quantitative analysis of diurnal variation in volume and water content of lumbar intervertebral discs. *Clinical Anatomy: The Official Journal of the American Association of Clinical Anatomists and the British Association of Clinical Anatomists*, 11(1):1–8, 1998.

[38] W Michael Lai, JS Hou, and Van C Mow. A triphasic theory for the swelling and deformation behaviors of articular cartilage. *Journal of biomechanical engineering*, 113(3):245–258, 1991.

[39] Sarah E Duclos and Arthur J Michalek. Residual strains in the intervertebral disc annulus fibrosus suggest complex tissue remodeling in response to in-vivo loading. *Journal of the mechanical behavior of biomedical materials*, 68:232–238, 2017.

[40] AJ Michalek, MG Gardner-Morse, and JC Iatridis. Large residual strains are present in the intervertebral disc annulus fibrosus in the unloaded state. *Journal of biomechanics*, 45(7):1227–1231, 2012.

[41] Marlène Mengoni, Oluwasegun Kayode, Sebastien NF Sikora, Fernando Y Zapata-Cornelio, Diane E Gregory, and Ruth K Wilcox. Annulus fibrosus functional extrafibrillar and fibrous mechanical behaviour: experimental and computational characterisation. *Royal Society Open Science*, 4(8):170807, 2017.

[42] Cheng-Jen Chuong and Yuan-Cheng Fung. Residual stress in arteries. In *Frontiers in biomechanics*, pages 117–129. Springer, 1986.

[43] A Rachev and SE Greenwald. Residual strains in conduit arteries. *Journal of biomechanics*, 36(5):661–670, 2003.

[44] U.S. Department of Health and Human Services. Low back pain fact sheet. https://www.ninds.nih.gov/Disorders/Patient-Caregiver-Education/Fact-Sheets/Low-Back-Pain-Fact-Sheet.

[45] E Kotilainen and S Valtonen. Clinical instability of the lumbar spine after microdiscectomy. *Acta neurochirurgica*, 125(1-4):120–126, 1993.

[46] Michael Putzier, Sascha V Schneider, Julia F Funk, Stephan W Tohtz, and Carsten Perka. The surgical treatment of the lumbar disc prolapse: nucleotomy with additional transpedicular dynamic stabilization versus nucleotomy alone. *Spine*, 30(5):E109–E114, 2005.

[47] Herniated disc. http://myspineassociates.com/herniated-disc/. [online; access 1-May-2019].

[48] Michael A Adams and Peter J Roughley. What is intervertebral disc degeneration, and what causes it? *Spine*, 31(18):2151–2161, 2006.

[49] Christian WA Pfirrmann, Alexander Metzdorf, Marco Zanetti, Juerg Hodler, and Norbert Boos. Magnetic resonance classification of lumbar intervertebral disc degeneration. *Spine*, 26(17):1873–1878, 2001.

[50] JP Thompson, RH Pearce, MT Schechter, ME Adams, IK Tsang, and PB Bishop. Preliminary evaluation of a scheme for grading the gross morphology of the human intervertebral disc. *Spine*, 15(5):411–415, 1990.

[51] Joseph A Buckwalter. Aging and degeneration of the human intervertebral disc. *Spine*, 20(11):1307–1314, 1995.

[52] Barrie Vernon-Roberts, Nicola L Fazzalari, and Beverley A Manthey. Pathogenesis of tears of the anulus investigated by multiple-level transaxial analysis of the t12-l1 disc. *Spine*, 22(22):2641–2646, 1997.

[53] Barrie Vernon-Roberts, Robert J Moore, and Robert D Fraser. The natural history of age-related disc degeneration: the pathology and sequelae of tears. *Spine*, 32(25):2797–2804, 2007.

[54] Heather Anne L Guerin and Dawn M Elliott. Degeneration affects the fiber reorientation of human annulus fibrosus under tensile load. *Journal of biomechanics*, 39(8):1410–1418, 2006.

[55] Hideki Murakami, Tim S Yoon, Emad S Attallah-Wasif, Chaiwat Kraiwattanapong, Ichiro Kikkawa, and William C Hutton. Quantitative differences in intervertebral disc–matrix composition with age-related degeneration. *Medical & biological engineering & computing*, 48(5):469–474, 2010.

[56] WY Gu, WM Lai, and VC Mow. Transport of multi-electrolytes in charged hydrated biological soft tissues. In *Porous Media: Theory and Experiments*, pages 143–157. Springer, 1999.

[57] S Roberts, J Menage, and JP Urban. Biochemical and structural properties of the cartilage end-plate and its relation to the intervertebral disc. *Spine*, 14(2):166–174, 1989.

[58] Grace D O'Connell, Wade Johannessen, Edward J Vresilovic, and Dawn M Elliott. Human internal disc strains in axial compression measured noninvasively using magnetic resonance imaging. *Spine*, 32(25):2860–2868, 2007.

[59] Jonathon H Yoder, John M Peloquin, Gang Song, Nick J Tustison, Sung M Moon, Alexander C Wright, Edward J Vresilovic, James C Gee, and Dawn M Elliott. Internal three-dimensional strains in human intervertebral discs under axial compression quantified noninvasively by magnetic resonance imaging and image registration. *Journal of biomechanical engineering*, 136(11):111008, 2014.

[60] Phillip Pollintine, Manon SLM van Tunen, Jin Luo, Matthew D Brown, Patricia Dolan, and Michael A Adams. Time-dependent compressive deformation of the ageing spine: relevance to spinal stenosis. *Spine*, 35(4):386–394, 2010.

[61] Nobuhiro Tanaka, Howard S An, Tae-Hong Lim, Atsushi Fujiwara, Chang-Hoon Jeon, and Victor M Haughton. The relationship between disc degeneration and flexibility of the lumbar spine. *The spine journal*, 1(1):47–56, 2001.

[62] Atsushi Fujiwara, Tae-Hong Lim, Howard S An, Nobuhiro Tanaka, Chang-Hoon Jeon, Gunnar BJ Andersson, and Victor M Haughton. The effect of disc degeneration and facet joint osteoarthritis on the segmental flexibility of the lumbar spine. *Spine*, 25(23):3036–3044, 2000.

[63] Hendrik Schmidt, Fabio Galbusera, Antonius Rohlmann, and Aboulfazl Shirazi-Adl. What have we learned from finite element model studies of lumbar intervertebral discs in the past four decades? *Journal of biomechanics*, 46(14):2342–2355, 2013.

[64] Nathan T Jacobs, Daniel H Cortes, John M Peloquin, Edward J Vresilovic, and Dawn M Elliott. Validation and application of an intervertebral disc finite element model utilizing independently constructed tissue-level constitutive formulations that are nonlinear, anisotropic, and time-dependent. *Journal of Biomechanics*, 47(11):2540–2546, 2014.

[65] Hendrik Schmidt, Annette Kettler, Antonius Rohlmann, Lutz Claes, and Hans-Joachim Wilke. The risk of disc prolapses with complex loading in different degrees of disc degeneration–a finite element analysis. *Clinical biomechanics*, 22(9):988–998, 2007.

[66] Qiaoqiao Zhu, Xin Gao, Howard B Levene, Mark D Brown, and Weiyong Gu. Influences of nutrition supply and pathways on the degenerative patterns in human intervertebral disc. *Spine*, 41(7):568, 2016.

[67] Clayton Adam, Philippe Rouch, and Wafa Skalli. Inter-lamellar shear resistance confers compressive stiffness in the intervertebral disc: An image-based modelling study on the bovine caudal disc. *Journal of Biomechanics*, 48(16):4303–4308, 2015.

[68] Antonius Rohlmann, Thomas Zander, Hendrik Schmidt, Hans-Joachim Wilke, and Georg Bergmann. Analysis of the influence of disc degeneration on the mechanical behaviour of a lumbar motion segment using the finite element method. *Journal of biomechanics*, 39(13):2484–2490, 2006.

[69] Frank Niemeyer, Hans-Joachim Wilke, and Hendrik Schmidt. Geometry strongly influences the response of numerical models of the lumbar spine—a probabilistic finite element analysis. *Journal of Biomechanics*, 45(8):1414–1423, 2012.

[70] Van C Mow, SC Kuei, W Michael Lai, and Cecil G Armstrong. Biphasic creep and stress relaxation of articular cartilage in compression: theory and experiments. *Journal of biomechanical engineering*, 102(1):73–84, 1980.

[71] Alireza Abazari, Janet AW Elliott, Garson K Law, Locksley E McGann, and Nadr M Jomha. A biomechanical triphasic approach to the transport of nondilute solutions in articular cartilage. *Biophysical journal*, 97(12):3054–3064, 2009.

[72] Gerard A Ateshian, Nadeen O Chahine, Ines M Basalo, and Clark T Hung. The correspondence between equilibrium biphasic and triphasic material properties in mixture models of articular cartilage. *Journal of biomechanics*, 37(3):391–400, 2004.

[73] Hai Yao and Wei Yong Gu. Three-dimensional inhomogeneous triphasic finite-element analysis of physical signals and solute transport in human intervertebral disc under axial compression. *Journal of biomechanics*, 40(9):2071–2077, 2007.

[74] Weiyong Gu, Qiaoqiao Zhu, Xin Gao, and Mark D Brown. Simulation of the progression of intervertebral disc degeneration due to decreased nutrition supply. *Spine*, 39(24):E1411, 2014.

[75] Joshua D Auerbach, Wade Johannessen, Arijitt Borthakur, Andrew J Wheaton, Carol A Dolinskas, Richard A Balderston, Ravinder Reddy, and Dawn M Elliott. In vivo quantification of human lumbar disc degeneration using t $1\rho$-weighted magnetic resonance imaging. *European spine journal*, 15(3):338–344, 2006.

[76] Liisa Kerttula, Mauno Kurunlahti, Jukka Jauhiainen, Antero Koivula, Jarkko Oikarinen, and O Tervonen. Apparent diffusion coefficients and t2 relaxation time measurements to evaluate disc degeneration: a quantitative mr study of young patients with previous vertebral fracture. *Acta radiologica*, 42(6):585–591, 2001.

[77] Semih E Bezci and Grace D O'Connell. *Annals of Biomedical Engineering*, 2019 in review.

[78] Nicholas L Marinelli, Victor M Haughton, Alejandro Muñoz, and Paul A Anderson. T2 relaxation times of intervertebral disc tissue correlated with water content and proteoglycan content. *Spine*, 34(5):520–524, 2009.

[79] Mark B Coventry, Ralph K Ghormley, and James W Kernohan. The intervertebral disc: Its microscopic anatomy and pathology: Part i. anatomy, development, and physiology. *JBJS*, 27(1):105–112, 1945.

[80] WG Horton. Further observations on the elastic mechanism of the intervertebral disc. *The Journal of bone and joint surgery. British volume*, 40(3):552–557, 1958.

[81] DS Hickey and DW Hukins. X-ray diffraction studies of the arrangement of collagenous fibres in human fetal intervertebral disc. *Journal of Anatomy*, 131(Pt 1):81, 1980.

[82] Jeremy A Klein and Hukins David WL. Collagen fibre orientation in the annulus fibrosus of intervertebral disc during bending and torsion measured by x-ray diffraction. *Biochimica et Biophysica Acta (BBA)-General Subjects*, 719(1):98–101, 1982.

[83] Edward W Hsu and Lori A Setton. Diffusion tensor microscopy of the intervertebral disc anulus fibrosus. *Magnetic Resonance in Medicine: An Official Journal of the International Society for Magnetic Resonance in Medicine*, 41(5):992–999, 1999.

[84] Tristan P Driscoll, Nandan L Nerurkar, Nathan T Jacobs, Dawn M Elliott, and Robert L Mauck. Fiber angle and aspect ratio influence the shear mechanics of oriented electrospun nanofibrous scaffolds. *Journal of the mechanical behavior of biomedical materials*, 4(8):1627–1636, 2011.

[85] M Dreischarf, T Zander, A Shirazi-Adl, CM Puttlitz, CJ Adam, CS Chen, VK Goel, A Kiapour, YH Kim, KM Labus, et al. Comparison of eight published static finite element models of the intact lumbar spine: predictive power of models improves when combined together. *Journal of biomechanics*, 47(8):1757–1766, 2014.

[86] Hendrik Schmidt, Frank Heuer, Ulrich Simon, Annette Kettler, Antonius Rohlmann, Lutz Claes, and Hans-Joachim Wilke. Application of a new calibration method for a three-dimensional finite element model of a human lumbar annulus fibrosus. *Clinical Biomechanics*, 21(4):337–344, 2006.

[87] A Shirazi-Adl, AM Ahmed, and SC Shrivastava. A finite element study of a lumbar motion segment subjected to pure sagittal plane moments. *Journal of biomechanics*, 19(4):331–350, 1986.

[88] Marco Cannella, Amy Arthur, Shanee Allen, Michael Keane, Abhijeet Joshi, Edward Vresilovic, and Michele Marcolongo. The role of the nucleus pulposus in neutral zone

human lumbar intervertebral disc mechanics. *Journal of biomechanics*, 41(10):2104–2111, 2008.

[89] Juying Huang, Huagang Yan, Fengzeng Jian, Xingwen Wang, and Haiyun Li. Numerical analysis of the influence of nucleus pulposus removal on the biomechanical behavior of a lumbar motion segment. *Computer methods in biomechanics and biomedical engineering*, 18(14):1516–1524, 2015.

[90] Abhijeet Bhaskar Joshi. Mechanical behavior of the human lumbar intervertebral disc with polymeric hydrogel nucleus implant: an experimental and finite element study. 2004.

[91] Judith R Meakin, Janet E Reid, and David WL Hukins. Replacing the nucleus pulposus of the intervertebral disc. *Clinical biomechanics*, 16(7):560–565, 2001.

[92] Grace D O' Connell, Neil R Malhotra, Edward J Vresilovic, and Dawn M Elliott. The effect of discectomy and the dependence on degeneration of human intervertebral disc strain in axial compression. *Spine*, 36(21):1765, 2011.

[93] Richard E Seroussi, Martin H Krag, David L Muller, and Malcolm H Pope. Internal deformations of intact and denucleated human lumbar discs subjected to compression, flexion, and extension loads. *Journal of Orthopaedic Research*, 7(1):122–131, 1989.

[94] Daniel GT Strange, Sandie T Fisher, Philip C Boughton, Thomas J Kishen, and Ashish D Diwan. Restoration of compressive loading properties of lumbar discs with a nucleus implant—a finite element analysis study. *The Spine Journal*, 10(7):602–609, 2010.

[95] Wilhelmina E Hoogendoorn, Mireille NM van Poppel, Paulien M Bongers, Bart W Koes, and Lex M Bouter. Physical load during work and leisure time as risk factors for back pain. *Scandinavian journal of work, environment & health*, pages 387–403, 1999.

[96] Judith I Kuiper, Alex Burdorf, Monique HW Frings-Dresen, P Paul FM Kuijer, Dick Spreeuwers, Freek JB Lötters, and Harald S Miedema. Assessing the work-relatedness of nonspecific low-back pain. *Scandinavian journal of work, environment & health*, 31(3):237–243, 2005.

[97] Freek Lotters, Alex Burdorf, Judith Kuiper, and Harald Miedema. Model for the work-relatedness of low-back pain., 2003.

[98] Andreas Seidler, Ulrike Euler, Ulrich Bolm-Audorff, Rolf Ellegast, Joachim Grifka, Johannes Haerting, Matthias Jager, Martina Michaelis, and Oliver Kuss. Physical workload and accelerated occurrence of lumbar spine diseases: risk and rate advancement periods in a german multicenter case-control study. *Scandinavian journal of work, environment & health*, pages 30–36, 2011.

[99] RR Goodwin, KS James, AU Daniels, and HK Dunn. Distraction and compression loads enhance spine torsional stiffness. *Journal of biomechanics*, 27(8):1049–1057, 1994.

[100] A Shirazi-Adl. On the fibre composite material models of disc annulus—comparison of predicted stresses. *Journal of Biomechanics*, 22(4):357–365, 1989.

[101] AAASS Shirazi-Adl, Abdul M Ahmed, and Suresh C Shrivastava. Mechanical response of a lumbar motion segment in axial torque alone and combined with compression. *Spine*, 11(9):914–927, 1986.

[102] Dirk L van Deursen, Chris J Snijders, Idsart Kingma, and van Die. In vitro torsion-induced stress distribution changes in porcine intervertebral discs.

[103] Samantha CW Chan, Stephen J Ferguson, Karin Wuertz, and Benjamin Gantenbein-Ritter. Biological response of the intervertebral disc to repetitive short-term cyclic torsion. *Spine*, 36(24):2021–2030, 2011.

[104] Jasper Homminga, Anne M Lehr, Gerdine JM Meijer, Michiel MA Janssen, Tom PC Schlosser, Gijsbertus J Verkerke, and ReneM Castelein. Posteriorly directed shear loads and disc degeneration affect the torsional stiffness of spinal motion segments: a biomechanical modeling study. *Spine*, 38(21):E1313–E1319, 2013.

[105] Jesse C Beckstein, Sounok Sen, Thomas P Schaer, Edward J Vresilovic, and Dawn M Elliott. Comparison of animal discs used in disc research to human lumbar disc: axial compression mechanics and glycosaminoglycan content. *Spine*, 33(6):E166–E173, 2008.

[106] Robert L Spilker. Mechanical behavior of a simple model of an intervertebral disk under compressive loading. *Journal of Biomechanics*, 13(10):895–901, 1980.

[107] Michael Y Lu, William C Hutton, and Vasanti M Gharpuray. Can variations in intervertebral disc height affect the mechanical function of the disc? *Spine*, 21(19):2208–2216, 1996.

[108] Raghu N Natarajan and Gunnar BJ Andersson. The influence of lumbar disc height and cross-sectional area on the mechanical response of the disc to physiologic loading. *Spine*, 24(18):1873, 1999.

[109] Victor M Haughton, Baxter Rogers, M Elizabeth Meyerand, and Daniel K Resnick. Measuring the axial rotation of lumbar vertebrae in vivo with mr imaging. *American journal of neuroradiology*, 23(7):1110–1116, 2002.

[110] Dawn M Elliott and Lori A Setton. Anisotropic and inhomogeneous tensile behavior of the human anulus fibrosus: experimental measurement and material model predictions. *Journal of biomechanical engineering*, 123(3):256–263, 2001.

[111] Andrea E Duncan, Ricki J Colman, and Patricia A Kramer. Sex differences in spinal osteoarthritis in humans and rhesus monkeys (macaca mulatta). *Spine*, 37(11):915, 2012.

[112] John M Peloquin, Jonathon H Yoder, Nathan T Jacobs, Sung M Moon, Alexander C Wright, Edward J Vresilovic, and Dawn M Elliott. Human l3l4 intervertebral disc mean 3d shape, modes of variation, and their relationship to degeneration. *Journal of biomechanics*, 47(10):2452–2459, 2014.

[113] Andy Tsai, Anthony Yezzi, William Wells III, Clare Tempany, Dewey Tucker, Ayres Fan, W Eric Grimson, and Alan S Willsky. A shape-based approach to the segmentation of medical imagery using level sets. 2003.

[114] Sung M Moon, Jonathon H Yoder, Alexander C Wright, Lachlan J Smith, Edward J Vresilovic, and Dawn M Elliott. Evaluation of intervertebral disc cartilaginous endplate structure using magnetic resonance imaging. *European Spine Journal*, 22(8):1820–1828, 2013.

[115] Azucena G Rodriguez, Ana E Rodriguez-Soto, Andrew J Burghardt, Sigurd Berven, Sharmila Majumdar, and Jeffrey C Lotz. Morphology of the human vertebral endplate. *Journal of Orthopaedic Research*, 30(2):280–287, 2012.

[116] Steve A Maas, Benjamin J Ellis, Gerard A Ateshian, and Jeffrey A Weiss. Febio: finite elements for biomechanics. *Journal of biomechanical engineering*, 134(1):011005, 2012.

[117] Frank Heuer, Hendrik Schmidt, Zdenek Klezl, Lutz Claes, and Hans-Joachim Wilke. Stepwise reduction of functional spinal structures increase range of motion and change lordosis angle. *Journal of biomechanics*, 40(2):271–280, 2007.

[118] Ruth S Ochia and Peter R Cavanagh. Reliability of surface emg measurements over 12 hours. *Journal of Electromyography and Kinesiology*, 17(3):365–371, 2007.

[119] Donna G Blankenbaker, Victor M Haughton, Baxter P Rogers, M Elizabeth Meyerand, and Jason P Fine. Axial rotation of the lumbar spinal motion segments correlated with concordant pain on discography: a preliminary study. *American Journal of Roentgenology*, 186(3):795–799, 2006.

[120] MJ Pearcy and SB Tibrewal. Axial rotation and lateral bending in the normal lumbar spine measured by three-dimensional radiography. *Spine*, 9(6):582–587, 1984.

[121] Nikolaus Berger-Roscher, Gloria Casaroli, Volker Rasche, Tomaso Villa, Fabio Galbusera, and Hans-Joachim Wilke. Influence of complex loading conditions on intervertebral disc failure. *Spine*, 42(2):E78–E85, 2017.

[122] Hans-Joachim Wilke, Annette Kienle, Sebastian Maile, Volker Rasche, and Nikolaus Berger-Roscher. A new dynamic six degrees of freedom disc-loading simulator allows to provoke disc damage and herniation. *European Spine Journal*, 25(5):1363–1372, 2016.

[123] HF Farfan. The torsional injury of the lumbar spine. *Spine*, 9(1):53–53, 1984.

[124] Samuel P Veres, Peter A Robertson, and Neil D Broom. The influence of torsion on disc herniation when combined with flexion. *European Spine Journal*, 19(9):1468–1478, 2010.

[125] Semih E Bezci, Aditya Nandy, and Grace D O'Connell. Effect of hydration on healthy intervertebral disk mechanical stiffness. *Journal of biomechanical engineering*, 137(10):101007, 2015.

[126] Smith L Johnston, Mark R Campbell, Rick Scheuring, and Alan H Feiveson. Risk of herniated nucleus pulposus among us astronauts. *Aviation, space, and environmental medicine*, 81(6):566–574, 2010.

[127] Alejandro A Espinoza Orias, Nicole M Mammoser, John J Triano, Howard S An, Gunnar BJ Andersson, and Nozomu Inoue. Effects of axial torsion on disc height distribution: an in vivo study. *Journal of manipulative and physiological therapeutics*, 39(4):294–303, 2016.

[128] Terri-Ann N Kelly, Brendan L Roach, Zachary D Weidner, Charles R Mackenzie-Smith, Grace D O'Connell, Eric G Lima, Aaron M Stoker, James L Cook, Gerard A Ateshian, and Clark T Hung. Tissue-engineered articular cartilage exhibits tension–compression nonlinearity reminiscent of the native cartilage. *Journal of Biomechanics*, 46(11):1784–1791, 2013.

[129] Chong Wang, Silvia Gonzales, Howard Levene, Weiyong Gu, and Chun-Yuh Charles Huang. Energy metabolism of intervertebral disc under mechanical loading. *Journal of orthopaedic research*, 31(11):1733–1738, 2013.

[130] Casey L Korecki, Jeffrey J MacLean, and James C Iatridis. Dynamic compression effects on intervertebral disc mechanics and biology. *Spine*, 33(13):1403, 2008.

[131] Hannes Haberl, Peter A Cripton, Tracy-E Orr, Thomas Beutler, Hanspeter Frei, Wolfgang R Lanksch, and L-P Nolte. Kinematic response of lumbar functional spinal units to axial torsion with and without superimposed compression and flexion/extension. *European Spine Journal*, 13(6):560–566, 2004.

[132] John M Popovich Jr, Judson B Welcher, Thomas P Hedman, Wafa Tawackoli, Neel Anand, Thomas C Chen, and Kornelia Kulig. Lumbar facet joint and intervertebral disc loading during simulated pelvic obliquity. *The Spine Journal*, 13(11):1581–1589, 2013.

[133] A Shirazi-Adl. Finite-element evaluation of contact loads on facets of an l2-l3 lumbar segment in complex loads. *Spine*, 16(5):533–541, 1991.

[134] A Shirazi-Adl. Nonlinear stress analysis of the whole lumbar spine in torsion — mechanics of facet articulation. *Journal of Biomechanics*, 27(3):289–299, 1994.

[135] Hans-Joachim Wilke, Peter Neef, Marco Caimi, Thomas Hoogland, and Lutz E Claes. New in vivo measurements of pressures in the intervertebral disc in daily life. *Spine*, 24(8):755–762, 1999.

[136] Grace D O' Connell, Heather L Guerin, and Dawn M Elliott. Theoretical and uniaxial experimental evaluation of human annulus fibrosus degeneration. *Journal of biomechanical engineering*, 131(11):111007, 2009.

[137] Grace D O' Connell, Sounok Sen, and Dawn M Elliott. Human annulus fibrosus material properties from biaxial testing and constitutive modeling are altered with degeneration. *Biomechanics and modeling in mechanobiology*, 11(3-4):493–503, 2012.

[138] Grace D O'Connell, J Kent Leach, and Eric O Klineberg. Tissue engineering a biological repair strategy for lumbar disc herniation. *BioResearch open access*, 4(1):431–445, 2015.

[139] Katsuhiko Sato, Shinichi Kikuchi, and Takumi Yonezawa. In vivo intradiscal pressure measurement in healthy individuals and in patients with ongoing back problems. *Spine*, 24(23):2468, 1999.

[140] Weiye Zhong, Sean J Driscoll, Minfei Wu, Shaobai Wang, Zhan Liu, Thomas D Cha, Kirkham B Wood, and Guoan Li. In vivo morphological features of human lumbar discs. *Medicine*, 93(28), 2014.

[141] Sarah E Gullbrand, Dong Hwa Kim, Edward Bonnevie, Beth G Ashinsky, Lachlan J Smith, Dawn M Elliott, Robert L Mauck, and Harvey E Smith. Towards the scale up of tissue engineered intervertebral discs for clinical application. *Acta biomaterialia*, 70:154–164, 2018.

[142] JT Martin, SE Gullbrand, DH Kim, K Ikuta, CG Pfeifer, BG Ashinsky, LJ Smith, DM Elliott, HE Smith, and RL Mauck. In vitro maturation and in vivo integration and

function of an engineered cell-seeded disc-like angle ply structure (daps) for total disc arthroplasty. *Scientific reports*, 7(1):15765, 2017.

[143] Keith L Markolf. Deformation of the thoracolumbar intervertebral joints in response to external loads: a biomechanical study using autopsy material. *JBJS*, 54(3):511–533, 1972.

[144] Semih E Bezci, Ananth Eleswarapu, Eric O Klineberg, and Grace D O'Connell. Contribution of facet joints, axial compression, and composition to human lumbar disc torsion mechanics. *Journal of Orthopaedic Research*, 36(8):2266–2273, 2018.

[145] Daniel J Cook, Matthew S Yeager, and Boyle C Cheng. Range of motion of the intact lumbar segment: a multivariate study of 42 lumbar spines. *International journal of spine surgery*, 9:5, 2015.

[146] Mark Pearcy, IAN Portek, and Janis Shepherd. Three-dimensional x-ray analysis of normal movement in the lumbar spine. *Spine*, 9(3):294–297, 1984.

[147] ISAO Yamamoto, MANOHAR M Panjabi, TREY Crisco, and T Oxland. Three-dimensional movements of the whole lumbar spine and lumbosacral joint. *Spine*, 14(11):1256–1260, 1989.

[148] Gerdine JM Meijer, J Homminga, Edsko EG Hekman, AG Veldhuizen, and Gijsbertus Jacob Verkerke. The effect of three-dimensional geometrical changes during adolescent growth on the biomechanics of a spinal motion segment. *Journal of Biomechanics*, 43(8):1590–1597, 2010.

[149] Manohar M Panjabi, TR Oxland, I Yamamoto, and JJ Crisco. Mechanical behavior of the human lumbar and lumbosacral spine as shown by three-dimensional load-displacement curves. *JBJS*, 76(3):413–424, 1994.

[150] Mack G Gardner-Morse and Ian AF Stokes. Structural behavior of human lumbar spinal motion segments. *Journal of biomechanics*, 37(2):205–212, 2004.

[151] Intervertebral disc degeneration alters lumbar spine segmental stiffness in all modes of loading under a compressive follower load', author=.

[152] DB Amin, IM Lawless, D Sommerfeld, RM Stanley, B Ding, and JJ Costi. The effect of six degree of freedom loading sequence on the in-vitro compressive properties of human lumbar spine segments. *Journal of Biomechanics*, 49(14):3407–3414, 2016.

[153] MA Adams, DS McNally, and P Dolan. 'stress' distributions inside intervertebral discs: The effects of age and degeneration. *The Journal of bone and joint surgery. British volume*, 78(6):965–972, 1996.

[154] DS McNally and MA Adams. Internal intervertebral disc mechanics as revealed by stress profilometry. *Spine*, 17(1):66–73, 1992.

[155] Peter Roughley, Caroline Hoemann, Eric DesRosiers, Fackson Mwale, John Antoniou, and Mauro Alini. The potential of chitosan-based gels containing intervertebral disc cells for nucleus pulposus supplementation. *Biomaterials*, 27(3):388–396, 2006.

[156] James C Iatridis, Lori A Setton, Mark Weidenbaum, and Van C Mow. Alterations in the mechanical behavior of the human lumbar nucleus pulposus with degeneration and aging. *Journal of Orthopaedic Research*, 15(2):318–322, 1997.

[157] Samantha CW Chan, Jochen Walser, Patrick Käppeli, Mohammad Javad Shamsollahi, Stephen J Ferguson, and Benjamin Gantenbein-Ritter. Region specific response of intervertebral disc cells to complex dynamic loading: an organ culture study using a dynamic torsion-compression bioreactor. *PloS one*, 8(8):e72489, 2013.

[158] Gloria Casaroli, Tomaso Villa, Tito Bassani, Nikolaus Berger-Roscher, Hans-Joachim Wilke, and Fabio Galbusera. Numerical prediction of the mechanical failure of the intervertebral disc under complex loading conditions. *Materials*, 10(1):31, 2017.

[159] Aaron J Fields, Gideon L Lee, and Tony M Keaveny. Mechanisms of initial endplate failure in the human vertebral body. *Journal of biomechanics*, 43(16):3126–3131, 2010.

[160] Javad Tavakoli, Dhara B Amin, Brian JC Freeman, and John J Costi. The biomechanics of the inter-lamellar matrix and the lamellae during progression to lumbar disc herniation: which is the weakest structure? *Annals of biomedical engineering*, 46(9):1280–1291, 2018.

[161] Samuel P Veres, Peter A Robertson, and Neil D Broom. The morphology of acute disc herniation: a clinically relevant model defining the role of flexion. *Spine*, 34(21):2288–2296, 2009.

[162] Paul Brinckmann, Wolfgang Frobin, Eberhard Hierholzer, and Manfred Horst. Deformation of the vertebral end-plate under axial loading of the spine. *Spine*, 8(8):851–856, 1983.

[163] Jorge O Galante. Tensile properties of the human lumbar annulus fibrosus. *Acta Orthopaedica Scandinavica*, 38(sup100):1–91, 1967.

[164] Meredith L Schollum, Peter A Robertson, and Neil D Broom. How age influences unravelling morphology of annular lamellae–a study of interfibre cohesivity in the lumbar disc. *Journal of anatomy*, 216(3):310–319, 2010.

[165] Vadalà. The transpedicular approach as an alternative route for intervertebral disc regeneration.

[166] Sandra Reitmaier, David Volkheimer, Nikolaus Berger-Roscher, Hans-Joachim Wilke, and Anita Ignatius. Increase or decrease in stability after nucleotomy? conflicting in vitro and in vivo results in the sheep model. *Journal of The Royal Society Interface*, 11(100):20140650, 2014.

[167] Etsuro Yorimitsu, Kazuhiro Chiba, Yoshiaki Toyama, and Kiyoshi Hirabayashi. Long-term outcomes of standard discectomy for lumbar disc herniation: a follow-up study of more than 10 years. *Spine*, 26(6):652–657, 2001.

[168] Hans-Joachim Wilke, Frank Heuer, Cornelia Neidlinger-Wilke, and Lutz Claes. Is a collagen scaffold for a tissue engineered nucleus replacement capable of restoring disc height and stability in an animal model? *European Spine Journal*, 15(3):433–438, 2006.

[169] Dawn M Elliott, Chandra S Yerramalli, Jesse C Beckstein, John I Boxberger, Wade Johannessen, and Edward J Vresilovic. The effect of relative needle diameter in puncture and sham injection animal models of degeneration. *Spine*, 33(6):588–596, 2008.

[170] Arthur J Michalek, Kristin L Funabashi, and James C Iatridis. Needle puncture injury of the rat intervertebral disc affects torsional and compressive biomechanics differently. *European Spine Journal*, 19(12):2110–2116, 2010.

[171] Arthur J Michalek and James C Iatridis. Height and torsional stiffness are most sensitive to annular injury in large animal intervertebral discs. *The Spine Journal*, 12(5):425–432, 2012.

[172] Rose G Long, Alexander Bürki, Philippe Zysset, David Eglin, Dirk W Grijpma, Sebastien BG Blanquer, Andrew C Hecht, and James C Iatridis. Mechanical restoration and failure analyses of a hydrogel and scaffold composite strategy for annulus fibrosus repair. *Acta biomaterialia*, 30:116–125, 2016.

[173] Clare C Guterl, Eugene Y See, Sebastien BG Blanquer, Abhay Pandit, Stephen J Ferguson, Lorin M Benneker, Dirk W Grijpma, Daisuke Sakai, David Eglin, Mauro Alini, et al. Challenges and strategies in the repair of ruptured annulus fibrosus. *European cells & materials*, 25:1, 2013.

[174] M Gorensek, C Joksimovic, NEVENKA Kregar-Velikonja, M Gorensek, M Knezevic, M Jeras, V Pavlovcic, and A Cor. Nucleus pulposus repair with cultured autologous elastic cartilage derived chondrocytes. *CELLULAR AND MOLECULAR BIOLOGY LETTERS.*, 9(2):363–374, 2004.

[175] Jeffrey C Lotz, Olivier K Colliou, and David S Bradford. Biodegradable/bioactive nucleus pulposus implant and method for treating degenerated intervertebral discs, January 2 2007. US Patent 7,156,877.

[176] Jean Lemaitre. *Handbook of Materials Behavior Models, Three-Volume Set: Nonlinear Models and Properties*. Elsevier, 2001.

[177] Adam P Rumian, Andrew L Wallace, and Helen L Birch. Tendons and ligaments are anatomically distinct but overlap in molecular and morphological features—a comparative study in an ovine model. *Journal of orthopaedic research*, 25(4):458–464, 2007.

[178] Yunjie Wang, Shahrokh Zeinali-Davarani, and Yanhang Zhang. Arterial mechanics considering the structural and mechanical contributions of ecm constituents. *Journal of biomechanics*, 49(12):2358–2365, 2016.

[179] Adam C Abraham, Christian R Edwards, Gregory M Odegard, and Tammy L Haut Donahue. Regional and fiber orientation dependent shear properties and anisotropy of bovine meniscus. *Journal of the mechanical behavior of biomedical materials*, 4(8):2024–2030, 2011.

[180] Heather Anne Lynch, Wade Johannessen, Jeffrey P Wu, Andrew Jawa, and Dawn M Elliott. Effect of fiber orientation and strain rate on the nonlinear uniaxial tensile material properties of tendon. *Journal of biomechanical engineering*, 125(5):726–731, 2003.

[181] Qingen Meng, Shuqiang An, Robin A Damion, Zhongmin Jin, Ruth Wilcox, John Fisher, and Alison Jones. The effect of collagen fibril orientation on the biphasic mechanics of articular cartilage. *Journal of the mechanical behavior of biomedical materials*, 65:439–453, 2017.

[182] R Shirazi and A Shirazi-Adl. Deep vertical collagen fibrils play a significant role in mechanics of articular cartilage. *Journal of Orthopaedic Research*, 26(5):608–615, 2008.

[183] Diane R Wagner and Jeffrey C Lotz. Theoretical model and experimental results for the nonlinear elastic behavior of human annulus fibrosus. *Journal of orthopaedic research*, 22(4):901–909, 2004.

[184] Michael A Adams. Biomechanics of back pain. *Acupuncture in medicine*, 22(4):178–188, 2004.

[185] Daniel H Cortes and Dawn M Elliott. Extra-fibrillar matrix mechanics of annulus fibrosus in tension and compression. *Biomechanics and modeling in mechanobiology*, 11(6):781–790, 2012.

[186] Tony W Lin, Luis Cardenas, and Louis J Soslowsky. Biomechanics of tendon injury and repair. *Journal of biomechanics*, 37(6):865–877, 2004.

[187] Mark L Wood, Gayle E Lester, and Laurence E Dahners. Collagen fiber sliding during ligament growth and contracture. *Journal of Orthopaedic Research*, 16(4):438–440, 1998.

[188] Semih E Bezci and Grace D O' connell. Osmotic pressure alters time-dependent recovery behavior of the intervertebral disc. *Spine*, 43(6):E334–E340, 2018.

[189] S Roccabianca, C Bellini, and JD Humphrey. Computational modelling suggests good, bad and ugly roles of glycosaminoglycans in arterial wall mechanics and mechanobiology. *Journal of The Royal Society Interface*, 11(97):20140397, 2014.

[190] Kyoko Yoshida, Mala Mahendroo, Joy Vink, Ronald Wapner, and Kristin Myers. Material properties of mouse cervical tissue in normal gestation. *Acta biomaterialia*, 36:195–209, 2016.

[191] Heather Lynch Guerin and Dawn M Elliott. Quantifying the contributions of structure to annulus fibrosus mechanical function using a nonlinear, anisotropic, hyperelastic model. *Journal of Orthopaedic Research*, 25(4):508–516, 2007.

[192] Gerhard A Holzapfel, Thomas C Gasser, and Ray W Ogden. A new constitutive framework for arterial wall mechanics and a comparative study of material models. *Journal of elasticity and the physical science of solids*, 61(1-3):1–48, 2000.

[193] Emre R Acaroglu, James C Iatridis, Lori A Setton, Robert J Foster, Van C Mow, and Mark Weidenbaum. Degeneration and aging affect the tensile behavior of human lumbar anulus fibrosus. *Spine*, 20(24):2690–2701, 1995.

[194] TP Green, MA Adams, and P Dolan. Tensile properties of the annulus fibrosus. *European Spine Journal*, 2(4):209–214, 1993.

[195] Woojin M Han, Nandan L Nerurkar, Lachlan J Smith, Nathan T Jacobs, Robert L Mauck, and Dawn M Elliott. Multi-scale structural and tensile mechanical response of annulus fibrosus to osmotic loading. *Annals of biomedical engineering*, 40(7):1610–1621, 2012.

[196] ASTM Standard. E8-96a, standard test methods for tension testing of metallic materials. *Annual book of ASTM standards*, 3:57–72, 2004.

[197] Pekka Kannus. Structure of the tendon connective tissue. *Scandinavian journal of medicine & science in sports*, 10(6):312–320, 2000.

[198] R Bruce Martin, David B Burr, Neil A Sharkey, and David P Fyhrie. Mechanical properties of ligament and tendon. In *Skeletal Tissue Mechanics*, pages 175–225. Springer, 2015.

[199] Alicia R Jackson, Tai-Yi Yuan, Chun-Yuh Huang, and Wei Yong Gu. A conductivity approach to measuring fixed charge density in intervertebral disc tissue. *Annals of biomedical engineering*, 37(12):2566–2573, 2009.

[200] William C Stadie and F William Sunderman. The osmotic coefficient of sodium in sodium hemoglobinate and of sodium chloride in hemoglobin solution. *Journal of Biological Chemistry*, 91(1):227–241, 1931.

[201] H Yasuda, CE Lamaze, and LD Ikenberry. Permeability of solutes through hydrated polymer membranes. part i. diffusion of sodium chloride. *Die Makromolekulare Chemie: Macromolecular Chemistry and Physics*, 118(1):19–35, 1968.

[202] ND Panagiotacopulos, WG Knauss, and R Bloch. On the mechanical properties of human intervertebral disc material. *Biorheology*, 16(4-5):317–330, 1979.

[203] Daria A Narmoneva, Herman S Cheung, Jean Y Wang, David S Howell, and Lori A Setton. Altered swelling behavior of femoral cartilage following joint immobilization in a canine model. *Journal of orthopaedic research*, 20(1):83–91, 2002.

[204] Theodore T Tower, Michael R Neidert, and Robert T Tranquillo. Fiber alignment imaging during mechanical testing of soft tissues. *Annals of biomedical engineering*, 30(10):1221–1233, 2002.

[205] Spencer P Lake, Kristin S Miller, Dawn M Elliott, and Louis J Soslowsky. Effect of fiber distribution and realignment on the nonlinear and inhomogeneous mechanical properties of human supraspinatus tendon under longitudinal tensile loading. *Journal of Orthopaedic Research*, 27(12):1596–1602, 2009.

[206] Kristi A Hansen, Jeffrey A Weiss, and Jennifer K Barton. Recruitment of tendon crimp with applied tensile strain. *Journal of biomechanical engineering*, 124(1):72–77, 2002.

[207] D Amiel, C Frank, F Harwood, J Fronek, and W Akeson. Tendons and ligaments: a morphological and biochemical comparison. *Journal of Orthopaedic Research*, 1(3):257–265, 1983.

[208] Heath B Henninger, Clayton J Underwood, Gerard A Ateshian, and Jeffrey A Weiss. Effect of sulfated glycosaminoglycan digestion on the transverse permeability of medial collateral ligament. *Journal of biomechanics*, 43(13):2567–2573, 2010.

[209] GP Riley, RL Harrall, CR Constant, MD Chard, TE Cawston, and BL Hazleman. Glycosaminoglycans of human rotator cuff tendons: changes with age and in chronic rotator cuff tendinitis. *Annals of the rheumatic diseases*, 53(6):367–376, 1994.

[210] Babak N Safa, Kyle D Meadows, Spencer E Szczesny, and Dawn M Elliott. Exposure to buffer solution alters tendon hydration and mechanics. *Journal of biomechanics*, 61:18–25, 2017.

[211] Brendon M Baker, Albert O Gee, Robert B Metter, Ashwin S Nathan, Ross A Marklein, Jason A Burdick, and Robert L Mauck. The potential to improve cell infiltration in composite fiber-aligned electrospun scaffolds by the selective removal of sacrificial fibers. *Biomaterials*, 29(15):2348–2358, 2008.

[212] John L Tan, Joe Tien, Dana M Pirone, Darren S Gray, Kiran Bhadriraju, and Christopher S Chen. Cells lying on a bed of microneedles: an approach to isolate mechanical force. *Proceedings of the National Academy of Sciences*, 100(4):1484–1489, 2003.

[213] Hasan Demirkoparan and Thomas J Pence. Swelling–twist interaction in fiber-reinforced hyperelastic materials: the example of azimuthal shear. *Journal of Engineering Mathematics*, 109(1):63–84, 2018.

[214] Nandan L Nerurkar, Robert L Mauck, and Dawn M Elliott. Modeling interlamellar interactions in angle-ply biologic laminates for annulus fibrosus tissue engineering. *Biomechanics and modeling in mechanobiology*, 10(6):973–984, 2011.

[215] SEYED A Shirazi-Adl, Suresh C Shrivastava, and Abdul M Ahmed. Stress analysis of the lumbar disc-body unit in compression. a three-dimensional nonlinear finite element study. *Spine*, 9(2):120–134, 1984.

[216] Johannes AG Rhodin. Architecture of the vessel wall. *Handbook of physiology, the cardiovascular system*, 2:1–31, 1980.

[217] Lucas H Timmins, Qiaofeng Wu, Alvin T Yeh, James E Moore, and Steve E Greenwald. Structural inhomogeneity and fiber orientation in the inner arterial media. *American Journal of Physiology-Heart and Circulatory Physiology*, 2010.

[218] Daniel H Cortes, Spencer P Lake, Jennifer A Kadlowec, Louis J Soslowsky, and Dawn M Elliott. Characterizing the mechanical contribution of fiber angular distribution in connective tissue: comparison of two modeling approaches. *Biomechanics and modeling in mechanobiology*, 9(5):651–658, 2010.

[219] Meredith L Schollum, Peter A Robertson, and Neil D Broom. A microstructural investigation of intervertebral disc lamellar connectivity: detailed analysis of the translamellar bridges. *Journal of anatomy*, 214(6):805–816, 2009.

[220] Nathan T Jacobs, Lachlan J Smith, Woojin M Han, Jeffrey Morelli, Jonathon H Yoder, and Dawn M Elliott. Effect of orientation and targeted extracellular matrix degradation on the shear mechanical properties of the annulus fibrosus. *Journal of the mechanical behavior of biomedical materials*, 4(8):1611–1619, 2011.

[221] Luzhong Yin and Dawn M Elliott. A biphasic and transversely isotropic mechanical model for tendon:: application to mouse tail fascicles in uniaxial tension. *Journal of biomechanics*, 37(6):907–916, 2004.

[222] Gerard A Ateshian, Kevin D Costa, Evren U Azeloglu, Barclay Morrison, and Clark T Hung. Continuum modeling of biological tissue growth by cell division, and alteration of intracellular osmolytes and extracellular fixed charge density. *Journal of biomechanical engineering*, 131(10):101001, 2009.

[223] Kaj S Emanuel, Albert J van der Veen, Christine ME Rustenburg, Theodoor H Smit, and Idsart Kingma. Osmosis and viscoelasticity both contribute to time-dependent behaviour of the intervertebral disc under compressive load: A caprine in vitro study. *Journal of Biomechanics*, 70:10–15, 2018.

[224] Pieter-Paul A Vergroesen, Albert J van der Veen, Kaj S Emanuel, Jaap H van Dieën, and Theodoor H Smit. The poro-elastic behaviour of the intervertebral disc: a new perspective on diurnal fluid flow. *Journal of biomechanics*, 49(6):857–863, 2016.

[225] Sohei Ebara, James C Iatridis, Lori A Setton, Robert J Foster, Van C Mow, and Mark Weidenbaum. Tensile properties of nondegenerate human lumbar anulus fibrosus. *Spine*, 21(4):452–461, 1996.

[226] Robby D Bowles, Rebecca M Williams, Warren R Zipfel, and Lawrence J Bonassar. Self-assembly of aligned tissue-engineered annulus fibrosus and intervertebral disc composite via collagen gel contraction. *Tissue Engineering Part A*, 16(4):1339–1348, 2010.

[227] Nandan L Nerurkar, Sounok Sen, Alice H Huang, Dawn M Elliott, and Robert L Mauck. Engineered disc-like angle-ply structures for intervertebral disc replacement. *Spine*, 35(8):867, 2010.

[228] S Rigozzi, R Müller, and Jess G Snedeker. Local strain measurement reveals a varied regional dependence of tensile tendon mechanics on glycosaminoglycan content. *Journal of biomechanics*, 42(10):1547–1552, 2009.

[229] DJ Botsford, SI Esses, and DJ Ogilvie-Harris. In vivo diurnal variation in intervertebral disc volume and morphology. *Spine*, 19(8):935–940, 1994.

[230] JP Urban and JF McMullin. Swelling pressure of the lumbar intervertebral discs: influence of age, spinal level, composition, and degeneration. *Spine*, 13(2):179–187, 1988.

[231] An M Nguyen, Wade Johannessen, Jonathon H Yoder, Andrew J Wheaton, Edward J Vresilovic, Arijitt Borthakur, and Dawn M Elliott. Noninvasive quantification of human nucleus pulposus pressure with use of t1$\rho$-weighted magnetic resonance imaging. *The Journal of Bone and Joint Surgery. American volume.*, 90(4):796, 2008.

[232] Ramesh N Vaishnav and Jafar Vossoughi. Estimation of residual strains in aortic segments. In *Biomedical Engineering II*, pages 330–333. Elsevier, 1983.

[233] Xiaomei Guo, Yoram Lanir, and Ghassan S Kassab. Effect of osmolarity on the zero-stress state and mechanical properties of aorta. *American Journal of Physiology-Heart and Circulatory Physiology*, 293(4):H2328–H2334, 2007.

[234] Yoram Lanir. Osmotic swelling and residual stress in cardiovascular tissues. *Journal of biomechanics*, 45(5):780–789, 2012.

[235] Wade Johannessen, Joshua D Auerbach, Andrew J Wheaton, Alykhan Kurji, Arijitt Borthakur, Ravinder Reddy, and Dawn M Elliott. Assessment of human disc degeneration and proteoglycan content using t1$\rho$-weighted magnetic resonance imaging. *Spine*, 31(11):1253, 2006.

[236] Prachi Pandit, Jason F Talbott, Valentina Pedoia, William Dillon, and Sharmila Majumdar. T1$\rho$ and t2-based characterization of regional variations in intervertebral discs to detect early degenerative changes. *Journal of Orthopaedic Research*, 34(8):1373–1381, 2016.

[237] Edward Bonnevie, Sarah Gullbrand, Beth Ashinsky, Tonia Tsinman, Dawn Elliott, Harvey Smith, and Robert Mauck. Release of residual strain activates mechanosensing and contractility-dependent apoptosis in af cells. *ORS abstract*, 2019.

[238] SS Sivan, S Roberts, JPG Urban, J Menage, J Bramhill, D Campbell, VJ Franklin, F Lydon, Y Merkher, A Maroudas, et al. Injectable hydrogels with high fixed charge density and swelling pressure for nucleus pulposus repair: biomimetic glycosaminoglycan analogues. *Acta biomaterialia*, 10(3):1124–1133, 2014.

[239] Pierre C Milette, Suzanne Fontaine, Luigi Lepanto, Étienne Cardinal, and Guy Breton. Differentiating lumbar disc protrusions, disc bulges, and discs with normal contour but abnormal signal intensity: Magnetic resonance imaging with discographic correlations. *Spine*, 24(1):44–53, 1999.

[240] Stuart M McGill and Craig T Axler. Changes in spine height throughout 32 hours of bedrest. *Archives of physical medicine and rehabilitation*, 77(10):1071–1073, 1996.

[241] Thomas Reilly, Adrian Tyrrell, and JD1G Troup. Orcadian variation in human stature. *Chronobiology International*, 1(2):121–126, 1984.

[242] Daniel L Belavy, Michael Adams, Helena Brisby, Barbara Cagnie, Lieven Danneels, Jeremy Fairbank, Alan R Hargens, Stefan Judex, Richard A Scheuring, Roope Sovelius, et al. Disc herniations in astronauts: What causes them, and what does it tell us about herniation on earth? *European Spine Journal*, 25(1):144–154, 2016.

[243] Douglas G Chang, Robert M Healey, Alexander J Snyder, Jojo V Sayson, Brandon R Macias, Dezba G Coughlin, Jeannie F Bailey, Scott E Parazynski, Jeffrey C Lotz, and Alan R Hargens. Lumbar spine paraspinal muscle and intervertebral disc height changes in astronauts after long-duration spaceflight on the international space station. *Spine*, 41(24):1917, 2016.

[244] Jeannie F Bailey, Stephanie L Miller, Kristine Khieu, Conor W O'Neill, Robert M Healey, Dezba G Coughlin, Jojo V Sayson, Douglas G Chang, Alan R Hargens, and Jeffrey C Lotz. From the international space station to the clinic: how prolonged unloading may disrupt lumbar spine stability. *The Spine Journal*, 18(1):7–14, 2018.

[245] Ruben Ngnitewe Massa and Fassil B Mesfin. Herniation, disc. In *StatPearls [Internet]*. StatPearls Publishing, 2017.

[246] Sean Gallagher, William S Marras, Kermit G Davis, and Kimberly Kovacs. Effects of posture on dynamic back loading during a cable lifting task. *Ergonomics*, 45(5):380–398, 2002.

[247] Mohamed Amine Chetoui, Olivier Boiron, Moncef Ghiss, Abdelwaheb Dogui, and Valérie Deplano. Assessment of intervertebral disc degeneration-related properties using finite element models based on rho h -weighted mri data. *Biomechanics and modeling in mechanobiology*, 18(1):17–28, 2019.

[248] M Ghiss, B Giannesini, P Tropiano, Z Tourki, and O Boiron. Quantitative mri water content mapping of porcine intervertebral disc during uniaxial compression. *Computer methods in biomechanics and biomedical engineering*, 19(10):1079–1088, 2016.

[249] Jalil Nazari, Malcolm H Pope, and Richard A Graveling. Feasibility of magnetic resonance imaging (mri) in obtaining nucleus pulposus (np) water content with changing postures. *Magnetic resonance imaging*, 33(4):459–464, 2015.

[250] Norbert Boos, Ake Wallin, Thomas Schmucker, Max Aebi, and Chris Boesch. Quantitative mr imaging of lumbar intervertebral discs and vertebral bodies: methodology, reproducibility, and preliminary results. *Magnetic resonance imaging*, 12(4):577–587, 1994.

[251] DH Carr, J Brown, GM Bydder, RE Steiner, HJ Weinmann, U Speck, AS Hall, and IR Young. Gadolinium-dtpa as a contrast agent in mri: initial clinical experience in 20 patients. *American Journal of Roentgenology*, 143(2):215–224, 1984.

[252] Stephen W Hughes. Archimedes revisited: a faster, better, cheaper method of accurately measuring the volume of small objects. *Physics education*, 40(5):468, 2005.

[253] Dosik Hwang, Sewon Kim, Nirusha A Abeydeera, Sheronda Statum, Koichi Masuda, Christine B Chung, Palanan Siriwanarangsun, and Won C Bae. Quantitative magnetic resonance imaging of the lumbar intervertebral discs. *Quantitative imaging in medicine and surgery*, 6(6):744, 2016.

[254] Mark Bydder, Andres Rahal, Gary D Fullerton, and Graeme M Bydder. The magic angle effect: a source of artifact, determinant of image contrast, and technique for imaging. *Journal of Magnetic Resonance Imaging: An Official Journal of the International Society for Magnetic Resonance in Medicine*, 25(2):290–300, 2007.

[255] Weili Lin, Ramesh Venkatesan, Kilichan Gurleyik, Yong Y He, William J Powers, and Chung Y Hsu. An absolute measurement of brain water content using magnetic resonance imaging in two focal cerebral ischemic rat models. *Journal of Cerebral Blood Flow & Metabolism*, 20(1):37–44, 2000.

[256] EM Shapiro, A Borthakur, JH Kaufman, JS Leigh, and R Reddy. Water distribution patterns inside bovine articular cartilage as visualized by1h magnetic resonance imaging. *Osteoarthritis and Cartilage*, 9(6):533–538, 2001.

[257] J Perry, V Haughton, PA Anderson, Y Wu, J Fine, and C Mistretta. The value of t2 relaxation times to characterize lumbar intervertebral disks: preliminary results. *American journal of neuroradiology*, 27(2):337–342, 2006.

[258] O Karakida, H Ueda, M Ueda, and T Miyasaka. Diurnal t2 value changes in the lumbar intervertebral discs. *Clinical radiology*, 58(5):389–392, 2003.

[259] Paul M Parizel, Homme AJ Dijkstra, GéP J Geenen, Peter AM Kint, Rob J Versteylen, Peter J van Wiechen, and Arthur M De Schepper. Low-field versus high-field mr imaging of the knee: a comparison of signal behaviour and diagnostic performance. *European journal of radiology*, 19(2):132–138, 1995.